JNC TN9400 2005-045

Interpretation of the CABRI-RAFT TPA2 Test

(Research Document)

June 2005

O-arai Engineering Center
Japan Nuclear Cycle Development Institute

〒319-1184　茨城県那珂郡東海村村松4番地49
核燃料サイクル開発機構
技術展開部　技術協力課
電話：029-282-1122（代表）
ファックス：029-282-7980
電子メール：jserv@jnc.go.jp

JNC TN9400 2005-045
June 2005

Interpretation of the CABRI-RAFT TPA2 Test

(Research Document)

Hidemasa YAMANO[*1], Yu-ichi ONODA[*2], Yoshiharu TOBITA[*2], Ikken SATO[*2]

Abstract

During the course of core disruptive accidents in liquid-metal fast reactors, a boiling pool of molten fuel/steel mixture could be formed. The stability of this boiling-pool, for which in-pile experimental data with real reactor materials are very limited, plays an important role in the determination of the accident scenarios.

In the TPA2 test of the CABRI-RAFT program (from 1996 to 2002), the fuel-to-steel heat transfer characteristic governing the pool behavior was investigated as a joint study with the French 'Institut de Radioprotection et de Sûreté Nucléaire' (IRSN). This test was performed in the CABRI reactor in 2001 using a test capsule that contains fresh 12.3 % enriched UO_2 pellets with embedded stainless steel balls. Following a pre-heating phase, the capsule was submitted to a transient overpower resulting in fuel melting and steel vaporization.

The steel vapor-pressure build-up observed during the transient was quite weak, suggesting the presence of a strong mechanism to limit the fuel-to-steel heat transfer. The detailed experimental data evaluation suggested a phenomenon that the steel vaporization at the surface of steel ball blanketed the steel from molten fuel. This vapor blanketing seems to be a mechanism reducing the fuel-to-steel heat transfer. An analysis with the SIMMER-III code, a multi-component multi-phase thermal-hydraulics code, was performed in this study. This code simulation could well reproduce the pressure buildup and boiling pool behavior which occurred in the test by applying specifically reduced heat transfer coefficients.

*1 FBR Cycle Safety Engineering Group, System Engineering Technology Division, O-arai Engineering Center, JNC.

*2 Nuclear System Safety Research Group, Advanced Technology Division, O-arai Engineering Center, JNC.

JNC TN9400 2005-045
2005年 6月

CABRI-RAFT TPA2 試験の解釈

（研究報告）

山野 秀将[*1], 小野田 雄一[*2], 飛田 吉春[*2], 佐藤 一憲[*2]

要旨

ナトリウム冷却高速炉の炉心損傷事故においては、溶融燃料／スティール混合物による沸騰プールを形成する可能性がある。このような沸騰プールの安定性に関する研究は事象推移に大きな影響を与えるため非常に重要であるが、実物質を用いた炉内試験はかなり限られている。

そこで、CABRI-RAFT 試験計画(1997 年～2002 年)の TPA2 試験は、炉心物質の沸騰プール挙動を支配する燃料－スティール間熱伝達特性を調べる目的で、仏国 IRSN との共同研究として 2001 年に CABRI 炉で実施された。試験では、12.3%濃縮度の UO_2 新燃料ペレットにステンレス・スティール球を埋め込んだテストカプセルを使用し、予熱段階を経て、燃料溶融およびスティール蒸発を生ずる過出力を印加した。

過渡中に観察されたスティール蒸気の圧力発生挙動は極めて弱く、燃料－スティール間熱伝達を抑制するメカニズムの存在が示唆された。詳細な試験データ評価により、スティール球表面で生成されたスティール蒸気がスティール球自身を覆い、溶融燃料との接触を阻害するという現象が推定された。この蒸気のブランケッティング挙動が燃料－スティール間熱伝達を抑制するメカニズムであると考えられる。多相多成分熱流動解析コード SIMMER-III を用いて解析を実施した結果、熱伝達係数を特別に低下させることによって、試験で起きた圧力上昇および沸騰プール挙動をよく再現できた。

*1 大洗工学センター システム技術開発部 FBR サイクル安全設計グループ
*2 大洗工学センター 要素技術開発部 リスク評価研究グループ

Contents

List of Tables

List of Figures

1 Introduction

In regard to the initiating phase of unprotected loss-of-flow (ULOF) accidents in liquid-metal fast reactors (LMFRs), a reasonable technical basis has been established to suppress mechanical energy release provided that appropriate consideration, such as limiting positive void worth, is paid to the core design so that an extremely rapid void-reactivity insertion can be avoided in the early initiating phase [1]. As far as this basic requirement is met, power increase due to the core-wide coolant voiding can be effectively terminated by fuel dispersal. The CABRI-1, -2 and -FAST programs [2, 3] gave reliable experimental database for this self-limiting fuel-dispersion mechanism.

Based on the success that severe recriticality is eliminated in the initiating phase, it was intended in the CABRI-RAFT program (from 1996 to 2002) [4] to step into the transition phase, for which in-pile experimental data were very limited, together with the French 'Institut de Radioprotection et de Sûreté Nucléaire' (IRSN). One of the key issues in the transition phase is a possibility of energetic recriticality with a large-scale whole-core pool sloshing, in which coherent inward radial movement of liquid fuel takes place. Such a sloshing can be driven by a rapid steel-vapor-pressure build-up in the core center pushing firstly the liquid fuel outward and allowing then inward fuel motion driven by the gravity force. This type of sloshing can lead to neutronic power excursions and resultant energetics. In the reactor safety analysis, it was often the case to have rapid steel vapor formation followed by the liquid sloshing. Because the steel-vapor formation behavior has a large uncertainty, the analytical results must be carefully examined.

One of the main subjects in the RAFT program is to obtain basic information on heat-transfer characteristics between molten fuel and entrapped steel using the reactor materials. The fuel-to-steel heat transfer with steel boiling condition is considerably dependent on development of the steel vapor bubbles, which may serve as the blanket. The two-component (fuel and steel) boiling behavior is believed to be different from a single component (fuel) one, in which no blanket is present. Therefore, in the RAFT program, using the fuel/steel mixture, it was intended to realize the two-component system.

It was considered that the heat transfer is initially high with effective liquid-to-liquid contact. In the RAFT program, the transient heat transfer characteristics with steel boiling were investigated in two types of tests. One is the TPA2 test discussed in this report. This test was performed in the CABRI reactor in July 2001. The other is the TP3 test series, which were carried out in the SILENE reactor. In the latter test, the free

volume was limited so that liquid-to-liquid heat transfer could be realized in a confined crucible. It is, however, very likely that a significant amount of impurity gas released from the zirconia crucible provided a very turbulent mixing, leading to rather high fuel-to-steel heat transfer. The liquid-to-liquid contact area had large uncertainty, whereas, the outcomes of the TP3 test series provided valuable information related to the heat transfer under significant mixing condition.

The main objective of the TPA2 test is to obtain experimental characteristics of the heat transfer from fuel to steel in the two-phase mixture of liquid fuel and steel. In contrast to the TP3 condition, the space for expansion of fuel and steel was available, thereby allowing development of two-phase condition, which is close to the reactor condition. Furthermore, it was intended to get information on characteristics of vapor-mixture momentum coupling under power transient through observation of material motion. As the background for this interest, there was an idea that a bubbly-flow-regime could continue in the high-void-fraction domain under a rapid transient condition in contrast with a steady-state condition due to more tight vapor-liquid momentum coupling.

In the present study, a most probable event progression during the transient was deduced from the experimental data interpretation and analytical evaluations with the SIMMER-III code, a multi-component multi-phase thermal-hydraulics computer code [5, 6].

2 Experimental conditions

2.1 Fuel capsule characteristics

The main characteristics of the three fuel capsules employed in the test are summarized in **Table 1** and **Fig. 1.** One capsule called as Capsule 1 contains fresh enriched UO_2 pellets without steel balls. The other two capsules called as Capsule 2 and Capsule 3 contain fresh enriched UO_2 pellets with embedded stainless steel balls.

Although Niobium was originally selected for the crucible because larger heat-resistance material was preferable, the Niobium tube was not allowed in this test because of expected eutectic formation with stainless steel at about 1400K. Thus, stainless steel (316L) was adopted for the crucible containing fuel pellets. Its tube thickness is 2.4mm and bottom thickness is 3mm. The gas plenum of each capsule is filled with 0.01MPa of Argon gas at room temperature. The axial positions at bottom of fissile column for Capsule 3, Capsule 2 and Capsule 1 are -6706.5mm, -6836.5mm and -6966.5mm, respectively, from the ground level in the reactor.

Pressure measurements inside Capsule 1 and Capsule 2 were performed by transducers located outside the neutron flux field in connection with the top ends of the capsules by capillary tubes. In order to protect the inlet hole of the capillary tube in the capsule from the molten mixture, labyrinth shielding structure was implemented at the upper part of each capsule.

2.1.1 Fuel pellets

The fuel pellets were made of fresh UO_2 powder enriched at 12.3 weight %. Each fuel column in the capsules was composed with four pellets, of which mean height and diameter were respectively 43.2mm (4 × 10.8mm) and 14.0mm. Porosity of these pellets was about 36%.

For Capsule 1, two holes of 2mm in diameter were drilled for W/Re thermocouples at the radius of 2.5mm from the center of the fuel column in order to know the temperature inside the fuel column before/during the transient and to identify the coupling factor between the core power and the fuel capsule.

For Capsule 2 and Capsule 3, 40 steel balls were embedded inside the fuel column. The diameter of the balls was 1mm. There were two levels with five balls in each pellet.

2.1.2 Impurities in the fuel pellets

Since volatile impurities included in the fuel pellets (fuel grains and steel balls) could

possibly be released during the power pulse, their gas pressure may affect measured pressures during the transient. Therefore, thermal treatment has been performed at every manufacturing stage of the fuel pellets in order to decrease the amount of impurity gas. The amounts of impurities obtained from the chemical analysis are listed in **Table 2**. Although only a very small part of the impurities is expected to contribute to gas release, maximum amount of potential gas release from the impurities is 3.2 μ mol/g$_{UO2}$.

2.1.3 Test section around the fuel capsules

The main characteristics of the test section around the fuel capsules are given in **Table 3**. Sodium coolant flowed at about 673K in the test channel around the fuel capsules. The flow rate was 6.4×10^{-4} m^3/s just before the transient. The channel was surrounded by a Niobium tube with diameter and thickness of respectively 24mm and 5.25mm. Its inner wall was CVD (Chemical Vapor Deposition) coated to avoid a steel/Niobium eutectic formation.

The radial heat loss was reduced by a 1.5mm-thickness Xenon gap just behind the Niobium tube. Some leakage detectors were installed in this gap at the top and the bottom of Niobium tube to indicate a hypothetical sodium leakage into this gap.

2.2 Instrumentation during the test

2.2.1 Core power detectors

The CABRI core power is usually measured by four Boron ionization chambers located in the pool. The power indicated by these chambers was checked by a thermal balance on the core coolant at a steady-state power plateau performed during the start-up campaign. Maximum deviation of the core power given by the chambers from the measurement of the thermal balance was 3.8%. Such deviation was already observed in the previous tests and was within the range of uncertainties, and hence the reliability of core power measurement was acceptable.

The coupling factor, defined as the ratio of the core power measured by the power chambers to the power released into the fissile fuel, was determined by hodoscope measurements. As a consequence of the estimation, the coupling factors with uncertainties of twice standard deviation for each capsule were given by

4018.6 ± 179.4 (2σ) for Capsule 1,

3496.9 ± 234.6 (2σ) for Capsule 2, and

4231.0 ± 268.6 (2σ) for Capsule 3.

Finally the mean power densities per unit of core power for each capsule were obtained:

5.54 ± 0.24 (2σ) W/g$_{UO2}$/MW$_{core}$ for Capsule 1,

6.21 ± 0.42 (2σ) W/g$_{UO2}$/MW$_{core}$ for Capsule 2, and

5.13 ± 0.32 (2σ) W/g$_{UO2}$/MW$_{core}$ for Capsule 3.

It should be noticed that these estimated values are close to results given by a pre-test neutronic calculation.

2.2.2 Thermocouples

All the thermocouples were Cr-Al (K-type) thermocouples except for two W/Re thermocouples (TC19-TC20) located inside the fuel column of Capsule 1. **Figure 1** depicts positions of all thermocouples in the capsules. These thermocouples were installed in the capsule wall, in the fuel column, in the upper part of the gas plenum, in the coolant channel, and in the fission chambers. For Capsule 2, double thermocouples (TC1-TC8) were adopted to estimate the heat flux across crucible wall at four axial levels, and several thermocouples (TC9-TC12) were placed to check the azimuthal asymmetry at two levels in the gas plenum.

2.2.3 Pressure transducers

To measure the pressures inside Capsule 1 and Capsule 2, two pressure transducers for each capsule were installed in a chamber, which was connected to the gas plenum of each capsule through a capillary tube of about 1mm in diameter as shown in **Fig. 1**. There was no pressure measurement for Capsule 3.

2.2.4 Other instrumentation devices

Two flowmeters were mounted at the inlet and exit of the coolant channel. To observe the fuel motion, the hodoscope measurement was applied during the transient and non-destructive examinations performed after the transient confirmed the final fuel configuration. Two different data acquisition devices at sampling rates of 500Hz and 4kHz worked properly during the whole test.

2.3 Low power operation

In order to heat the fuel pellets to target temperature well below the melting point of steel balls, five power plateaus were gradually performed before the transient. Then, a steady-state power plateau at 900kW was performed for about 8 minutes. During this phase, the measurements of the temperatures inside the fuel column, core power and an axial power form by the hodoscope were checked. The axial power profile of the CABRI core measured by the hodoscope is shown in **Fig. 2**. The peak power node of

the core is nearly placed at Capsule 2. Thus the power shape of Capsule 2 is almost flat near the peak power level. The power in Capsule 1 is slightly higher at the upper part of fuel column, whereas the power in Capsule 3 is much lower at the upper part than at the lower part. Axial and radial power profiles derived from pre-test neutronic calculation are respectively presented in **Figs. 3** and **4**. The axial profiles were used to define the mean axial form factors for the coupling factor determination from the hodoscope measurement. During the steady state at 900kW, the mean power densities for each capsule are given by

5.0 ± 0.4 (2σ) W/g$_{UO2}$ for Capsule 1,

5.6 ± 0.5 (2σ) W/g$_{UO2}$ for Capsule 2, and

4.6 ± 0.4 (2σ) W/g$_{UO2}$ for Capsule 3.

As for the cooling conditions, the channel flow rate was 6.4×10^{-4} m^3/s, and inlet and outlet of sodium temperatures were 673.9K and 675.5K, respectively. The thermocouples of TC19 and TC20 inside fuel column of Capsule 1 indicated respectively 1156K and 1282K before the transient.

2.4 Transient characteristics

In order to quantify fuel-to-steel heat transfer, transient duration was an important factor and a slow heating was preferable. Therefore, feasibility of a flat-TOP pulse, which rose in 0.1s and stayed at a plateau for 1.5s, followed by a pulse of half-height width of 200ms was studied at the beginning. However, it became clear that Doppler effect was much higher than that in conventional CABRI transients because of the initial low-power operation required in the TPA2 test. As a result, the half-height width could not be larger than 100ms.

Following the pre-heating phase, the transient power pulse was injected. A dual-peak pulse was adopted so as to obtain the maximum energy deposit in the CABRI reactor. **Figure 5** shows core power and core energy histories after TOP triggering. Scram time was 0.666s after TOP onset. The core energy deposits at 0.6s and 1.2s after TOP onset were 190 ± 10 (2σ) MJ and 201.6 ± 10 (2σ) MJ, respectively. Using the coupling factors described above, mean energy deposits in each capsule at 0.6s were

1053 ± 71 (2σ) J/g$_{UO2}$ for Capsule 1,

1179 ± 99 (2σ) J/g$_{UO2}$ for Capsule 2, and

975 ± 79 (2σ) J/g$_{UO2}$ for Capsule 3.

Similarly the mean energy deposits for each capsule at 1.2s were

1117 ± 76 (2σ) J/g$_{UO2}$ for Capsule 1,

1251 ± 105 (2σ) J/g$_{UO2}$ for Capsule 2, and

1035 ± 84 (2σ) J/g$_{UO2}$ for Capsule 3.

3 Experimental results

3.1 Experimental data during the transient

3.1.1 Pressure transducer measurement

Figure 6 compares short-term pressure histories detected by the pressure transducer P1 for Capsule 1 and P3 for Capsule 2 from 0.3s to 1.0s, together with the core energy trace. Measurement range of these transducers was between 0MPa and 1.4MPa, and the data were recorded with the fast digital recording device. Initial pressures were determined 2.7×10^{4}Pa for Capsule 1 and 2.3×10^{4}Pa for Capsule 2 by averaging the values between 0.0s and 0.3s. During the transient, two discrete pressure rise phases were observed for both capsules. For Capsule 1, the signal P1 started to increase at 0.45s and reached about 3.5×10^{4}Pa at 0.48s, and then it decreased slowly close to the initial value at 0.55s. At almost the end of power transient at 0.55s, the pressure began to increase gradually again and reached about 4.3×10^{4}Pa at about 0.9s. For Capsule 2, the signal P3 started to increase at 0.43s and reached about 5.7×10^{4}Pa at 0.48s. After sudden decrease to about 4.5×10^{4}Pa at 0.55s, a slow pressure rise up to about 7.0×10^{4}Pa occurred till 0.68s, and then the pressure decreased gradually.

The short-term pressure histories measured by the other pressure transducers P2 for Capsule 1 and P4 for Capsule 2 are presented in **Fig. 7**. It should be noticed that the measurement range of P2 and P4 was rather large (0-14MPa), and the absolute values were not meaningful in the range of interest here (0-0.1MPa). Their trend, however, was useful to confirm that the other pressure transducers P1 and P3 were measuring real physical processes. Initial pressures for each capsule are given about 3.0×10^{4}Pa for Capsule 1 and about 3.1×10^{4}Pa for Capsule 2, and maximum values of two pressures peaks are indicated about 1.5×10^{5}Pa and about 1.6×10^{5}Pa for Capsule 1 and about 2.4×10^{5}Pa and about 2.5×10^{5}Pa for Capsule 2.

Shown in **Fig. 8** are long-term pressure histories measured by P1 and P3 from 0s to 15s. After the pressure peaks around 1s, the pressures decreased slowly to constant pressures at 8s. The pressures continued from 8s to 15s are about 2.7×10^{4}Pa for Capsule 1 and about 3.9×10^{4}Pa for Capsule 2. Similar pressure-decrease histories were obtained by averaging 10 data points of the P2 and P4 measurements as displayed in **Fig. 9**.

3.1.2 Thermocouple measurement

- Fuel temperature inside Capsule 1

The two thermocouples TC19 and TC20 indicated respectively 1156K and 1282K as the initial fuel temperatures. Since the local power was almost the same at these thermocouple positions, the discrepancy seems to be caused by heat loss to the crucible bottom cooled by sodium flow. **Figure 10** shows the short-term fuel temperatures recorded by TC19 and TC20 along with the core energy. At 0.43s and 0.53s, two small increases corresponding to the two core power peaks were observed: the thermocouples were in fact heated by the incoming neutron and gamma fluxes. After the rapid temperature increase starting at about 0.65s, the fuel temperatures reached 2573K, above which the measured values were no more qualified. The signal perturbations with fast slope inversion and the amplifier saturation occurred several times as can be observed in **Fig. 11**. Therefore, the thermocouples were considered to have been failed from about 0.75s to about 4s. It should be noted that the thermocouple signals recovered to indicate the apparently correct behavior during the cooling phase after 4s as if new hot junctions were established. This was confirmed by the good measurement of the isothermal condition at 680K after the test. Furthermore, the time response of the W/Re thermocouples of 1.6mm in diameter was very slow (several hundreds of milliseconds) compared with 40ms of the K-type thermocouples commonly used in the sodium channel.

- Capsule 1

Figure 12 shows the temperatures inside the crucible wall at the fuel level in Capsule 1. Since TC14 was placed 0.25mm closer to the fuel than TC15, the former temperature was higher than the latter one, although the former thermocouple was located near the crucible bottom cooled by sodium flow. After around 1s, the signals decreased slowly.

The other thermocouples in Capsule 1 measured the temperatures in the crucible wall at the gas-plenum level and in the gas-plenum top part as shown in **Fig. 13**. After the heating by neutron and gamma fluxes, small temperature increases were observed in all the thermocouples. These seem to have been heated not by the expanded liquid fuel but by the high-temperature gas generated inside the capsule.

- Capsule 2

The temperatures in the crucible wall at lower and upper fuel levels in Capsule 2 are indicated in **Figs. 14** and **15**. These data also exhibited the temperature difference between the two thermocouples at the same level, which provided the heat flux

estimation across the wall. After the two small increase steps due to the power pulse effect, sharp temperature rises occurred leading to the maximum values at about 1s, and then they decreased slowly. The heat flux seems to have been smaller at the lower part because of the heat loss toward the crucible bottom.

Figures 16 and **17** show the temperatures in the crucible wall at lower and upper gas-plenum levels in Capsule 2, together with the temperature differences between the thermocouples at the same level. Following the temperature rises due to the power effect, all the temperature data increased slightly faster than that of Capsule 1, and then decreased slowly. One can notice that the temperature differences at the two levels became negative before the cooling phase. This suggests that the coolant at this axial level have been hotter than the capsule wall because of the rapid heating during its passage along the fuel region.

Since the temperature differences between the thermocouples located at different azimuth were small (maximum about 5K) as indicated in **Fig. 18**, we can say that the azimuthal temperature distributions were approximately uniform in the gas-plenum level. These signals did not show any evidence of the fuel expansion into the gas-plenum zone.

- Capsule 3

For Capsule 3, the thermocouples measured the temperatures in the crucible wall at the fuel level, at the gas-plenum level, and at the top of crucible. First one and last two of them are presented respectively in **Figs. 19** and **20**. Following the small jump due to the power effect, the temperature in the fuel level rose and decreased slowly, similarly to those in the other capsules. The temperatures were slightly lower compared with the other capsules because of the smaller injected power.

3.1.3 Hodoscope observation

Figures 21, **22** and **23** give the variation of the signal versus time during the power transient for the hodoscope rows viewing respectively the region of Capsule 1, Capsule 2 and Capsule 3. The corresponding positions of each row and the capsule locations are drawn in these figures. For Capsule 1, signal decreases in row 31 corresponding to the top of the fuel column and in row 32 were observed at 0.559s and at 0.560s, respectively. In rows 33 and 34, signal increases can be seen respectively at 0.553s and 0.583s, and hence it was found that the fuel accumulated at the lower part of the fuel column. For Capsule 2, signals in row 25, 26 and 27 slightly increased at about 0.533s. This might have resulted from the event corresponding to the first pressure increase. We can see that successive signal fall took place in row 25 corresponding to the top of the fuel column at 0.547s, and small signal decrease were detected in row 26 from 0.561s to

0.633s. Since no signal variations were obtained in row 24 located 3.5mm above the fuel column, it was obvious that molten fuel did not expand nor disperse into the cover-gas region. For Capsule 3, signal decrease was seen in row 19 corresponding to the top of the fuel column. The hodoscope observation evidenced that the fuel shrinkage began without expansion at about 0.55s when the core energy was injected sufficiently into the fissile fuel.

3.2 Post-test examination (PTE)

3.2.1 Non-destructive examination

The post-test non-destructive examinations (X-ray radiography, X-ray tomography and γ-scanning) were performed in order to compare the initial and final states of the fuel distribution. **Figure 24** compares the pre-test and post-test X-ray radiographs for all the capsules. Large reductions of the fuel column heights due to the fuel melting were confirmed in all the capsules. The fuel length was reduced from 43mm to about 33mm with a small residual fuel crust on the crucible wall and heterogeneous upper surface. This significant contraction corresponds to about 23% against 36% of the initial porosity. Since the fuel crust cannot be seen over the initial fuel column, no fuel expansion is considered to have occurred in the gas plenum for all the capsules. For each of the fuel stacks, the fuel bottom part seems not to have been molten, because a small gap between the fuel and the upper surface of the crucible bottom was kept even after the test. The X-ray tomograms and γ-scans also indicated the fuel accumulation at the lower part of the fuel columns and neither fuel expansion nor dispersion into the cover-gas region. Furthermore, neither erosion nor damage of the crucible wall was observed from the tomograms.

3.2.2 Destructive examination

Axial cutting was applied for Capsule 2 and Capsule 3. For each of these capsules, a 33mm-long sample with its bottom level at 5.8mm above the capsule bottom was selected. We focused here only on Capsule 2 defined as the main capsule. This is because a great number of findings from the sample of Capsule 2 could serve for interpretation of the TPA2 test.

- Metallographic examination

A macrograph of the sample of Capsule 2 without a chemical etching is presented in **Fig. 25**. The rectangle regions depicted in the figure represent the location of microstructural examinations described below. In the following, main features observed in the examination are described and the numbers presented in the figure denotes the

location uttered to in this description.

1. Neither deformation nor damage of the steel crucible can be observed in the cutting in accordance with the non-destructive examination results.
2. The gap between the fuel and the crucible in the right side of the cut tends to be wider at the upper level. If the solidification process was a uniform one, a parallel gap should have been created. The present situation shows that the fuel outer part froze rather early compared with the inner part. Thus, the probable fuel shrinkage near the upper surface in the late cooling phase is considered to have created the wide gap as well as the conical shape at the fuel upper surface (see number 3 presented below).
3. Subsidence of the frozen fuel can be seen at the upper fuel part, where the fuel is dense without large porosities.
4. A discontinuous thin layer of fine porosities (about 50 μ m to 70 μ m thickness) is observed at the extreme fuel periphery of the sample as shown in "Radius 1" in **Fig. 26**. Such microstructure in this area can be clearly distinguished from that in the inner part, where the fuel has been certainly molten. From this aspect, this thin layer at the fuel-pellet periphery is expected to have been unmolten. The formation of the unmolten fuel shell has been investigated by calculating temperature inside the fuel capsule using a heat conduction code (see **Appendix A**). In this analysis, the actual heat loss to crucible was simulated by giving an appropriate thermal resistance in a gap between fuel pellet and crucible wall. The calculation showed that the fuel temperature became the highest at the intermediate part between the central part and the outer part just after the power injection due to the neutron-flux enhancement. In the outer part, in spite of the highest neutron flux, the temperature was considerably low due to the significant heat loss toward the wall. The calculated temperature at the 50 μ m-thickness layer was always lower than the melting point, whereas the fuel in the inner part was completely molten. This evaluation supports that a very thin shell of unmolten fuel obviously remained in this test. It should also be added that, in this part, oxidation might create a large number of porosities inside the material during the pre-heating phase. This phenomenon is commonly observed for fuel sintered under no reducing atmosphere such as Argon gas.
5. A line of tiny pores (porosity line) is observed in parallel with the crucible wall. From the observation of **Fig.-27**, these porosities are aligned on an about

200 μ m-thickness layer at about 1.5mm away from the external fuel boundary. Inside this line, large and elongated pores can be seen, while outside this line up to the fuel periphery, fuel is characterized by high density with few porosities.

6. Porosities with an elongated shape in radial direction can be seen in the intermediate region between the central fuel region and the outer fuel region. Accumulation of large porosities is observed in the central fuel region. This situation suggests coalescences of porosities during the cooling phase after the transient.

7. In **Fig. 26** after the chemical etching, very long columnar grains of several millimeters can be seen along the radial direction. Such appearance has also been obtained in the CABRI-A5 test, which was a transient-over-power test with an energy release of 1.56kJ/g using a fresh UO_2 pin. In this test, the power trace with half-height width of about 100ms was used similarly to the TPA2 test. The morphology of fuel samples in both tests revealed a typical feature of slow solidification of molten fuel in the direction of the thermal gradient. In the center of the sample, the grains are smaller and lose their columnar characteristic.

8. Except for the upper surface of the sample in the macrograph, the porosity distribution looks like axially uniform and likely to have been dominated by the radial temperature distribution.

9. Some superficial metallic deposits appear at the upper surface of the fuel stack. The thickness of the thin layers reaches locally more than 50 μ m. This steel could come either from the steel balls or steel foil placed initially above the fuel column. This steel foil, which was introduced in order to avoid any motion of the pellets prior to the transient, had a thickness of about 0.1mm.

10. A steel agglomerate of equivalent diameter of about 1.5mm is seen in a bubble of about 2mm in diameter. As shown in **Fig. 28**, since large quantity of small steel droplets were detected around the bubble with high density, steel vapor seems to have been present in the bubble. Another steel agglomerate is observed between the fuel external boundary and the crucible wall. This is due probably to overflow of liquid steel into the gap between the shrinking fuel and the crucible during the cooling phase.

11. An enlarged picture at the "central area" of the upper part is shown in **Fig. 29**. The pores are very large at the center side and are connected with many large cracks which finally form the continuous network. The steel phase is

essentially localized inside the porosity and the cracking network, and only very few small metallic inclusions are detected inside the fuel matrix. This may be explained with liquid-steel penetration into the cracks after the fuel freezing. The little empty cracks in the vicinity of the steel phase seem to have been created during the cooling phase after the steel solidification.

12. From the macrograph, "Radius 2" seems to represent a typical porosity distribution of the sample except for the upper part. A general view of "Radius 2" and an enlarged photograph in a certain part are presented in **Fig. 30**. Although the steel phase is invisible in the macrograph, the enlarged figure reveals many metallic fragments on the internal surface of several large pores and no metallic inclusion in the fuel matrix in the half part close to the centerline. In the neighboring part, very small steel droplets of a few micrometers can be seen and their quantity tends to increase in the vicinity of the "porosity line", although there is a certain scattering. These fine droplets imply to result from condensation of once vaporized steel. Near the fuel periphery where porosities are almost absent, such small steel particles are not detected within the solidified fuel.

- Image analysis

An image analysis has been carried out in order to quantify surface fractions of steel droplets observed in the metallographic examination in Capsule 2. As previously described, the lower part "Radius 2" is regarded as representative for the overall fuel part (except the upper part) from a macroscopic point-of-view. This part, however, was initially chosen to characterize radial steel distribution and there was a natural intention to seek the location where steel particles were more visible. It means that the steel quantity in "Radius 2" is likely to be somewhat higher than the average. Therefore, the surface fraction deduced from the image analysis data with "Radius 2" may overestimate the real value. Although one must keep this aspect in mind, it is worthwhile evaluating the vaporized steel mass in the capsule from the surface fraction observed in "Radius 2".

As illustrated in **Fig. 31**, the image of "Radius 2" is divided into 10 portions along the lateral direction. The analysis of each image allows us to characterize with a better accuracy the evolution of the steel surface fraction along the radial position. The surface fraction of steel is presented at the lower part in the figure, where the fraction at the most outer part is neglected because the steel droplets observed outside the fuel are not considered to be condensed vapor. The surface fraction reaches a maximum value of about 0.05% around the "porosity line" located 1.5mm from the external boundary.

The second peak of about 0.03% is obtained at about 5mm from the outer surface of the fuel, where the small steel droplets are detected in the large porosities.

Since the steel surface fraction in each portion of the cross section is equal to the volume fraction in the fuel cylinder, from the droplet distribution, the mass of vaporized steel is evaluated to be 0.218mg in "Radius 2". Assuming that the vaporized steel distribution is applied to the whole fuel sample of 35mm, the steel mass becomes 7.63mg. This value corresponds to 5.23% of the initial steel mass (146mg). Although this estimation has a large uncertainty and a possible bias toward a larger value, it is clear that the small steel particles formed probably with condensation correspond to only a small fraction of the entire steel.

4 Estimation of event sequence

In this section, we estimate the event sequence which occurred in Capsule 2, which is the main capsule in the test, from the measured data and the observation. **Figure 32** shows the average specific internal energy of the fuel in the Capsule 2 obtained from the energy balance between the energy deposit and the heat loss toward the crucible wall, which was evaluated by an inverse conduction method [7] using the double-thermocouple data. The specific internal energy reached the solidus energy of fuel at 0.55s, and then the fuel energy was retained between the solidus energy and the liquidus energy for several seconds. Note that this method tends to underestimate the heat flux toward the wall at about 0.6s, because no heat flux is evaluated while the heat penetrates from the inner surface being in contact with liquid fuel up to the position of thermocouples. Accordingly, the actual specific internal energy of fuel should be slightly lower than this evaluation. However, the appearance of columnar grain structure in the morphology of the cutting sample supported that the fuel energy injected from the pulse was sufficiently high.

As indicated in **Fig. 6**, the pressure increase started at about 0.45s, earlier than the fuel melting time. Since neither fuel nor steel vapor could be generated prior to the fuel melting, this pressure rise is considered to have been caused by expansion of the gas trapped inside the fuel pellet and/or the gasification of some volatile impurities.

The pressures inside Capsule 1 and Capsule 2 became almost constant from 8s to 15s as shown in **Fig. 8**. These pressure levels are believed to have consisted of filling gas and impurity gas, because the steel vapor could not be present at that time due to the low fuel temperature. In **Fig. 33**, excess pressures inside Capsule 1 and Capsule 2 above the values at 15s after TOP onset are compared. Presupposing the same fuel temperature between Capsule 1 and Capsule 2, we can assume that the difference between these excess pressures corresponds to the steel vapor, since Capsule 1 pressure consisted only of the filling gas and impurity gas. The shaded region represents duration, in which the average specific internal energy of fuel is estimated to have been larger than the solidus energy. The thermal evaluation looks quite consistent with the pressure comparison. Furthermore, the presence of numerous fine steel particles, which was embedded in once molten fuel in the microstructure examinations, corroborates the steel vaporization, because it is difficult to explain these particles only by the fluid-dynamics fragmentation. The measured pressure, however, was unexpectedly smaller than the prediction before the test (see **Appendix B**). This fact implies that a mechanism reducing the fuel-to-steel heat transfer played a role in the test.

For the cooling phase, it is possible to apply a hypothesis that an inward bubble migration under the high temperature gradient occurred in the molten fuel. This phenomenon is known to be due to the stresses resulting from the thermal variation of surface tension at the bubble surface. N. O. Young et al. [8] theoretically calculated the migration velocity of a spherical fluid droplet of radius R_d placed in an infinite expanse of suspending fluid of viscosity μ with prescribed temperature gradient $|\nabla T_\infty|$. By neglecting the effect of gravity, its velocity v_d is related to the constant temperature gradient by the following formulation [9]:

$$v_d = \frac{2}{3} \cdot \frac{R_d}{2\mu + 3\mu_d} \cdot \frac{3k}{2k + 3k_d} \left(-\frac{\partial \sigma}{\partial T} \right) \nabla T_\infty | \quad , \tag{1}$$

where μ_d is the viscosity of the droplet, k_d is the thermal conductivity of the droplet, and k is the thermal conductivity of the continuous liquid. $\partial\sigma/\partial T$ stands for the variation of the surface tension σ between the droplet and the continuous phase with respect to the local temperature T. The small steel droplets of 2μm in diameter observed in the destructive examination correspond to vapor bubbles of about 30μm in diameter in the test. Supposing that a steel vapor bubble moves in the continuous liquid fuel just above the melting point under the temperature gradient of 10^5K/m, the migration velocity of the bubble is given 31.2mm/s using R_d =0.03mm, μ =4.34 × 10^{-3}Pa s, μ_d =1.20 × 10^{-4}Pa s, k =3.1W/m/K, k_d =0.066W/m/K and $\partial\sigma/\partial T$ = -1.9 × 10^{-4}N/m/K.

As far as the bubble migration is more rapid than the inward motion of the fuel solidification front, solidified fuel does not catch migrating bubbles. The solidification velocity can be obtained with the established equation known as the solution of Neumann [10]. The frozen thickness ξ is calculated as follows:

$$\xi_s = \sqrt{\frac{2k_s(T_{mp} - T_s)t}{L_f \rho_s}} \quad , \tag{2}$$

where k_s is the thermal conductivity of the solid fuel, T_{mp} is the melting point of the fuel, T_s is the surface temperature of the solid fuel at the opposite side of the phase change interface, t is the time, L_f is the latent heat of fusion of the fuel, and ρ_s is fuel density. Taking into account the gap conductance between the fuel crust and the wall, the crust surface temperature T_s may be assumed to be 2500K as a very rough estimation. At 0.1s, the fuel crust thickness becomes about 0.4mm using k_s =3.4W/m/K, L_f =2.77 × 10^5J/kg, ρ_s =9650kg/m^3, T_{mp} =3120K and T_s =2500K. Compared with the expected freezing speed of fuel, the calculated bubble motion velocity is large. This result supports the hypothesis of temperature-gradient driven bubble migration during the cooling phase.

As drawn in **Fig. 34**, the experimental results and interpretation lead to the following scenario.

1) Fuel melting and steel vaporization began at about 0.55s. Then the steel vaporization at the surface of steel balls led to vapor blanketing. This vapor blanketing seems to be the mechanism reducing the fuel-to-steel heat transfer.
2) The main part of the steel ball, which was composed of liquid steel of smaller density than that of liquid fuel, and the surrounding vapor bubble moved upward by buoyancy force. Thus, steel separated from the hot fuel eventually. During this separation process, some part of steel was entrapped into the molten fuel, either as small vapor bubbles or steel droplets. The entrapped steel resulted in numerous vapor bubbles.
3) In the pore-free region near the fuel outer surface seen in the axial cutting, the bubble migration process allowed the vapor bubbles to remove from this region.
4) In the course of the bubble migration, the temperature decreased and the steel vapor condensation started. The isotherm corresponding to the initial steel vapor condensation created the vertical line where many steel particles were present. The inward bubble migration continued further with coalescence leading to larger non-condensable gas bubbles, so that the steel condensation occurred in the combined porosities in the large pore region. Two groups of bubbles moving inward, small vapor-rich ones and large non-condensable gas-rich ones, yielded the dual-peak steel distribution along the radius, which was confirmed by the image analysis.
5) The liquid steel which has moved up toward the top of the fuel specimen penetrated into the cracks due to the contraction of frozen fuel, as observed in the metallographic examination.

5 Analytical evaluation with SIMMER-III

In the preceding section, two issues to be solved quantitatively remain: (1) the reduction of fuel-to-steel heat transfer due to the local steel vapor blanketing, and (2) the separation of steel from fuel due to the buoyancy-driven upward steel motion. These issues are evaluated here with a two-dimensional fluid-dynamics code, SIMMER-III.

5.1 Analytical geometry and conditions

In the SIMMER-III calculations, the fuel capsule with the surrounding test channel was modeled by a two-dimensional cylindrical geometry. A schematic view of the geometry used in the present analysis is illustrated in **Fig. 35**. The fuel column consisted of 7 horizontal- and 22 vertical-computational cells. The fuel pellets were simulated by 10 μ m-diameter particles with about 35% of porosity. The 1mm-diameter steel balls and the 0.1mm-thickness steel membrane are placed at the same position as in the experiment. The fuel capsule was cooled at the side and bottom by the sodium coolant at the same flow rate and at 674K as in the test. Although the Niobium was actually adopted for the outer tube surrounding the test channel in the test, the same material as the crucible was adopted for the outer tube in this analysis because the effect of the properties was negligible.

SIMMER-III defines the normalized power at each computational cell by multiplying the radial normalized power by the axial one. This multiplication, however, is likely to exaggerate the relative power at the fuel edge regions consisting of upper and lower ends of the outer fuel rim. For a better simulation, the power at the edge cells was slightly decreased: for instance from 1.74 to 1.65 at the lowest outer computational cell.

In order to obtain the correct heat transfer toward the wall before the transient, we conducted a steady-state calculation for Capsule 1 with the constant power, because the fuel temperatures inside the capsule were measured only in Capsule 1. Initial fuel temperature profiles in Capsule 1 are plotted in **Fig. 36**, where the calculated temperatures are in good agreement with the measured values by the thermocouples TC19 and TC20. Using the same heat loss condition to the wall, a steady state of Capsule 2 before TOP was established. **Figure 37** shows initial fuel temperature profiles, which are almost uniform along the axial level. This uniform temperature profile is provided as a result of the larger heat loss toward the bottom and the higher power generation there. Although the radial temperature profile looks like a parabolic one with its peak at the center before TOP triggering, it is expected to get almost uniform temperature due to the radial power profile, which had peak in the outer part, after

sufficient injection of the pulse energy.

As noted above, the fuel pellets were made from pressed fuel powder in this test. The thermophysical properties, especially the thermal conductivity, of solid fuel might be different from the usual fuel pellet. In the present analyses, the modified conductivity was used as described in **Appendix C**.

Radiative heat loss from the fuel surface cannot be negligible in the high-temperature boiling pool experiment. In the SCARABEE BF2 test, the radiative heat loss from the pool upper surface was estimated to have been 4% of input nuclear power during the fuel boiling from the heat balance [11]. Therefore, we introduced a simple model which subtracted the radiative heat flux from the internal energy of liquid fuel depending on its areal fraction projected in upward direction. The radiative heat-up of cover gas was also reported to have been important in the BF2 test. Reflecting the interpretation of this experiment, 1% of the radiative heat transfer from the pool surface was assumed to have heated the cover gas uniformly in this study.

For better code simulation, some code modifications were made as described in **Appendix D**. A sample input data set is listed in **Appendix E**.

5.2 Calculated results

5.2.1 Capsule 2

- Reference case

The pressure histories (the first calculated result called as "Reference case" and the measured data) in Capsule 2 are compared in **Fig. 38**. The calculated pressure is smaller than the experimental one before fuel-melting onset at 0.55s, and then becomes larger. In the calculation, heating of the gas within the porous fuel pellet was responsible for the small increase during the first pressure peak. As mentioned above, the gasification of volatile impurities would have influenced the first pressure increase in the test. On the other hand, the discrepancy on the second pressure rise after fuel melting seems due to overestimation of the steel vapor pressure. Material motion in Reference case is depicted in **Fig. 39**. In the calculation, the fuel already moves upward even before fuel-melting onset at 0.55s, and it drastically disperses in the capsule due to overestimated steel vapor pressure. Such material motion differs from the observation by the hodoscope and the post-test examination.

Originally the SIMMER-III code contains a fission gas release model from fuel pellet, liquid fuel and particulate fuel, and hence this model can apply to release the impurity gas from the fuel. To simulate the first pressure increase, 0.5 μ mol/g-$_{UO2}$ of impurity

gas was assumed to be released from the fuel particles with a time constant of 10ms after 0.45s. The second calculation with the impurity gas release called as "Impurity case" is shown in **Fig. 40**. A fairly good agreement can be seen for the first pressure increase between this calculation and the experiment, while the discrepancy for the second pressure increase from the test still remains expectedly. The fuel and steel distributions of Impurity case are presented in **Fig. 41**. Notice that the upward fuel motion at the pellet surface cannot be seen before the fuel melting at 0.55s in this case. The reason for this stagnation is stated below. The impurity gas released from the fuel particles went through the fuel column into the cover gas region, and the released hot gas became dense in the gas plenum due to the cooling from outside of the capsule. Finally, the cover gas pressure increased additionally by the radiation heat transfer from the upper surface of the hot fuel column and it prevented the fuel column from dispersing into the gas plenum.

- Single droplet calculation

In order to investigate the reason of the overestimation of steel-vapor pressure build-up in the previous calculations, the steel vaporization behavior at the droplet surface was examined with a single droplet for facilitation. Two cases with different mesh sizes were selected for the single droplet calculations as illustrated in **Fig. 42**. In order to simulate local vaporization at the surface of only one steel droplet, the fuel-pellet size was 2mm in radius and 3mm high, and composed of 20-radial and 30-axial computational cells. Cover gas region of 2mm height was placed over the fuel pellet. This case is called as "Fine mesh case". To compare with Fine mesh case, the other was calculated with the geometric model of 2-radial and 3-axial computational cells, called as "Coarse mesh case" hereafter. In this case, a steel ball was located in a computational mesh. Such arrangement of the ball was the same as in the preceding TPA2 calculations. Since this droplet represents a steel ball located in the fuel column in the test, its initial temperature was assumed to be uniform at 1230K. The same power pulse as in the TPA2 calculations was applied to the fuel under a uniform power profile to simplify the calculation. Moreover, adiabatic wall was assumed because the fuel temperature around steel balls was expected to have been almost uniform during the transient in the experiment.

Pressure histories of both cases are compared in **Fig. 43**. The sudden pressure increase of Coarse mesh case can be seen at 0.55s corresponding to the fuel melting onset, while the pressure of Fine mesh case gradually increases at 0.55s. These pressure histories are similar to those presented in **Fig. 38**, i.e. the reference-TPA2 calculation

result and the experimental observation. To put it more precisely, Coarse mesh case showed the same characteristic as the preceding TPA2 calculation, whereas Fine mesh case reproduced the pressure-history characteristic common to the experiment. Steel ball motions of both cases are depicted in **Figs. 44** and **45**. Compared with Fine mesh case, the fuel/steel mixture of Coarse mesh case is likely to disperse in the calculational system due to the high pressure. In both cases, the buoyancy force enables the steel droplet to move upward and to stay at the upper fuel surface.

Material distributions of Fine mesh case are shown in **Fig. 46**, where pink, red, lime, green and white colors represent respectively fuel particle, liquid fuel, steel particle, liquid steel and gas. At 0.55s, liquid fuel contacted with steel, followed by steel vapor generation which occurred at the surface of steel droplet. It is noted that a large amount of fuel particles and surrounding steel vapor can be seen around the steel droplet. The former means that the fuel temperature was locally reduced in the vicinity of the steel droplet surface, while the latter gives an interpretation that steel vapor blanketing interrupted contacts between liquid fuel and liquid steel. To quantify the effect of vapor blanketing, we compared total interfacial areas between liquid fuel and liquid steel in **Fig. 47**. Although the interfacial area in Coarse mesh case sharply increases, the area in Fine mesh case is considerably small just after fuel melting.

It can be best summarized in the following sentences. Material distributions and fuel temperature distributions are diagrammatically drawn in **Fig. 48**. In this figure, (a) represents either the experimental condition or the calculation with fine meshes, while (b) stands for the calculation with coarse meshes. In the former, the steel vapor surrounds the steel ball, and the fuel temperature decreases near the ball. In the latter, the steel vapor bubbles of the same void fraction as the former one distribute in a computational cell, and the averaged fuel temperature of the former one is employed. Therefore, we can say that SIMMER-III with the coarse mesh condition overestimates heat flux at the interface between liquid fuel and liquid steel due to the absence of vapor blanketing as well as higher fuel temperature. Although its effect is much less, heat flux from the molten fuel to the steel ball through the vapor bubble is also overestimated with the coarse-mesh condition because of the higher fuel temperature.

In SIMMER-III, steel vaporization and condensation are treated through three phase change paths:

- steel vaporization by contact between liquid fuel and liquid steel,
- steel vaporization by contact between liquid steel and gas, and
- steel condensation by contact between liquid steel and gas.

Total steel vaporization rates of the three paths can be compared between Fine mesh case and Coarse mesh case in **Fig. 49**. Maximum value in Coarse mesh case is considerably larger than that in Fine mesh case at about 0.55s. Based on this finding, it was intended to simulate the realistic situation introducing low heat transfer coefficients for the above three interfaces adopting the coarse mesh geometry. This analytical case is called hereafter as "Coarse mesh with low HTC case". Exactly speaking, 1/200 of the nominal values were applied here as the low heat transfer coefficients. **Figure 50** shows pressure histories of Coarse mesh with low HTC case together with the other cases in the simple geometry. The new calculated result can well trace pressure-history characteristic of Fine mesh case. Thus, SIMMER-III can satisfactorily simulate the steel vapor formation behavior by taking into account the reduction of heat transfer even in the coarse mesh geometry. Steel ball motion in Coarse mesh with low HTC case is presented in **Fig. 51**. The dynamic dispersion of fuel and steel cannot be seen in this case due to significant reduction of steel vapor formation.

- Low HTC case

Since the single droplet calculations suggested that SIMMER-III could simulate the realistic heat-transfer condition by introducing the reduced heat transfer coefficients even with the coarse mesh geometry, we attempted to reproduce the actual pressure-increase behavior with the whole test-fuel geometry applying this method. Here, a new calculation case is called as "Low HTC case", where the effect of impurity gas release was considered as well as Impurity case. **Figure 52** shows pressure histories in Low HTC case together with the other cases. The Low HTC case gives a quite good agreement with the experimental result thereby suggesting appropriateness of the assumptions used in this case. Furthermore, material motion in Low HTC case shown in **Fig. 53** provides excellent consistency with the experimental observation. As previously mentioned in Impurity case, the upward fuel motion cannot be seen before fuel melting at 0.55s due to the impurity gas release into the gas plenum region. Just after fuel melting, steel vapor was formed in the fuel column. However, the limited level of steel vapor pressure and the slightly higher pressure in the cover-gas region prevented molten fuel dispersion into the upper part. This non-expansion behavior agrees with the hodoscope observation and the non-destructive examination results. Furthermore, it can be seen that the steel droplets move upward to accumulate at the upper surface of the molten fuel due to the buoyancy force. This steel motion behavior is consistent with the metallographic examination. The only difference in the analysis to be noticed is the presence of a fuel crust remaining on the capsule wall above the plunged fuel upper surface which was absent in the experiment. Absence of such crust

in the experiment could be explained with possible adhesion of fuel crust to the shrinking fuel. It should be noted that thermal resistance at the gap between fuel crust and the capsule is neglected in the present SIMMER-III evaluation. This treatment might overestimate the heat transfer toward the capsule wall and thus underestimate the local temperature near the outer surface region. However, inside the thick fuel crust in the analysis, hot fuel condition was satisfactorily preserved as well as the realistic situation leading to reasonable simulation of the global behavior.

Judging from the pressure history and the material-motion behavior, one can say that SIMMER-III successfully reproduces the transient behavior in the TPA2 experiment provided that special treatment is applied taking realistic mechanisms into account.

5.2.2 Capsule 1

It is likely that the amount of impurity gas released in Capsule 1 was smaller than that in Capsule 2, because the first pressure peak in Capsule 1 was pronouncedly lower than that in Capsule 2 in spite of almost the same energy deposit in both cases. From the measured pressure histories presented in **Fig. 6**, the pressure increases from the TOP onset up to the first peak in Capsule 1 and in Capsule 2 are 0.8×10^4Pa and 3.4×10^4Pa, respectively. The value in Capsule 1 is about 0.2 times that in Capsule 2. Since $0.5\,\mu$mol/g$_{UO2}$ of impurity gas was necessary in Capsule 2 to simulate the first pressure rise, $0.1\,\mu$mol/g$_{UO2}$ of impurity gas was assumed to have been released from fuel particles with a time constant of 10ms after 0.45s in Capsule 1. In this case, absence of steel balls did not necessitate the special treatment for the fuel-to-steel heat transfer. The fuel mass, the power profiles and the power history were selected for Capsule 1 in accordance with the real situations. Similarly to the Capsule 2 analyses, the steady-state calculation was followed by the transient calculation.

In **Fig. 54**, pressure histories (the calculated result and the experimental data) in Capsule 1 are compared each other. The calculation is in good agreement with the experimental pressure behavior. The calculated material motion is presented in **Fig. 55**. After fuel-melting onset at 0.55s, the molten fuel shrinks to accumulate at the lower part of fuel column. Thus, SIMMER-III reproduces the material kinetics observed by the hodoscope except for the fuel-crust formation above the settled-down fuel surface. The same explanation for Capsule 2 is applicable for this difference.

5.2.3 Capsule 3

In Capsule 3, the analytical geometry was slightly changed, because the cover-gas region in this capsule was axially extended when compared with the other capsules. Since the fuel pellet contains steel balls in this capsule, the same amount of impurity gas

as for Capsule 2 was used in this analysis. The calculation was conducted in the same manner as Low HTC case in the Capsule 2 calculations.

Figure 56 shows the calculated pressure history in Capsule 3. Compared with the pressure in Capsule 2, the calculated pressure is considerably small, because little steel vapor seems to have generated due to the lower energy deposit. The calculated motion of fuel and steel is shown in **Fig. 57**. The mixture of fuel and steel slightly dispersed upward into the gas-plenum region in this calculation, although the molten-fuel shrinkage without dispersion was obtained from the observation of the hodoscope and non-destructive examination in the test. As presented in **Fig. 58**, the metallographic observation showed that the fuel pellet was molten except for the thin solid shell at the fuel periphery. It should be noted that many large pores were present in the outer fuel region of Capsule 3 in contrast with Capsule 2. This suggests that the maximum fuel temperature was just above the melting point and bubble migration under the temperature gradient did not occur. In this analysis, overestimation of heat loss toward the wall combined with the lower energy injection in this capsule prevented melting of the central part. This situation prevented the fuel from shrinking, and the subsequent upward motion was caused by numerical diffusion at the upper surface of the fuel column.

6 Conclusion

The main objective of the TPA2 test was to improve the knowledge on the fuel-to-steel heat transfer under two-phase condition with development of steel-vapor bubbles. Although slow fuel heating was preferable for this objective, the limitation of the CABRI facility led to adopt a relatively rapid fuel-heating condition in which the main fuel heating was performed within 100ms. The neutron hodoscope and the pressure-transducer measurements consistently showed that there was no rapid steel-vapor formation leading to meaningful expansion of the fuel/steel mixture in each capsule. PTE observation in Capsule 2 indicated that fuel had reached melting enthalpy during the transient. This aspect was confirmed from the fact that the fuel in Capsule 3 was molten, in spite of the significantly lower energy injection. Also PTE observation strongly suggested that steel-vapor formation was taking place and it had lasted for a rather long time. Comparison of Capsule 2 (with steel) and Capsule 1 (without steel) contributed to clarifying the role of steel during the transient in this test. These experimental evidences illustrate that there was a rather mild fuel-to-steel heat transfer even though fuel was sufficiently heated.

It had been already predicted before the test that steel vapor would serve as limiter for fuel-to-steel heat transfer because steel vapor was likely to be formed mainly between fuel and steel. The observation, however, demonstrated that the reduction of the heat transfer was far more effective than the previous expectation. As a result of this mild heat transfer, the transient time scale was dominated by the cooling time, which is rather long.

The analytical investigation with the SIMMER-III code, which was conducted in an iterative manner together with close PTE-data evaluation, revealed a scenario of mild heat-transfer behavior. From this investigation, it was estimated that blanketing of the steel vapor was the main mechanism for the limited fuel-to-steel heat transfer as well as buoyancy driven upward steel motion leading to steel separation from fuel. This TPA2 result suggests a very important mechanism which has high potential to mitigate fuel-to-steel heat transfer, leading to a mild fuel/steel boiling-pool behavior; thus recriticality potential could be alleviated.

Since this estimation is based on various supporting information, a visual direct evidence should be obtained. In order to apply this knowledge to reactor evaluations, confirmation of the mechanism by additional experimental efforts seems necessary. The on-going BALL-TRAP experiments using simulant (water and hexane) in CEA/Grenoble have high potential to provide important information related to this aspect.

To obtain precise information on the hexane-water interface and hexane-vapor bubble behavior, new BALL-TRAP experiments with a large-size hexane-droplet are under progression. It is expected that these series of new experiments reinforce the CABRI RAFT tests.

Acknowledgements

The authors would like to express their profound gratitude to the members of the CABRI experimental team and the experimental program working group for their excellent work on the in-pile tests and the collaborative contributions to data evaluations.

References

[1] H. Niwa, "A Comprehensive Approach of Reactor Safety Research Aiming at Elimination of Recriticality in CDA for Commercialization of LMFBR," Progress in Nuclear Energy, Vol. 32, No. 3/4, pp. 621-629 (1998).

[2] N. Nonaka and I. Sato, "Improvement of Evaluation Method for Initiating-phase Energetics Based on CABRI-1 In-Pile Experiments," Nuclear Technology, Vol. 98, pp. 54-69 (April 1992).

[3] J. Papin, F. Lemoine, I. Sato, D. Struwe and W. Pfrang, "Fuel Pin Behaviour under Conditions of Control Rod Withdrawal Accident in CABRI-2 Experiments," Proc. IAEA/IWGFR Technical Committee Meeting on Material-Coolant Interactions and Material Movement and Relocation in Liquid Metal Fast Reactors, O-arai, Japan, pp. 483-497 (June 6-9, 1994).

[4] G. Kayser and J. Papin, "The Reactivity Risk in Fast Reactors and the Related International Experimental Programmes CABRI and SCARABEE," Progress in Nuclear Energy, Vol. 32, No. 3/4, pp. 631-638 (1998).

[5] Sa. Kondo, Y. Tobita, K. Morita, D. J. Brear, K. Kamiyama, H. Yamano, S. Fujita, W. Maschek, E. A. Fischer, E. Kiefhaber, G. Buckel, E. Hesserschwerdt, M. Flad, P. Coste and S. Pigny, "Current Status and Validation of the SIMMER-III LMFR Safety Analysis Code," Proc. 7th. International Conference on Nuclear Engineering, Tokyo, Japan, ICONE-7249 (April 19-23, 1999).

[6] H. Yamano, S. Fujita, Y. Tobita, K. Kamiyama, Sa. Kondo, K. Morita, E. A. Fischer, D. J. Brear, N. Shirakawa, X. Cao, M. Sugaya, M. Mizuno, S. Hosono, T. Kondo, W. Maschek, E. Kiefhaber, G. Buckel, A. Rineiski, M. Flad, T. Suzuki, P. Coste, S. Pigny, J. Louvet and T. Cadiou, "SIMMER-III: A Computer Program for LMFR Core Disruptive Accident Analysis, Version 3.A Model Summary and Program Description," JNC TN9400 2003-071 (August 2003).

[7] H. Hamada and A. Kurihara, "Development of Tube Rupture Evaluation Code for FBR Steam Generator (II) - Modification of Heat Transfer Model in Sodium Side -," JNC TN9400 2003-031 (May 2003) (in Japanese).

[8] N. O. Young, J. S. Goldstein and M. J. Block, "The Motion of Bubbles in a Vertical Temperature Gradient," Journal of Fluid Mechanics, Vol. 6, pp. 350-356 (1959).

[9] R. P. Chhabra and D. De. Kee, "Transport Processes in Bubbles, Drops, and Particles," Hemisphere Publishing Corporation (1992).

[10] H. S. Carslaw and J. C. Jaeger, "Conduction of Heat in Solids," Oxford University Press (1959).

[11] Y. Tobita, "An analysis of Boiling Fuel Pool Experiment by SIMMER-III," Proc. 8th. International Topical Meeting on Nuclear Reactor Thermal-Hydraulics (NURETH-8), Kyoto, Japan, pp. 1357-1364 (September 30 – October 4, 1997).

Table 1. Main characteristics of fuel capsules.

Fuel column (Fuel/Steel mixture)			
	Capsule 1	*Capsule 2*	*Capsule 3*
Mean diameter of fuel column	13.959mm	13.956mm	13.954mm
Height of fuel column	43.137mm	43.181mm	43.176mm
Total mass	44.9000g	46.2269g	46.1876g
UO_2 mass	44.9000g	46.0805g	46.0412g
Steel mass (40 balls)	0.0000g	0.1464g	0.1464g
Enrichment of fuel	12.3% fresh UO_2		
Material of steel balls	Stainless steel (316L)		
Diameter of steel balls	1.0mm		
Component of cover gas	Argon		
Cover gas pressure at room temperature	0.01MPa		
Crucible			
	Capsule 1	*Capsule 2*	*Capsule 3*
Inner height of crucible	106mm		226.5mm
Inner diameter of crucible	14.2mm		
Tube thickness of crucible	2.4mm		
Bottom thickness of crucible	3.0mm		
Material of crucible	Stainless steel (316L)		

Table 2. The amount of impurities in the fuel pellets.

Element	**Analysis result** (ppm)	**Analysis result** (μ mol/g$_{UO2}$)
C	18.3 μ g/g$_{UO2}$	1.53 μ mol/g$_{UO2}$
F	<12.0 μ g/g$_{UO2}$	<0.63 μ mol/g$_{UO2}$
N	7.6 μ g/g$_{UO2}$	0.54 μ mol/g$_{UO2}$
Cl	<11.0 μ g/g$_{UO2}$l	<0.31 μ mol/g$_{UO2}$
Fe	<5.0 μ g/g$_{UO2}$l	<0.08 μ mol/g$_{UO2}$
Ni	<5.0 μ g/g $_{UO2}$	<0.08 μ mol/g$_{UO2}$

Table 3. Main characteristics of the test section around the fuel capsules.

Test section around the fuel capsules	
Flow rate of sodium coolant	6.4×10^{-4} m^3/s
Temperature of sodium coolant	673K
Inner diameter of Niobium tube	24mm
Thickness of Niobium tube	5.25mm
Thickness of Xenon gap layer	1.5mm

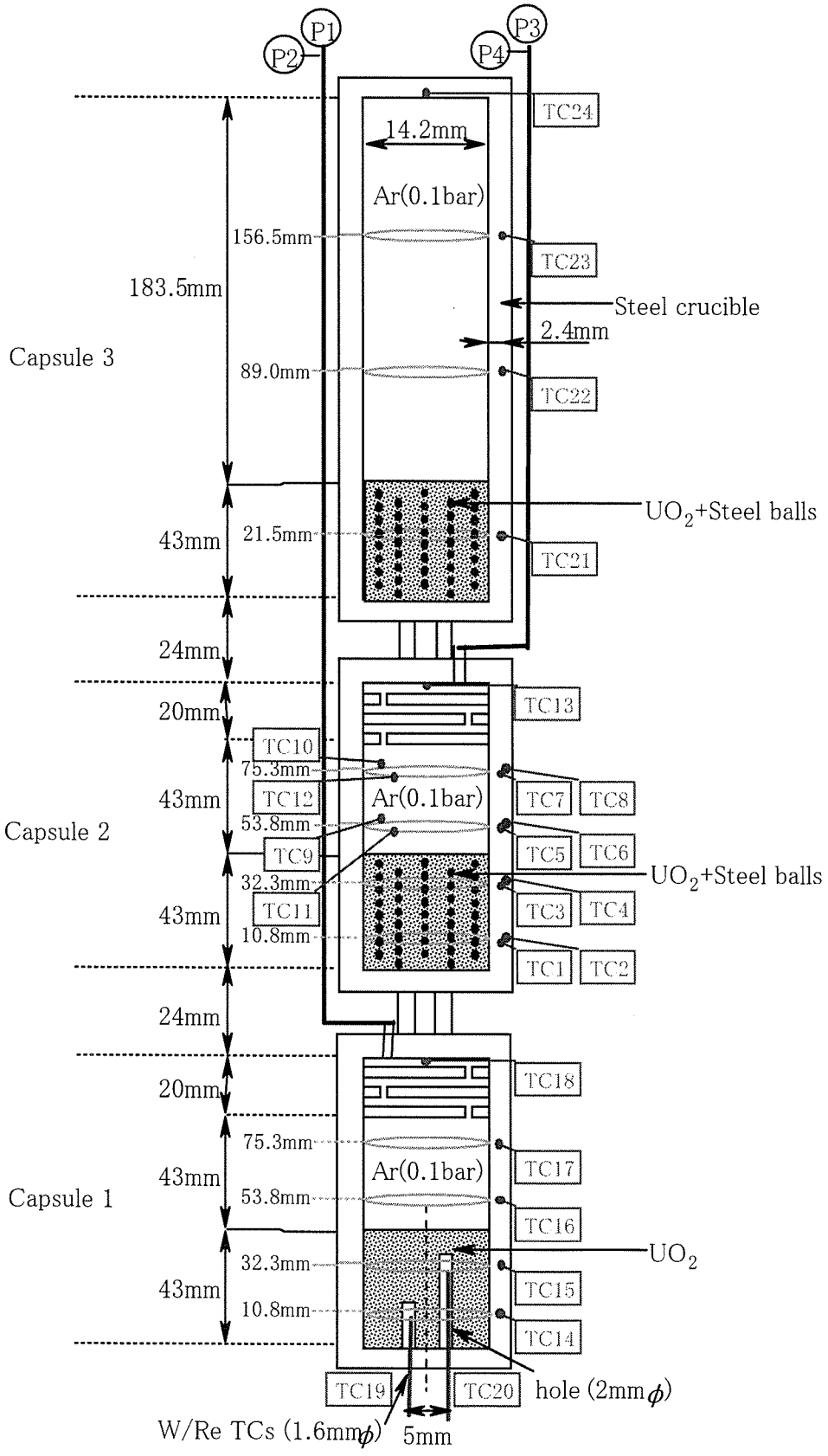

Fig. 1. Schematic view of the fuel capsules.

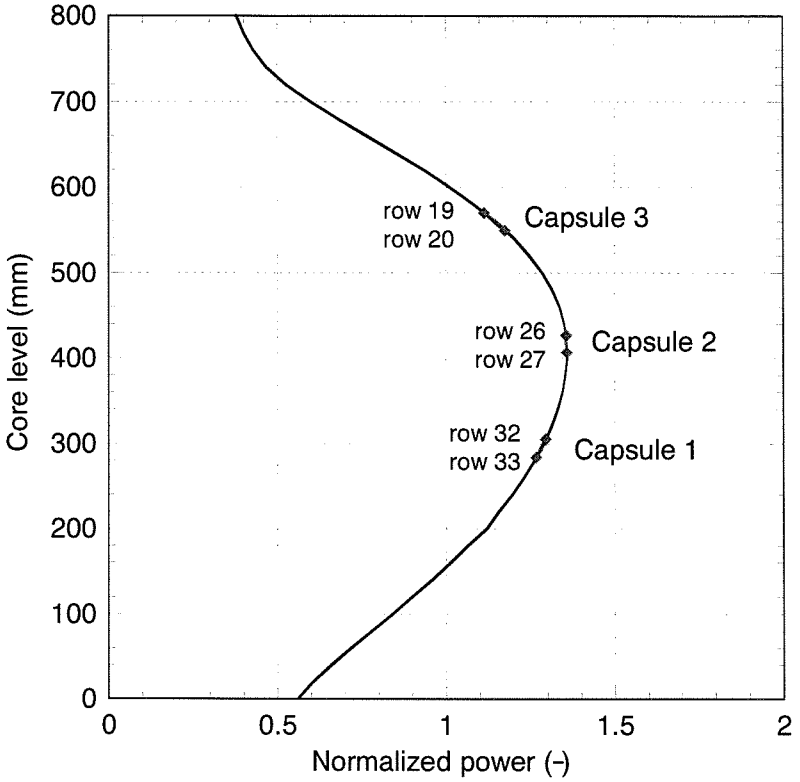

Fig. 2. CABRI core axial power profile measured by the hodoscope.

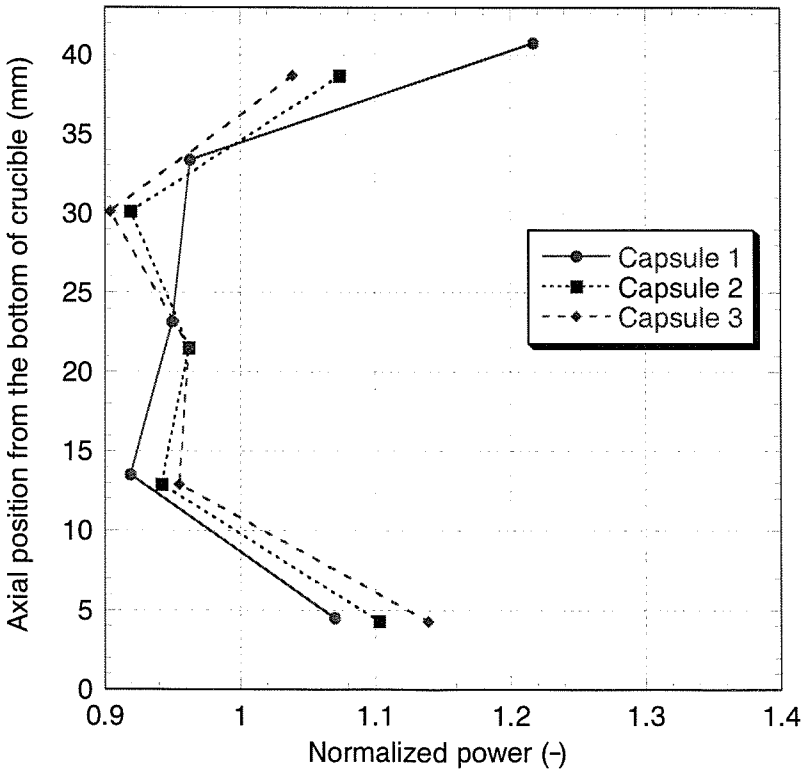

Fig. 3. Axial power profiles in each capsule.

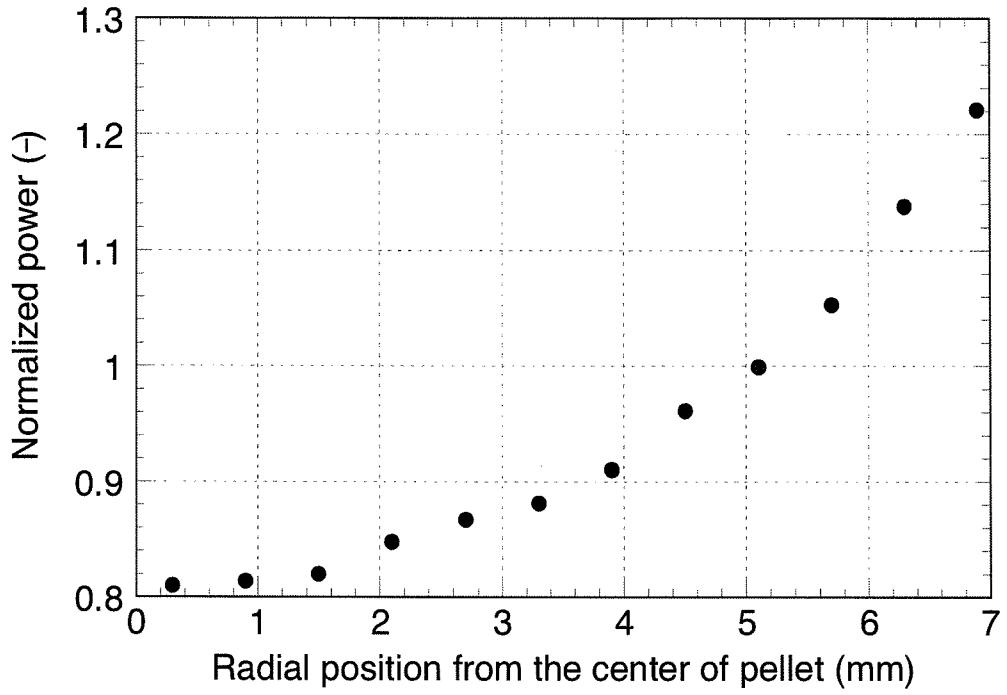

Fig. 4. Radial power profile.

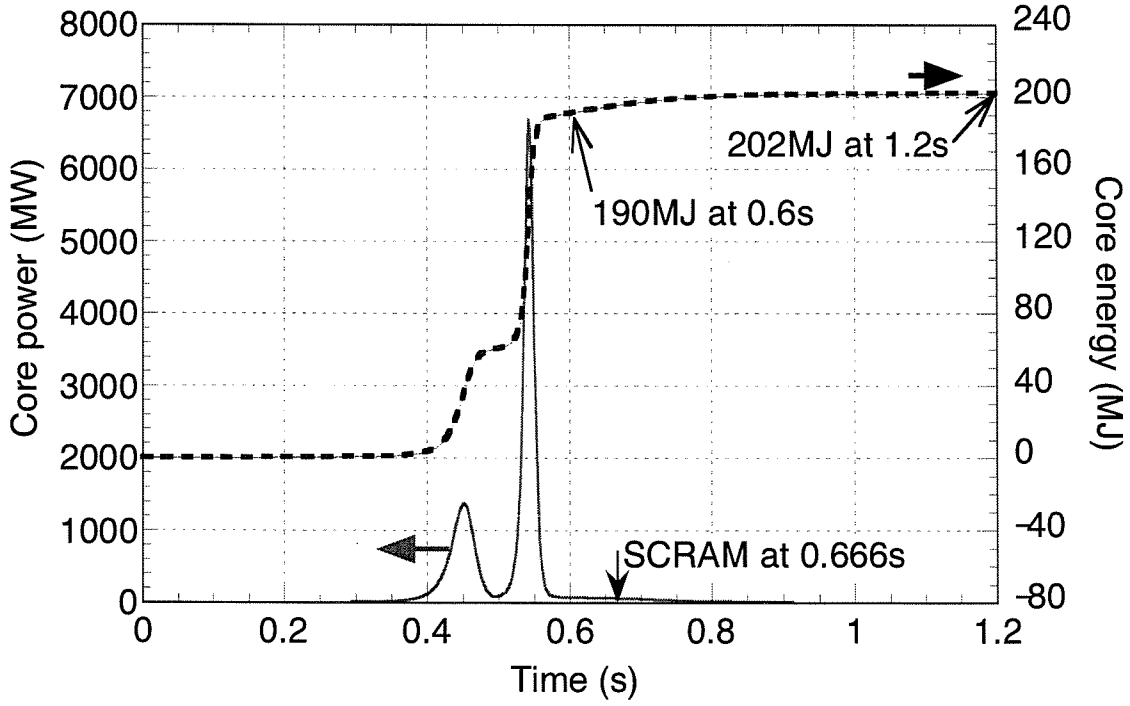

Fig. 5. Core power and energy histories.

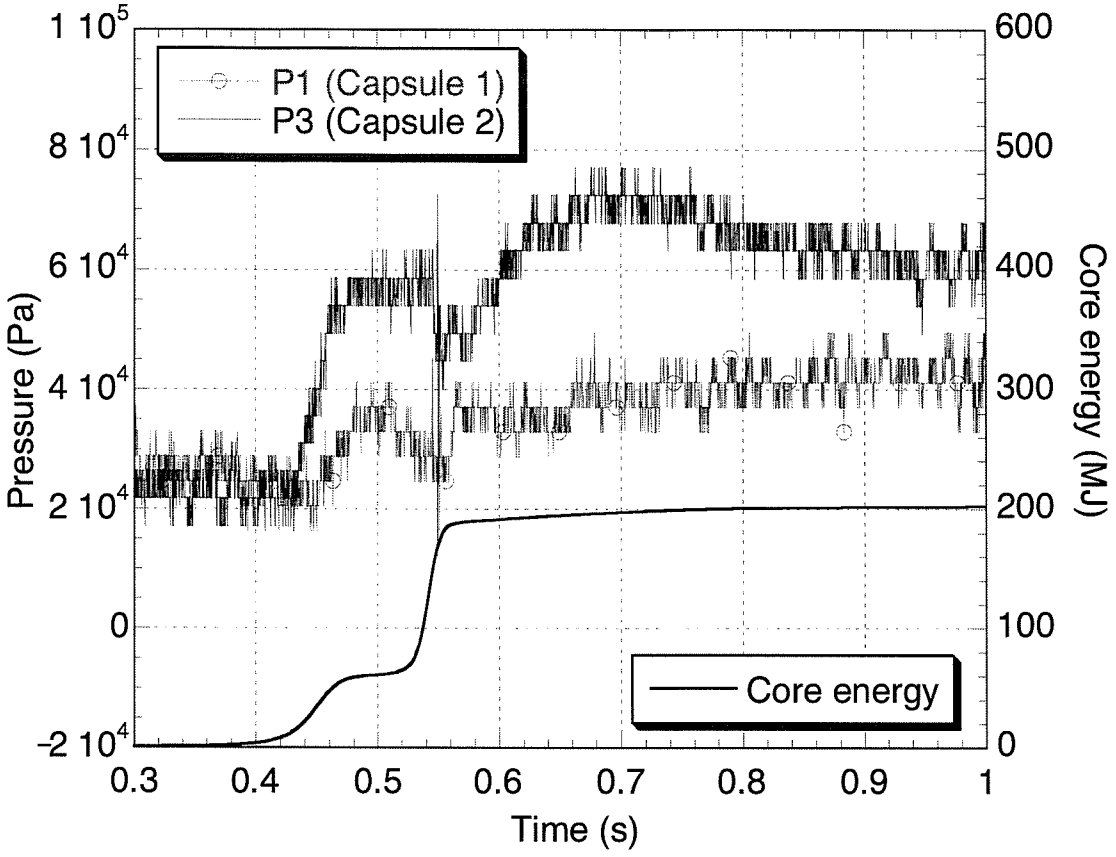

Fig. 6. Short-term pressure histories by P1 and P3.

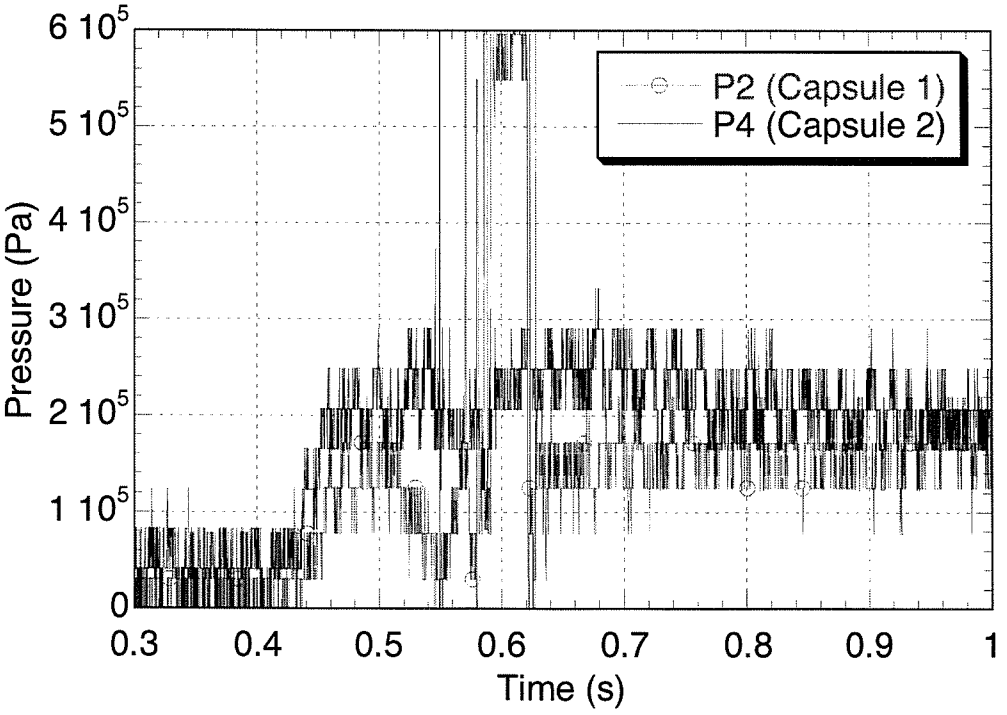

Fig. 7. Short-term pressure histories by P2 and P4.

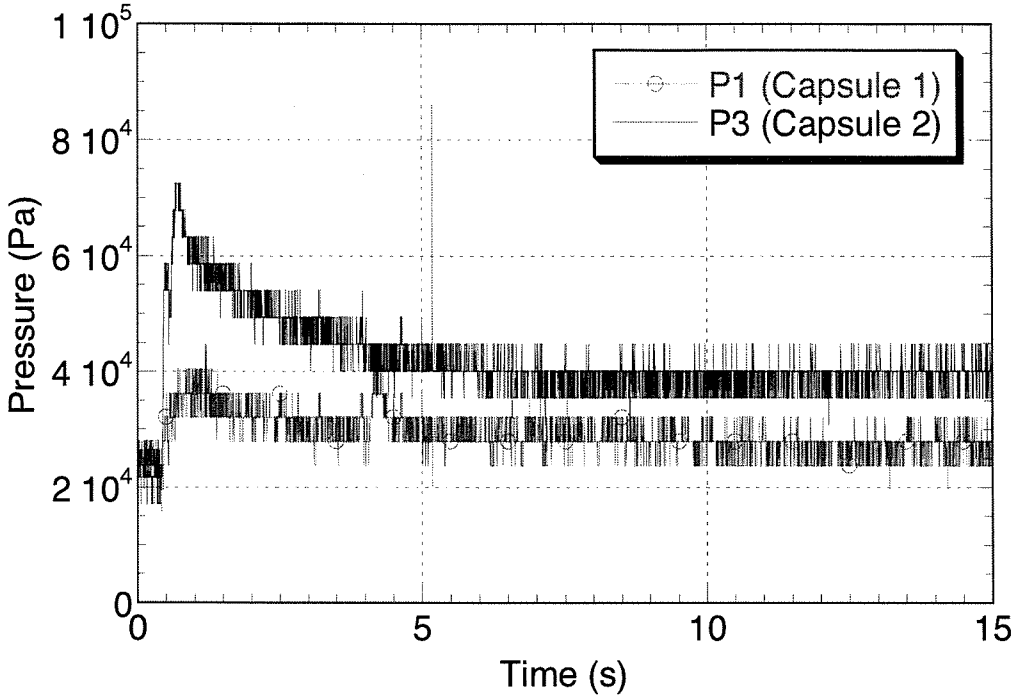

Fig. 8. Long-term pressure histories by P1 and P3.

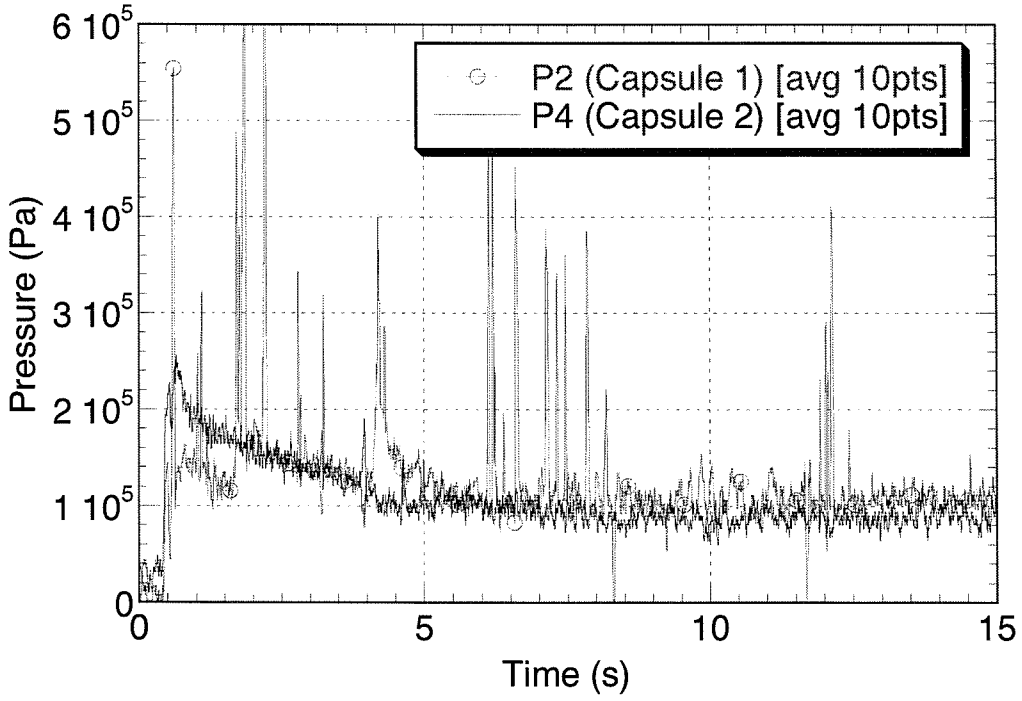

Fig. 9. Long-term pressure histories by P2 and P4.

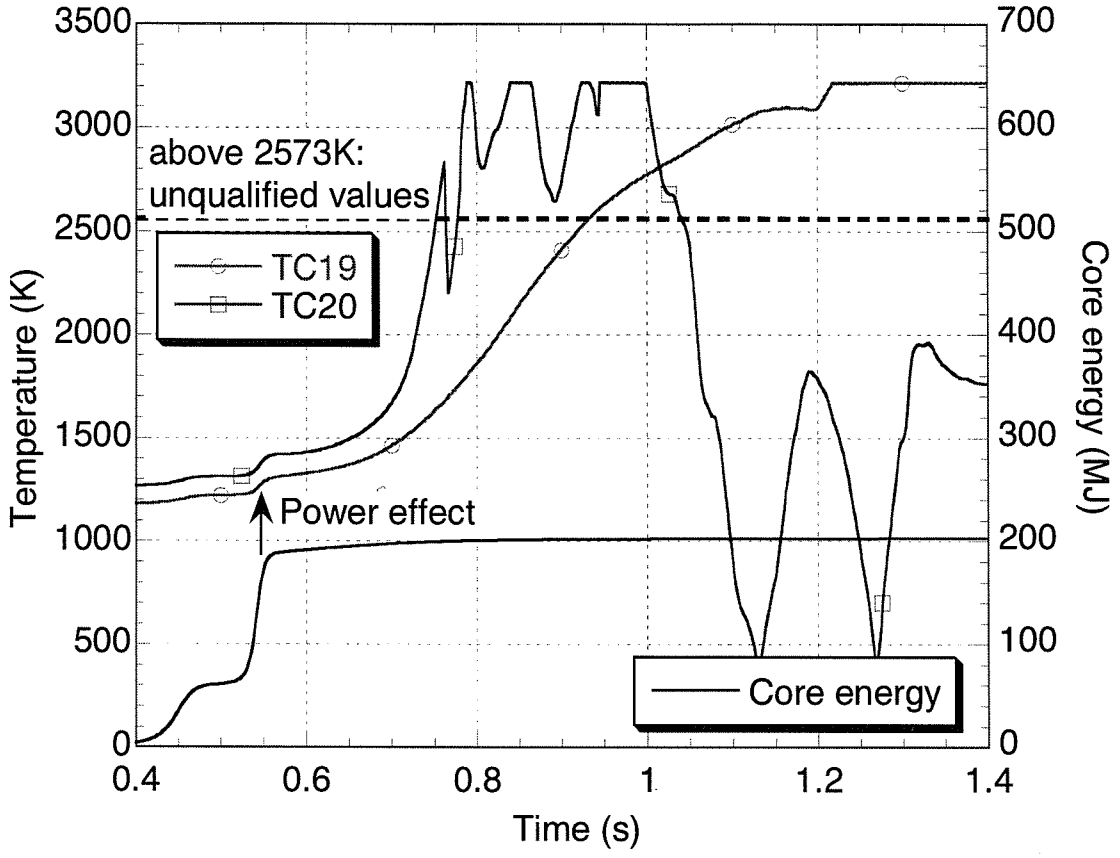

Fig. 10. Short-term behavior of fuel temperatures inside Capsule 1.

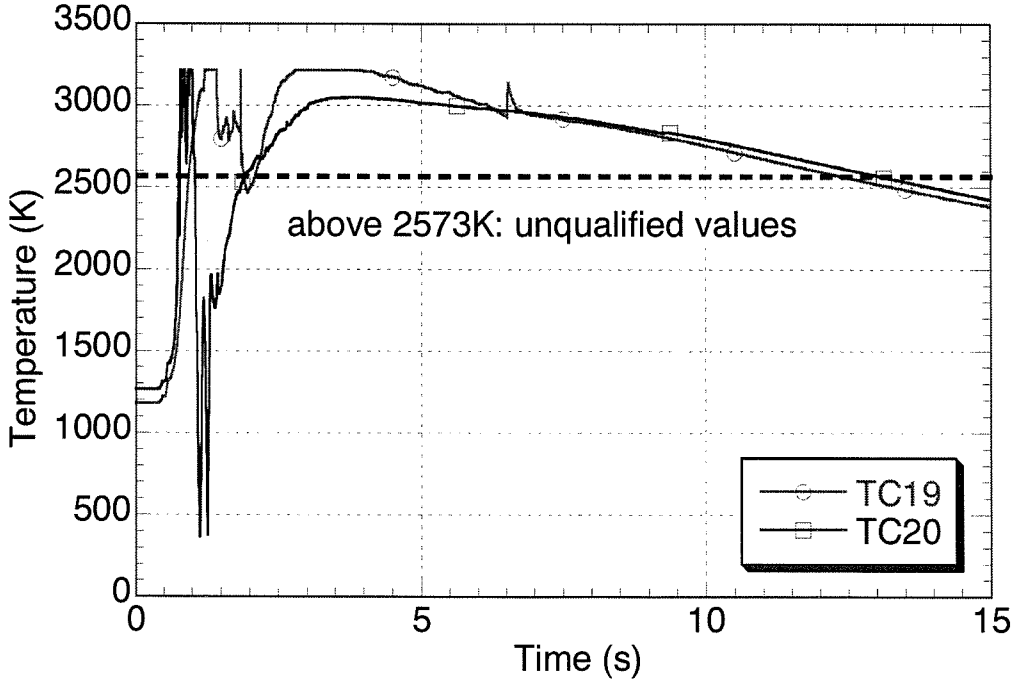

Fig. 11. Long-term behavior of fuel temperatures inside Capsule 1.

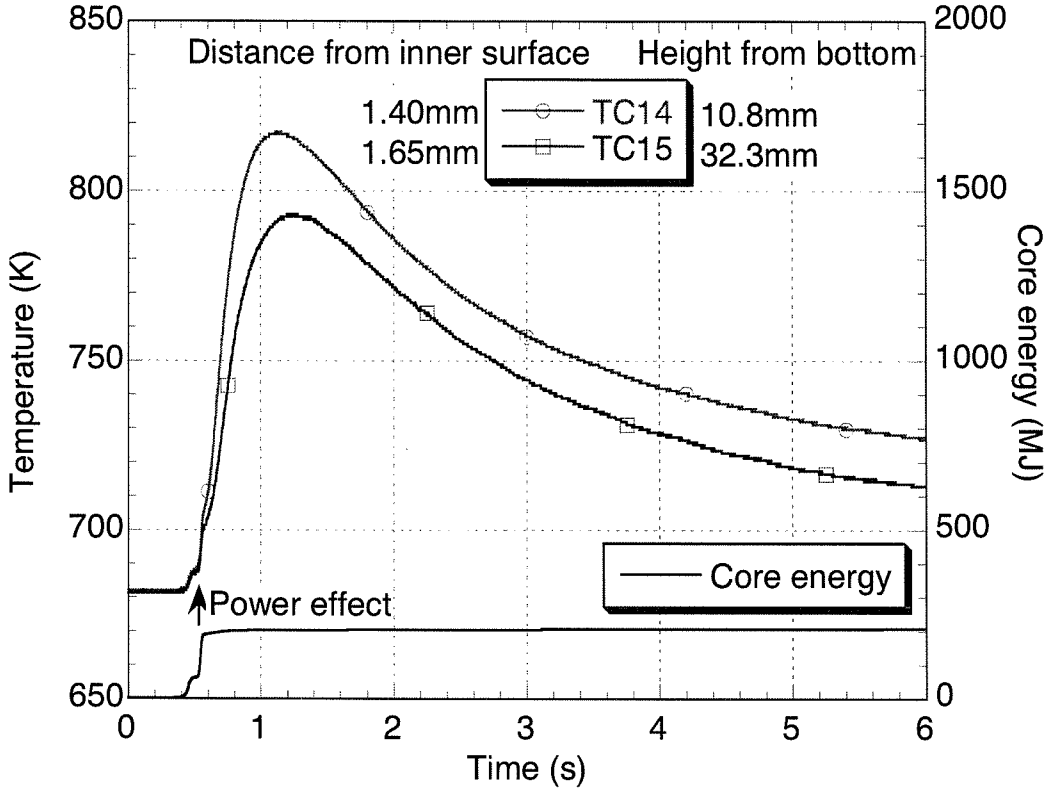

Fig. 12. Temperatures at fuel level in Capsule 1.

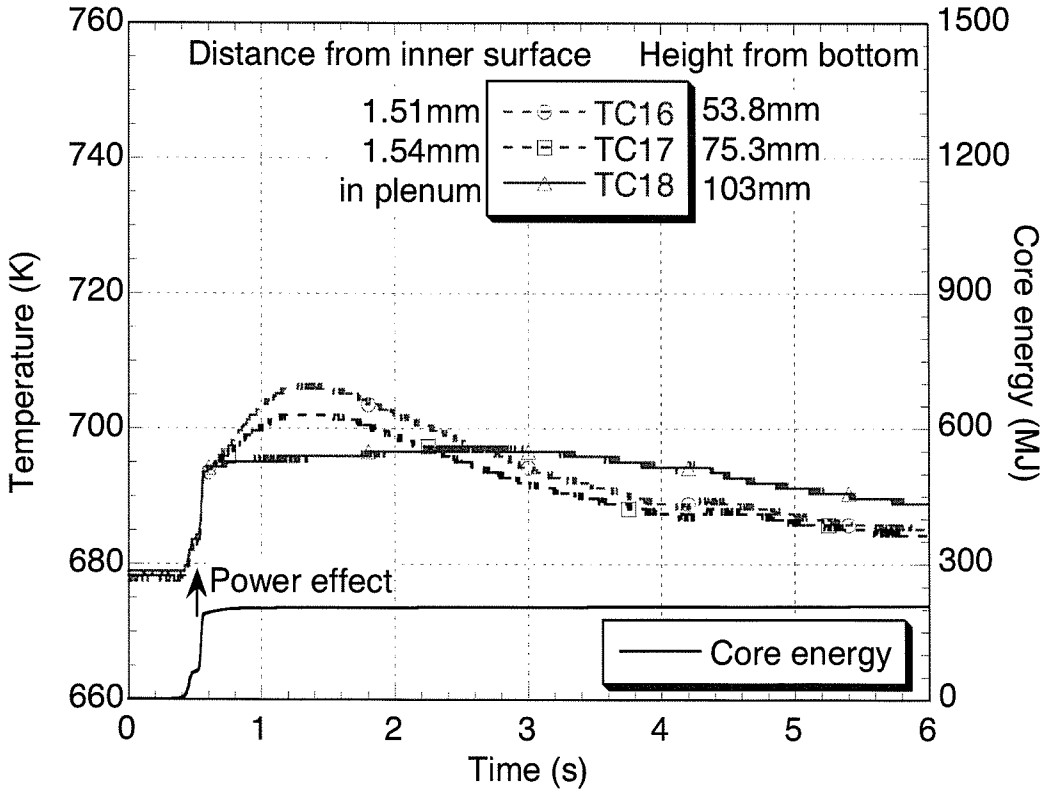

Fig. 13. Temperatures at gas plenum level in Capsule 1.

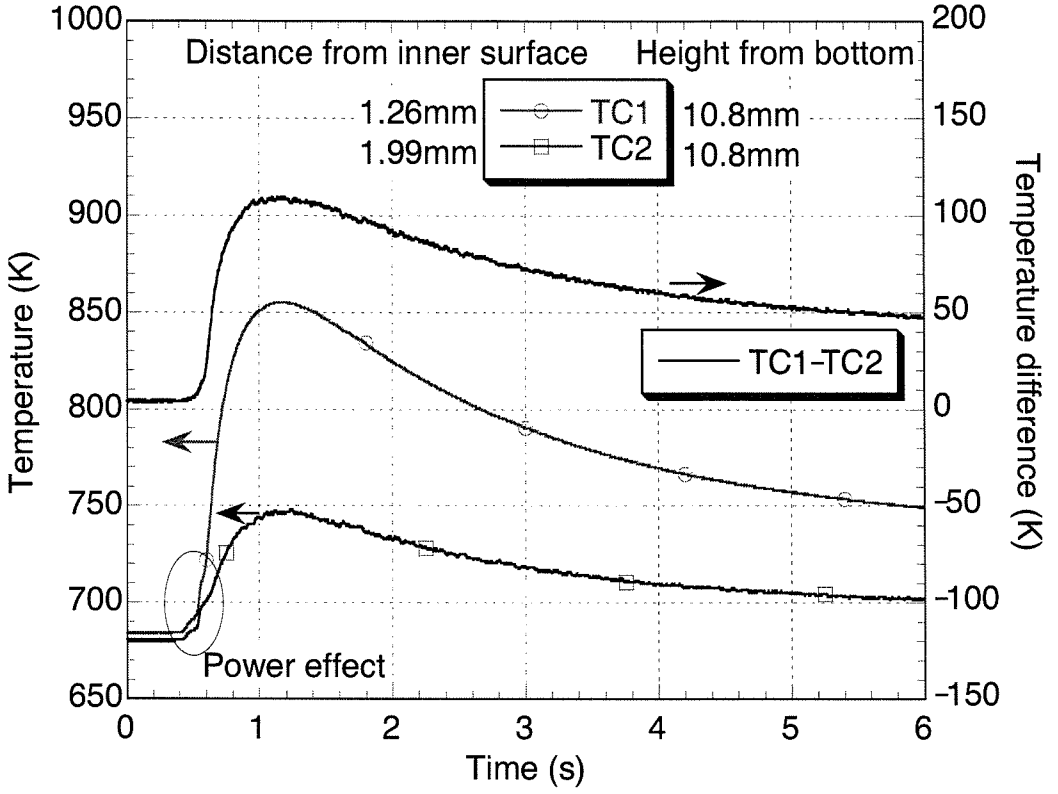

Fig. 14. Temperatures at lower fuel level in Capsule 2.

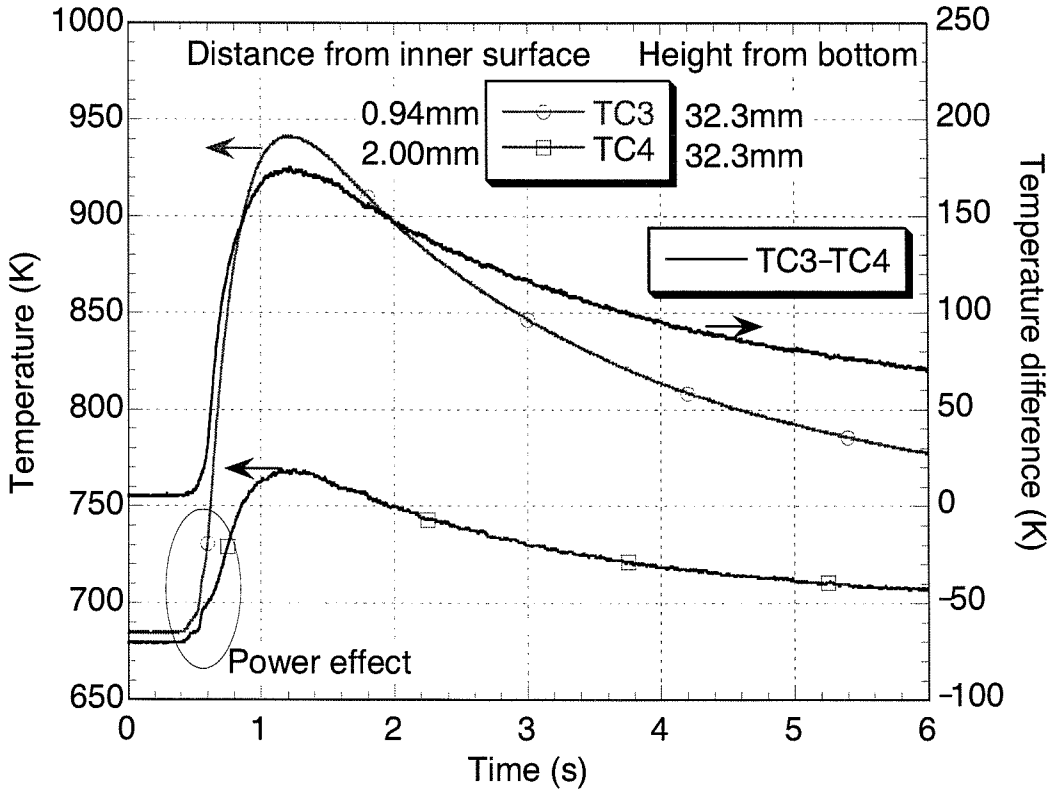

Fig. 15. Temperatures at upper fuel level in Capsule 2.

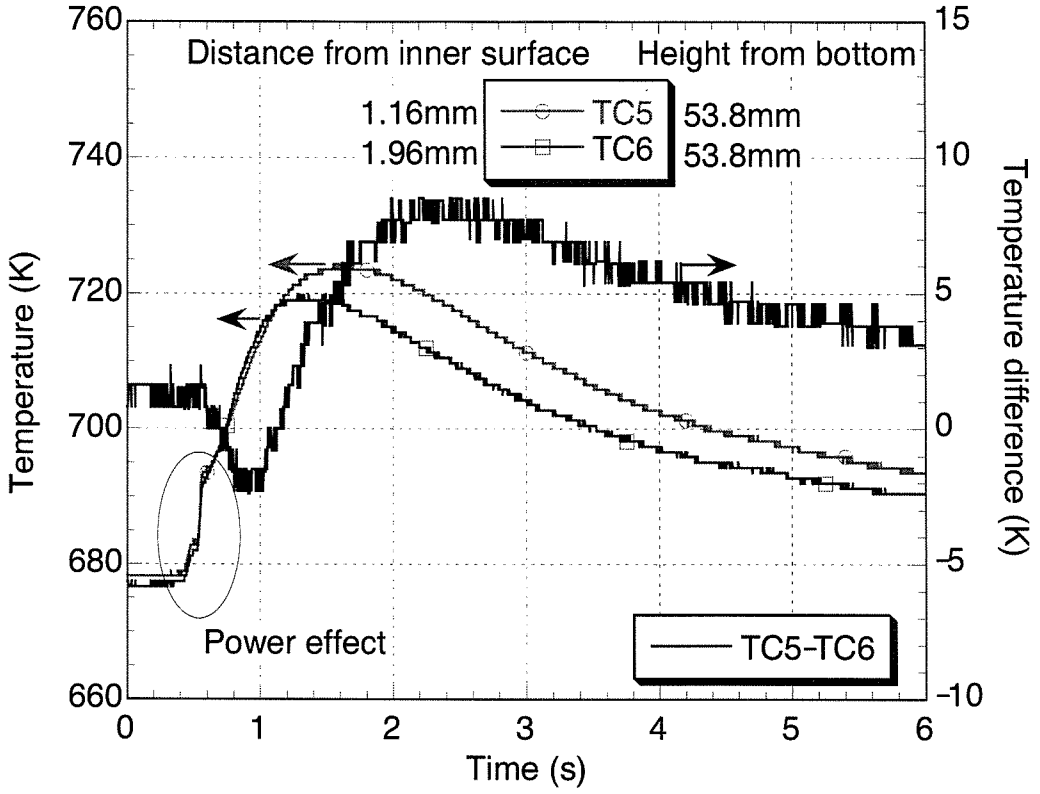

Fig. 16. Temperatures at lower gas plenum level in Capsule 2.

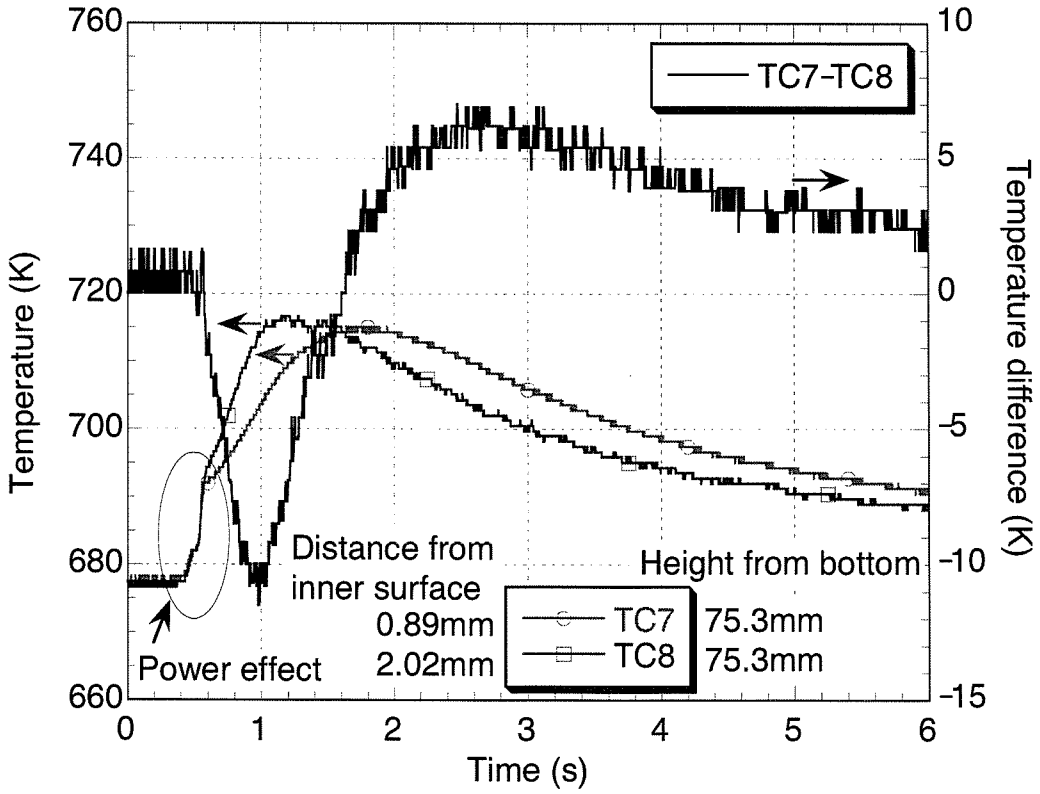

Fig. 17. Temperatures at upper gas plenum level in Capsule 2.

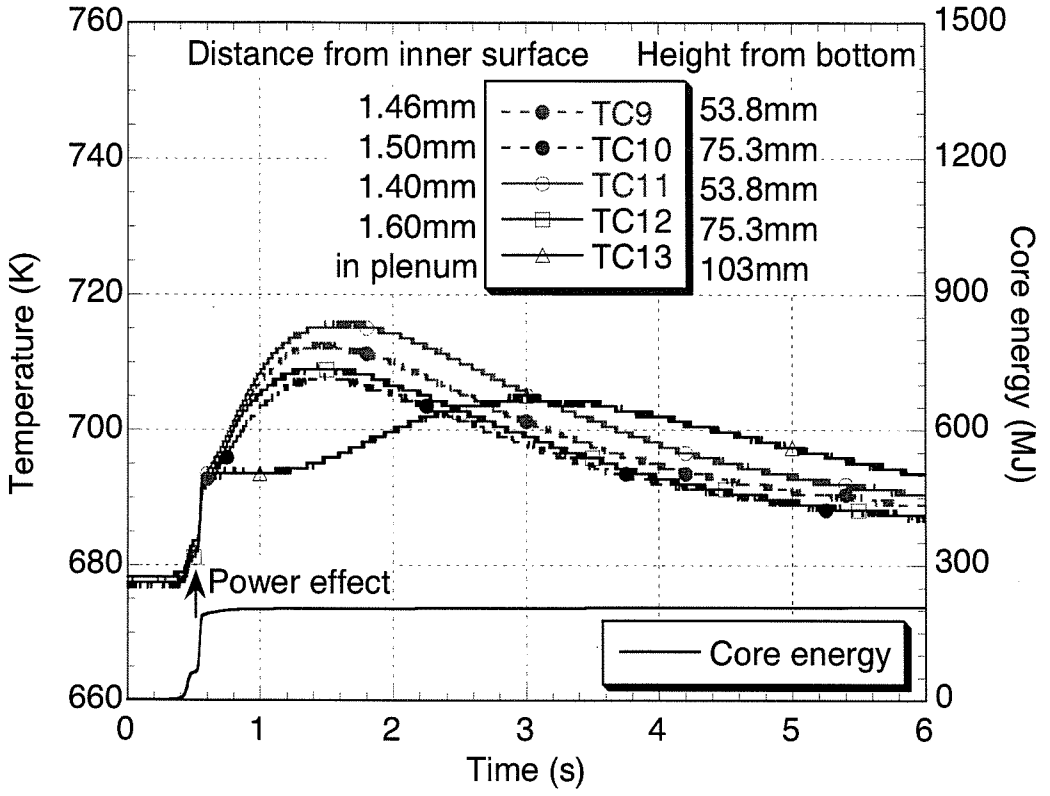

Fig. 18. Temperatures at gas plenum level in Capsule 2.

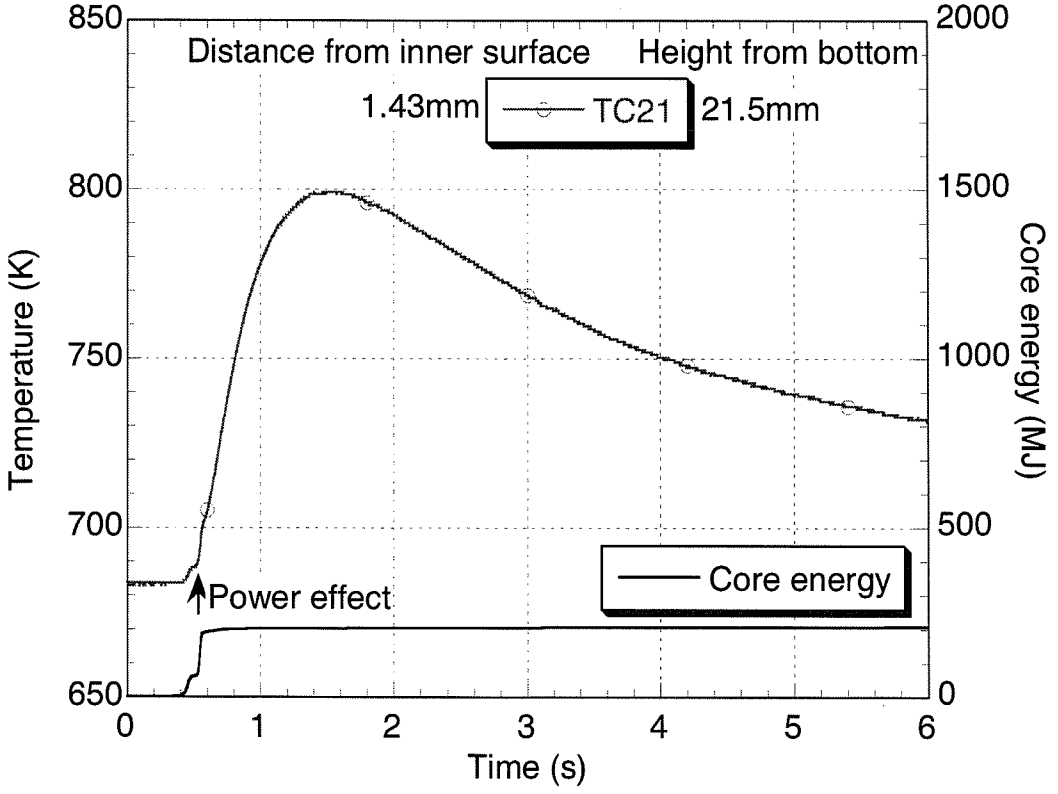

Fig. 19. Temperatures at fuel level in Capsule 3.

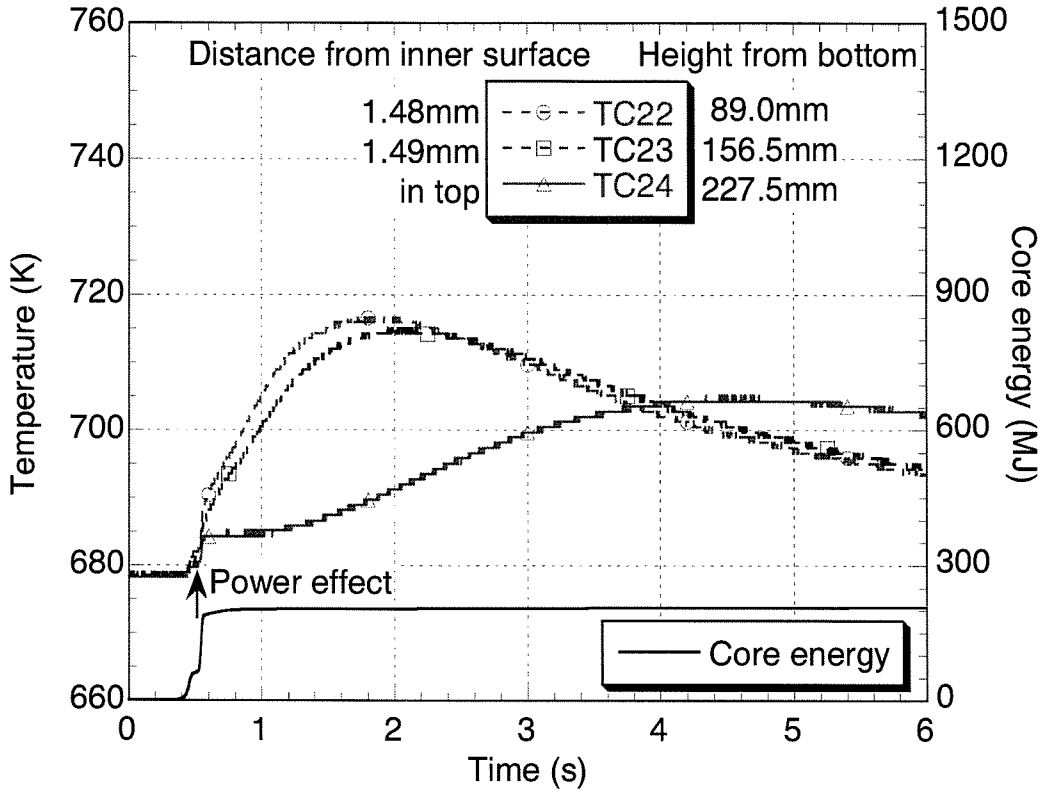

Fig. 20. Temperatures at gas plenum level in Capsule 3.

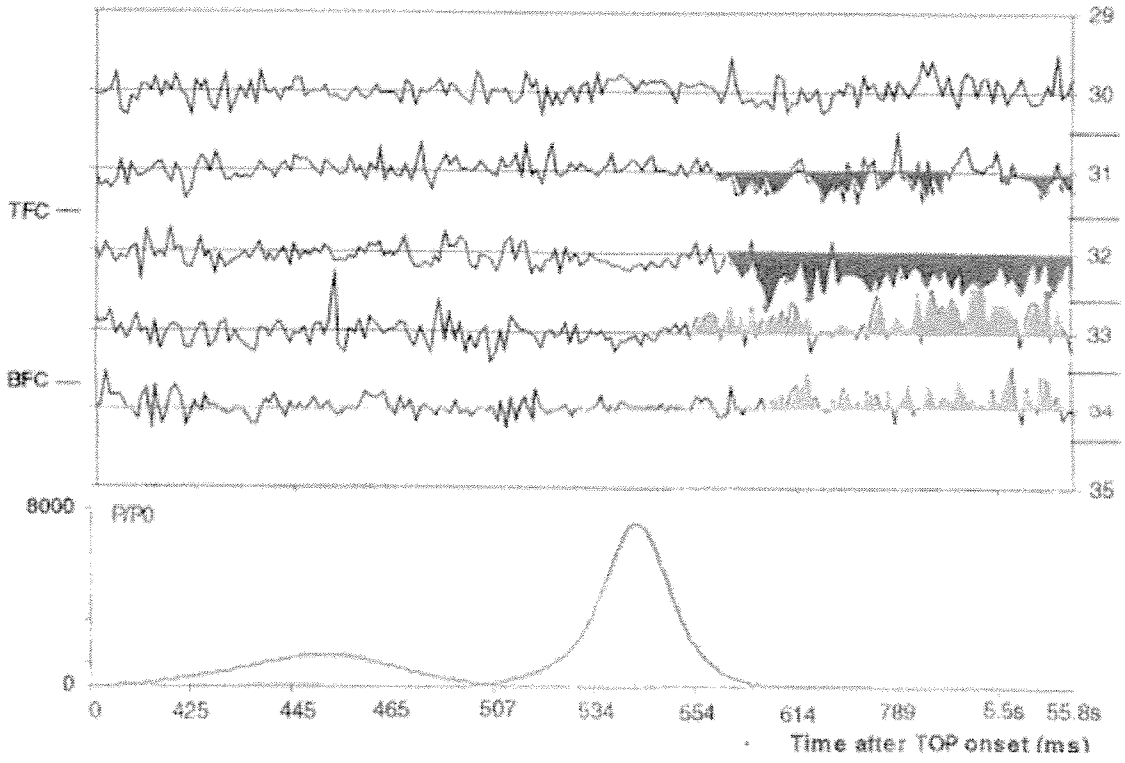

Fig. 21. Hodoscope signals viewing Capsule 1.

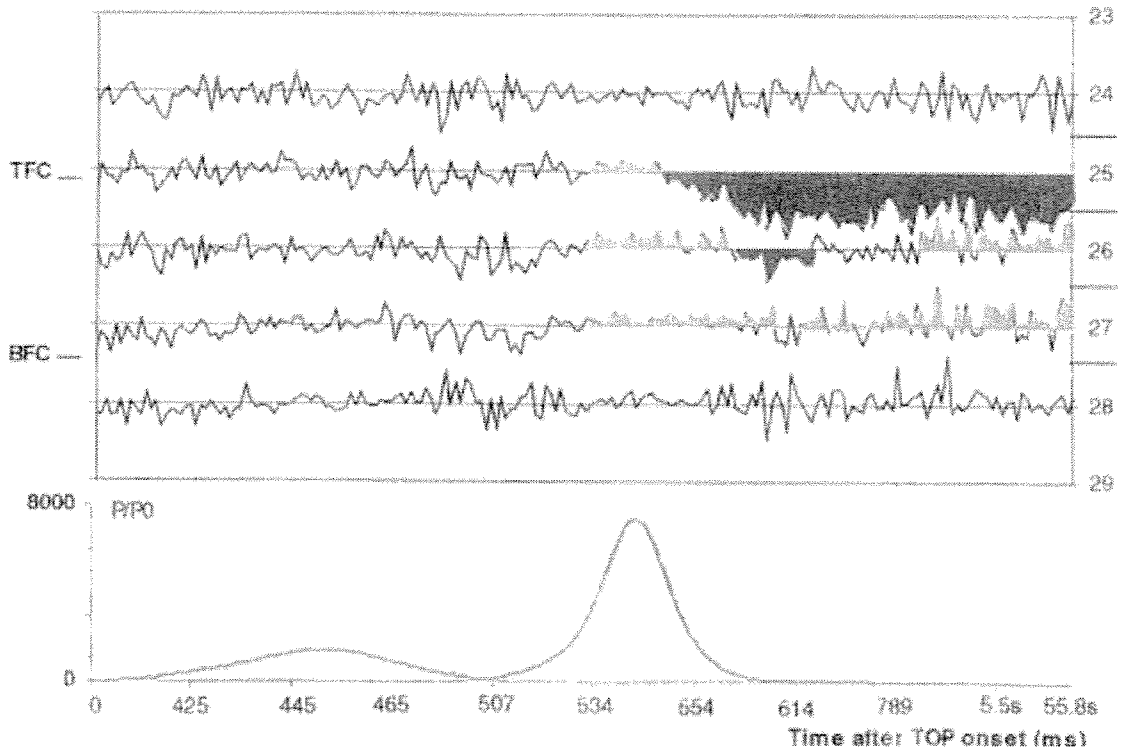

Fig. 22. Hodoscope signals viewing Capsule 2.

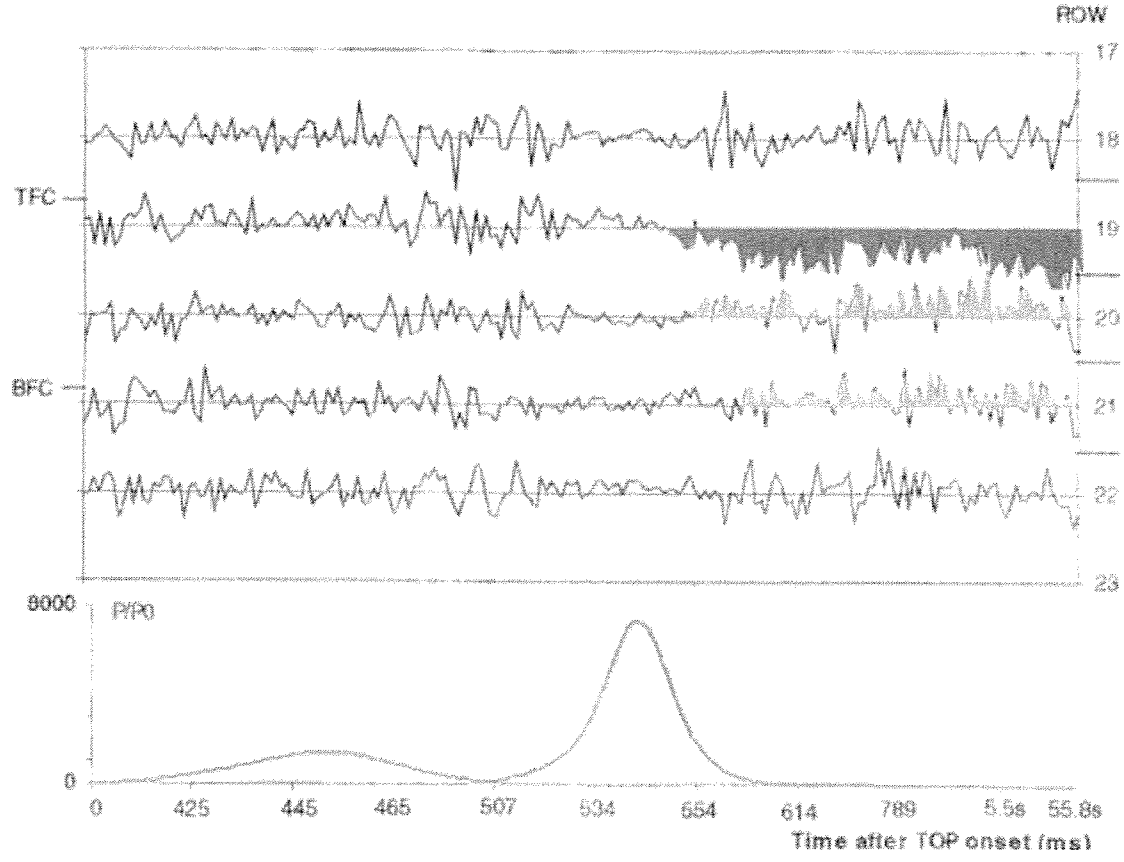

Fig. 23. Hodoscope signals viewing Capsule 3.

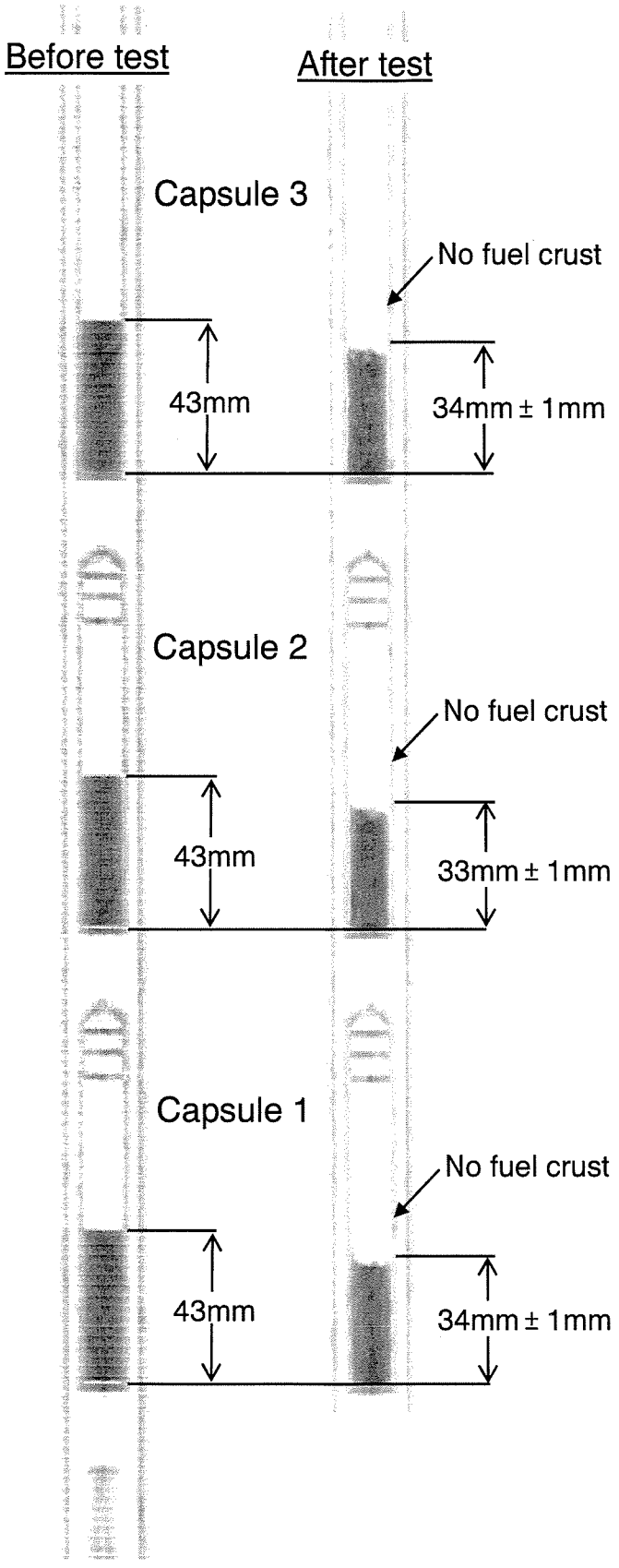

Fig. 24. Pre-test and post-test X-radiographs.

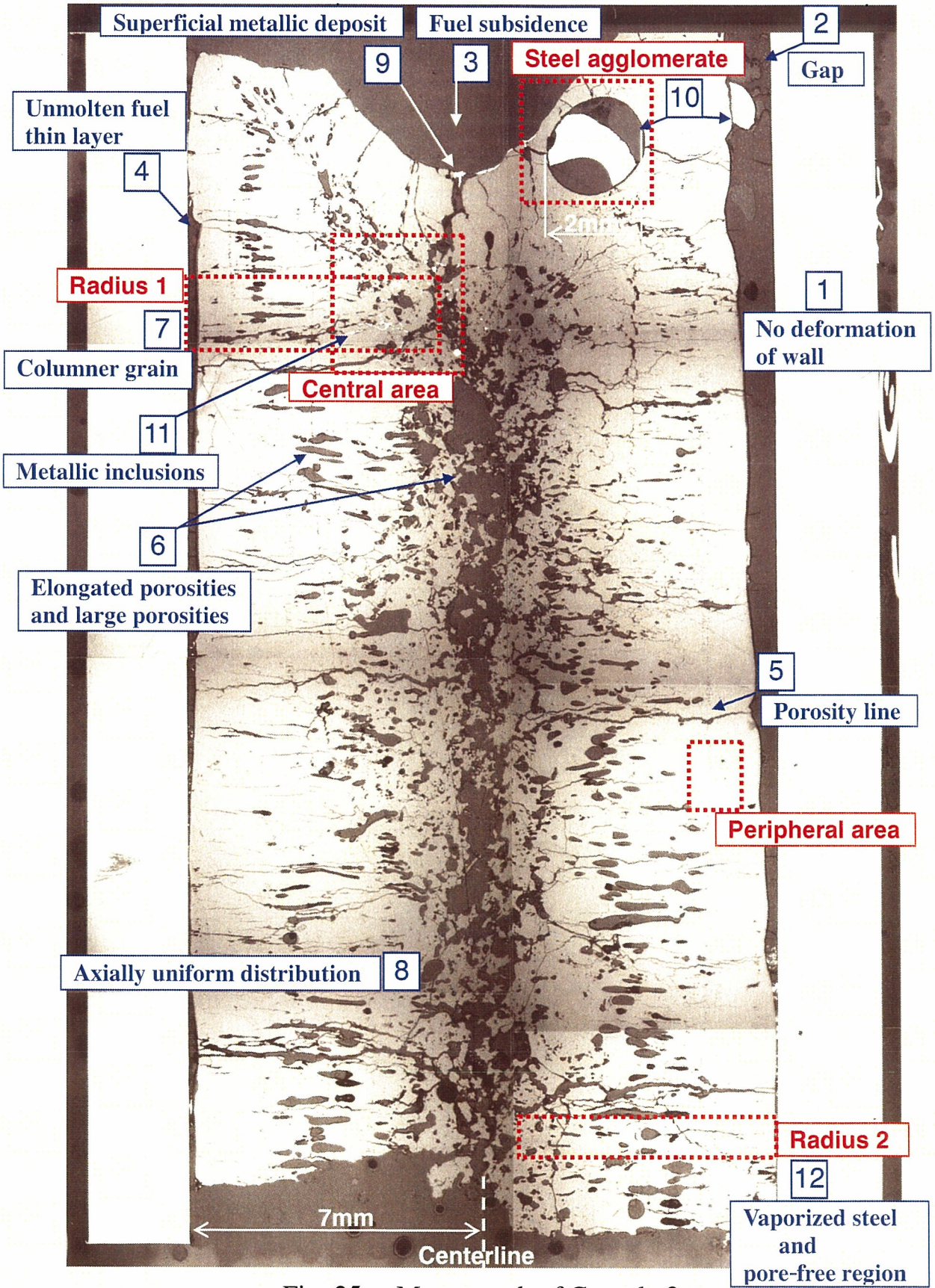

Fig. 25. Macrograph of Capsule 2.

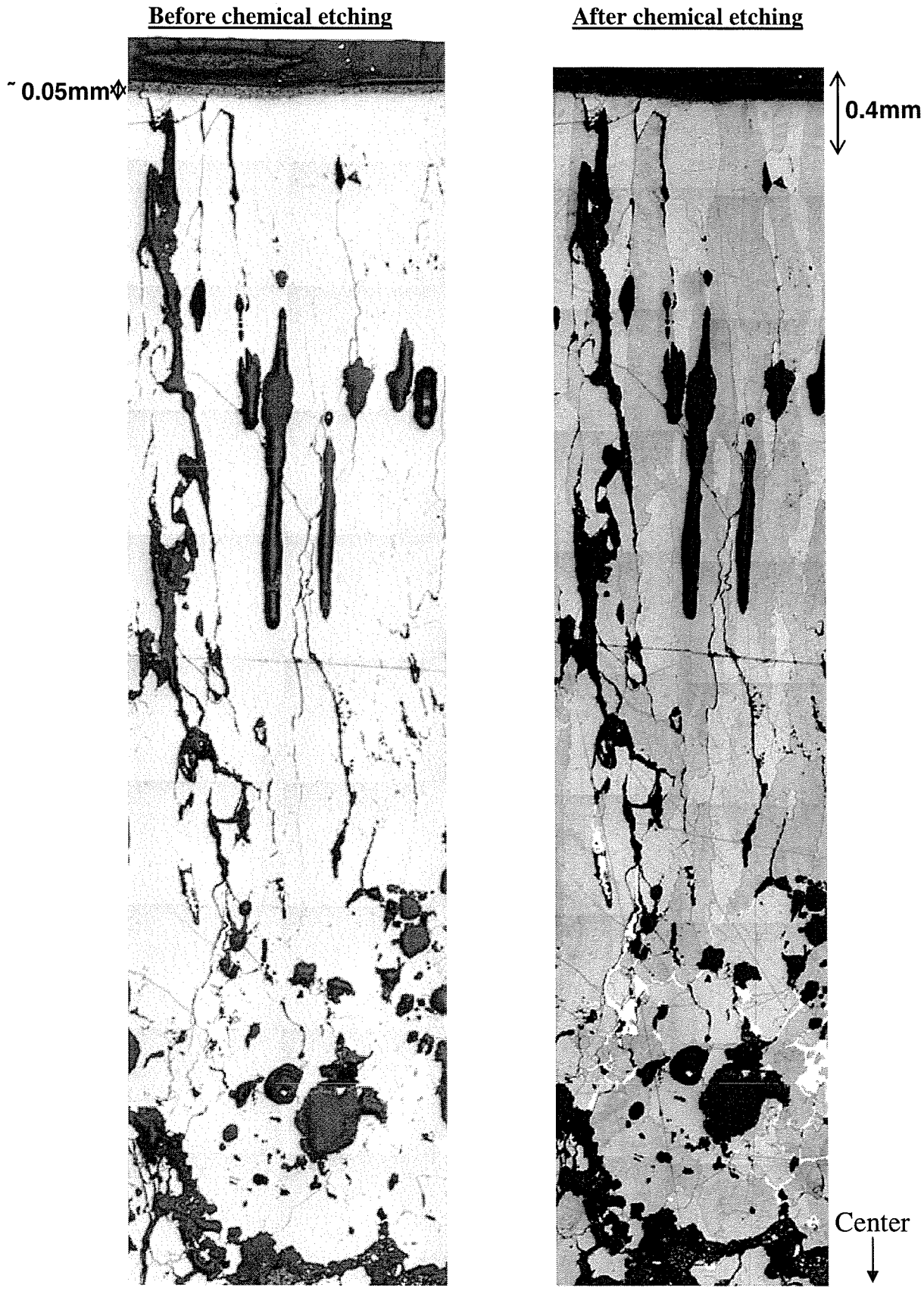

Fig. 26. Radius 1 of Capsule 2.

Fig. 27. Peripheral area of Capsule 2.

Fig. 28. Steel agglomerate in Capsule 2.

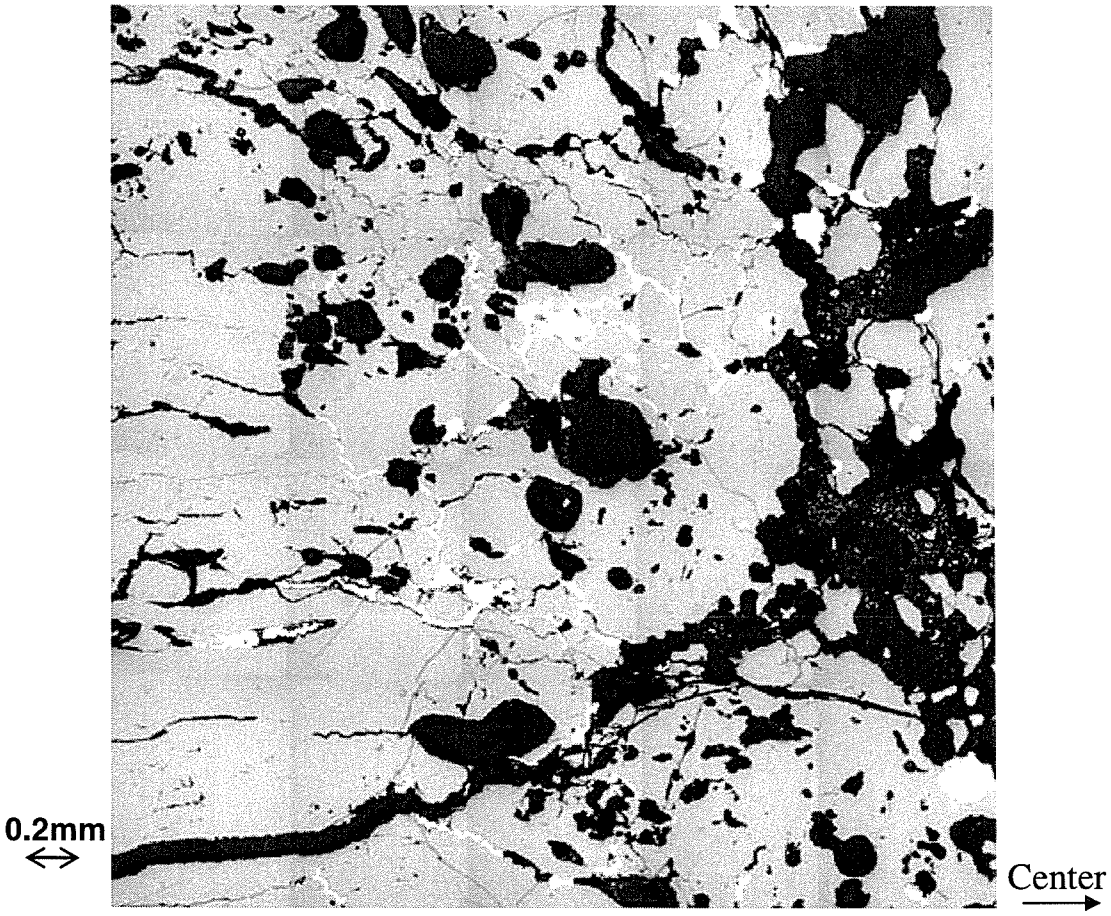

Fig. 29. Central area of Capsule 2.

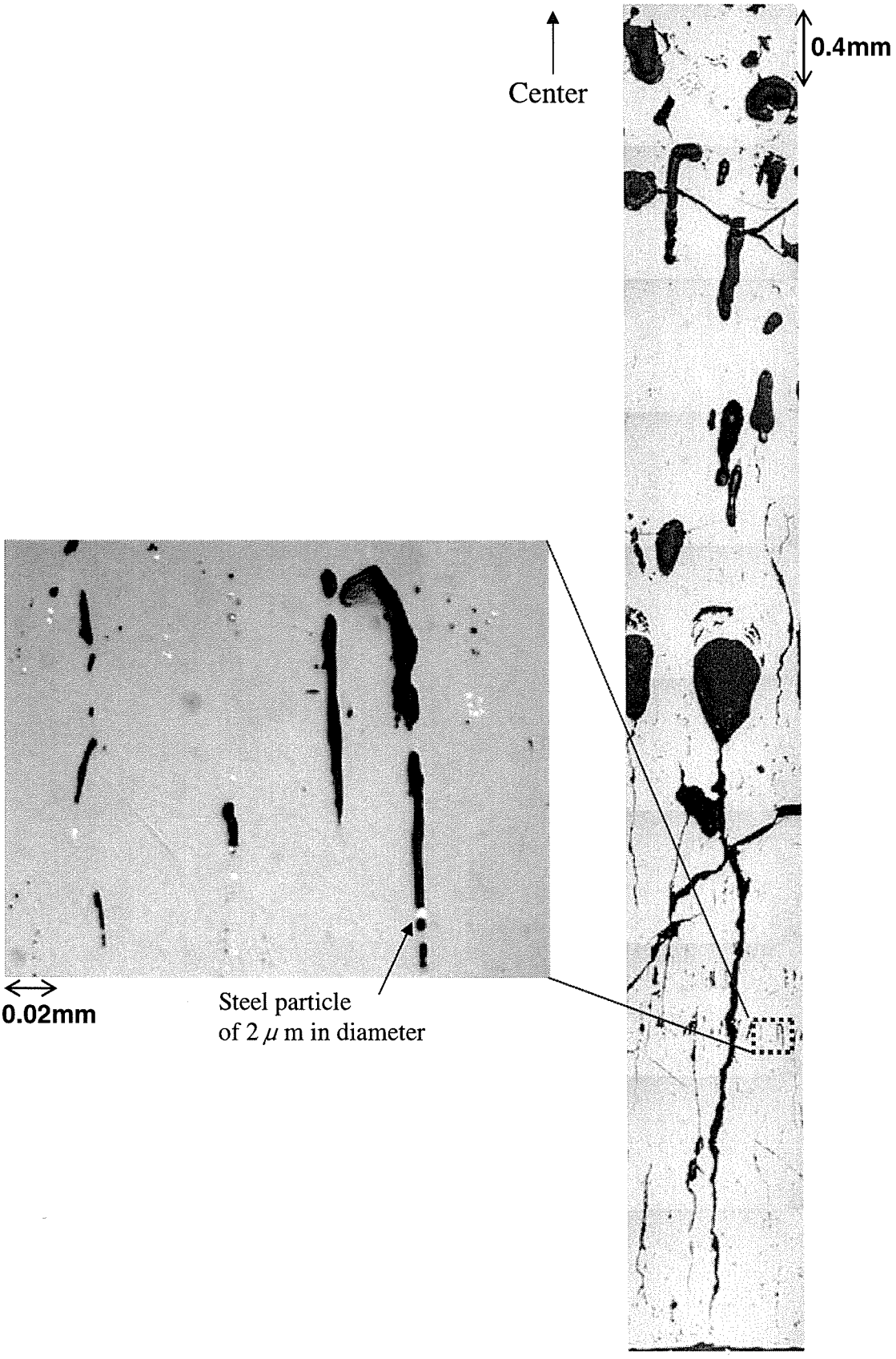

Fig. 30. Radius 2 of Capsule 2.

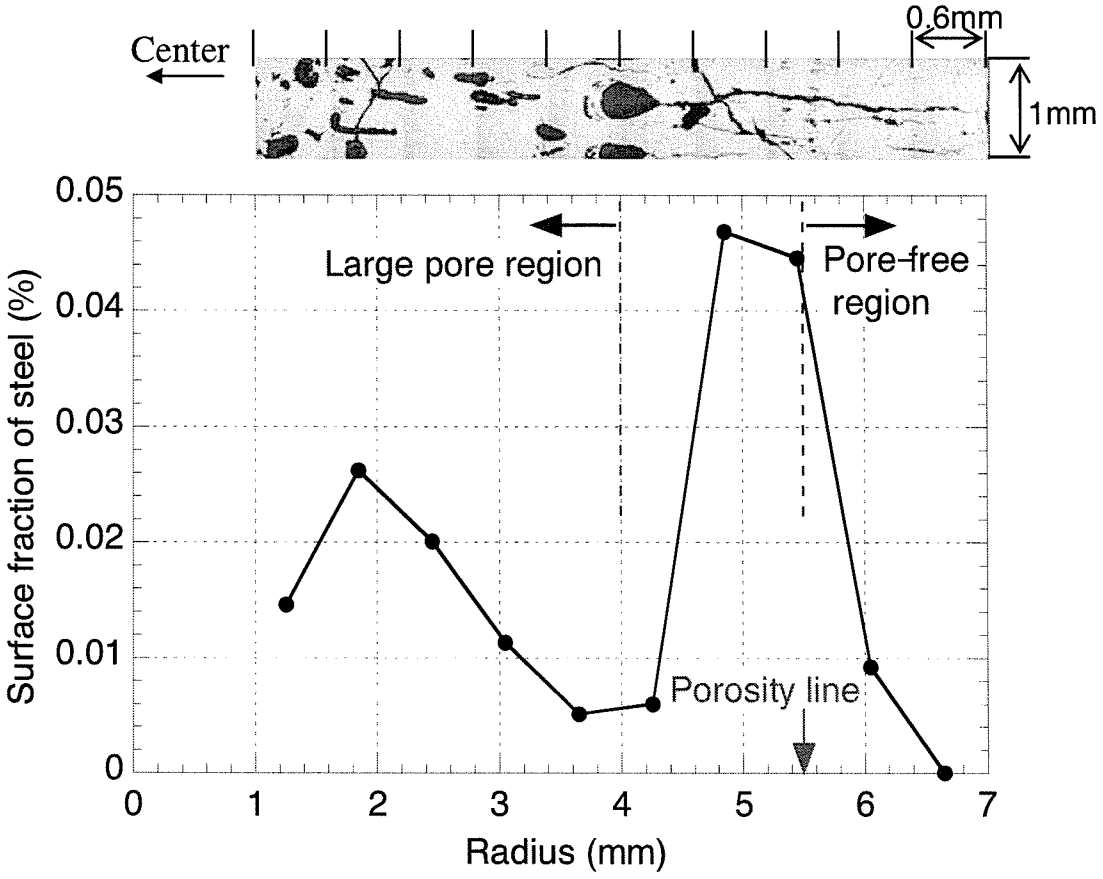

Fig. 31. Image analysis of Radius 2 of Capsule 2.

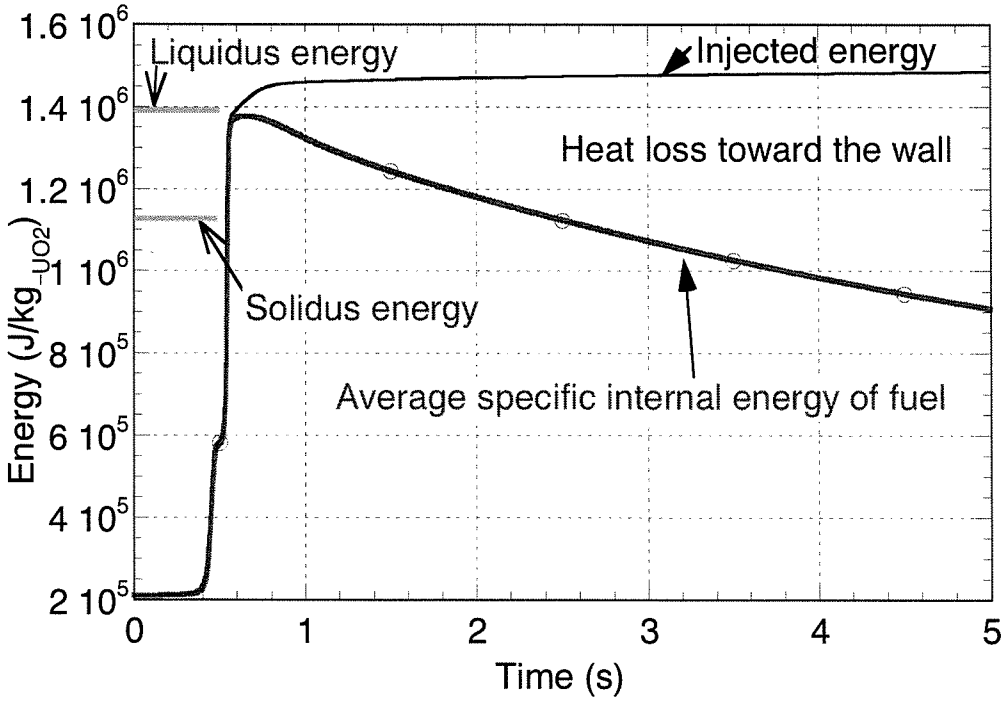

Fig. 32. Average specific internal energy of the fuel in Capsule 2 by the inverse conduction method using the double thermocouples.

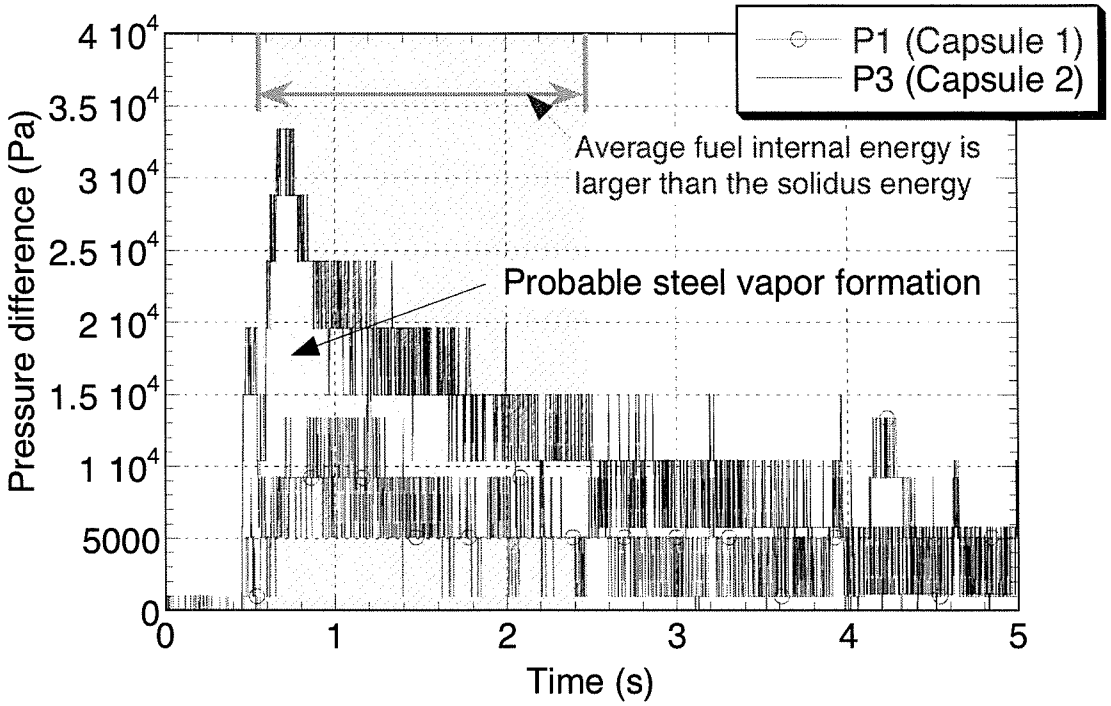

Fig. 33. Pressures in Capsule 1 and Capsule 2 (the constant pressures at 15s are subtracted from the measured data by P1 and P3).

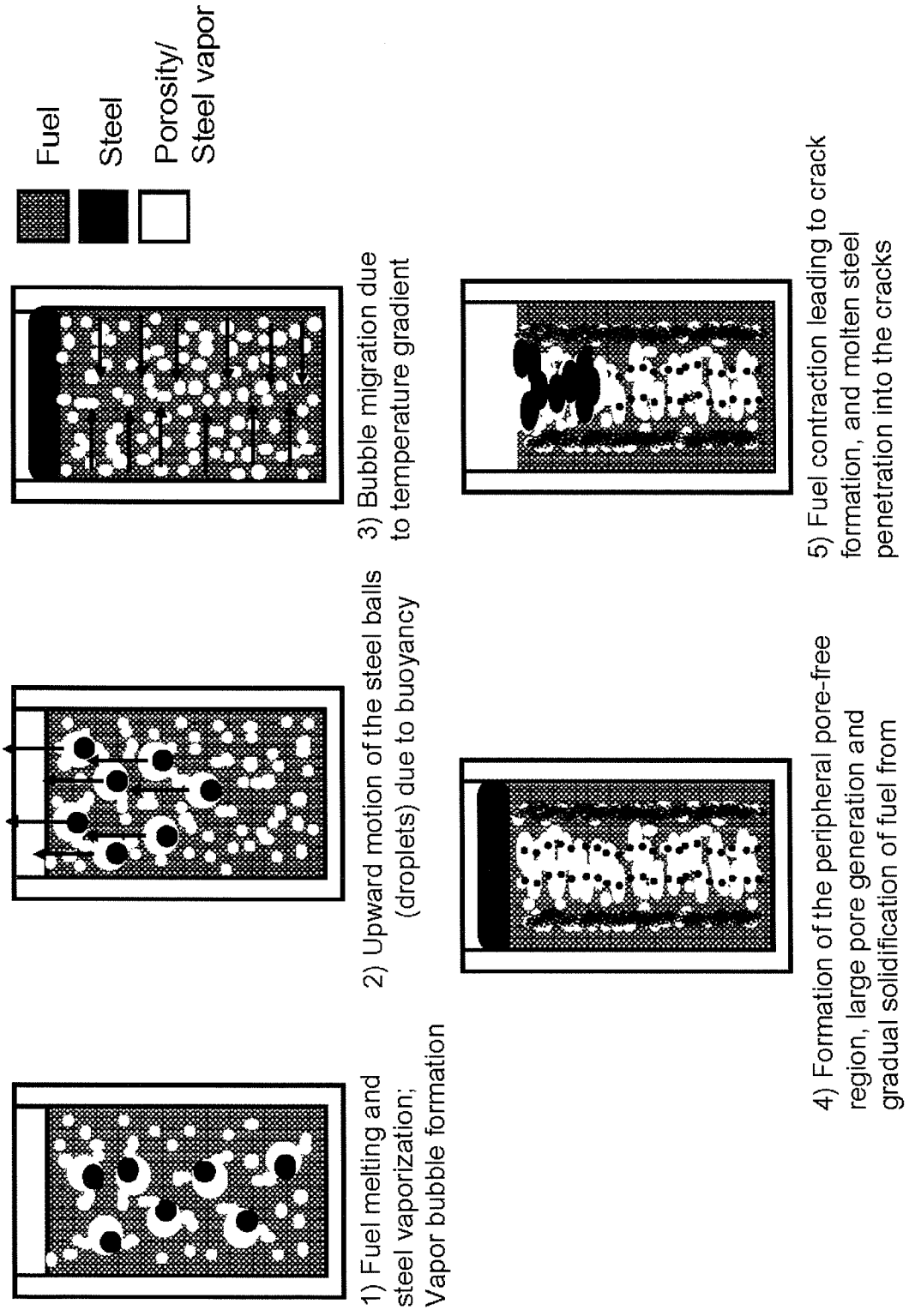

Fig. 34. Estimated event sequence in Capsule 2 in the TPA2 test.

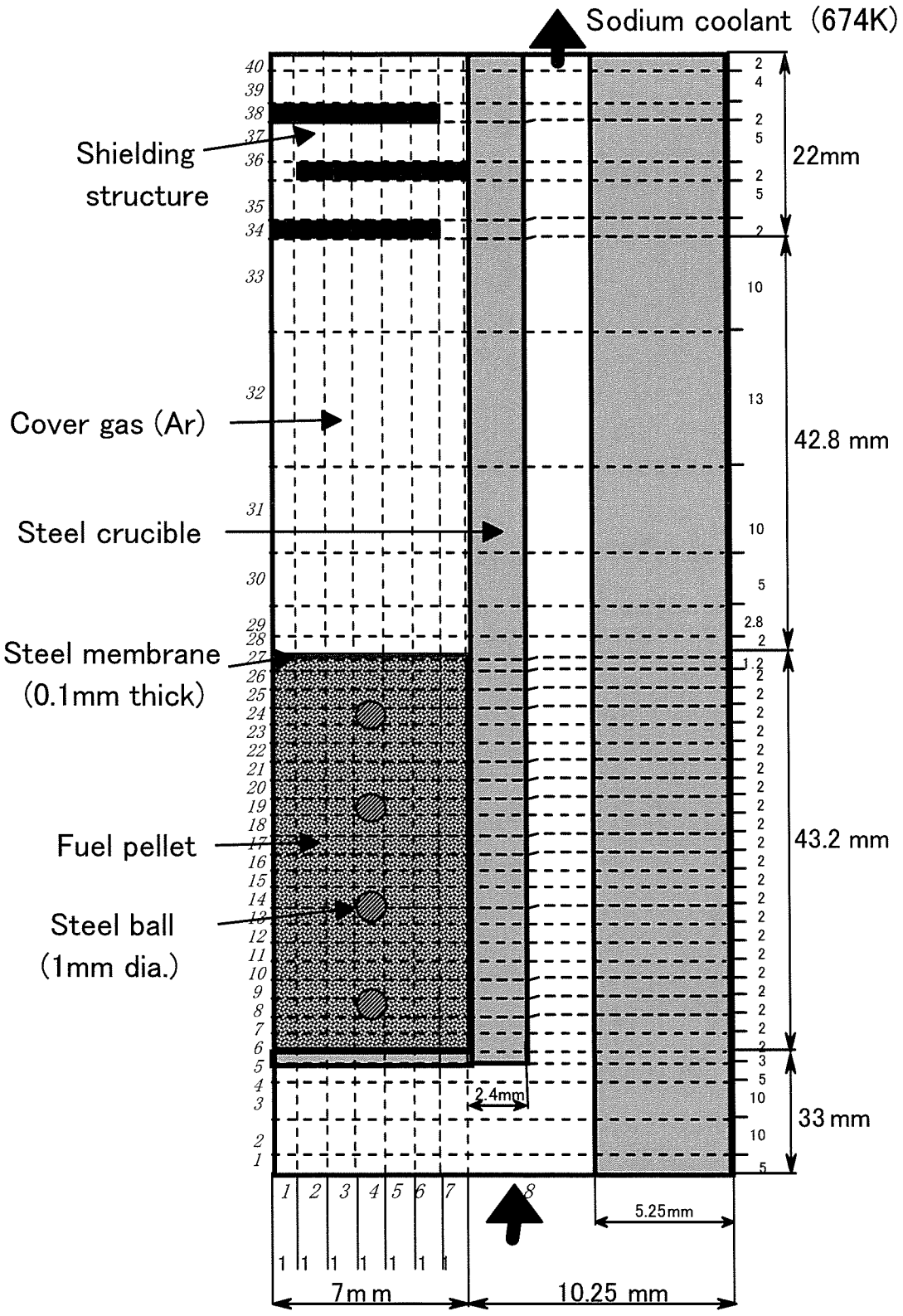

Fig. 35. Analytical geometry for the SIMMER-III calculation.

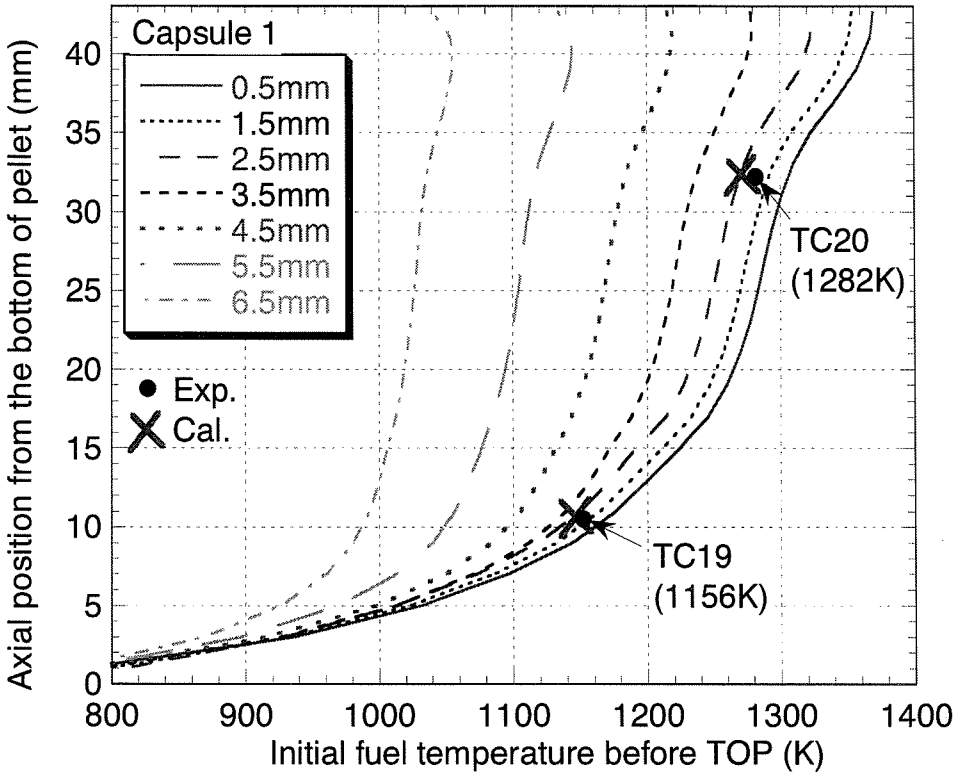

Fig. 36. Initial fuel temperature profile inside Capsule 1.

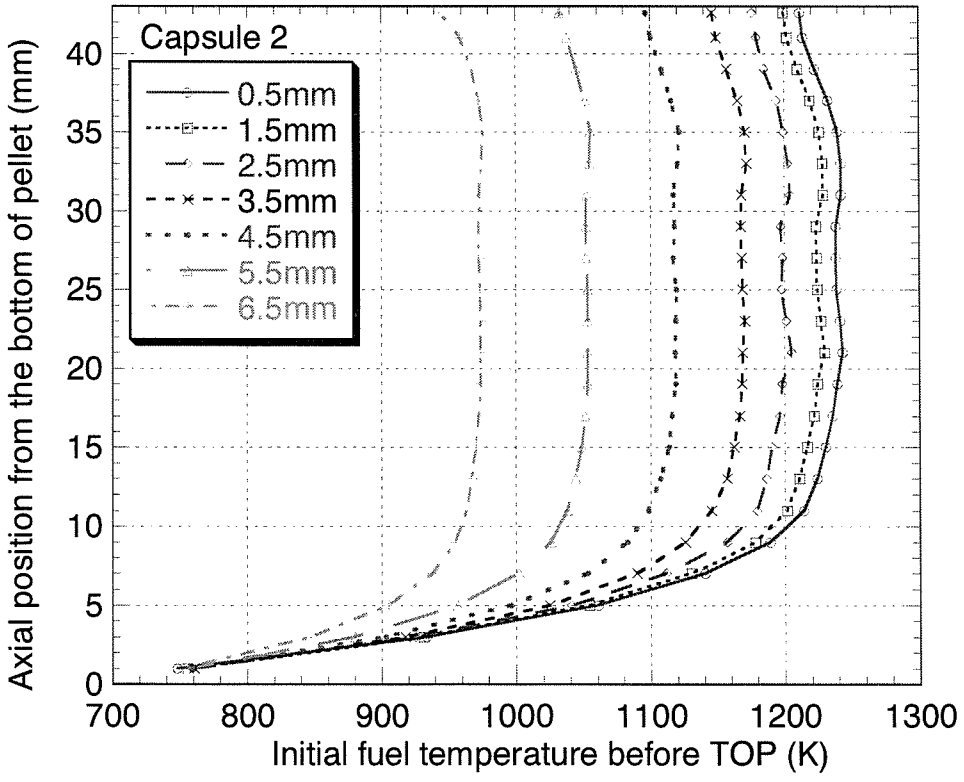

Fig. 37. Initial fuel temperature profile inside Capsule 2.

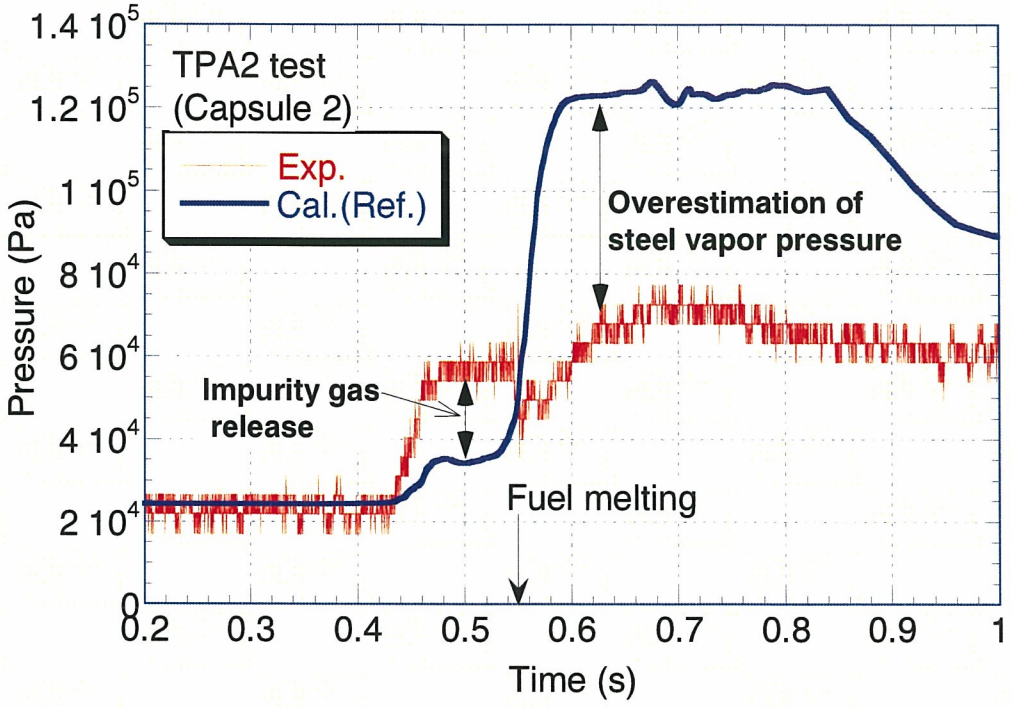

Fig. 38. Pressure history in Capsule 2 in TPA2 (Reference case).

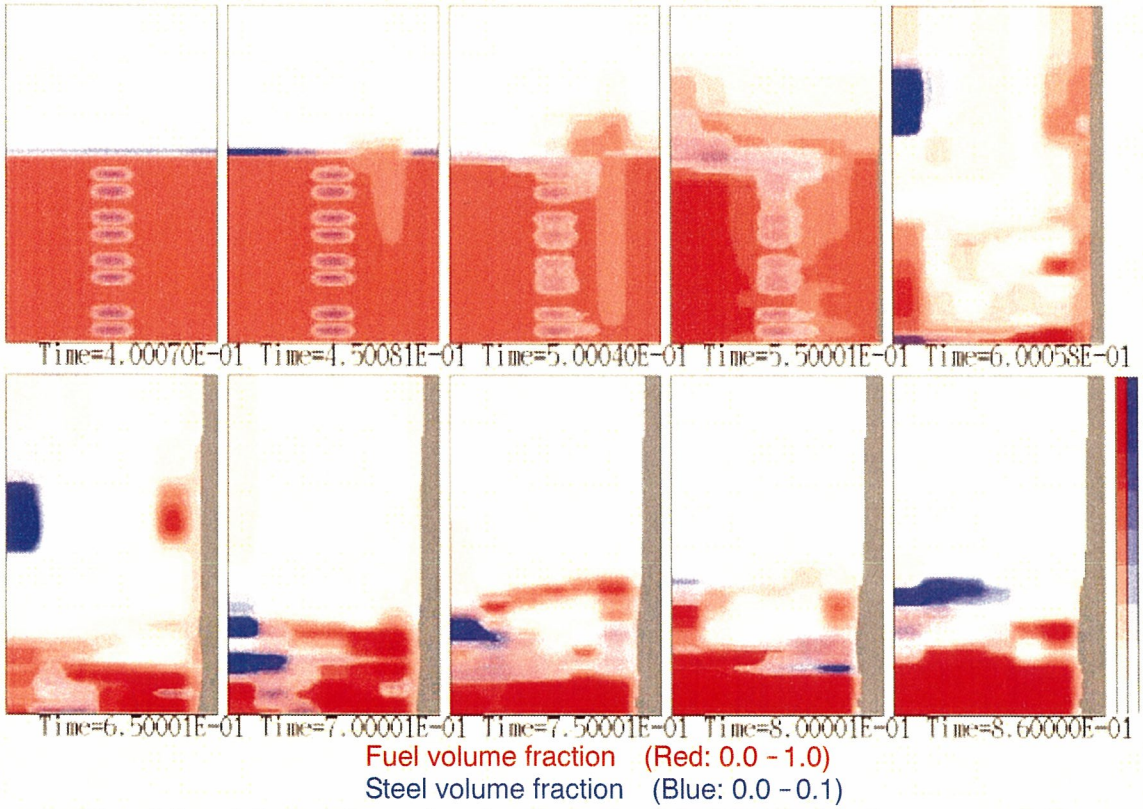

Fig. 39. Material motion in Capsule 2 in TPA2 (Reference case).

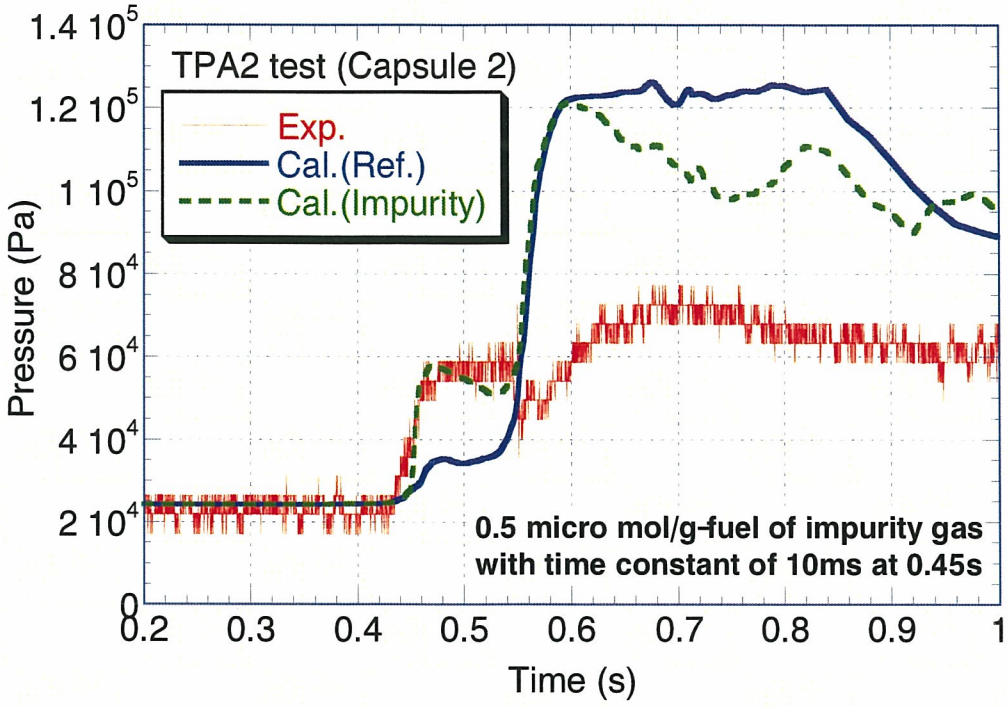

Fig. 40. Pressure history in Capsule 2 in TPA2 (Impurity case).

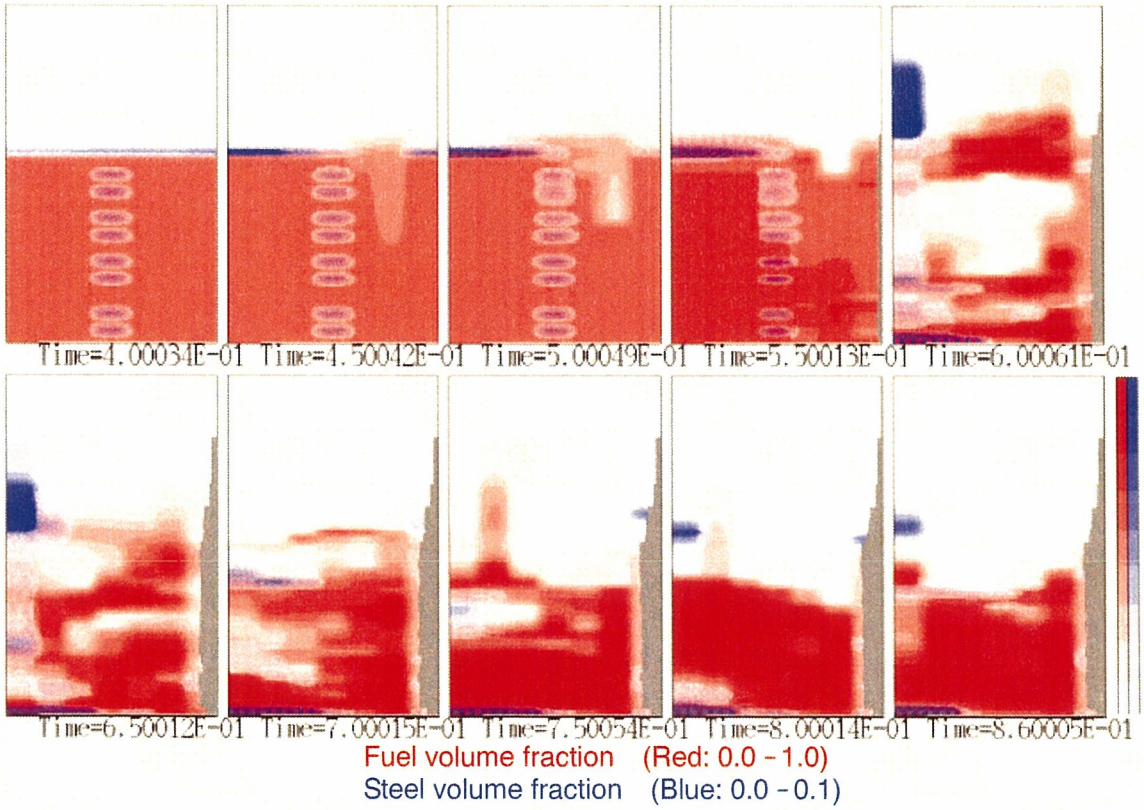

Fig. 41. Material motion in Capsule 2 in TPA2 (Impurity case).

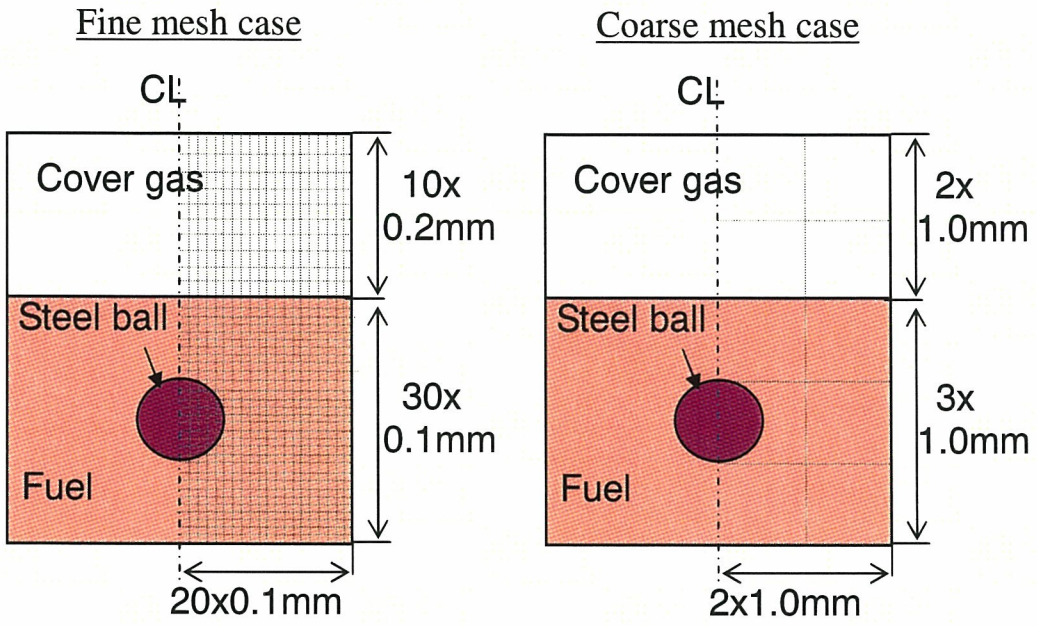

Fig. 42. Geometric models for the single droplet calculations.

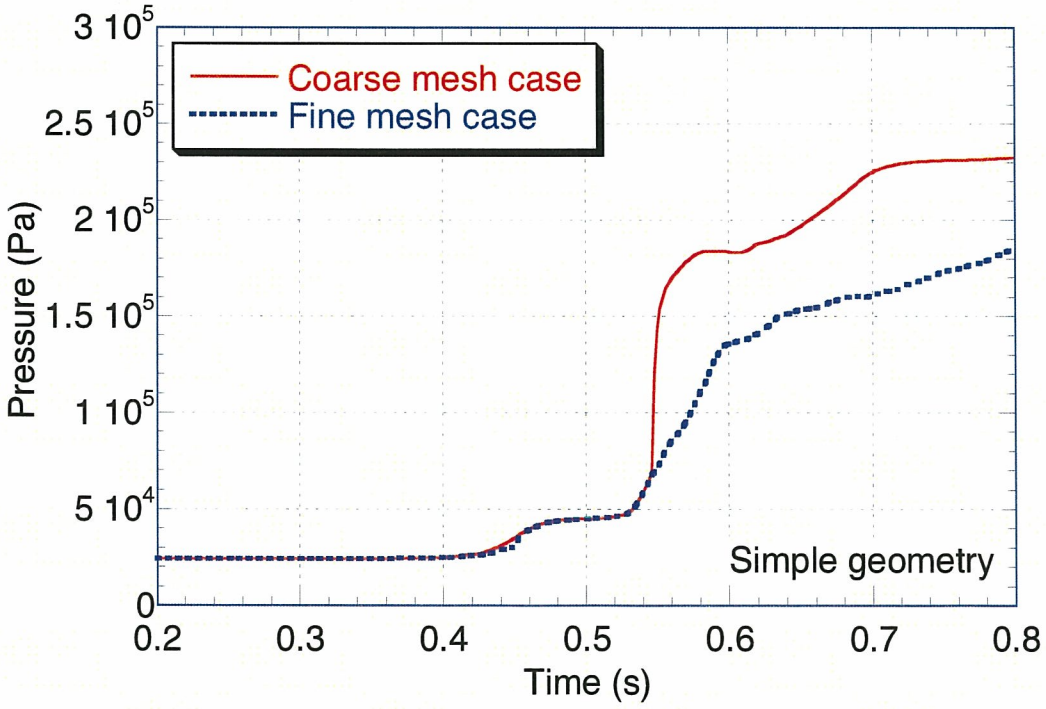

Fig. 43. Pressure history in the simple geometry.

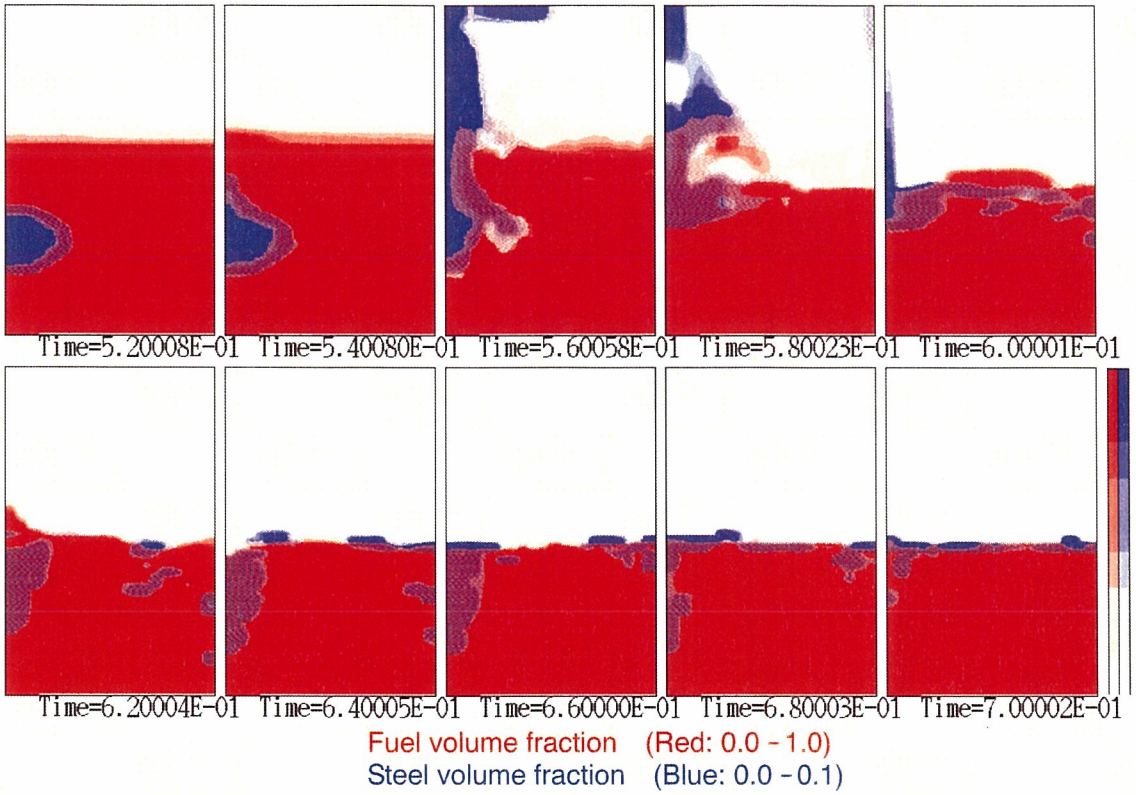

Fig. 44. Steel ball motion of Fine mesh case in the simple geometry.

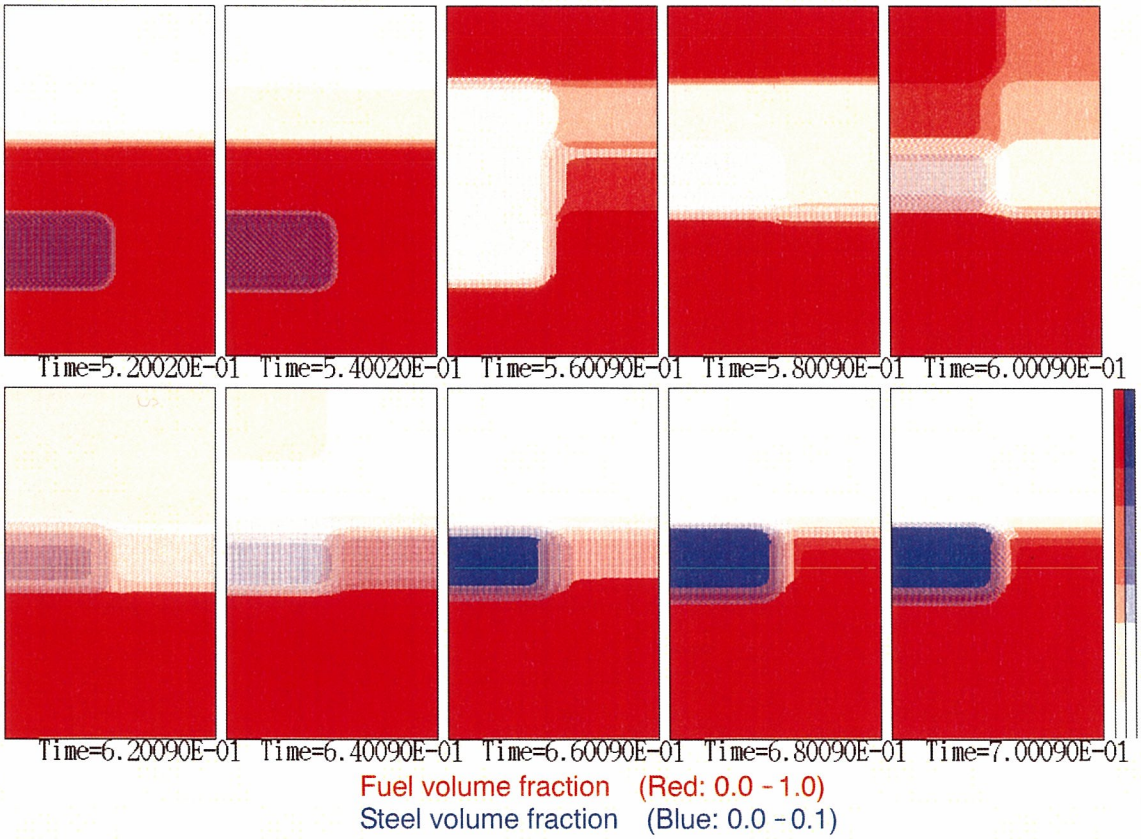

Fig. 45. Steel ball motion of Coarse mesh case in the simple geometry.

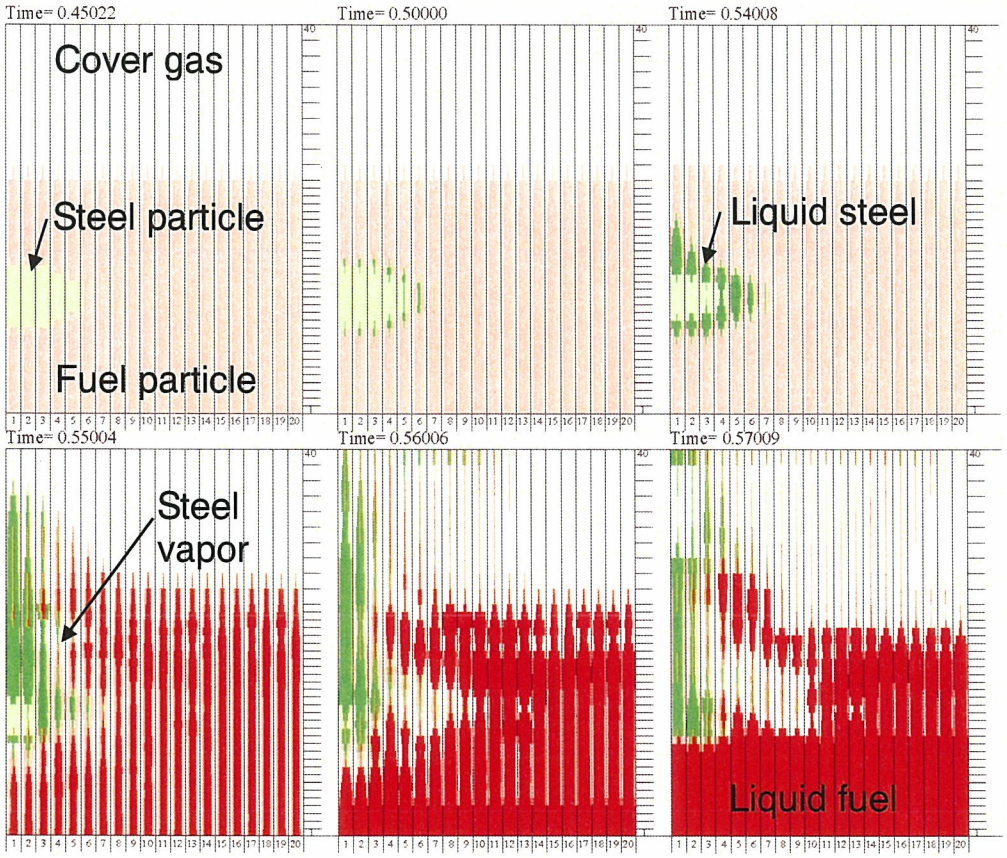

Fig. 46. Material distributions of Fine mesh case in the simple geometry.

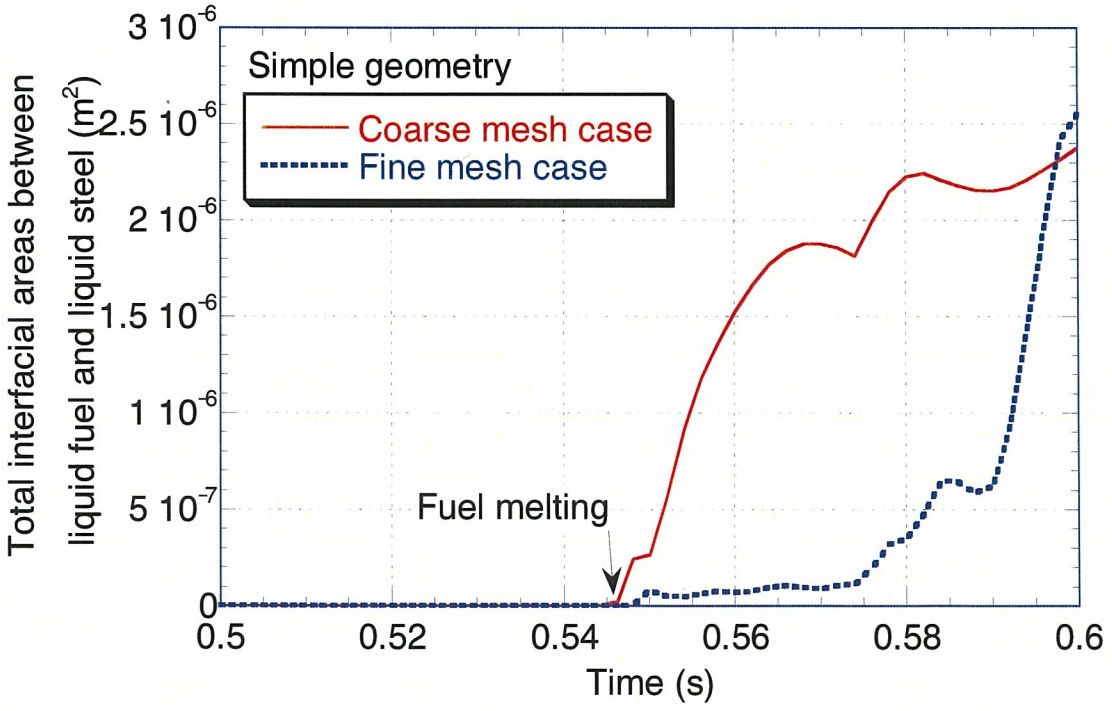

Fig. 47. Interfacial areas between liquid fuel and liquid steel in the simple geometry.

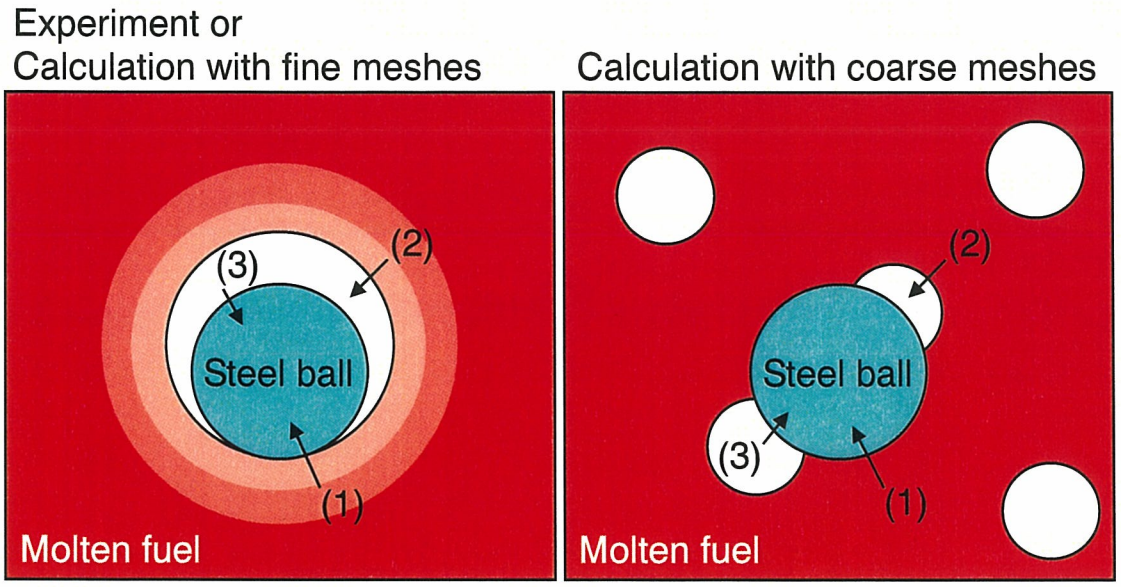

(1) Overestimation of heat flux due to higher fuel temperature and vapor blanketing.
(2) Overestimation of heat flux due to higher fuel temperature.
(3) Overestimation of heat flux due to higher gas temperature.

Fig. 48. Heat transfer mechanism from fuel to steel.

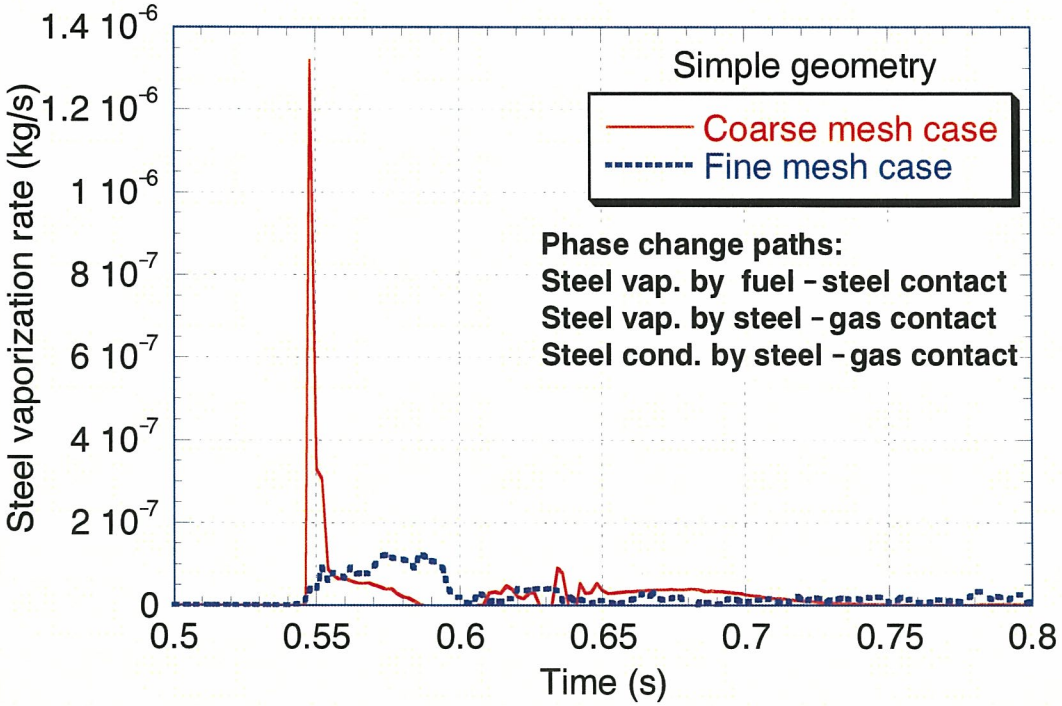

Fig. 49. Steel vaporization rate in the simple geometry.

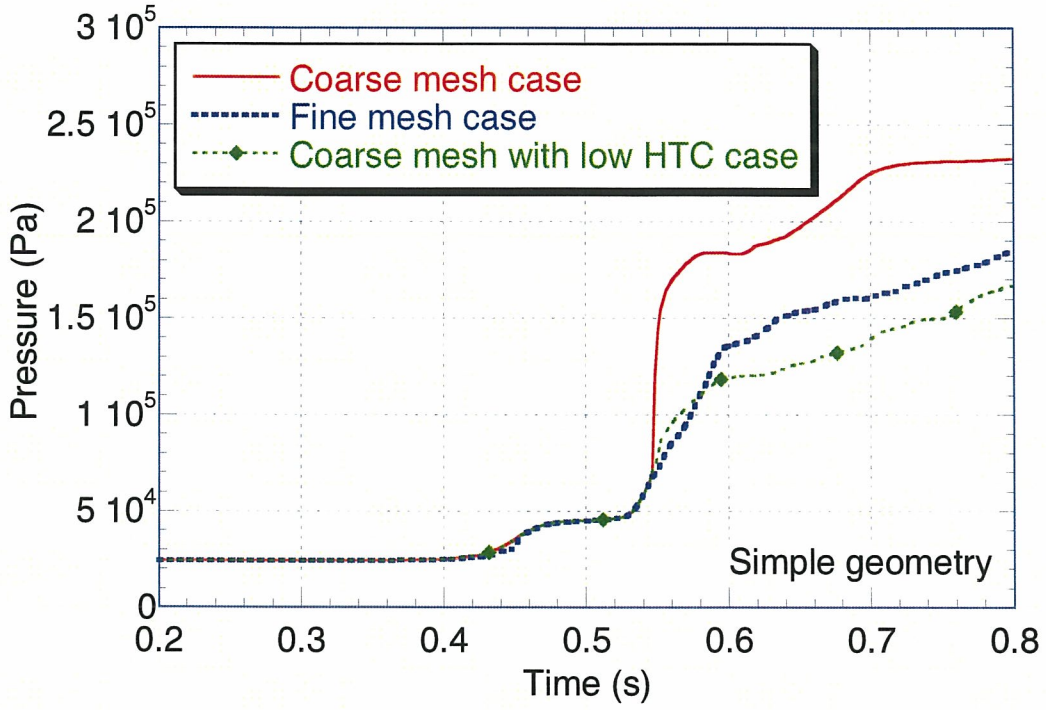

Fig. 50. Pressure history of Coarse mesh with low HTC case in the simple geometry.

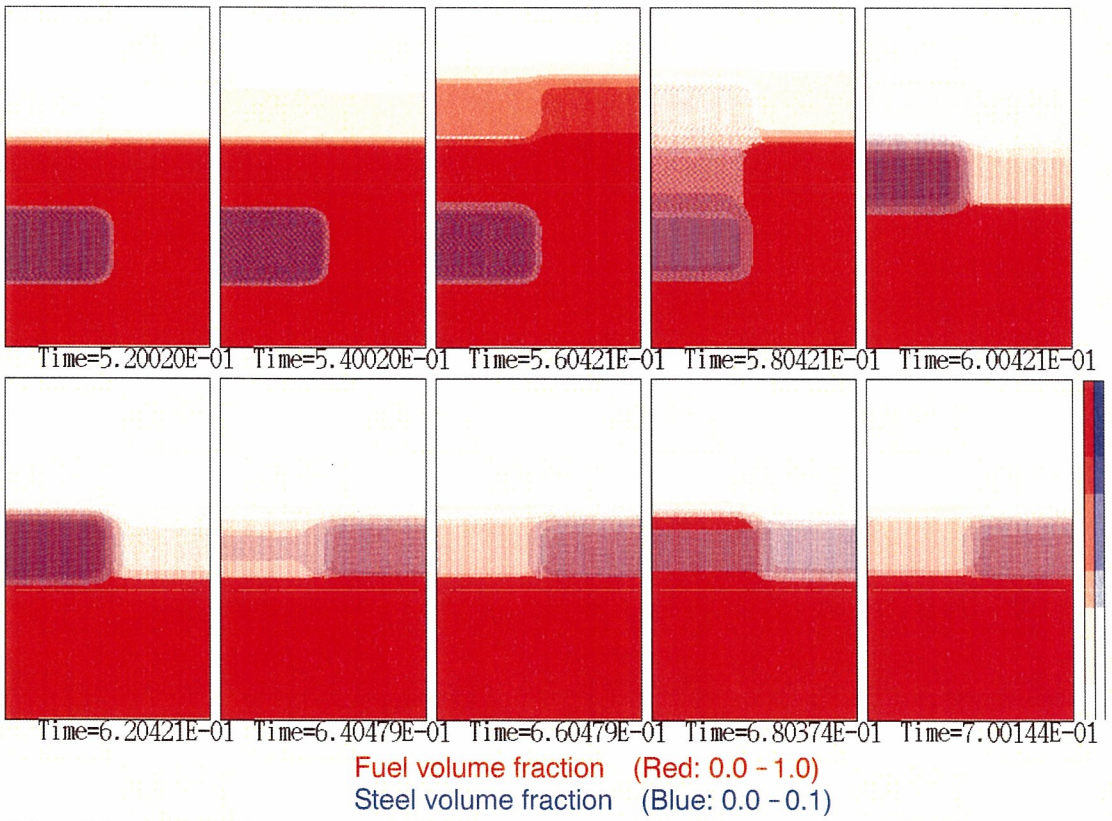

Fig. 51. Steel ball motion of the Coarse mesh with low HTC case in the simple geometry.

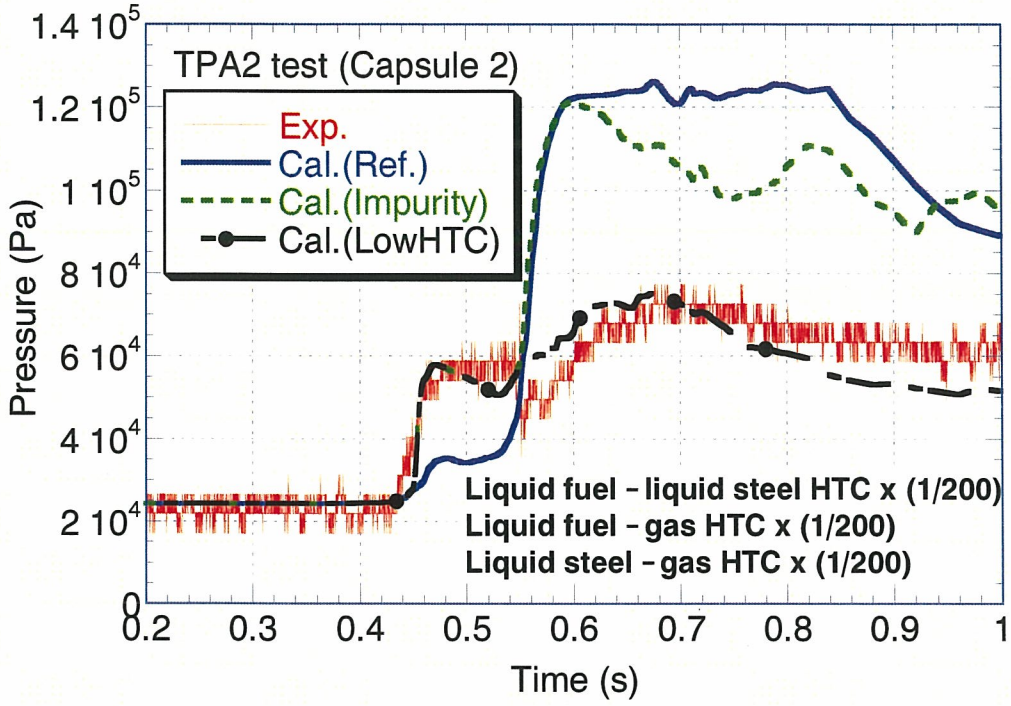

Fig. 52. Pressure history in Capsule 2 in TPA2 (Low HTC case).

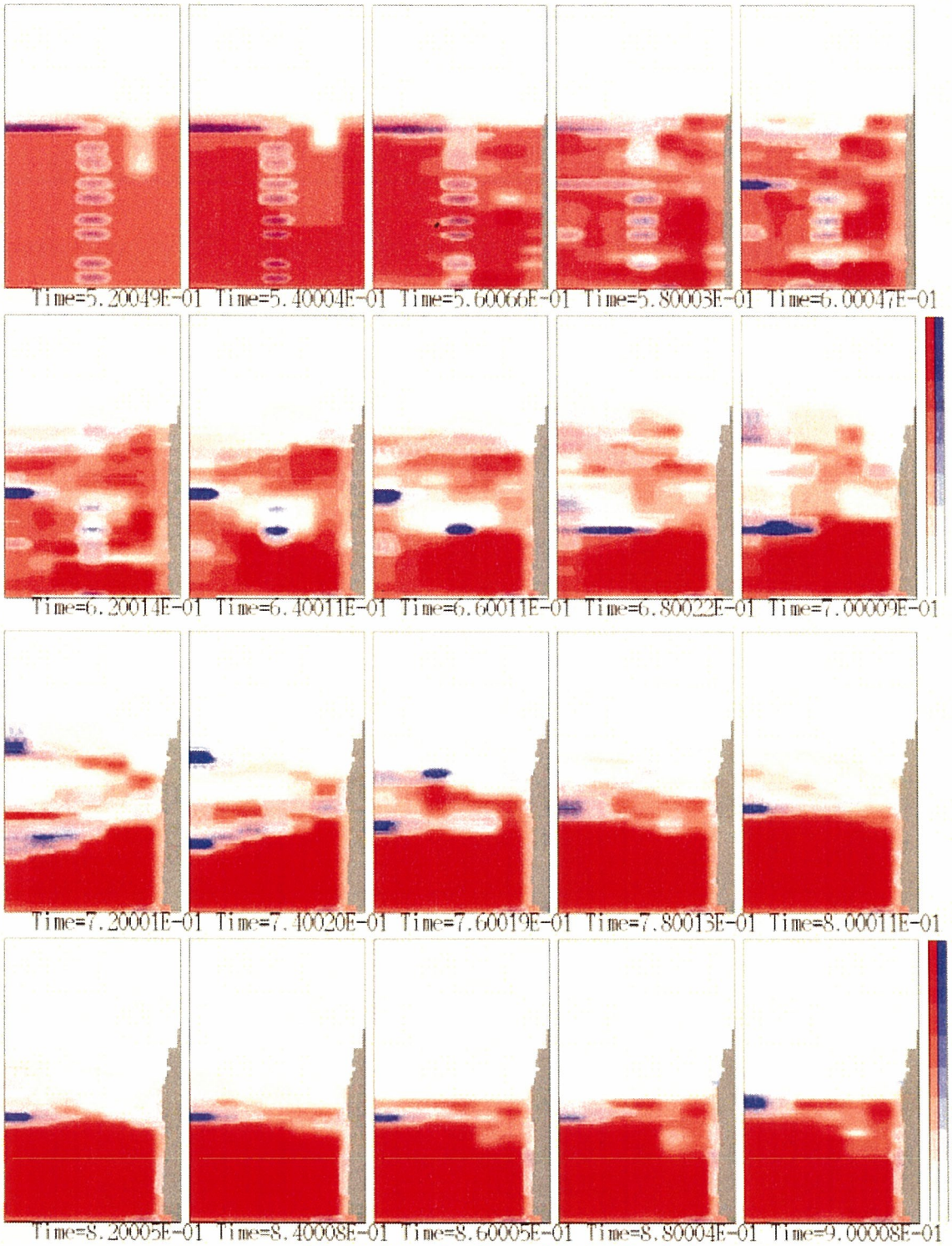

Fig. 53. Material motion in Capsule 2 in TPA2 (Low HTC case).

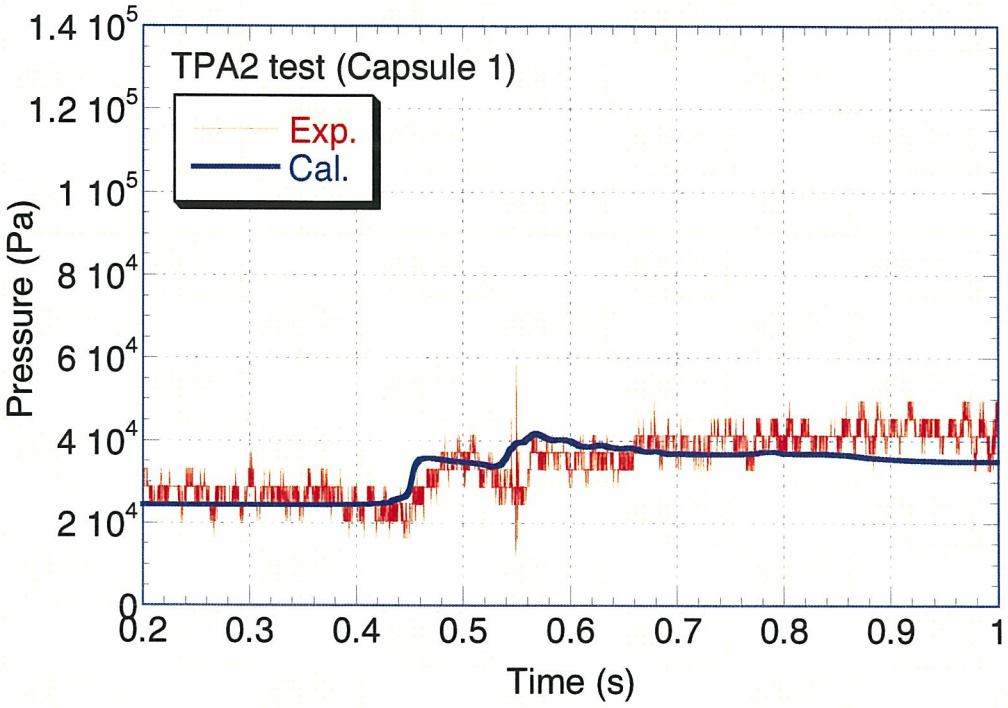

Fig. 54. Pressure history in Capsule 1 in TPA2.

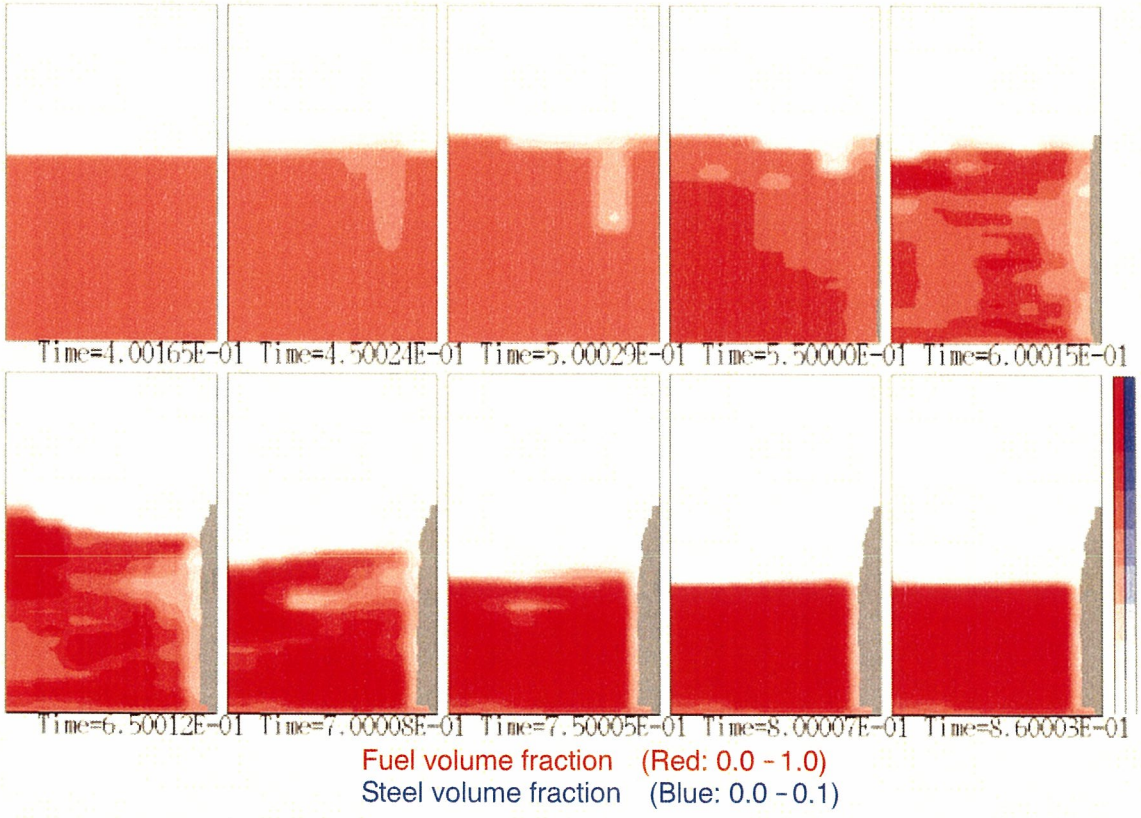

Fig. 55. Material motion in Capsule 1 in TPA2.

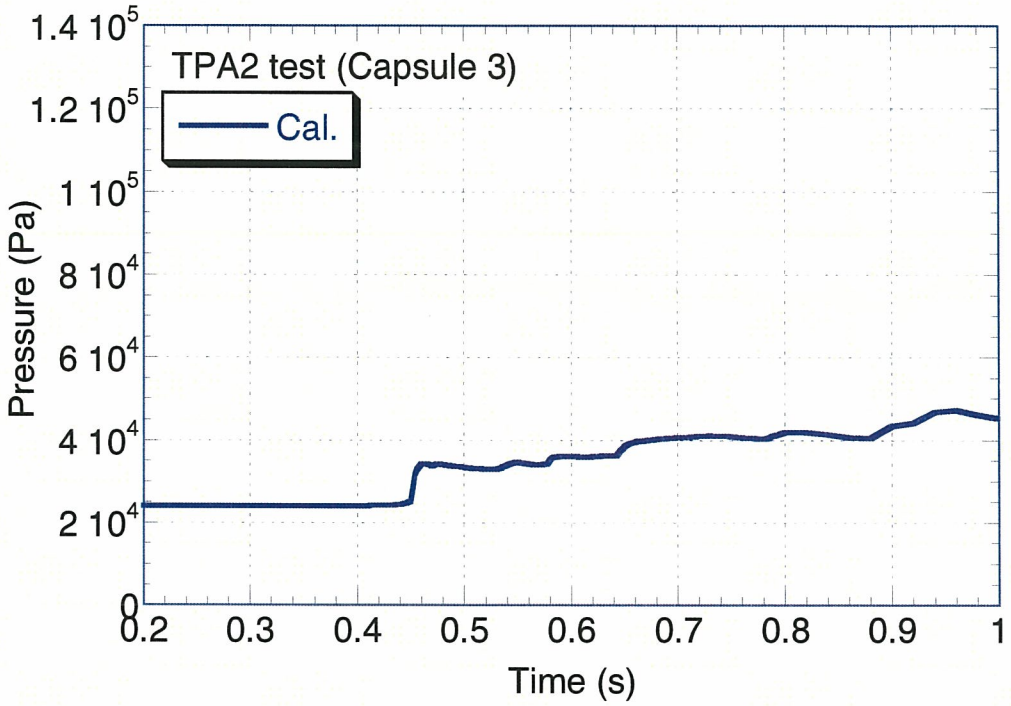

Fig. 56. Pressure history in Capsule 3 in TPA2.

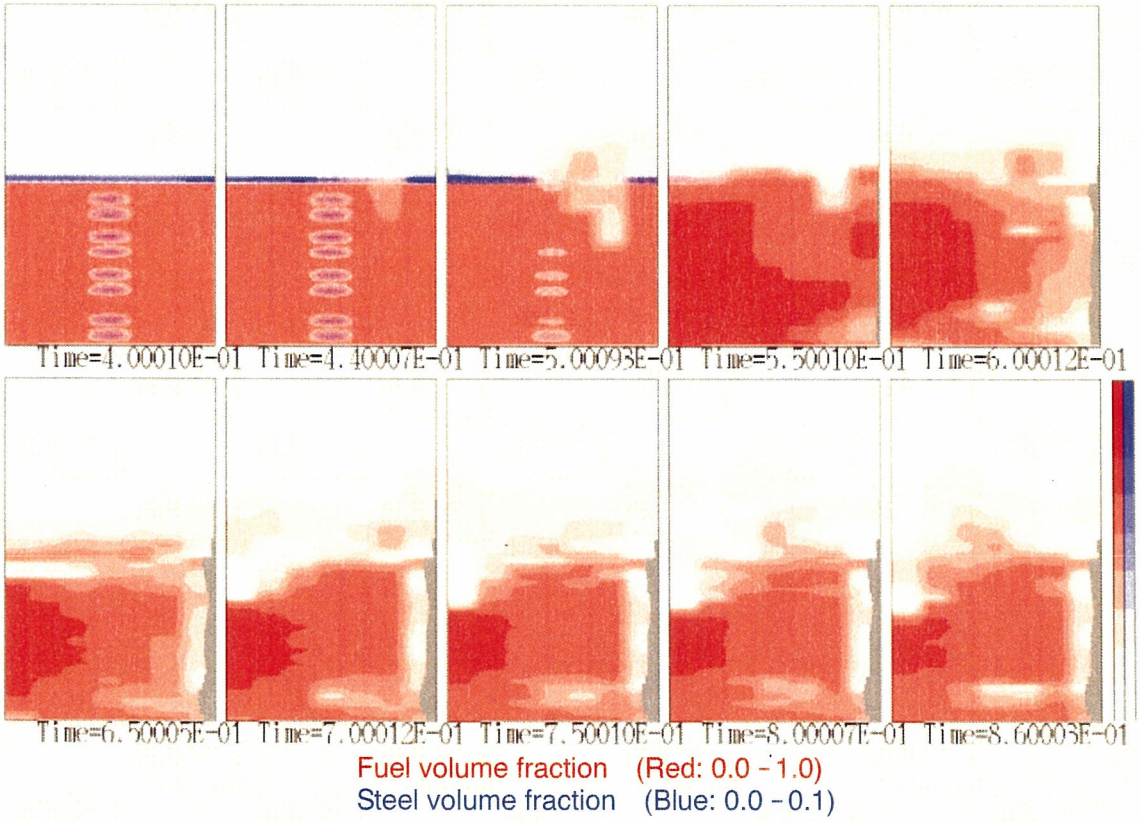

Fig. 57. Material motion in Capsule 3 in TPA2.

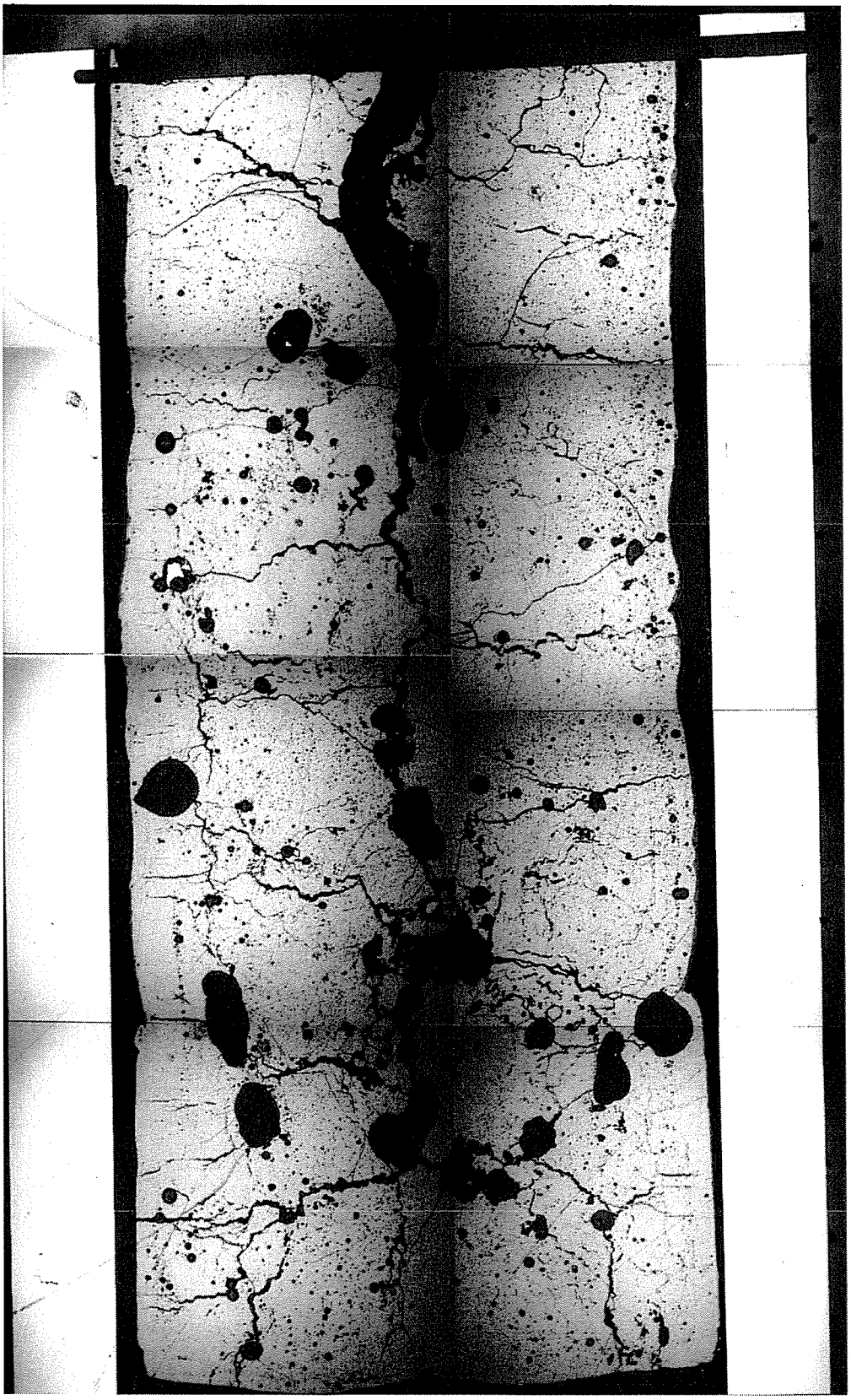

Fig. 58. Macrograph of Capsule 3.

Appendix A: Formation of solid fuel shell

Metallographic examination revealed that an about 50 μ m-thickness shell of unmolten fuel has been formed at the fuel-pellet periphery. Possible mechanism of the fuel-shell formation is evaluated here. Assuming that the convection heat transfer from fuel pool to wall was negligible because the molten fuel pool looked like almost stagnant flow inside the capsule in the test, we performed a thermal-response evaluation of the fuel column using a two-dimensional analysis code of heat conduction for fuel pellet, TAC-2D [A-1].

Analytical geometry and conditions

Similarly to the SIMMER-III calculations described in **Chapter 5**, the fuel capsule with the surrounding coolant channel was modeled by a two-dimensional cylindrical geometry. A schematic view of the analytical geometry is illustrated in **Fig. A-1**. To precisely calculate the heat flow from fuel to crucible wall, very fine computational meshes in radial direction were used at the outer side of the fuel column and inside the steel wall. The thermal effects of steel balls and membrane were ignored in this analysis, because their heat losses are rather small compared with the energy deposit. The fuel capsule was cooled outside and at the bottom by the sodium coolant at the same flow rate and at 674K as in the test. Argon gas initially at 674K covered the fuel column, and an adiabatic condition was imposed at the upper boundary over the cover gas. The radiative heat transfer from fuel pool to cover gas and structure was not taken into account.

A constant 0.01mm-thickness gap simulating steady-state conditions was placed between the outer fuel surface and the inner crucible wall in order to evaluate the thermal resistance. The heat flux in the gap was calculated with a gap conductance by both heat conduction and radiation.

Although the relative power at each computational mesh is given by multiplying the radial normalized power by the axial one, the power at the fuel-edge regions was slightly reduced for a better simulation as in the SIMMER-III calculations. The power history is in accordance with the real situation.

First, a steady-state calculation of Capsule 1 was carried out in order to obtain the heat loss toward the wall by comparing the calculation results with the thermocouple data inside the fuel column. Then, a steady-state calculation of Capsule 2 gave initial fuel temperature profile using the same heat loss condition as in the Capsule 1 calculation. Finally, we conducted a transient calculation of Capsule 2.

Calculated results

The upper thermocouple measurements, TC3 and TC4, are compared with the calculation results, because the lower thermocouples, TC1 and TC2, were affected by the heat loss to crucible bottom.

The experimental wall temperatures and the TAC-2D calculation results are presented in **Fig. A-2**. The calculated temperatures are in quite good agreement with the measured results. **Figure A-3** shows radial temperature distributions of fuel at the same axial level as TC3. The fuel temperatures were lower due to the significant heat loss toward the wall in the outer region, where the neutron-flux enhancement gave nevertheless enough energy to melt. The temperature of fuel is always lower than the melting point at the fuel-pellet periphery from 6.95mm to 7mm, while the temperatures in the inner part exceed the melting point. This calculated result is consistent with the experimental observation obtained from the metallographic examination.

Reference

[A-1] J. F. Petersen, "TAC-2D, A General Purpose Two-Dimensional Heat Transfer Computer Code – User's Manual," USAEC Report GA-8868, Gulf General Atomic (September 1969).

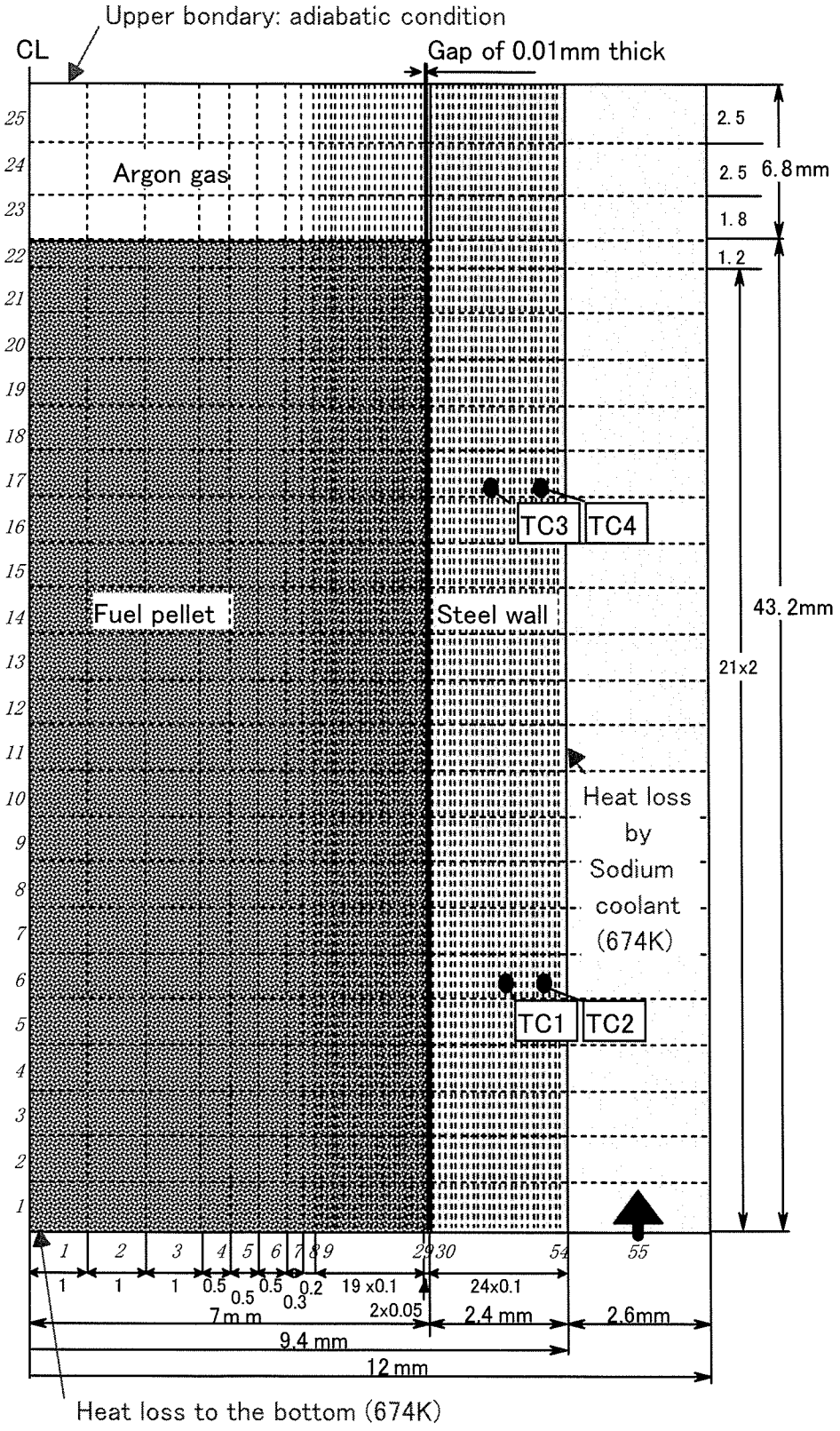

Fig. A-1. Analytical geometry in the TAC-2D calculation for the TPA2 test.

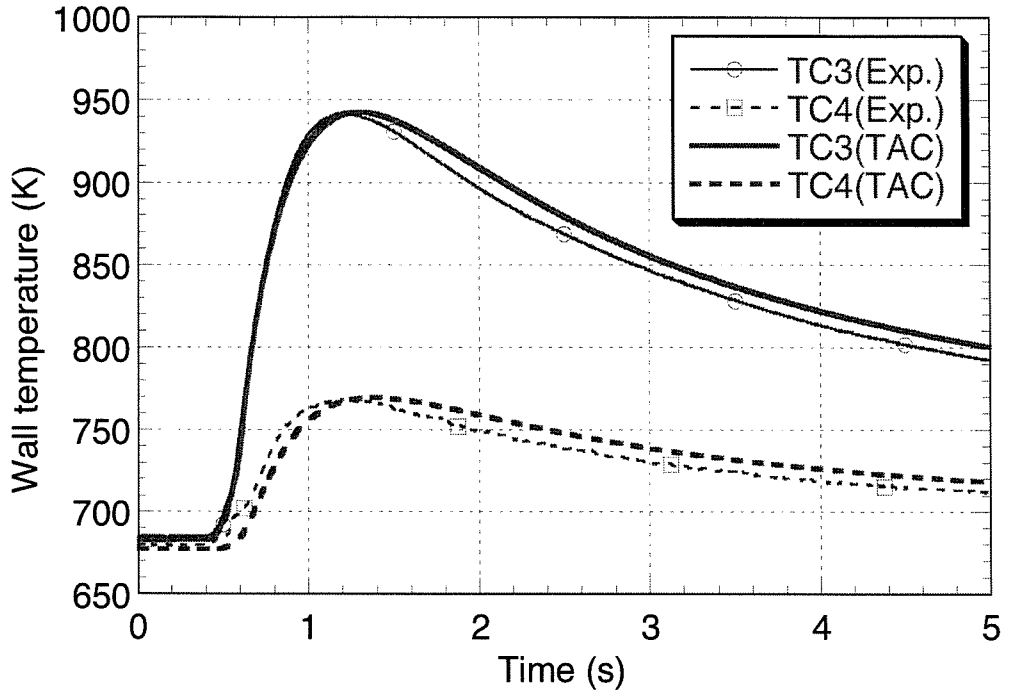

Fig. A-2. Comparison of calculated wall temperature with measured data.

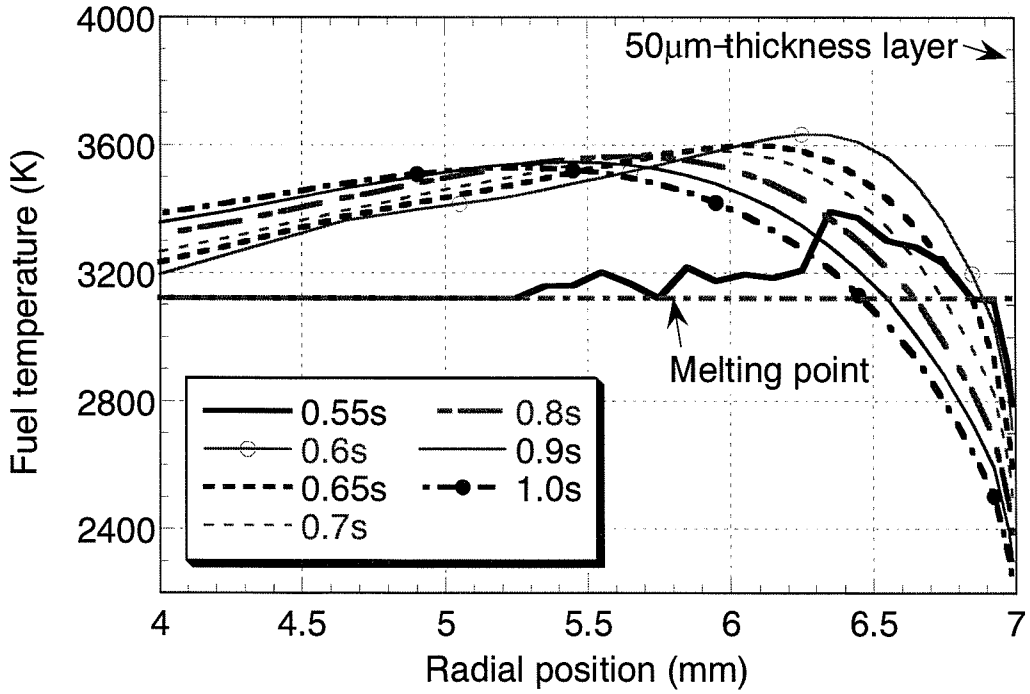

Fig. A-3. Calculated radial temperature distributions of fuel at the same axial level as TC3.

Appendix B: Pre-test calculations

As already mentioned, the objectives of the TPA2 test are to obtain experimental characteristics for the fuel-to-steel heat transfer in the two-phase fuel/steel mixture. The main purpose of the pre-test calculations is to confirm appropriateness of the selected test conditions to fulfill the test objectives. In addition, the calculations are based on the test conditions determined up to September 2000.

B-1 Analytical conditions and assumptions

B-1.1 Analytical geometry

Figure B-1 illustrates the analytical geometry modeled by 5 times 40 computational cells for the inner part of the capsule, which consists of fuel/steel mixture, cover gas region and shielding structure. The pressure transducer is located outside the CABRI core in connection with the capsule by a capillary tube of about 400mm long. The labyrinth shielding structure is adopted so as to protect the inlet hole of the capillary tube in the capsule from the molten mixture. The capsule is cooled by sodium flow.

The SIMMER-III analysis in R-Z cylindrical geometry might be inappropriate judging from the consequence that material motion was exaggerated due to local driving force and liquid concentration around the center axis. In the present analysis, we calculated in X-Z geometry using the SIMMER-III code instead of R-Z geometry of the actual test capsule.

B-1.2 Initial conditions

Table B-1 lists the analytical geometry and initial conditions of the test capsule and the fuel/steel mixture. The test capsule of 14mm in inner diameter and 122mm high is made of stainless steel. Since greater heat-resistance material of the crucible is preferable, Niobium was selected originally. However, the Niobium tube is not allowed in this type of test because of eutectic formation with stainless steel at about 1400K. Therefore, stainless steel was adopted as the crucible material. In the cover gas region, Argon gas is used and its pressure is initially set 0.03MPa in this analysis. Initial ambient temperature is assumed to be 700K, which would be the initial temperature of the sodium coolant. Temperature of the opposite wall surface from the mixture is always kept to 700K by strong sodium cooling through the wall of 2.4mm thick, because the temperature increase of the coolant along the short fissile column would be negligible during the power transient.

The fuel/steel mixture pellet is placed at the lower part of the capsule and its height is

43mm. The pellet was manufactured by sintering fresh UO_2 powder enriched at 12% with steel balls. To reduce the impurities of the fuel powder, purification process under high temperature after the manufacturing stage was performed. According to a chemical analysis, a maximum potential impurity of 3.0μmol/g-fuel is likely in the fuel. However, all the impurities will not be actually transferred into gas during the test. In this study, 0.3μmol/g-fuel of impurity gas is adopted as the nominal value for Reference case defined in **Section B-1.5**. The diameters of the fuel powder and of the steel balls are assumed to be 0.01mm and 1.0mm, respectively. We used 0.275% of steel volume fraction in the calculation. The steel balls are uniformly placed in the pellet. At the axial ends of the pellet, steel balls are not placed in order to avoid local steel vaporization due to the flux enhancement. On the contrary, the volume fraction of the fuel powder is assumed to be 64% in the pellet to take into account about 36% of porosity.

The initial radial temperature profile in the pellet due to the low power heating was taken from the steady-state calculation with the PAPAS-2S code as the initial condition for SIMMER-III. For the steady-state calculation, a pellet thermal conductivity multiplier of 0.5, a pellet-to-crucible HTC of $10kW/m^2/K$ and a constant axial linear power rating of 145W/cm were adopted (the presence of steel was neglected). The consequent radial temperature profile shown in **Fig. B-2** depicts that the maximum fuel temperature is around 1600K, just below the melting point of steel, and is used as the initial condition for the transient calculation. The initial axial temperature profile was not considered in this analysis because we confirmed that the axial temperature profile did not significantly affect the pressure transient in another previous calculation.

B-1.3 Axial and radial power profile

Since the short capsule (122mm high) compared with the driver core (~800mm) is located near the peak power node of the CABRI neutron flux, the axial power profile might be regarded as flat. However, the power becomes high on the upper and lower surface of the pellet due to the flux depression, as shown in **Fig. B-3**. The radial power profile is presented in **Fig. B-4**. SIMMER-III gives the normalized power at each computational cell by multiplying the radial normalized power profile by the axial one, and hence the power is higher at the outer rim on the upper and lower surface of the pellet. In reality, the radial power profile on the upper and lower surfaces of the pellet seems to be almost uniform because of the uniform neutronic absorption on the both faces of the pellet. In the calculation, the relative power at the upper and lower corners of the pellet is slightly decreased, for instance from 1.32 to 1.18 at the outer computational cell on the lower surface of the pellet, in order to improve the situation.

B-1.4 Power history

At first, we suggested a flat-top pulse, which rises in 0.1s and stays at a plateau for 1.5s, followed by a pulse of half height width of 200ms in order to obtain useful information on the fuel/steel mixture motion. However, the principal experimental restraint is that starting at low power, the width at mid-height cannot be larger than 100ms because of the Doppler effect. The experimental restraints allow us the half-height width of the power pulse within 100ms.

As previously described, the pellet is heated just below the melting point of the steel balls during the pre-heating phase by low power. Following the pre-heating phase, the transient power pulse is injected. Its shape is expected to show a dual-peak pulse in order to get the maximum energy deposit in the CABRI reactor, as shown in **Fig. B-5**. The fuel temperature overpasses the steel boiling point of about 3400K by injecting this power pulse, of which full width at mid-height is around 80ms. **Figure B-6** indicates the resultant energy histories, in which the energy deposit is 1.2kJ/g-fuel during first 0.3s. With this power history, additional 0.3kJ/g-fuel energy deposit is available in the later transient after 0.3s. This is because the rather long-tail power history is preferable to see the fuel relocation by the hodoscope.

B-1.5 Calculational cases

The present calculational cases are summarized in **Table B-2**. Analytical parameters in the calculations are: the amount of impurity gas, the fuel-to-steel HTC, the momentum coupling between vapor and liquid, and the energy deposit during the first 0.3s of the pulse. In addition, special cases without steel balls are chosen to clarify the steel-vapor effect in the analyses. Reference case as the representative of the test situation uses: 0.3μmol/g-fuel of impurity gas, nominal value of fuel-to-steel HTC and nominal momentum coupling between vapor and liquid, and 1.2kJ/g-fuel of energy deposit during the first-0.3s pulse. For the amount of impurity gas, 1.0μmol/g-fuel is adopted in the parametric cases, and seems higher than the reality considering the fact that the test fuel was degassed sufficiently. In this analysis, the bubbly flow regime is applied to the high void fraction flow for achievement of the tight vapor-mixture momentum coupling under rapid transient condition. In addition, we evaluated the maximum pressure generation considering the integrity of the crucible.

B-2 Results and discussion

B-2.1 Reference case

Figure B-7 describes the material motion in the reference case (N03H1E12) defined

in **Section B-1.5**. In this figure, blue color signifies the volume fraction of the fuel particle, while red color represents the summed volume fraction of the liquid fuel and fuel particle. Pressure histories at the lower steel-ball cell and the bottom of fissile column are indicated in **Fig. B-8** and **Fig. B-9**, respectively. For the cover-gas pressure, long and short-term behavior are shown in **Fig. B-10** and **Fig. B-11**, respectively. Long and short-term behavior of phase-change rate summed in the capsule are plotted in **Fig. B-12** and **Fig. B-13**, respectively. **Figure B-14** shows the total mass of steel vapor in the capsule. As shown in **Fig. B-15**, the overall test scenario obtained from this case is described in the following.

B-2.1.1 Overall test scenario

The pellet temperature rises as the result of the pulse injection, and hence the porosity gas is pressurized locally in the confined pellet by the gas heating at around 0.16s after TOP triggering as shown in **Fig. B-8**. The steel ball at the bottom of the pellet melts at 0.17s and then steel vaporizes at 0.2s as depicted in **Fig. B-8**. At almost same time, the axial ends of the pellet begin to disrupt prior to the coherent disintegration of the main fuel part as the consequence of the axial power profile. This early disruption, by which the impurity gas is ejected from the liquid fuel and pressurized locally the bottom of the confined pellet, does not give any large impact on the subsequent material-relocation behavior. **Figure B-14** shows the steel vapor increase before the global fuel disintegration.

After the global fuel disintegration, rapid fuel frothing takes place by the steel-vapor driving pressure. As indicated in **Fig. B-11**, the cover gas is compressed and pressure increase occurs rapidly during this fuel-frothing stage. The fuel relocation with the increased cover-gas pressure stops when the moving front of the fuel-steel mixture reaches the capsule upper part.

At the end of this frothing, dispersed fuel distribution within the capsule is established. With the dispersed fuel distribution, significant heat loss to the crucible wall takes place. The rapid heat loss reduces steel vapor temporally due to condensation (**Fig. B-13**) and forms the fuel crust on the wall (**Fig. B-7**). As shown in **Fig. B-14**, the steel vapor increases again due to the blanketing by the fuel crust, and then general fuel fall-down takes place leaving fuel crust on the capsule wall.

The dispersed fuel falls down to shrink at the lower part of the capsule, and the resultant steel vaporization occurs by the increase of heat transfer from fuel. Following the steel vaporization, the steel vapor drives the fuel frothing again, and such behavior repeatedly occurs in this case.

B-2.1.2 Pressure-transducer measurement

As illustrated in **Fig. B-7**, the molten fuel does not flow into the shielding structure and does not reach the capillary tube inlet. If we assume pressure equilibrium, the pressure in the capillary tube and the shielding structure equivalences to the pressure generated by the molten mixture. For the capillary tube, it is better to minimize its inner diameter to prevent the arrival of the mixture to the tube inlet. On the contrary, the larger friction with smaller tube diameter may deteriorate the time response of the pressure measurement in the test capsule.

Figure B-16 depicts the response of the pressure transducer compared with the cover-gas pressure. During the fuel upward movement, the pressure transducer can measure the cover-gas pressure accurately. From this calculation, however, it may not be able to detect the pressure appropriately just after the molten mixture penetration into the shielding structure. During the later phase of the transient, the response of pressure transducer is quite well because of the fuel fall-down from the shielding structure in the calculation.

B-2.2 Effect of fuel-to-steel HTC

Figures B-17 and **B-18** show the history of cover-gas pressure assuming 0.3 and 1.0μmol/g-fuel of impurity gas, respectively. In these figures, solid circles represent the fuel arrival time at the entrance of shielding structure. The pressure transient in the case without steel ball shows the pressure build-up by the impurity gas and cover gas.

From these results, time scale of the pressure increase is an important element to quantify the steel-vaporization characteristics. For both of the assumed impurity gas levels, different HTCs lead to variation in pressure-increase time-scale and pressure-increase level at the end of frothing. Moreover, the time scale of frothing, which takes place at a certain transient power level, seems possible to be detected by the hodoscope observation. Especially, in case of smaller fuel-to-steel HTC, which is favorable for stability of whole-core boiling pool behavior, time scale becomes much longer. Taking the cover-gas pressure history without steel ball away from the pressure history with steel ball, **Figs. B-19** and **B-20** can be obtained. The first peak of differential-pressure appears at the end of fuel frothing in the cases with nominal and higher HTCs. With the smaller HTC, steel vapor is so small that the gas pressure is not sufficient to complete the frothing at this first peak. Therefore, fuel frothing continues in these smaller heat-transfer cases leading to delayed completion of the frothing. If one look at the differential pressure, the effect of fuel-to-steel heat transfer becomes clearer. In this respect, interpretation based on the obtained results of the

fuel-only capsule and the main capsule will be effective.

Histories of the steel-vapor mass produced in the test capsule are plotted in **Figs. B-21** and **B-22** for 0.3 and 1.0μmol/g-fuel of impurity gas, respectively It is confirmed that the steel-vapor formation is dominated by fuel-to-steel heat transfer and does not depend on the impurity gas in the early phase of the transient up to 0.3s.

For the later part of the transient, the mixture moves repeatedly upward and downward because of steel evaporation and gravity fall in the cases with steel ball. In the cases without steel ball, the mixture initially expanding in the capsule falls down and then accumulates at the bottom of the capsule. Long-term behavior of the cover-gas pressure are presented in **Figs. B-23** and **B-24**. The pressure in the cases with steel ball is much larger than the one without steel ball, and hence the balance of steel evaporation and condensation dominates the pressure history during the later transient.

B-2.3 Effect of vapor-liquid momentum coupling

Figure B-25 illustrates the material motion until 0.95s in the case (N03H1E12X) with the tight momentum coupling between vapor and liquid. For the reference case shown in **Section B-2.1**, the molten fuel/steel mixture oscillates vertically in the capsule due to the gravity fall-down of the mixture and the expansion driven by the steel-vapor generation. In the case with tight momentum coupling between vapor and liquid, it is difficult for the expanding mixture to fall down due to the tight drag between vapor and liquid. Although the hodoscope may not be able to observe the fuel movement after the fuel-crust formation, the thermocouples embedded in the crucible wall will provide information on the existence of mixture behind the wall.

Long and short-term behaviors of cover-gas pressure in this case are shown in **Figs. B-26** and **B-27**, respectively. The pressure, when the fuel arrived at the top of test capsule, becomes higher than in the nominal case due to the pronounced mixing of the liquid fuel and gas. During the long-term transient up to 1.0s, the tight momentum coupling keeps the system pressure higher than in the nominal case.

B-2.4 High-pressure case

To provide the information relating to the safety consideration of the test capsule, the maximum pressure generation is evaluated using realistic and also conservative conditions. 1.0μmol/g-fuel of impurity gas, five-times nominal HTC from fuel to steel, 1.3kJ/g-fuel of energy deposit during the first part of the pulse are adopted for this case. The peak pressure becomes 0.3MPa as shown in **Fig. B-28** and **B-29**, which show the long- and short-term pressure transient.

B-3 Conclusion

The pre-test calculations of the TPA2 test were performed using the SIMMER-III code. The main purpose of this work is to select the best test geometry and conditions for realizing the test objectives, which aims at investigating the fuel-to steel HTC in the expanding two-phase mixture as well as the vapor-mixture momentum coupling under power transient.

The calculational results show that, in the selected test conditions, the fuel/steel mixture frothing in the capsule will give us valuable information, such as the fuel arrival time at the capsule upper part and the pressure build-up, which is dominated by the steel-vapor driving pressure. In particular, it is expected to get meaningful difference on the HTC from fuel to steel from the time scale of the fuel frothing. Concerning the vapor-liquid momentum coupling, the time scale necessary for collapse of the fuel frothing seems possible to give the magnitude of the momentum coupling. Therefore, it is confirmed that the selected test conditions are appropriate to fulfill the test objectives.

Table B-1 Analytical geometry and initial conditions.

Test capsule	
Height of capsule (mixture, cover gas and shielding structure)	122mm *1)
Height of shielding structure region	22mm *2)
Initial height of cover gas region	57mm *3)
Inner diameter of crucible	14mm *4)
Thickness of crucible	2.4mm
Material of crucible	Stainless steel
Initial wall temperature	700K *5)
Initial cover gas temperature	700K *5)
Initial cover gas pressure	0.03MPa *6)
Fuel/Steel mixture	
Initial height of mixture	43mm
Enrichment of fuel	12% fresh UO2
Fuel mass	~46g
Diameter of fuel powder	0.01mm
Diameter of steel balls	1.0mm
Fuel volume fraction	0.64
Steel volume fraction	0.00275
Porosity	36%
Initial average temperature	~1400K

NB) The geometric values listed in the table above were based on the data determined up to September 2000. In fact, the following data were adopted in the test.

*1) 106mm
*2) 20mm
*3) 43mm
*4) 14.2mm
*5) ~673K
*6) ~0.01MPa at room temperature (~293K)

Table B-2 Calculation cases.

Case	Amount of impurity gas (μmol/g-fuel)	Fuel-to-steel HTC or with/without steel	Momentum coupling between vapor and liquid	Energy deposit during pulse (kJ/g-fuel)
N03H1E12 (Reference)	0.3	Nominal	Nominal	1.2
N03H5E12	0.3	Nominal×5	Nominal	1.2
N03H02E12	0.3	Nominal×0.2	Nominal	1.2
N03HNOE12	0.3	No steel ball	Nominal	1.2
N1H1E12	1.0	Nominal	Nominal	1.2
N1H5E12	1.0	Nominal×5	Nominal	1.2
N1H02E12	1.0	Nominal×0.2	Nominal	1.2
N1HNOE12	1.0	No steel ball	Nominal	1.2
N03H1E12X	0.3	Nominal	Tight	1.2
N1H5E13	1.0	Nominal×5	Nominal	1.3

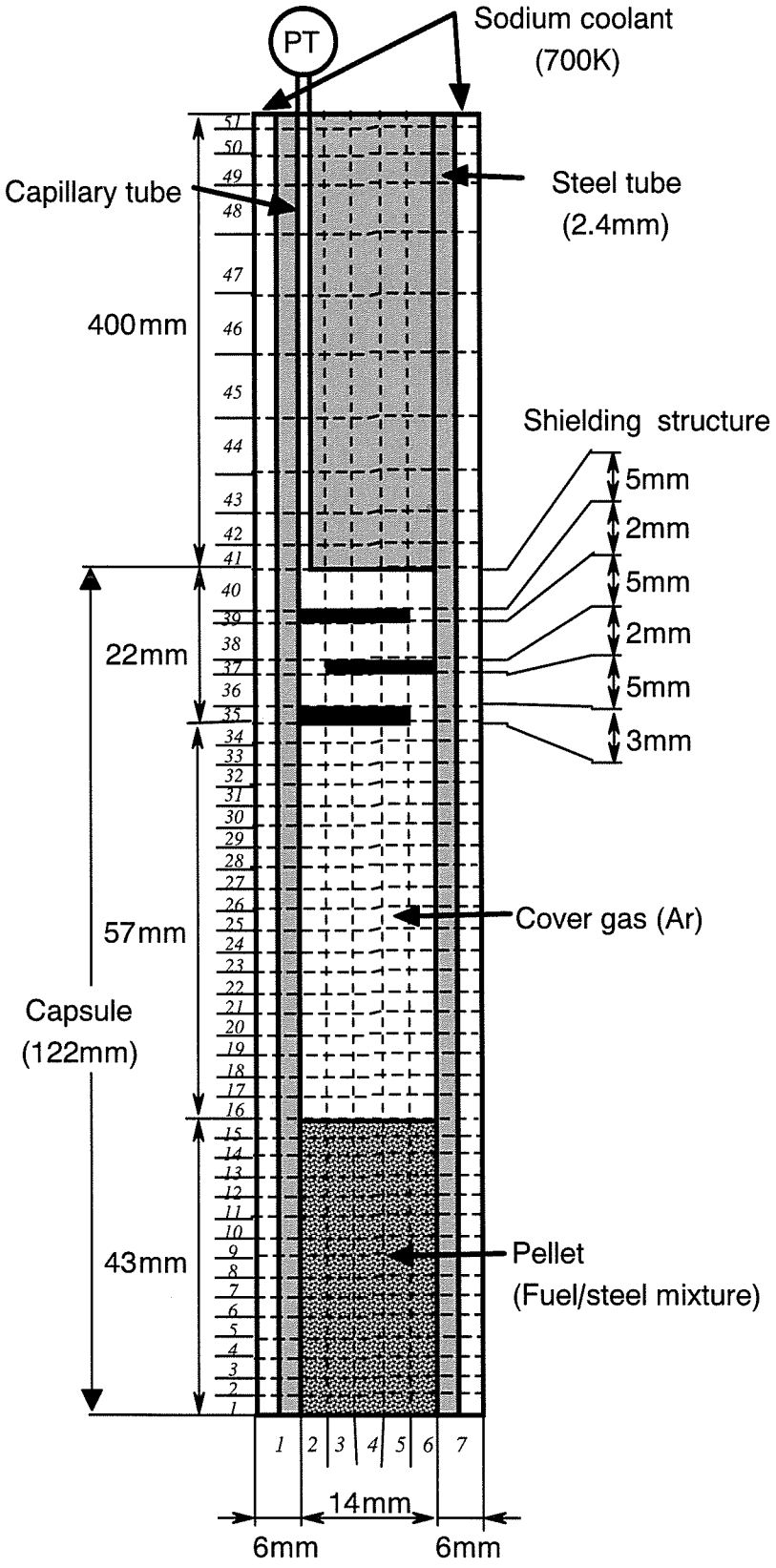

Fig. B-1 SIMMER-III meshing for the TPA2 test.

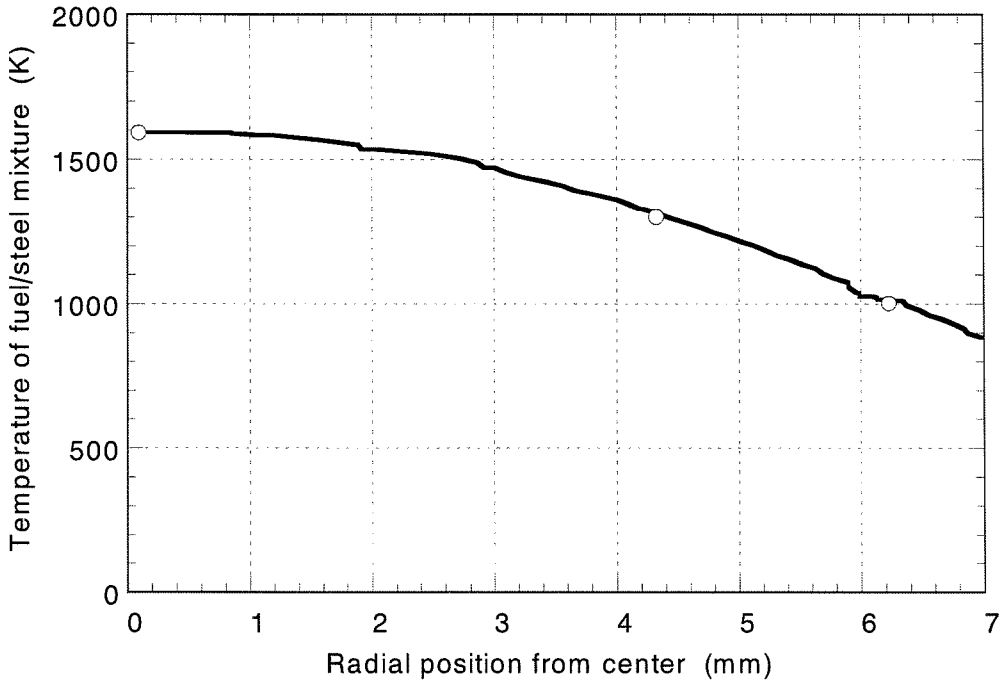

Fig. B-2 Initial radial temperature profile.

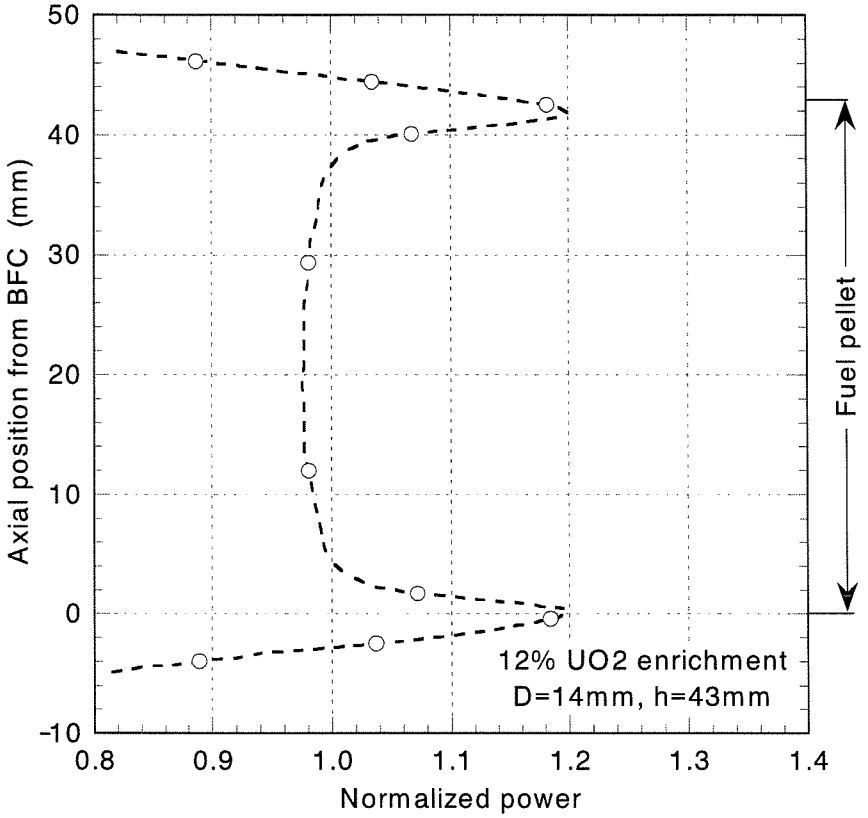

Fig. B-3 Axial power profile.

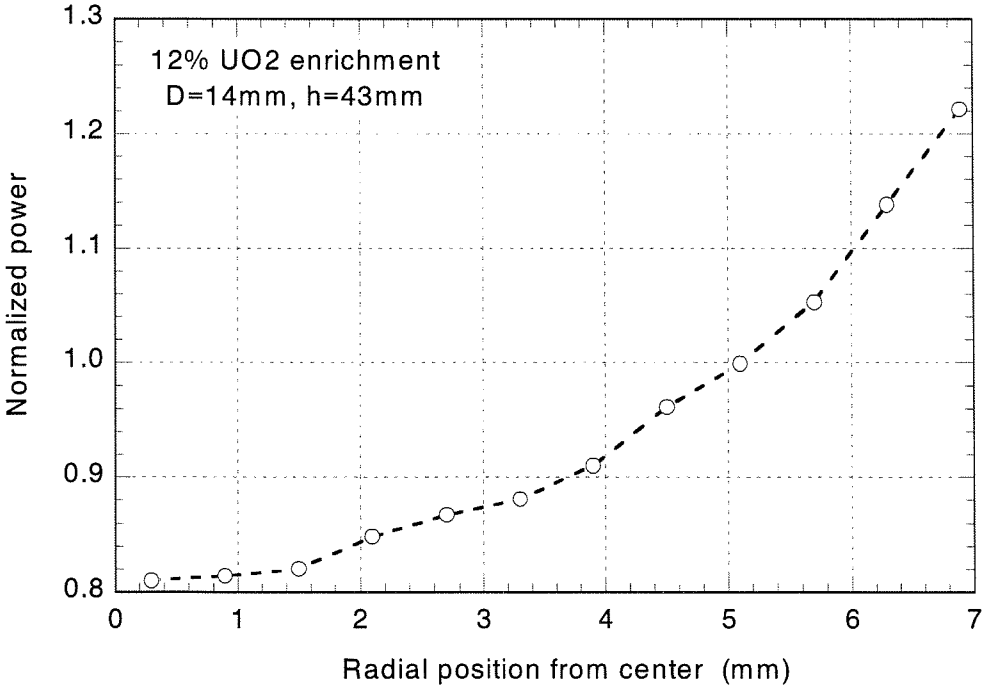

Fig. B-4 Radial power profile.

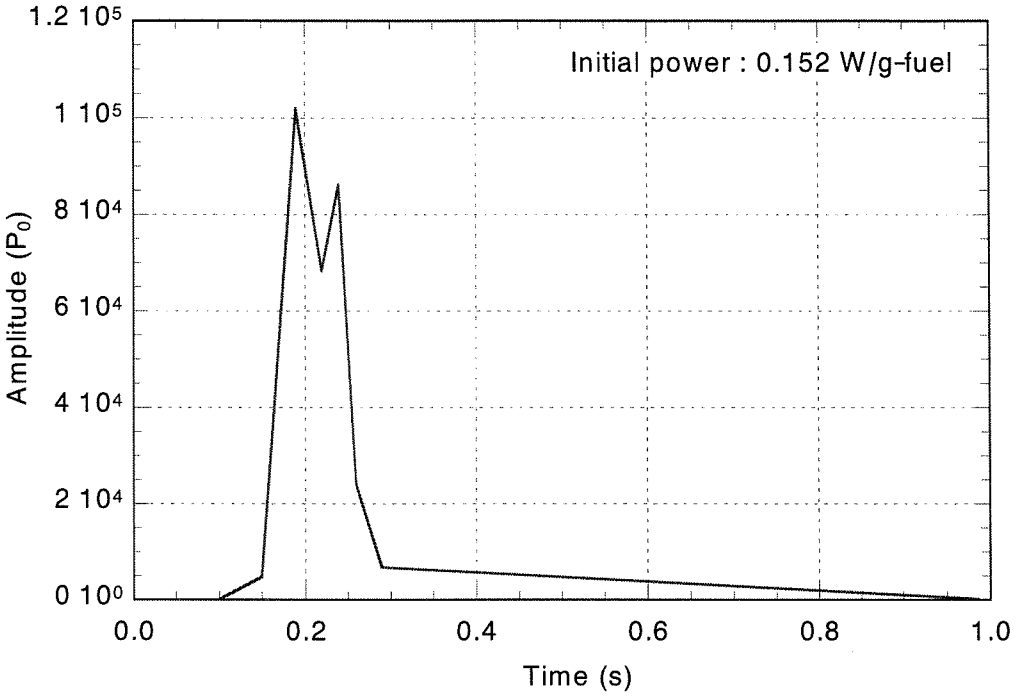

Fig. B-5 Power histories.

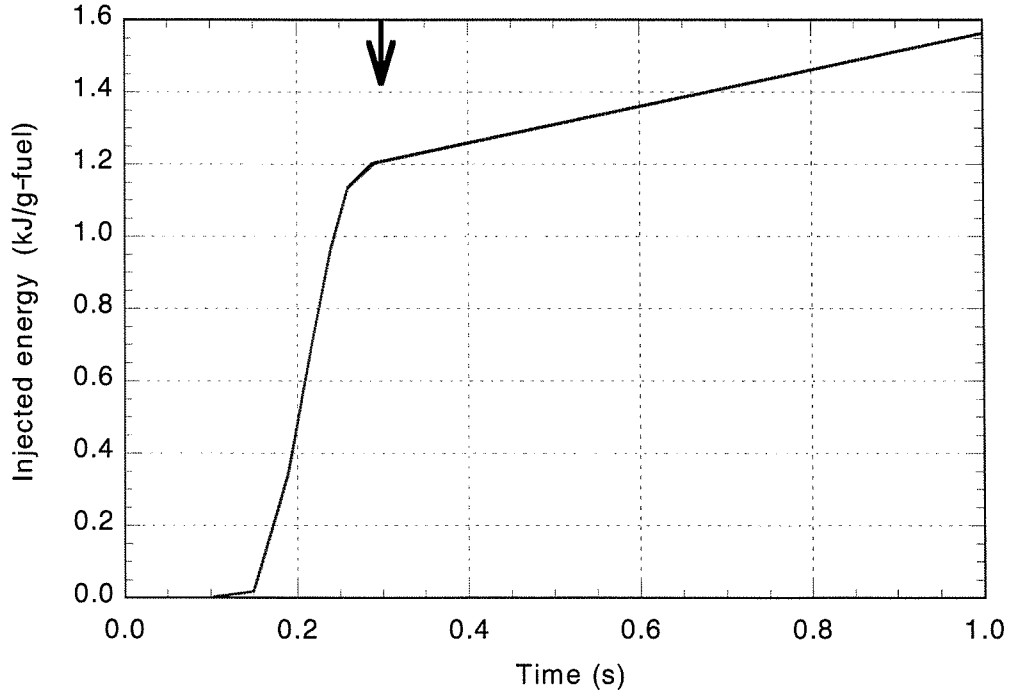

Fig. B-6 Integrated power histories.

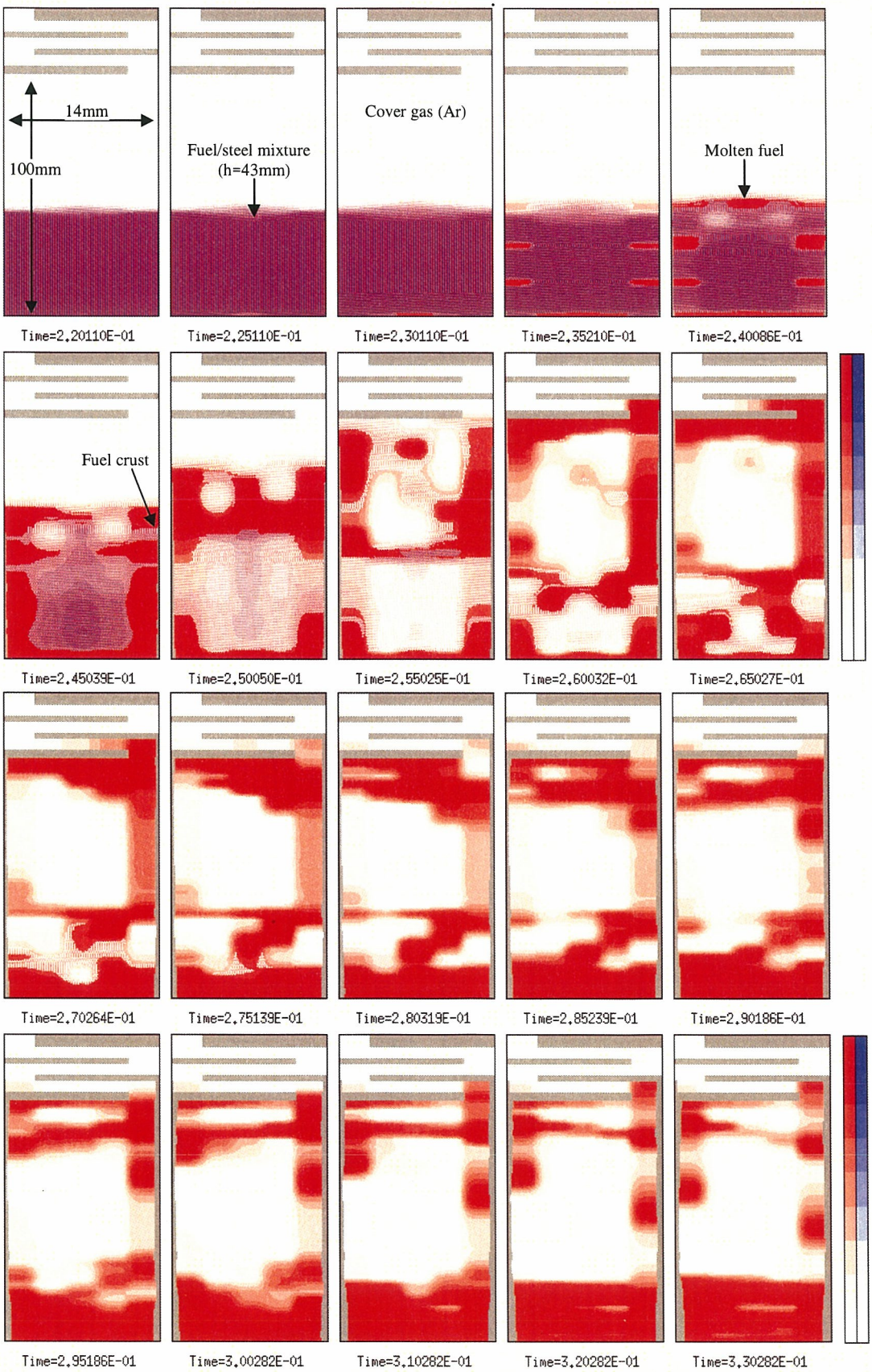

Fig. B-7 Material motion in Case N03H1E12.

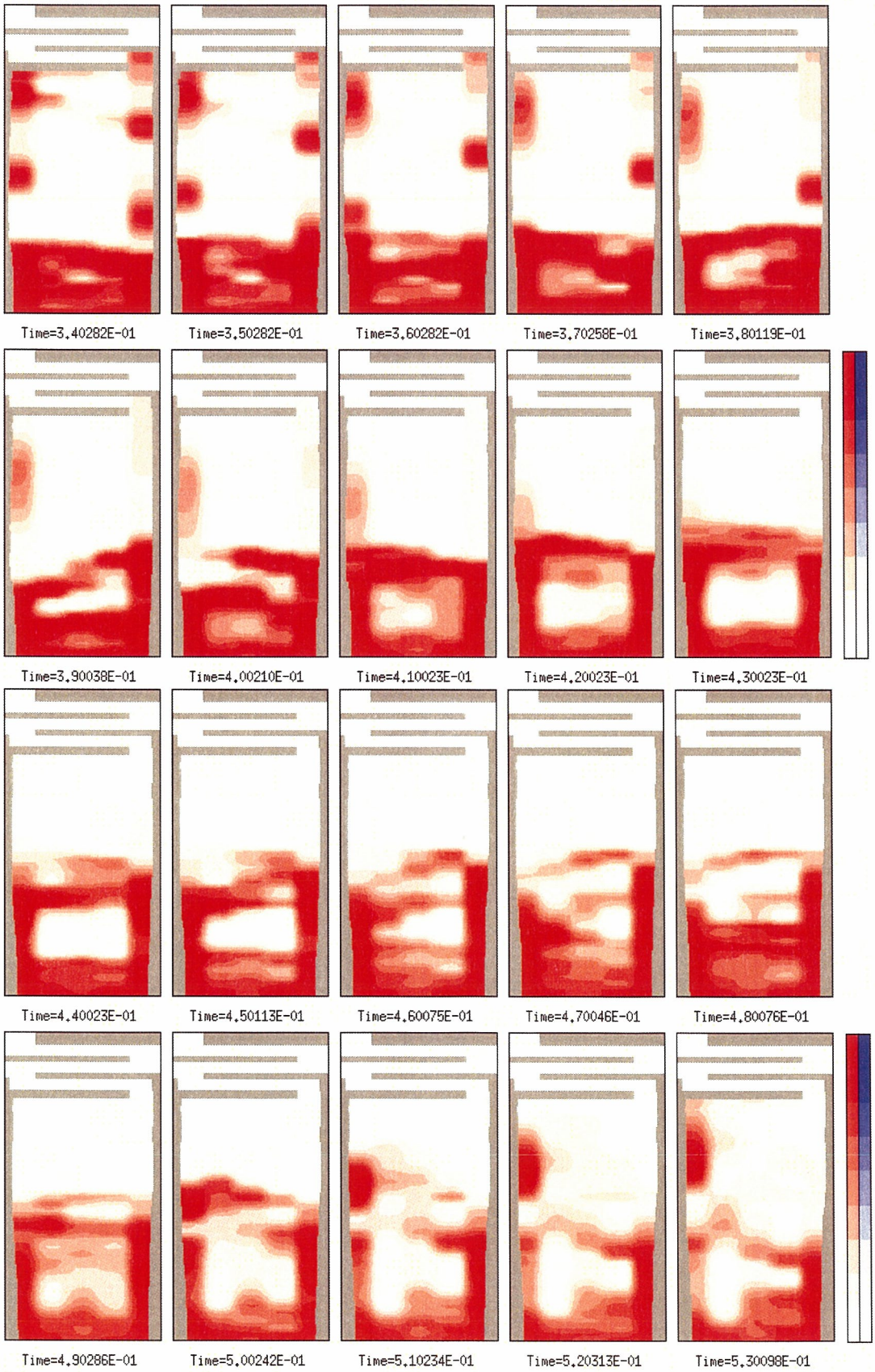

Fig. B-7 Material motion in Case N03H1E12 (cont.).

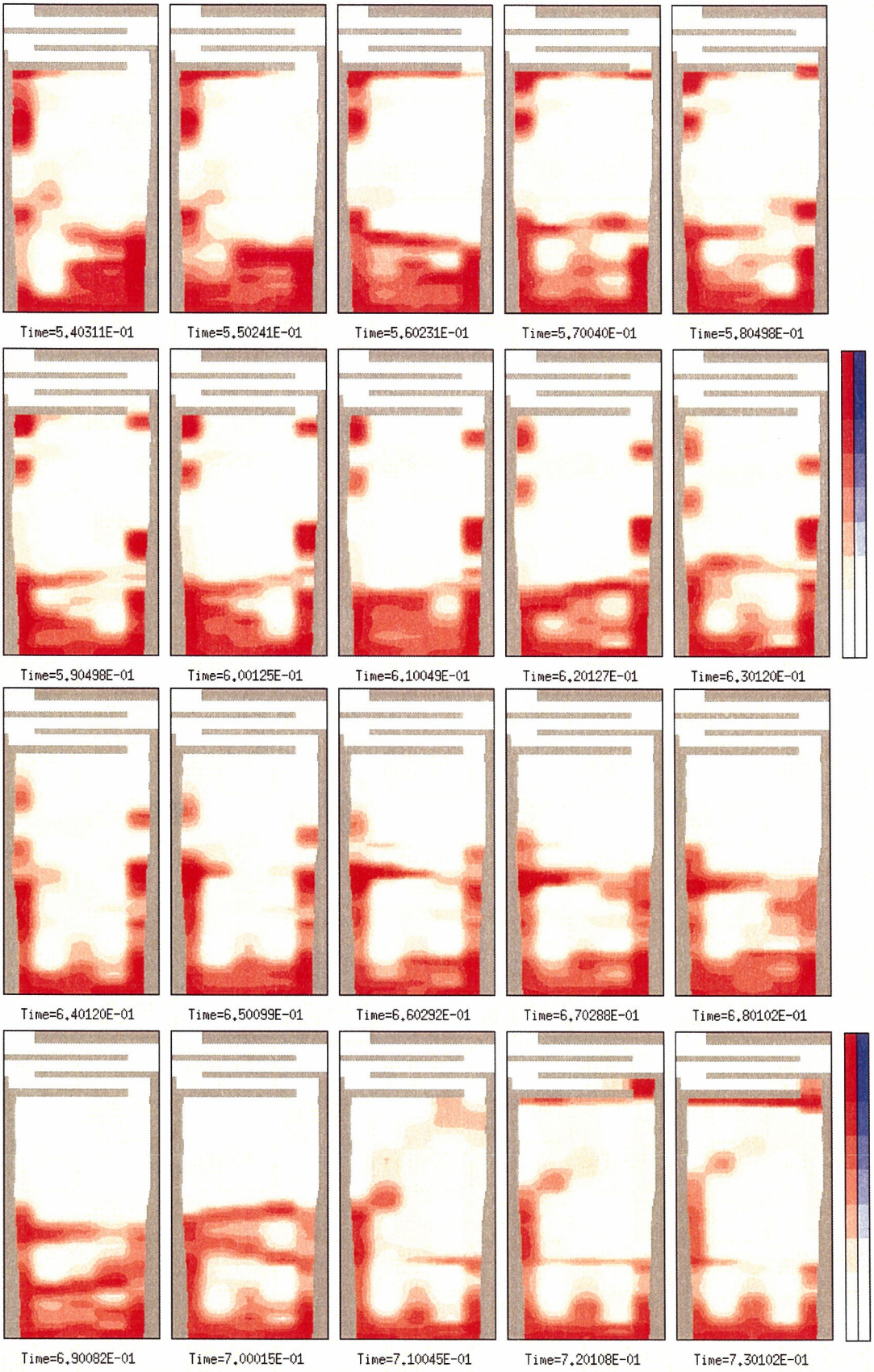

Fig. B-7 Material motion in Case N03H1E12 (cont.).

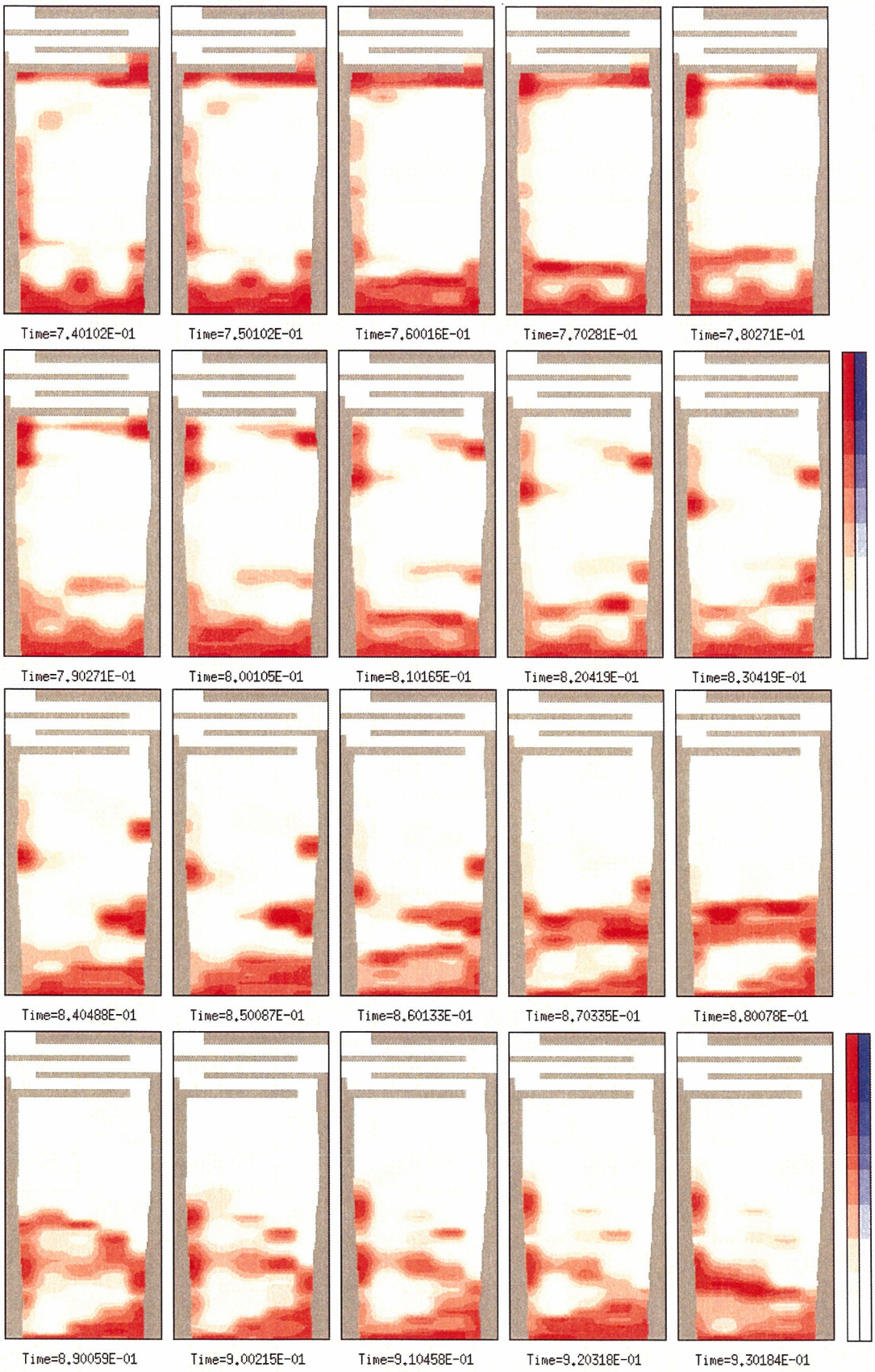

Fig. B-7 Material motion in Case N03H1E12 (cont.).

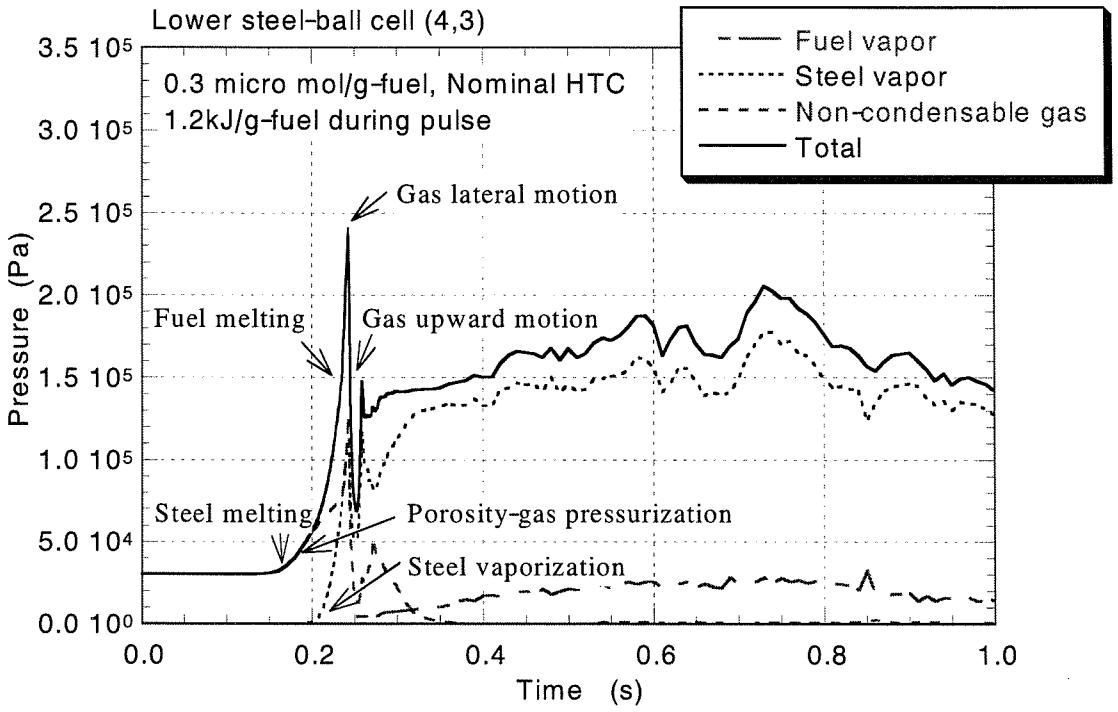

Fig. B-8 Pressure histories at the lower steel-ball cell in Case N03H1E12.

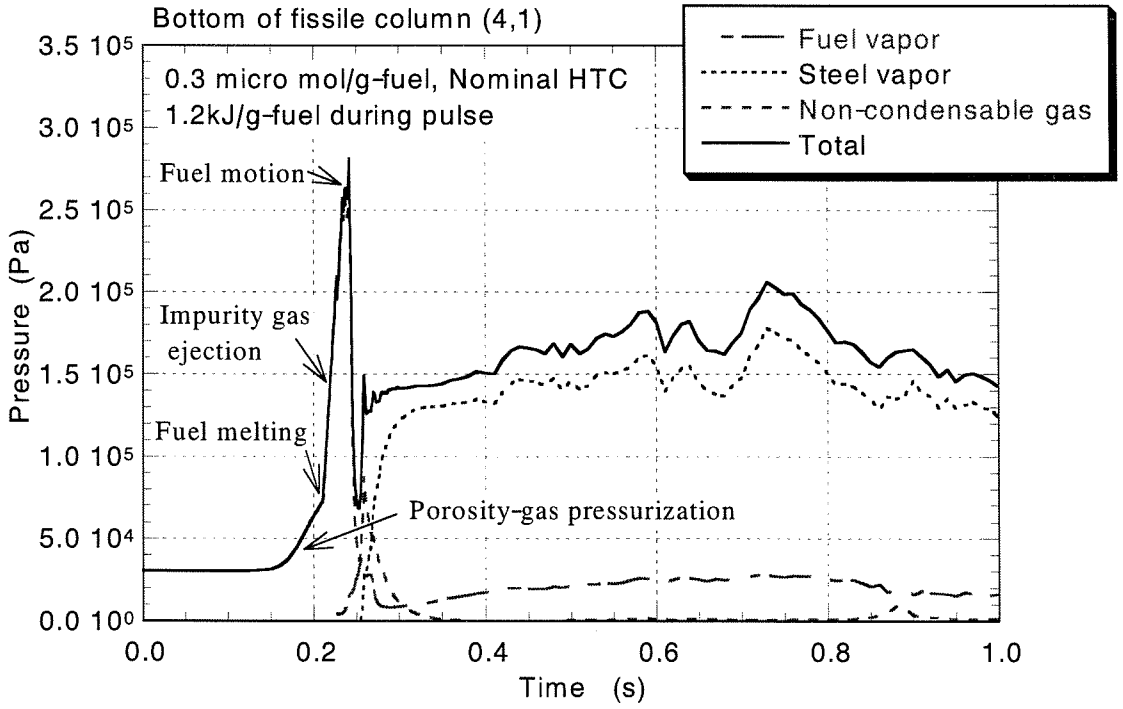

Fig. B-9 Pressure histories at the bottom of the pellet in Case N03H1E12.

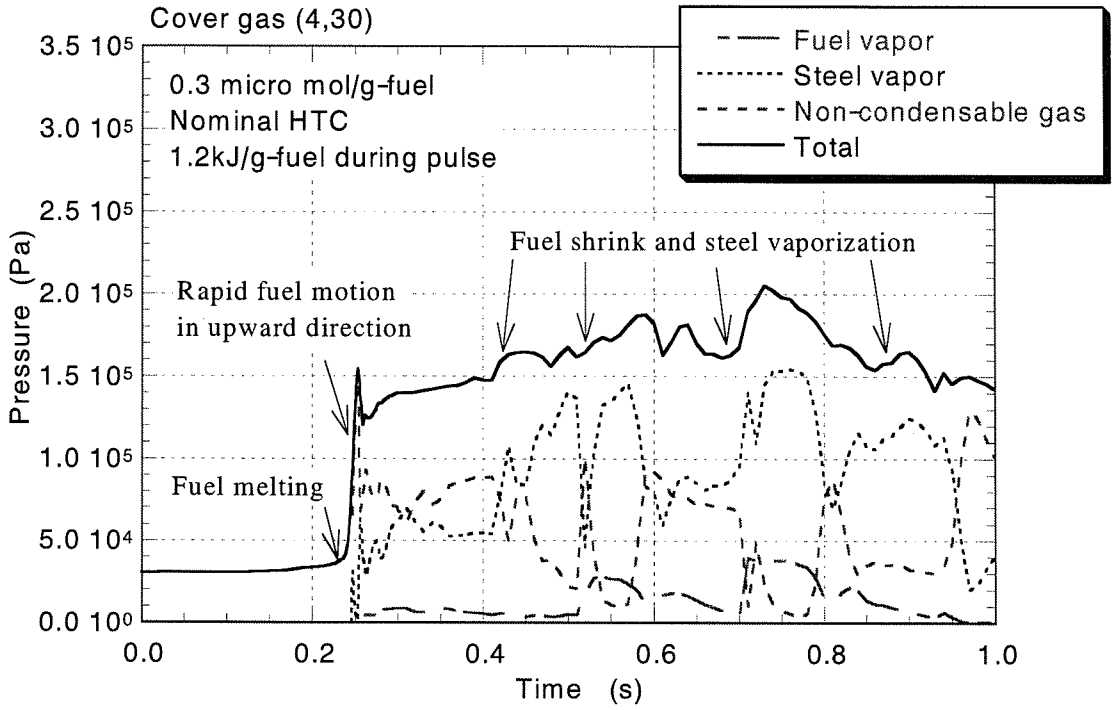

Fig. B-10 Long-term behavior of cover-gas pressure in Case N03H1E12.

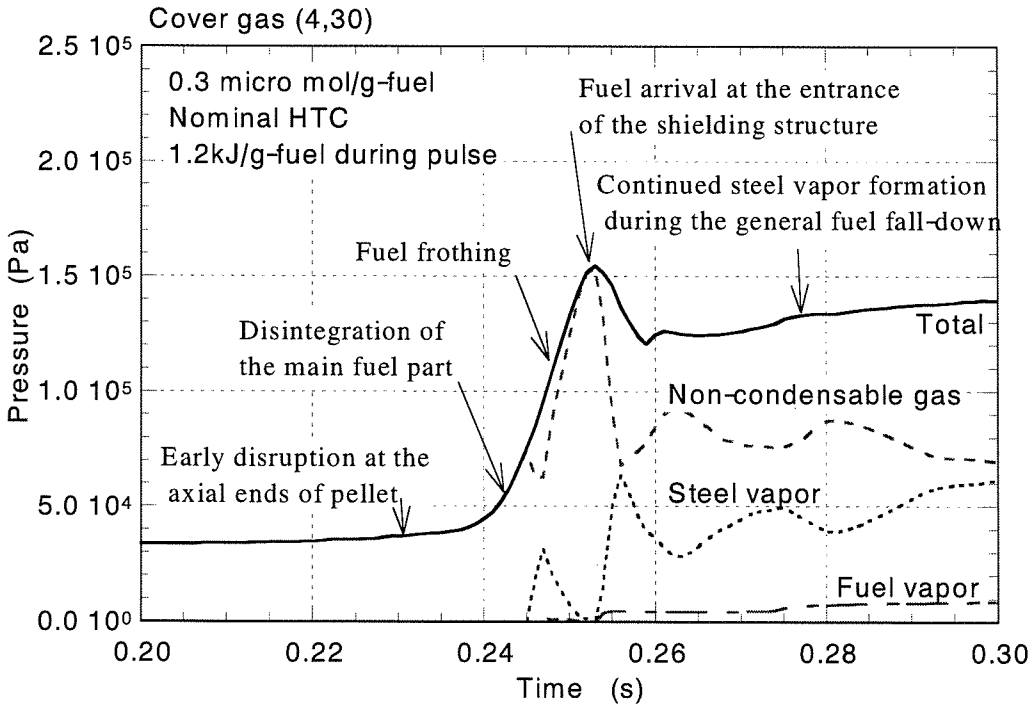

Fig. B-11 Short-term behavior of cover-gas pressure in Case N03H1E12.

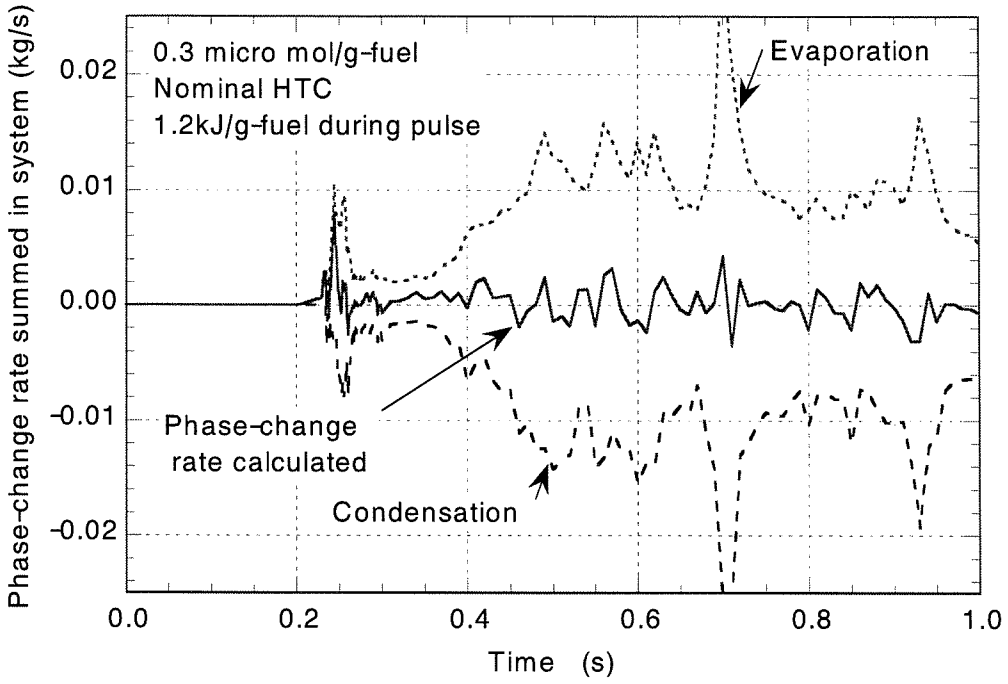

Fig. B-12 Long-term behavior of phase-change rate summed in total system in Case N03H1E12.

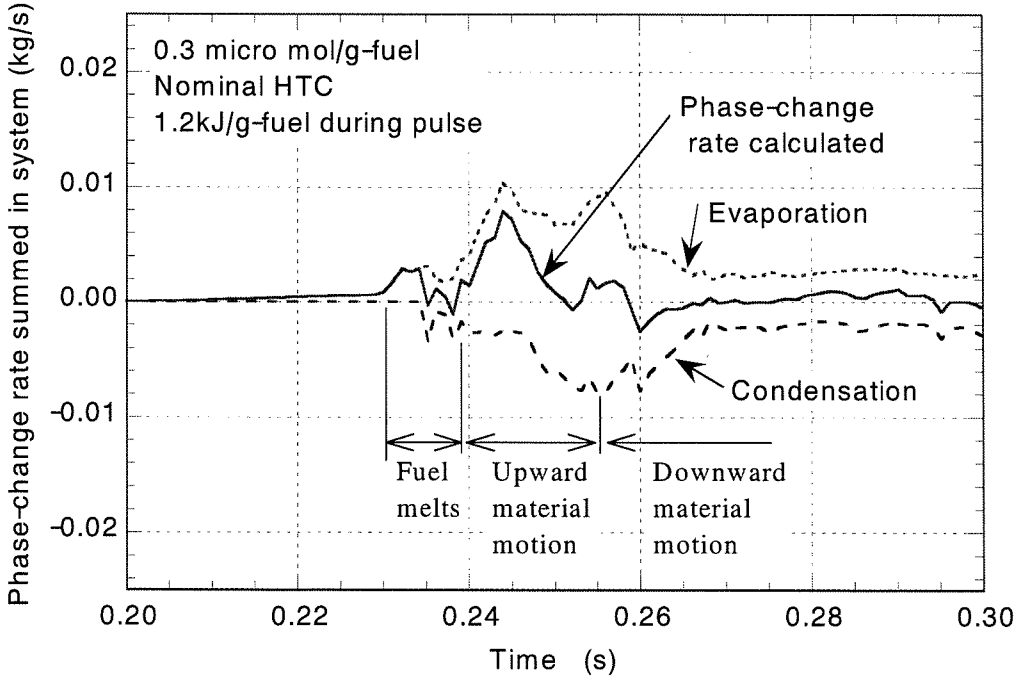

Fig. B-13 Short-term behavior of phase-change rate summed in total system in Case N03H1E12.

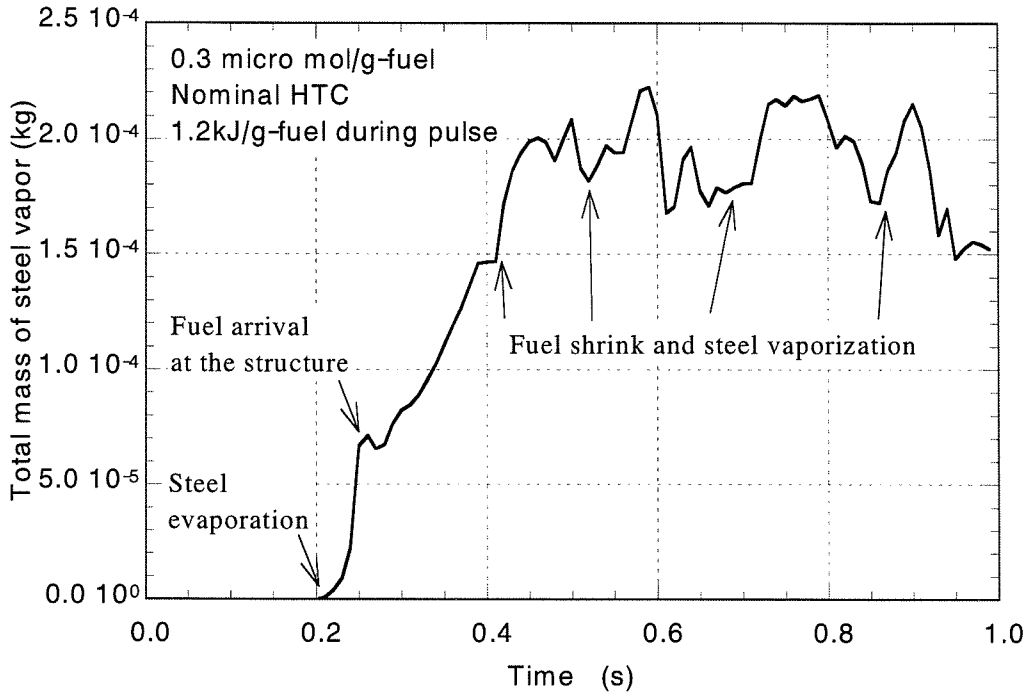

Fig. B-14 Total mass of steel vapor in Case N03H1E12.

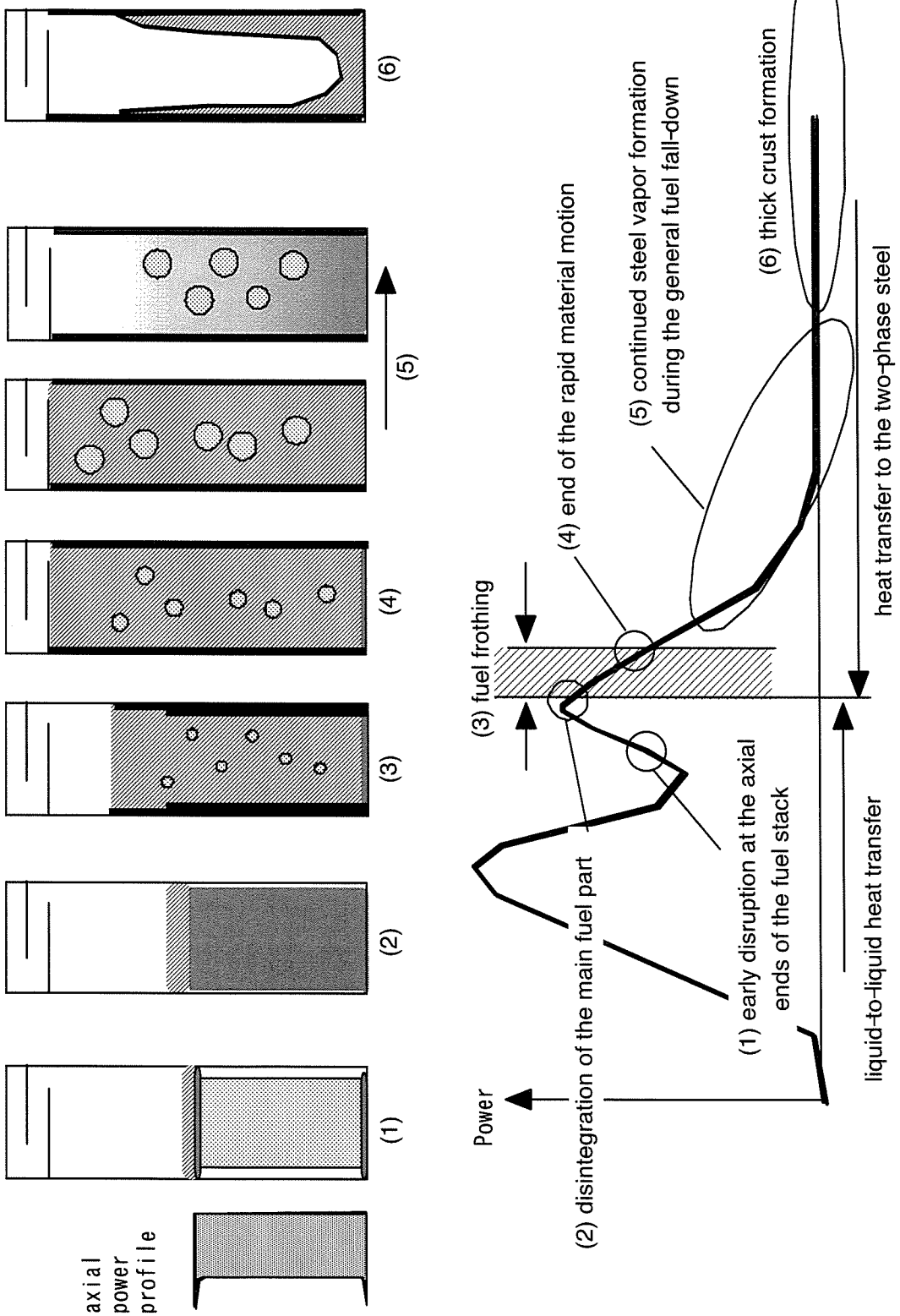

Fig. B-15 Overall test scenario.

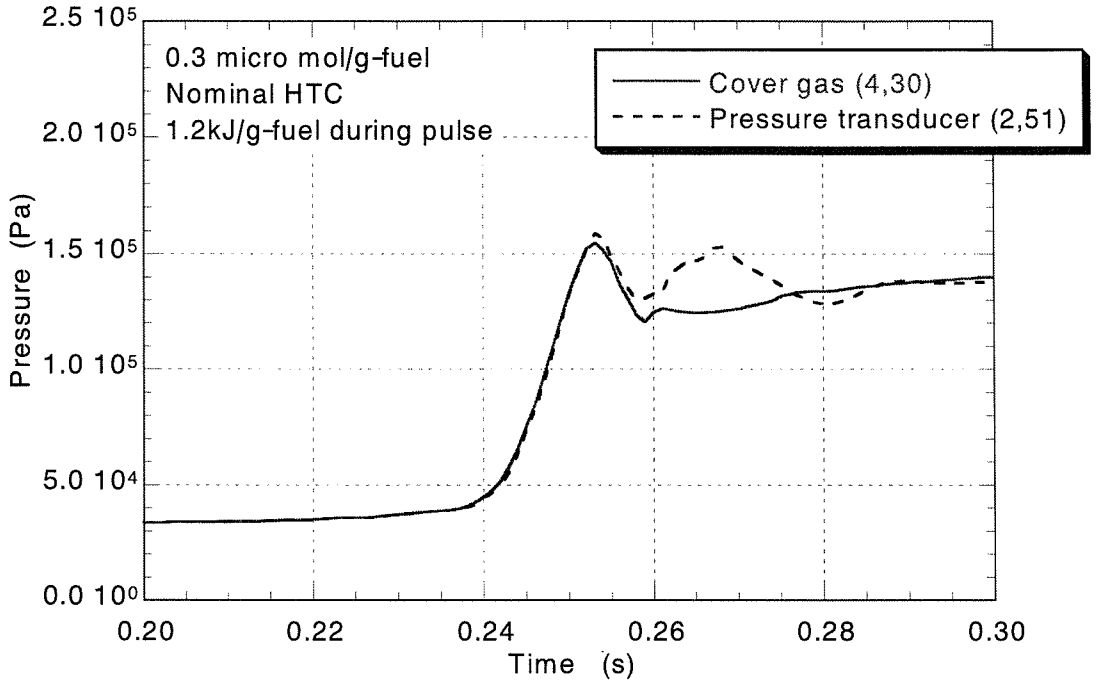

Fig. B-16 Response of the pressure transducer in Case N03H1E12.

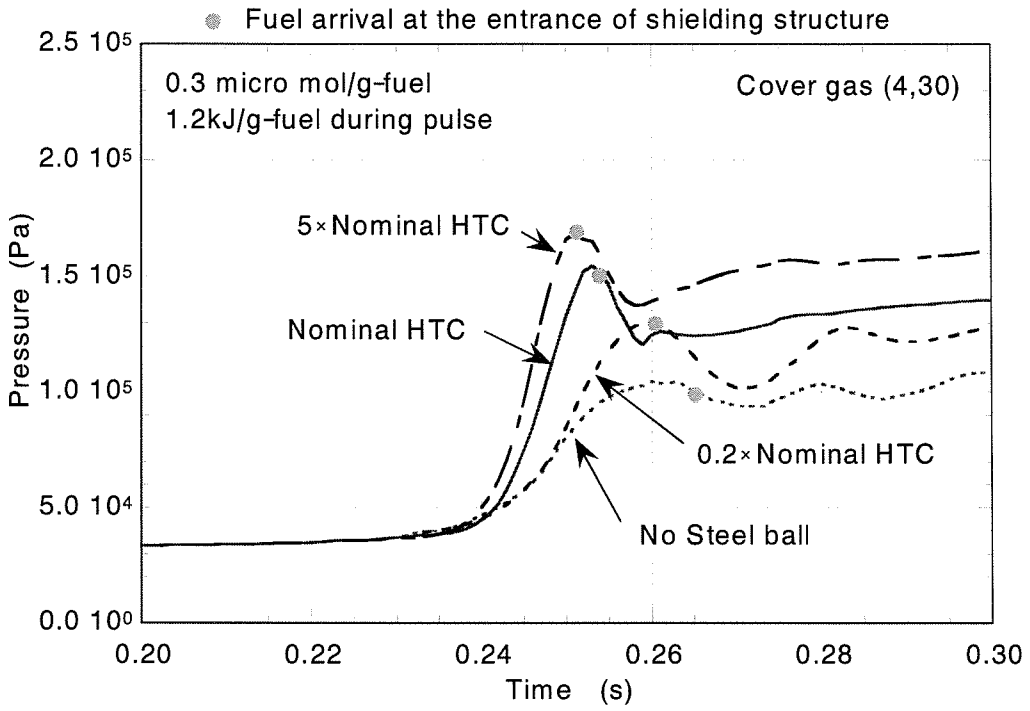

Fig. B-17 Cover-gas pressure with the impurity gas of 0.3μmol/g-fuel.

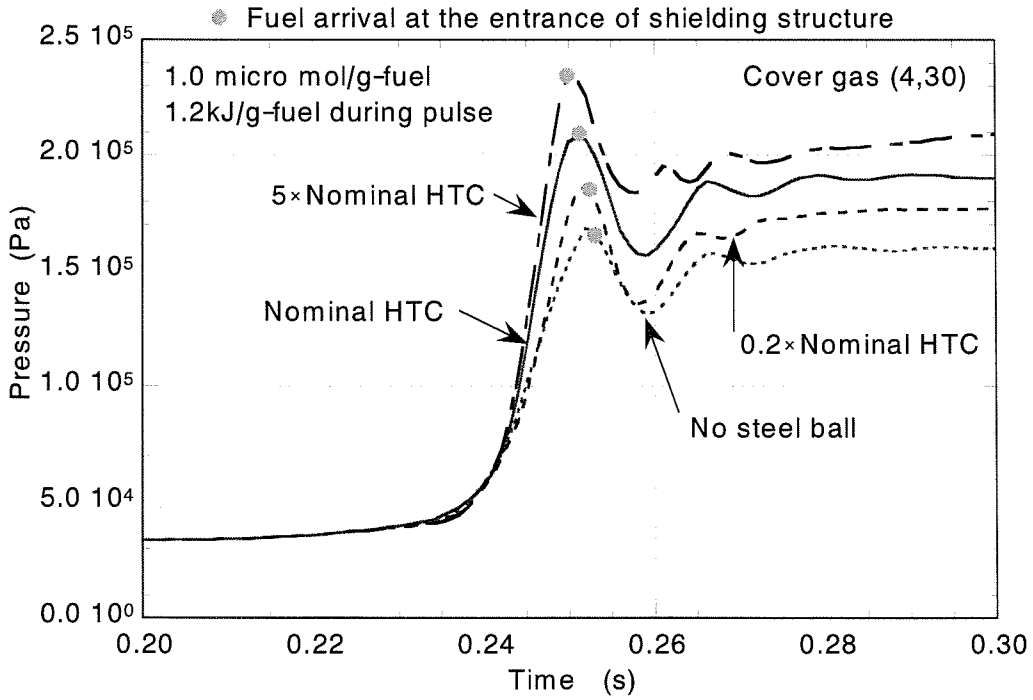

Fig. B-18 Cover-gas pressure with the impurity gas of 1.0μmol/g-fuel.

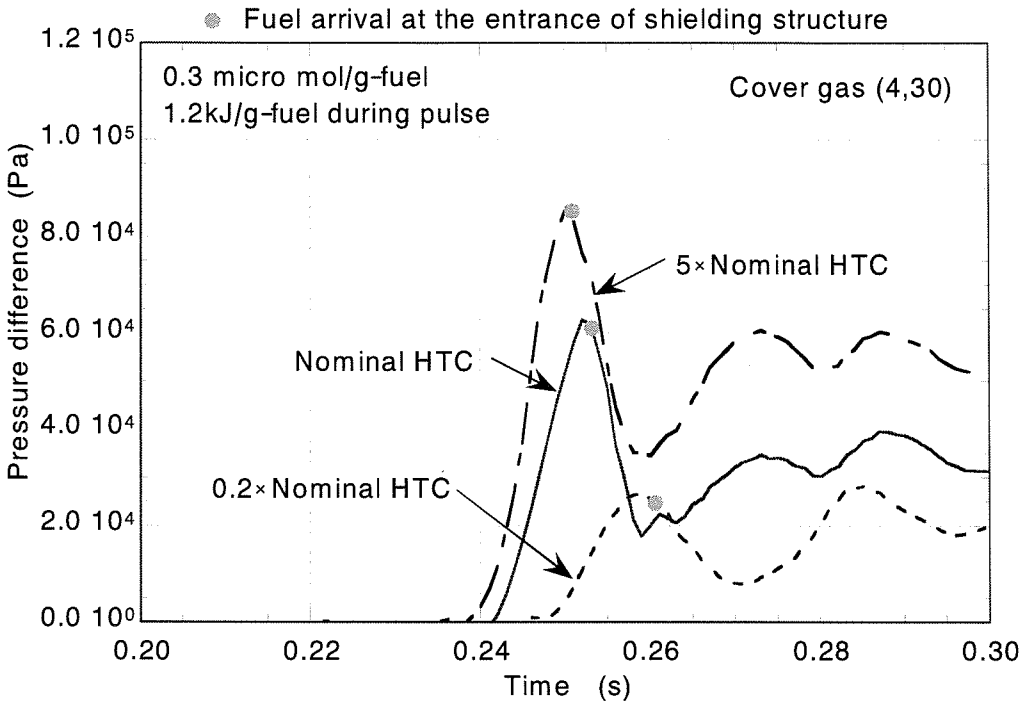

Fig. B-19 Pressure difference at cover gas with the impurity gas of 0.3μmol/g-fuel.

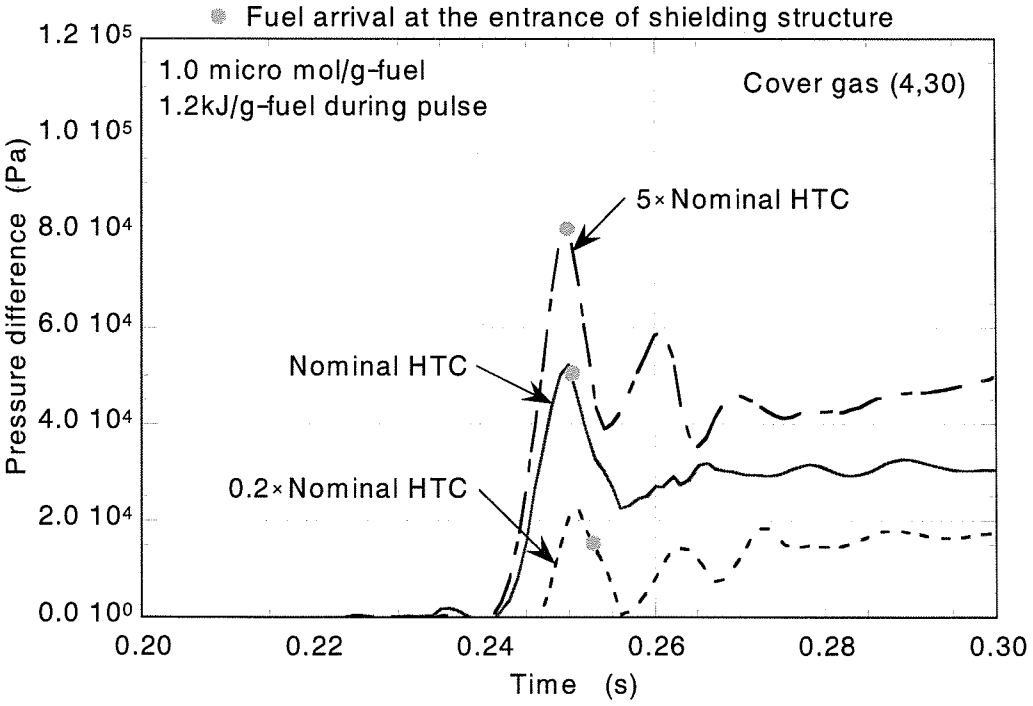

Fig. B-20 Pressure difference at cover gas with the impurity gas of 1.0μmol/g-fuel.

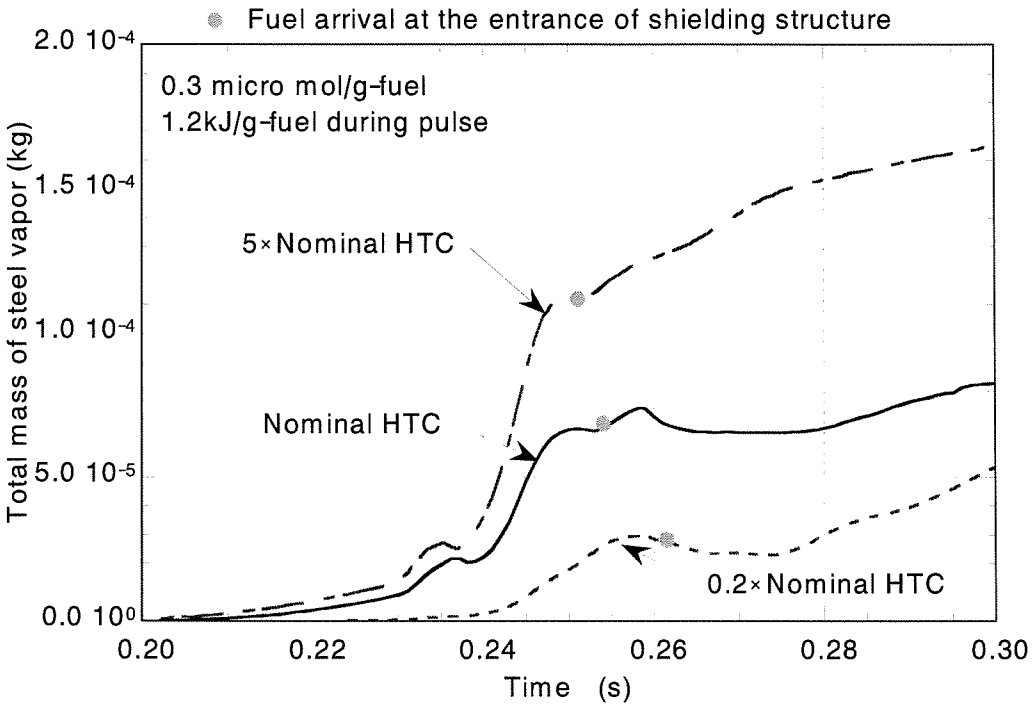

Fig. B-21 Total mass of steel vapor with the impurity gas of 0.3μmol/g-fuel.

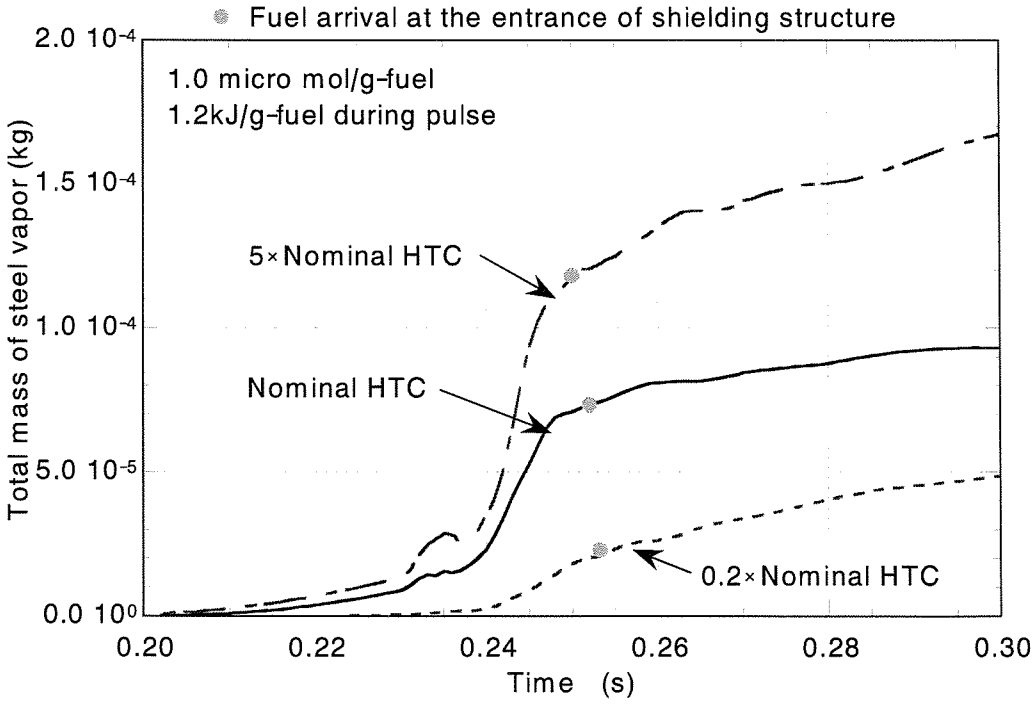

Fig. B-22 Total mass of steel vapor with the impurity gas of 1.0μmol/g-fuel.

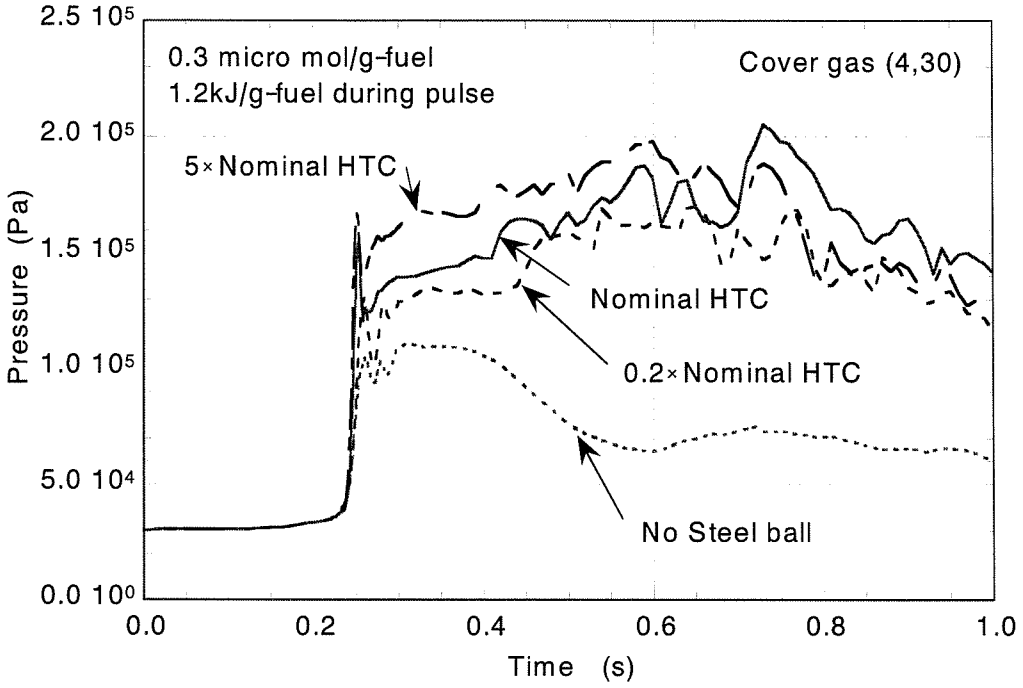

Fig. B-23 Long-term behavior of cover-gas pressure with the impurity gas of 0.3μmol/g-fuel.

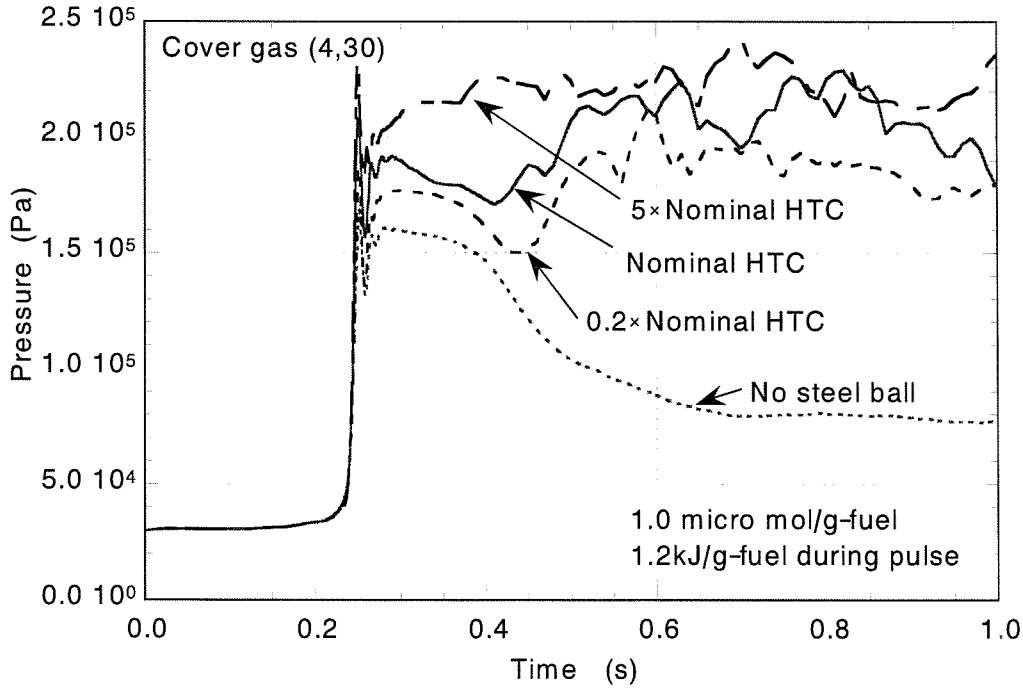

Fig. B-24 Long-term behavior of cover-gas pressure with the impurity gas of 1.0μmol/g-fuel.

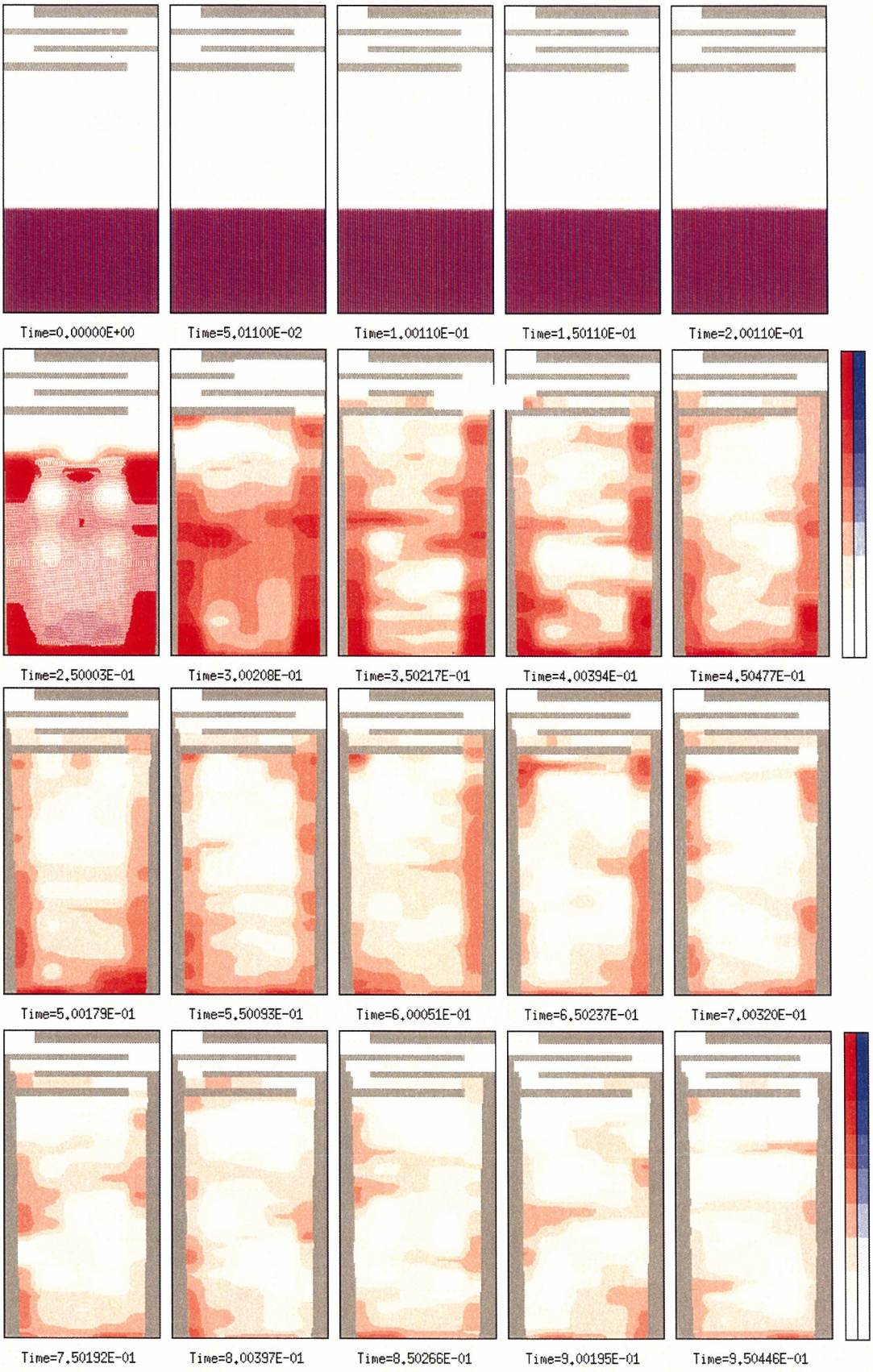

Fig. B-25 Material motion in case considering tight momentum coupling.

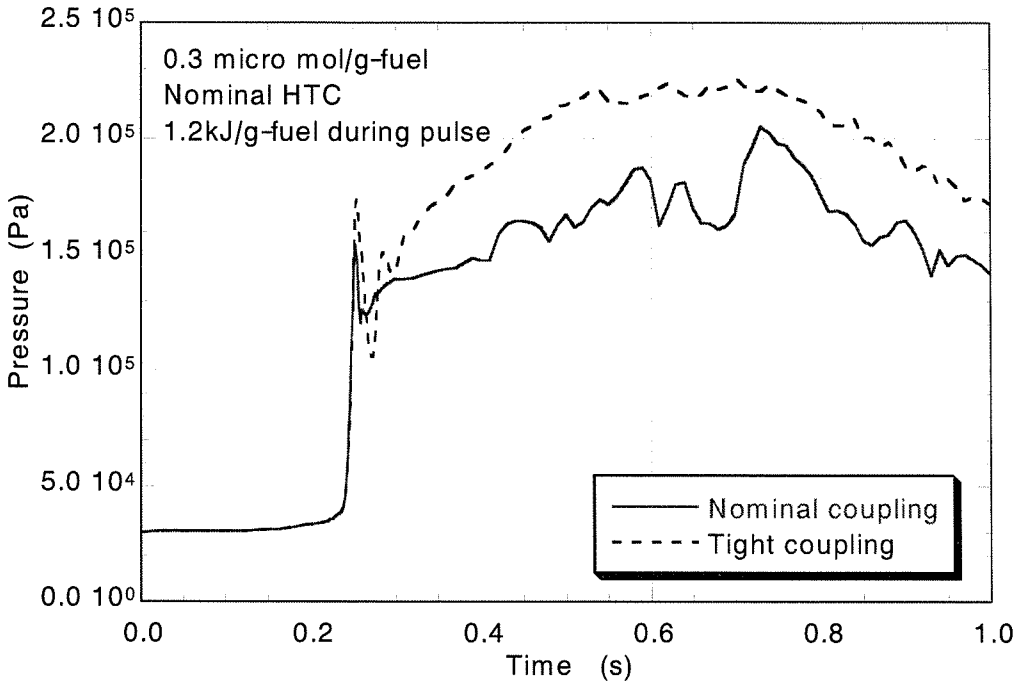

Fig. B-26 Long-term behavior of cover-gas pressure in case considering tight momentum coupling.

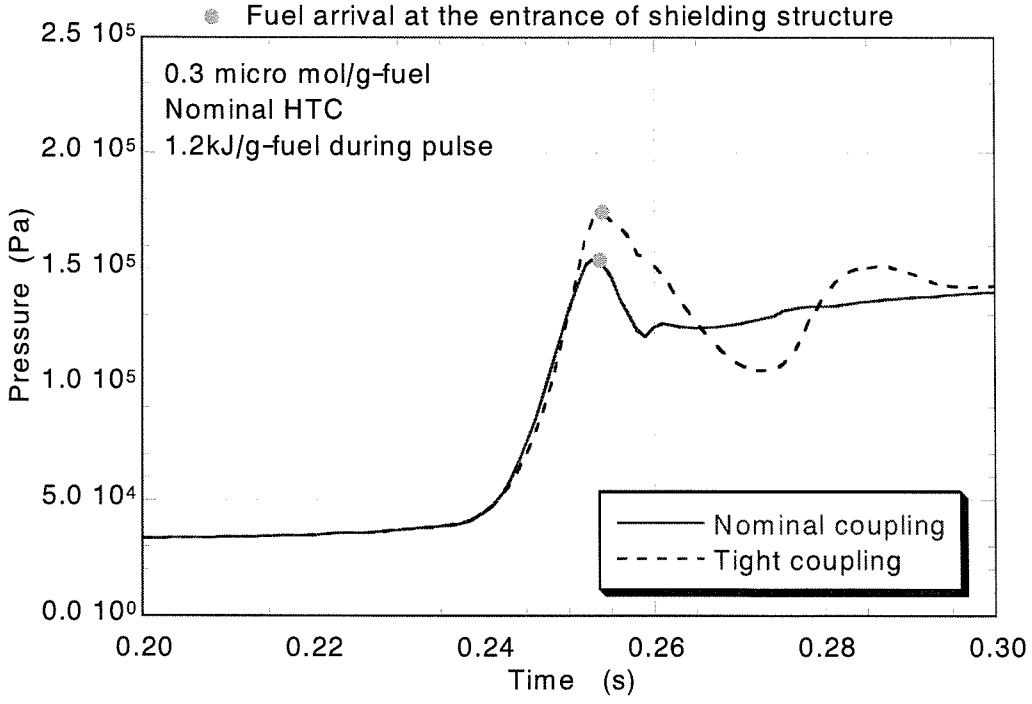

Fig. B-27 Short-term behavior of cover-gas pressure in case considering tight momentum coupling.

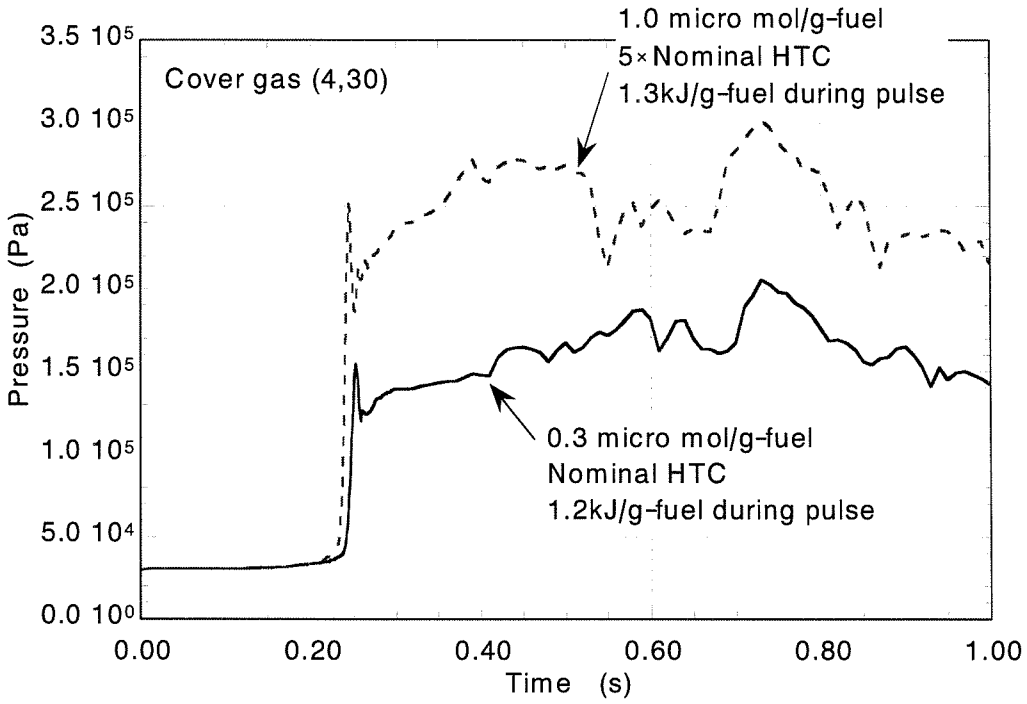

Fig. B-28 Long-term behavior of cover-gas pressure in High-pressure case.

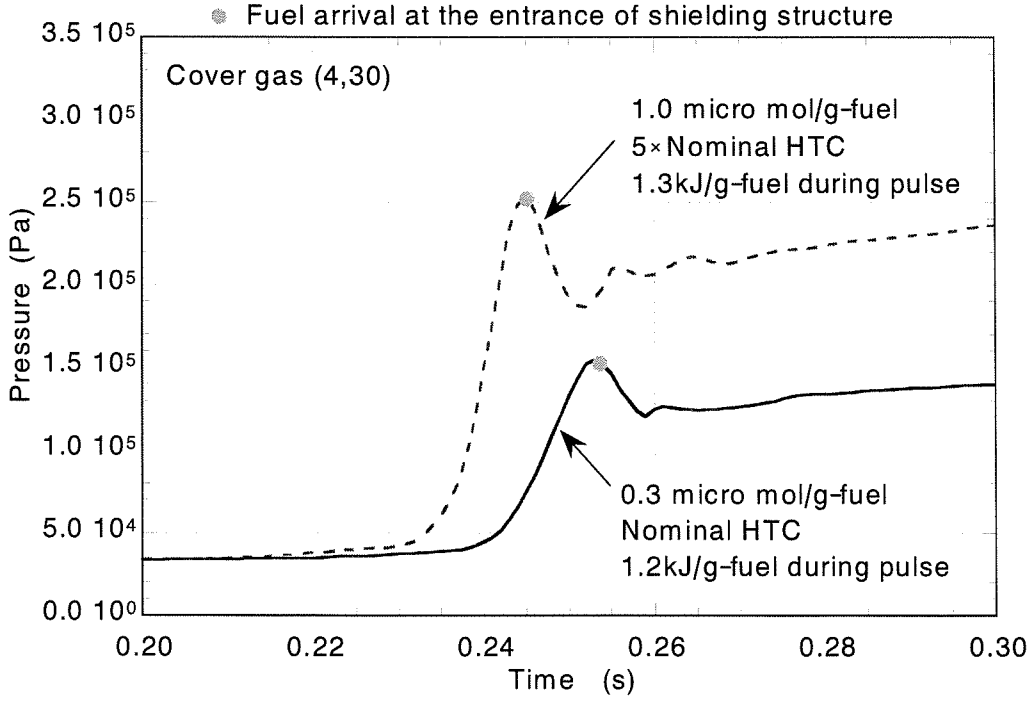

Fig. B-29 Short-term behavior of cover-gas pressure in High-pressure case.

Appendix C: Physical properties of solid fuel

In the TPA2 test, the fuel pellets were fabricated not by sintering but by pressing fuel powder. The thermophysical properties, especially the thermal conductivity, of solid fuel might be different from the usual pellet. Therefore, the thermal conductivity is here modified in order to provide the SIMMER-III calculations.

Thermal conductivity of solid fuel

In the SIMMER-III analytical thermophysical property model [C-1], the solid thermal conductivity k_{f0} is expressed as a function of temperature T_f:

$$k_{f0} = a_{S1} + \frac{a_{S2}}{T_f} + \frac{a_{S3}}{T_f^2} + a_{S4}T_f + a_{S5}T_f^2, \qquad \text{(C-1)}$$

where the coefficients are fitting constants: a_{S1} = 2.0207, a_{S2} = 4.6844×10^{3}, a_{S3} = -1.0443×10^{6}, a_{S4} = -2.6031×10^{-3}, and a_{S5} = 8.9378×10^{-7} for solid fuel. Since the thermal conductivity of solid fuel decreases with increasing porosity, the following equation is used to correct for this porosity effect:

$$k_f = k_{f0}(1-\varepsilon_f)^{2.5}, \qquad \text{(C-2)}$$

where ε_f is the fractional porosity of solid fuel and k_f is the corresponding thermal conductivity.

As previously mentioned, the fuel pellet used in the tests might differ from the usual one. The thermal conductivity of packed beds has been investigated by W. Shotte [C-2] and S. Imura and E. Takegoshi [C-3]. They showed that the effect of radiation becomes significant for high temperatures. A simplified equation derived from these studies is given by

$$k_{f,packed} = 0.2018 + 2.409 \times 10^{-4}T_f - 2.627 \times 10^{-8}T_f^2 + 5.607 \times 10^{-11}T_f^3. \qquad \text{(C-3)}$$

This correlation is applied to the packed beds with 40% of porosity. Reflecting the effect of radiation for high temperatures with this equation, the thermal conductivity of the pressed fuel-particle pellet used in the tests can be modified with Eq. (C-1) and the following fitting constants: a_{S1} = 2.0053, a_{S2} = 3.7762×10^{3}, a_{S3} = -3.6784×10^{5}, a_{S4} = -2.9685×10^{-3}, and a_{S5} = 1.4590×10^{-6}. The previous correlations are plotted in **Fig. C-1**. The modified thermal conductivity, which was taking into account the radiation contribution in the high temperature range, has been used for the SIMMER-III calculations.

References

[C-1] K. Morita, Y. Tobita, Sa. Kondo and E. A. Fischer, "SIMMER-III Analytic Thermophysical Property Model," JNC TN9400 2000-004 (May 1999).

[C-2] W. Shotte, "Thermal Conductivity of Packed Beds," AIChe J, Vol. 6, No. 1, pp. 63-67 (March 1960).

[C-3] S. Imura and E. Takegoshi, "Effect of Gas Pressure on the Effective Thermal Conductivity of Packed Beds," Heat Transfer Japanese Research, pp.13-26 (1974).

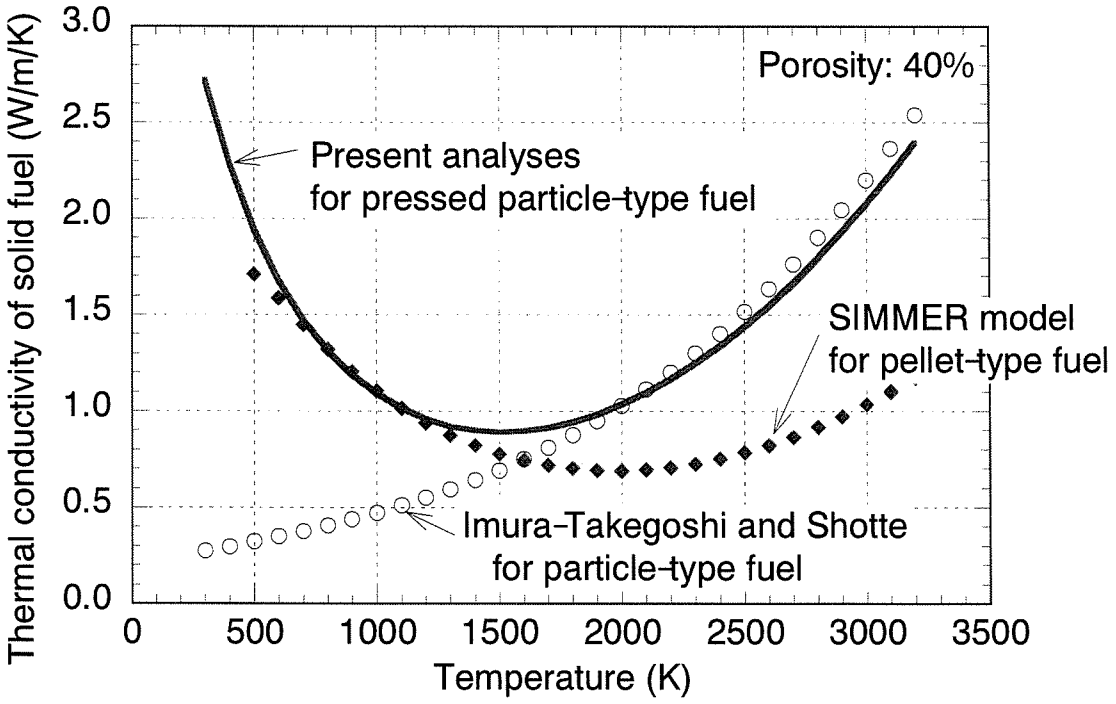

Fig. C-1. Modified thermal conductivity of solid fuel.

Appendix D: Correction sets.

D-1: Radiation model

```
*/ @TITLE
*/ RADIATION HEAT TRANSFER MODEL FOR TPA2 TEST ANALYSIS.
*/ @CONTENTS
*/ THE ENERGY OF BOILING POOL SURFACE IS TRANSFERED TO
*/ COVER GAS AND CRUCIBLE SURFACE BY RADIATION.
*/ @HOW
*/ IMPROVE
*/ @DECK
*/ EOSPRU RDINP STEP1
*/ @INPUT
*/  XCNTL#ADD#ALGOPT#80#0#=0:DO  NOT  APPLY  RADIATIVE  HEAT
TRANSFER
*/  MODEL. <BR>
*/  >1:APPLY RADIATIVE HEAT TRANSFER MODEL.
*/  XCNTL#ADD#ALGOPT#81#0#=0:DO  NOT  APPLY  RADIATIVE  HEAT
TRANSFER
*/  TO COVER GAS. <BR>
*/  >1:APPLY RADIATIVE HEAT TRANSFER TO COVER GAS.
*/  XCNTL#ADD#ALGOPT#82#0#=0:DO  NOT  APPLY  RADIATIVE  HEAT
TRANSFER
*/  TO CRUCIBLE. <BR>
*/  >1:APPLY RADIATIVE HEAT TRANSFER TO CRUCIBLE.
*/ XEOS#ADD#FGRAD###0.0#FRACTION OF RADIATIVE HEAT TRANSFER TO
*/  COVER GAS
*/ XEOS#ADD#ICRBL1###CELL IN LEFT OF RADIATION CALCULATION
REGION.
*/ XEOS#ADD#ICRBL2###CELL IN RIGHT OF RADIATION CALCULATION
REGION.
*/ XEOS#ADD#JCRBL1###CELL IN BOTTOM OF RADIATION CALCULATION
REGION.
*/ XEOS#ADD#JCRBL2###CELL IN TOP OF RADIATION CALCULATION
REGION.
*/ @REFERENCE
*/ ---
*/ @DATE
*/ 12/8/2002
*/
*ID YNRAD
*/
*/ #### EOSPRU ####
*/
*I EOSPRU.23
    * ,FGRAD
*I EOSPRU.23
    * ,ICRBL1,ICRBL2,JCRBL1,JCRBL2
*/
*/ #### RDINP ####
*/
*I MRCN0.2
    *           ,FGRAD  ,ICRBL1 ,ICRBL2 ,JCRBL1 ,JCRBL2
*/
*/ #### STEP1 ####
*/
*I SWCWMXF.19
*CA EOSPRU
      DOUBLEPRECISION SIGMA,        EPSRAD
      DATA          SIGMA/5.67D-8/ EPSRAD/0.8D0/
*I MR6K0.27
C
C     ================================================
C     CALCULATE THE RADIATIVE HEAT LOSS FROM THE SURFACE OF
C     THE BOILING POOL
C     ================================================
      IF ( ALGOPT(80).GE.1 ) THEN
C
      QRTOTL = ZERO
      DO 1010 I=1,IB-1
      AFRAC = ONE
      DO 1000 J=JB,1,-1
         IJ=J*IBP2+I+1
C     ------------------------------------------------
C     IF THE VOLUME FRACTION OF THE FUEL IS LESS THAN
C     0.05, GO TO THE LOWER CELL.
C     ------------------------------------------------
      IF ( ALPLK(IJ,1)+ALPLK(IJ,4).LT.C5M2 ) GO TO 1000
C     ------------------------------------------------
C     CALCULATE THE AREAL FRACTION OF THE PROJECTED AREA OF
C     THE DROPLETS TO THE POOL SURFACE IN THE CELL.
C     ------------------------------------------------
C     --- FOR L1 ---
      FP1= THREE*ALPLK(IJ,1)*DZC(IJ)
     &       /(MIN(CP1,MAX(RLMDK(IJ,1),C1M3))*EIGHT)
      FP1= MIN(FP1,ONE)
C     --- FOR L4 ---
      FP4= THREE*ALPLK(IJ,4)*DZC(IJ)
     &       /(MIN(CP1,MAX(RLMDK(IJ,4),C1M3))*EIGHT)
      FP4= MIN(FP4,ONE)
C     ------------------------------------------------
C     REDUCE THE INTERNAL ENERGY BY THE RADIATIVE HEAT LOSS.
C     ------------------------------------------------
C     --- FOR L1 ---
      QR = EPSRAD * SIGMA * TLK(IJ,1)**4
      DQ = DT*FP1*QR*(ONE - ASM(IJ))*AFRAC
     &     /EFRBLK(IJ,1)/DZC(IJ)
      DQ = MAX( ZERO, MIN( DQ,
     &          SIELK(IJ,1)-ELIQUS(REGTAB(IJ,1),1) ) )
      SIELK(IJ,1) = SIELK(IJ,1) - DQ
C
      QRTOTL = QRTOTL + DQ*EFRBLK(IJ,1)*VOLC(IJ)/DT
C     --- FOR L4 ---
      QR = EPSRAD * SIGMA * TLK(IJ,4)**4
      DQ = DT*FP4*QR*(ONE - ASM(IJ))*AFRAC
     &     /EFRBLK(IJ,4)/DZC(IJ)
      DQ = MAX( ZERO, DQ )
      SIELK(IJ,4) = SIELK(IJ,4) - DQ
C
      QRTOTL = QRTOTL + DQ*EFRBLK(IJ,4)*VOLC(IJ)/DT
C     ------------------------------------------------
C     CALCULATE THE REMAINING SURFACE AREA FOR THE LOWER
CELLS.
C     ------------------------------------------------
      AFRAC = AFRAC*(ONE - (FP1+FP4))
      IF ( AFRAC.LE.C1M2 ) GO TO 1010
 1000 CONTINUE
 1010 CONTINUE
C
      IF ( MOD(CYCLE,ALGOPT(80)).EQ.0 )
     &WRITE(6,'(A,1PE12.5)')  'RADIATIVE  HEAT  LOSS  [W]
='',QRTOTL
C
      ENDIF
C
C     ================================================
C     CALCULATE THE RADIATIVE HEATING OF THE COVER GAS.
C     THE CELLS IN WHICH THE VOID FRACTION IS GREATER
C     THAN 0.7 ARE EMPLOYED IN THIS CALCULATION.
C     THE 5% OF THE RADIATIVE LOSS FROM THE POOL SURFACE
C     IS ASSUMED TO BE ABSORBED BY THE GAS.
C     (REF. NOTE SCARABEE 177/88  ANNEXE 2)
C     ================================================
      IF ( ALGOPT(81).GE.1 ) THEN
C     ------------------------------------------------
C     CALCULATE THE TOTAL MASS OF THE GAS AND EVALUATE
C     THE ENERGY PRODUCTION DENSITY BY THE RADIATION.
C     ------------------------------------------------
      GMASS = ZERO
      DO 1110 I=1,IB-1
      DO 1100 J=JB,1,-1
         IJ=J*IBP2+I+1
         IF ( ALPGK(IJ)/(ONE-ASM(IJ)).LT.CP7 ) GO TO 1100
         GMASS = GMASS+VOLC(IJ)
      &
*( CVMGT(EFRBGK(IJ,1),ZERO,EFRBGK(IJ,1).GT.TOSMAL)
      &
+CVMGT(EFRBGK(IJ,2),ZERO,EFRBGK(IJ,2).GT.TOSMAL)
      &
+CVMGT(EFRBGK(IJ,3),ZERO,EFRBGK(IJ,3).GT.TOSMAL)
      &
+CVMGT(EFRBGK(IJ,4),ZERO,EFRBGK(IJ,4).GT.TOSMAL) )
 1100 CONTINUE
 1110 CONTINUE
      EPRDEN = QRTOTL*FGRAD/GMASS
C     ------------------------------------------------
C     INCREASE THE INTERNAL ENERGY OF COVER GAS
C                              BY THE RADIATIVE HEATING.
C     ------------------------------------------------
      QGTOTL = ZERO
      DO 1130 I=1,IB-1
      DO 1120 J=JB,1,-1
         IJ=J*IBP2+I+1
         IF ( ALPGK(IJ)/(ONE-ASM(IJ)).LT.CP7 ) GO TO 1120
         DQ = EPRDEN*DT
         SIEGK(IJ) = SIEGK(IJ) + DQ
C           QGTOTL = QGTOTL + EPRDEN*VOLC(IJ)             &
*( CVMGT(EFRBGK(IJ,1),ZERO,EFRBGK(IJ,1).GT.TOSMAL)
      &
+CVMGT(EFRBGK(IJ,2),ZERO,EFRBGK(IJ,2).GT.TOSMAL)
      &
+CVMGT(EFRBGK(IJ,3),ZERO,EFRBGK(IJ,3).GT.TOSMAL)
      &
+CVMGT(EFRBGK(IJ,4),ZERO,EFRBGK(IJ,4).GT.TOSMAL) )
 1120 CONTINUE
 1130 CONTINUE
C
      IF ( MOD(CYCLE,ALGOPT(81)).EQ.0 )
     &WRITE(6,'(A,1PE12.5)') 'RADIATIVE HEATING OF THE COVER
GAS [W] ='
     &                    ,QGTOTL
C
      ENDIF
```

```
C
C    ================================================
C    CALCULATE THE RADIATIVE HEATING OF THE CRUCIBLE.
C    ================================================
     IF ( ALGOPT(82).GE.1 ) THEN
C    ------------------------------------------------------
C    CALCULATE THE TOTAL MASS OF THE CRUCIBLE SURFACE AND
C    EVALUATE THE ENERGY PRODUCTION DENSITY BY THE RADIATION.
C    ------------------------------------------------------
     SMASS = ZERO
     DO 1210 I=ICRBL1,ICRBL2
     DO 1200 J=JCRBL1,JCRBL2
        IJ=J*IBP2+I+1

AAA=ALPSK(IJ,5)+ALPSK(IJ,6)+ALPSK(IJ,7)+ALPSK(IJ,8)
        IF ( AAA.LT.C1M10 .OR. ALPSK(IJ,3).GT.C1M10) GO TO 1200
        SMASS = SMASS+VOLC(IJ)
     &
*( CVMGT(EFRBSK(IJ,5),ZERO,EFRBSK(IJ,5).GT.TOSMAL)
     &
+CVMGT(EFRBSK(IJ,6),ZERO,EFRBSK(IJ,6).GT.TOSMAL)
     &
+CVMGT(EFRBSK(IJ,7),ZERO,EFRBSK(IJ,7).GT.TOSMAL)
     &
+CVMGT(EFRBSK(IJ,8),ZERO,EFRBSK(IJ,8).GT.TOSMAL) )
 1200  CONTINUE
 1210  CONTINUE
     EPRDEN = QRTOTL*(ONE-FGRAD)/SMASS
C
C    ------------------------------------------------------
C    INCREASE THE INTERNAL ENERGY OF THE CRUCIBLE SURFACE
C                              BY THE RADIATIVE HEATING.
C
C    ------------------------------------------------------
     QSTOTL = ZERO
     DO 1230 I=ICRBL1,ICRBL2
     DO 1220 J=JCRBL1,JCRBL2
        IJ=J*IBP2+I+1

AAA=ALPSK(IJ,5)+ALPSK(IJ,6)+ALPSK(IJ,7)+ALPSK(IJ,8)
        IF ( AAA.LT.C1M10 .OR. ALPSK(IJ,3).GT.C1M10) GO TO 1220
        DQ = EPRDEN*DT
        SIESK(IJ,5)=
SIESK(IJ,5)+CVMGT(DQ,ZERO,EFRBSK(IJ,5).GT.TOSMAL)
        SIESK(IJ,6)=
SIESK(IJ,6)+CVMGT(DQ,ZERO,EFRBSK(IJ,6).GT.TOSMAL)
        SIESK(IJ,7)=
SIESK(IJ,7)+CVMGT(DQ,ZERO,EFRBSK(IJ,7).GT.TOSMAL)
        SIESK(IJ,8)=
SIESK(IJ,8)+CVMGT(DQ,ZERO,EFRBSK(IJ,8).GT.TOSMAL)
C
        QSTOTL = QSTOTL + EPRDEN*VOLC(IJ)
     &
*( CVMGT(EFRBSK(IJ,5),ZERO,EFRBSK(IJ,5).GT.TOSMAL)
     &
+CVMGT(EFRBSK(IJ,6),ZERO,EFRBSK(IJ,6).GT.TOSMAL)
     &
+CVMGT(EFRBSK(IJ,7),ZERO,EFRBSK(IJ,7).GT.TOSMAL)
     &
+CVMGT(EFRBSK(IJ,8),ZERO,EFRBSK(IJ,8).GT.TOSMAL) )
 1220  CONTINUE
 1230  CONTINUE
C
      IF ( MOD(CYCLE,ALGOPT(82)).EQ.0 )
     &WRITE(6,'(A,1PE12.5)')  'RADIATIVE  HEATING  OF  THE
CRUCIBLE [W] ='
     &                    ,QSTOTL
C
      ENDIF
C
```

D-2: Improvement of inter-cell heat transfer model for steel balls

```
*ID TPA2F
*/
*/  ADJUST THE INTER-CELL HEAT TRANSFER CALCULATION
*/        FOR SOLID PARTICLES
*/
*/  ##### ITCHTR #####
*/
*D ITCHTR.343,344
C
          IF( K.EQ.5 .AND. CEKL.NE.ONE ) THEN
          IF((ALPLK(IJ,K).GT.C1M3                    .AND.
ALPLK(IJL,K).GT.0.95) .OR.
     &                          (ALPLK(IJ,K).GT.0.95   .AND.
ALPLK(IJL,K).GT.C1M3))THEN
            EKIJ  = KPLM(IJ ,K)
            EKIJL = KPLM(IJL,K)
          ELSEIF((ALPLK(IJ,K).GT.C1M3                    .AND.
ALPLK(IJT,K).GT.0.95) .OR.
     &                          (ALPLK(IJ,K).GT.0.95   .AND.
ALPLK(IJT,K).GT.C1M3))THEN
            EKIJ  = KPLM(IJ ,K)
            EKIJT = KPLM(IJT,K)
          ENDIF
          ENDIF
C
          KLAM(IJ)     =     CEKI*(     EKIJ*DRC(IJL)     +
EKIJL*DRC(IJ) )/DRIJL
          KTHE(IJ)     =     CEKJ*(     EKIJ*DZC(IJT)     +
EKIJT*DZC(IJ) )/DZIJT
*/
*I YNBD2.17
C
          IF( K.EQ.5 .AND. CEKL.NE.ONE .AND.
     &                          ((ALPLK(IJ,K).GT.C1M3    .AND.
ALPLK(IJL,K).GT.0.95) .OR.
     &                           (ALPLK(IJ,K).GT.0.95   .AND.
ALPLK(IJL,K).GT.C1M3)) ) THEN
           RB1=HALF*ALPLK(IJ ,K)*(RB(IJL  )-RB(IJ ))+RB(IJ )

RB2=HALF*ALPLK(IJL,K)*(RB(IJL+1)-RB(IJL))+RB(IJL)
           DRL=RB(IJL)*LOG(RB2/RB1)
           FCOND=ONE
          ENDIF
C
*D ITCHTR.389
          DZT=DZB(IJ)
          IF( K.EQ.5 .AND. CEKL.NE.ONE .AND.
     &                          ((ALPLK(IJ,K).GT.C1M3    .AND.
ALPLK(IJT,K).GT.0.95) .OR.
     &                           (ALPLK(IJ,K).GT.0.95   .AND.
ALPLK(IJT,K).GT.C1M3)) ) THEN
          FCOND = ONE
          DZT     =     HALF*(     DZC(IJ)*ALPLK(IJ,K)     +
DZC(IJT)*ALPLK(IJT,K) )
          ENDIF
          QQTHE(IJ) = KTHE(IJ)*( TLK(IJ,K) - TLK(IJT,K) )/DZT
*/
*/ ### COMMON/CHTC/ ###
*/
*I DB4N7.1
     &          ,CEKI          ,CEKJ          ,CEKL
*/
*/ ### RDINP ###
*/
*I YN282.96
     *           ,CEKI   ,CEKJ   ,CEKL
*/
*/ ### DEFULT ###
*/
*I DEFULT.453
      DATA  CEKI           / 1.00D+0 /
      DATA  CEKJ           / 1.00D+0 /
      DATA  CEKL           / 1.00D+0 /
```

D-3: Prevention of can wall surface melting under fuel crust

```
*ID TPHMT
*/ ==== PREVENTION OF MELTING OF CAN WALL SURFACE NODE UNDER
CRUST.
*/
*/ ### EQUIMF ###
*/
*D EQUIMF.168,SWEOS.1716
     IF((HMTOPT(68).EQ.1)  .AND.  (EFRBSK(IJ,2).GT.TOSMAL))
THEN
       ETHRES=ELIQUS(REGTAB(IJ,MES5),M2)
      ELSE
       ETHRES=ESOLUS(REGTAB(IJ,MES5),M2)
      ENDIF
     IF((EFRBSK(IJ,5).GT.SMALL)         .AND.         (SIESK
(IJ,5).GT.ETHRES)) THEN
*D EQUIMF.178,SWEOS.1717
     IF((HMTOPT(68).EQ.1)  .AND.  (EFRBSK(IJ,3).GT.TOSMAL))
THEN
       ETHRES=ELIQUS(REGTAB(IJ,MES7),M2)
      ELSE
       ETHRES=ESOLUS(REGTAB(IJ,MES7),M2)
      ENDIF
     IF((EFRBSK(IJ,7).GT.SMALL)         .AND.         (SIESK
(IJ,7).GT.ETHRES)) THEN
```

D-4: Prevention of steel ball motion in fuel pellet before its melting

```
*ID TPA2J
*/ ==== PREVENTION OF STELL BALL MOTION IN FUEL PELLET.
*/
*/ #### KQQC ####
*/
*I KQQC.5
     *          ,APJA1  ,APJA2  ,APJT1  ,APJT2
```

```
*/
*/ #### RDINP ####
*/
*I RDINP.132
     *           ,APJA1  ,APJA2  ,APJT1  ,APJT2
*/
*/ #### DEFULT ####
*/
*I DEFULT.412
     DATA APJA1  ,APJA2          / 0.7D+0, 0.7D+0 /
     DATA APJT1  ,APJT2          / 1.0D+9, 1.0D+9 /
*/
*/ #### MXF ####
*/
*I MXF.1856
       IF(T.GT.APJT1 .AND. T.LT.APJT2) THEN
         APJ=APJA1
       ELSEIF(T.GT.APJT2) THEN
         APJ=APJA2
       ENDIF
*I MXF.1870
       IF(T.GT.APJT1 .AND. T.LT.APJT2) THEN
         APJ=APJA1
       ELSEIF(T.GT.APJT2) THEN
         APJ=APJA2
       ENDIF
*I MXF.1906
       IF(T.GT.APJT1 .AND. T.LT.APJT2) THEN
         APJ=APJA1
       ELSEIF(T.GT.APJT2) THEN
         APJ=APJA2
       ENDIF
*I MXF.1920
       IF(T.GT.APJT1 .AND. T.LT.APJT2) THEN
         APJ=APJA1
       ELSEIF(T.GT.APJT2) THEN
         APJ=APJA2
       ENDIF
```

D-5: Modification of fuel-pellet thermal conductivity

```
*ID TPA2X
*/ ==== MODIFICATION OF FUEL THERMAL CONDUCTIVITY.
*/
*/ ### XKPSM ###
*/
*I XKPSM.17
*CA OPTION
*I XKPSM.23
     IF( TPPOPT(90).EQ.1 .AND. N.EQ.2 .AND. M.EQ.1) THEN
     XKPSM =  AKPS(1,N,M)*T**3+AKPS(2,N,M)*T**2
    *       +AKPS(3,N,M)*T   +(AKPS(4,N,M)    +AKPS(5,N,M))
     ENDIF
```

D:6: Prevention of can-wall surface melting even if crust forms

```
*ID TPA2N
*/  NO METALIC-WALL MELTING, BUT CRUST FORMATION
*/
*/  ##### MFGAM #####
*/
*I MFGAM.225
     if( ip.ne.2 .and. qill.lt.zero ) then
      ti(ij,6) = tll
      qill     = zero
     endif
*I MFGAM.237
     if( ip.ne.2 .and. qill.lt.zero ) then
      ti(ij,8) = tll
      qill     = zero
     endif
*I MFGAM.292
     if( ip.ne.3 .and. qill.lt.zero ) then
      ti(ij,7) = tll
      qill     = zero
     endif
*I MFGAM.304
     if( ip.ne.3 .and. qill.lt.zero ) then
      ti(ij,9) = tll
      qill     = zero
     endif
*/
*/  ##### MFGAFC #####
*/
*I MFGAFC.124
     if( ip.ne.2 .and. qill.lt.zero ) then
      qill     = zero
     endif
*I MFGAFC.135
     if( ip.ne.2 .and. qill.lt.zero ) then
      qill     = zero
     endif
*I MFGAFC.146
     if( ip.ne.3 .and. qill.lt.zero ) then
      qill     = zero
     endif
*I MFGAFC.157
     if( ip.ne.3 .and. qill.lt.zero ) then
      qill     = zero
     endif
```

D-7: Avoidance of numerical trouble

```
*ID TP3ONO
*/
*/  *** XVSM **
*I MRCE1.2
      if(m.eq.2.and.n.eq.1)xvsm=1.41420e-04
*I MRC50.98
      if(m.eq.2.and.n.eq.1)xvsm=1.41420e-04
*/  *** DISMX **
*I DISMX.27
     dimension iflg(mms)
*/
*I DISMX.38
       iflg(n)=0
       bunbo=alplm(n,1)+alplm(n,2)+alplm(n,3)+alpgm(n)
       if(bunbo .lt. 0.1)then
         iflg(n)=1
         go to 600
       end if
*/
*I DISMX.71
       bunbo=alphaf(n,1)+alphaf(n,2)+alphaf(n,3)+alpghf
       if(bunbo .lt. 0.1)then
         iflg(n)=1
         go to 700
       end if
*/
*I DISMX.206
        if(iflg(n) .eq. 1)go to 410
```

D-8: Addition of input variables of MXF

```
*ID TPA2G
*/ ==== MOMENTUM COUPLING BETWEEN
*/ CCD1G : CONTINUOUS LIQUID FUEL AND GAS BUBBLE (L1-G),
*/ CCD17 : LIQUID FUEL DROPLET AND CONTINUOUS GAS (L1-G),
*/ CCD27 : LIQUID STEEL DROPLET AND CONTINUOUS GAS (L2-G),
*/ CCD47 : FUEL PARTICLE AND CONTINUOUS GAS (L4-G),
*/ CCD57 : STEEL PARTICLE AND CONTINUOUS GAS (L5-G),
*/ CCD12 : CONTINUOUS LIQUID FUEL AND LIQUID STEEL DROPLET
(L1-L2),
*/ CCD24 : CONTINUOUS LIQUID STEEL AND FUEL PARTICLE (L2-L4),
AND
*/ CDD24 : LIQUID STEEL DROPLET AND FUEL PARTICLE (L2-L4).
*/ ===
*/
*/ ### COMMON/KQQC ###
*/
*I KQQC.3

&          ,CCD1G  ,CCD17  ,CCD27  ,CCD47  ,CCD57  ,CCD12
    &          ,CCD24  ,CDD24
*/
*/ ### MXF ###
*/
*/ === LIQUID STEEL DROPLET AND FUEL PARTICLE (L2-L4) ===
*/
*I MXF.563
       IF( (D1.EQ.2.AND.D2.EQ.4).OR.(D1.EQ.4.AND.D2.EQ.2) )
THEN
        BQQR(N,ID(D1,D2)) = C1M2*ARTB1(N,ID(D1,D2))
    &                     * ( ALPLB1(N,D1)/SVLK(N,D1)
    &                     +   ALPLB1(N,D2)/SVLK(N,D2) )
    &                       /Z( ALPLB1(N,D1)+ALPLB1(N,D2) ) *
CDD24
    &                     *ABS(ALPLB1(N,D1))/Z(ALPLB1(N,D1))
    &                     *ABS(ALPLB1(N,D2))/Z(ALPLB1(N,D2))
       ELSE
*I MXF.569
       ENDIF
*I MXF.826
       IF( (D1.EQ.2.AND.D2.EQ.4).OR.(D1.EQ.4.AND.D2.EQ.2) )
THEN
        BQQR(N,ID(D1,D2)) = C1M2*ARTB2(N,ID(D1,D2))
    &                     * ( ALPLB2(N,D1)/SVLK(N,D1)
    &                     +   ALPLB2(N,D2)/SVLK(N,D2) )
    &                       /Z( ALPLB2(N,D1)+ALPLB2(N,D2) ) *
CDD24
    &                     *ABS(ALPLB2(N,D1))/Z(ALPLB2(N,D1))
    &                     *ABS(ALPLB2(N,D2))/Z(ALPLB2(N,D2))
       ELSE
*I MXF.832
```

```
       ENDIF
*/
*/ === CONTINUOUS LIQUID STEEL AND FUEL PARTICLE (L2-L4) ===
*/
*I TB5H8.1
       IF( C.EQ.2.AND.D.EQ.4 ) THEN
         CD     = CCD24*MAX(CDPLUS,CDASTR)
       ELSEIF( C.EQ.1.AND.D.EQ.2 ) THEN
         CD     = CCD12*MAX(CDPLUS,CDASTR)
       ELSE
*I MXF.549
       ENDIF
*I MXF.550
       IF( C.EQ.2.AND.D.EQ.4 ) THEN
         AQQR(N,ID(C,D))                                          =
C15E0*ARTB1(N,ID(C,D))*MUA/Z(RLMBK(N,D))
     &                  *   ABS(ALPLB1(N,C))/Z(ALPLB1(N,C))
     &                                                            *
ABS(ALPLB1(N,D))/Z(ALPLB1(N,D))*CCD24
       ELSEIF( C.EQ.1.AND.D.EQ.2 ) THEN
         AQQR(N,ID(C,D))                                          =
C15E0*ARTB1(N,ID(C,D))*MUA/Z(RLMBK(N,D))
     &                  *   ABS(ALPLB1(N,C))/Z(ALPLB1(N,C))
     &                                                            *
ABS(ALPLB1(N,D))/Z(ALPLB1(N,D))*CCD12
       ELSE
*I MXF.553
       ENDIF
*I TB5H8.4
       IF( C.EQ.2.AND.D.EQ.4 ) THEN
         CD     = CCD24*MAX(CDPLUS,CDASTR)
       ELSEIF( C.EQ.1.AND.D.EQ.2 ) THEN
         CD     = CCD12*MAX(CDPLUS,CDASTR)
       ELSE
*I MXF.812
       ENDIF
*I MXF.813
       IF( C.EQ.2.AND.D.EQ.4 ) THEN
         AQQR(N,ID(C,D))                                          =
C15E0*ARTB2(N,ID(C,D))*MUA/Z(RLMBK(N,D))
     &                  *   ABS(ALPLB2(N,C))/Z(ALPLB2(N,C))
     &                                                            *
ABS(ALPLB2(N,D))/Z(ALPLB2(N,D))*CCD24
       ELSEIF( C.EQ.1.AND.D.EQ.2 ) THEN
         AQQR(N,ID(C,D))                                          =
C15E0*ARTB2(N,ID(C,D))*MUA/Z(RLMBK(N,D))
     &                  *   ABS(ALPLB2(N,C))/Z(ALPLB2(N,C))
     &                                                            *
ABS(ALPLB2(N,D))/Z(ALPLB2(N,D))*CCD12
       ELSE
*I MXF.816
       ENDIF
*/
*/ === CONTINUOUS LIQUID FUEL AND GAS BUBBLE (L1-G) ===
*/
*I TB5H8.3
       IF( C.EQ.1 ) THEN
        CD     = CCD1G*MAX(CDPLUS,CDASTR)
       ELSE
*I MXF.636
       ENDIF
*I MXF.637
       IF( C.EQ.1 ) THEN
        AQQR(N,ID(C,D))                                           =
C15E0*ARTB1(N,ID(C,D))*MUA/Z(RGBK(N))
     &                  * ABS(ALPLB1(N,C))/Z(ALPLB1(N,C))
     &                  * ABS(ALPGBK(N))/Z(ALPGBK(N))*CCD1G
       ELSE
*I MXF.640
       ENDIF
*I TB5H8.6
       IF( C.EQ.1 ) THEN
       CD     = CCD1G*MAX(CDPLUS,CDASTR)
C
        AQQR(N,ID(C,D))                                           =
C15E0*ARTB2(N,ID(C,D))*MUA/Z(RGBK(N))
     &                  * ABS(ALPLB2(N,C))/Z(ALPLB2(N,C))
     &                  * ABS(ALPGBK(N))/Z(ALPGBK(N))*CCD1G
       ELSE
*I MXF.903
       ENDIF
*/
*/ === LIQUID FUEL DROPLET AND CONTINUOUS GAS (L1-G) ===
*/ === LIQUID STEEL DROPLET AND CONTINUOUS GAS (L2-G) ===
*/ === FUEL PARTICLE AND CONTINUOUS GAS (L4-G) ===
*/ === STEEL PARTICLE AND CONTINUOUS GAS (L5-G) ===
*/
*I TB5H8.7
C
       IF( D.EQ.1 ) THEN
        CD     = CCD17*MAX(CDPLUS,CDASTR)
C
        AQQR(N,ID(C,D))                                           =
C15E0*ARTD(N,ID(C,D))*MUA/Z(RLMDK(N,D))
     &                  *   ABS(ALPGD(N))/Z(ALPGD(N))
     &                                                            *
ABS(ALPLMD(N,D))/Z(ALPLMD(N,D))*CCD17
C
       ELSEIF( D.EQ.2 ) THEN
        CD     = CCD27*MAX(CDPLUS,CDASTR)
C
        AQQR(N,ID(C,D))                                           =
C15E0*ARTD(N,ID(C,D))*MUA/Z(RLMDK(N,D))
     &                  *   ABS(ALPGD(N))/Z(ALPGD(N))
     &                                                            *
ABS(ALPLMD(N,D))/Z(ALPLMD(N,D))*CCD27
C
       ELSEIF( D.EQ.4 ) THEN
        CD     = CCD47*MAX(CDPLUS,CDASTR)
C
        AQQR(N,ID(C,D))                                           =
C15E0*ARTD(N,ID(C,D))*MUA/Z(RLMDK(N,D))
     &                  *   ABS(ALPGD(N))/Z(ALPGD(N))
     &                                                            *
ABS(ALPLMD(N,D))/Z(ALPLMD(N,D))*CCD47
C
       ELSEIF( D.EQ.5 ) THEN
        CD     = CCD57*MAX(CDPLUS,CDASTR)
C
        AQQR(N,ID(C,D))                                           =
C15E0*ARTD(N,ID(C,D))*MUA/Z(RLMDK(N,D))
     &                  *   ABS(ALPGD(N))/Z(ALPGD(N))
     &                                                            *
ABS(ALPLMD(N,D))/Z(ALPLMD(N,D))*CCD57
       ELSE
*I MXF.1071
       ENDIF
*/
*/ ### RDINP ###
*/
*I CAB60.12

*           ,CCD1G  ,CCD17  ,CCD27  ,CCD47  ,CCD57  ,CCD12
     *           ,CCD24  ,CDD24
*/
*/ ### DEFULT ###
*/
*I DEFULT.411
      DATA CCD1G                / 1.0D+0  /
      DATA CCD17                / 1.0D+0  /
      DATA CCD27                / 1.0D+0  /
      DATA CCD47                / 1.0D+0  /
      DATA CCD57                / 1.0D+0  /
      DATA CCD24                / 1.0D+0  /
      DATA CDD24                / 1.0D+0  /
```

D-9: Print of heat flux to wall

```
*ID YNFLX
*/
*/ #### EOSPRU ####
*/
*I EOSPRU.23
     *           ,HTFLUX(MMS)
*/
*/ #### LCWCHT ####
*/
*I LCWCHT.13
*CA TIME
*I LCWCHT.28
      DIMENSION SIECRT(MMS)
C
*I LCWCHT.51
      SIECRT(IJ)=SIESK(IJ,3)
*I LCWCHT.510
C
C     CALCULATE HEAT FLUX TO CAN WALL.
C
      DO 1000 J=1,JB
      DO 1000 I=1,IB
      IJ=IBP2*J+I+1
      IF(EFRBSK(IJ,3).GT.TOSMAL) THEN

HTFLUX(IJ)=(SIECRT(IJ)-SIESK(IJ,3))*EFRBSK(IJ,3)/DT/SARK(I
J,3)
      ENDIF
 1000 CONTINUE
*/
*/ #### WBF ####
*/
*I WBF.80
C       ===== HEAT FLUX TO CAN WALL =====
      IF ( SN(I).EQ.'HTFLUX' ) THEN
        DO 359 IJ=1,IJBP2
        WRK(IJ) =HTFLUX(IJ)
 359     CONTINUE
        WRITE(BFU) ( REAL( WRK(NRC(IJ)) ), IJ=1,IBJB)
        GO TO 100
      ENDIF
C
```

Appendix E: Sample input data set

```
START TPA2 ANALYSIS : CAPSULE2-TOP

 &XCNTL
  ALGOPT(24)=2,
  ALGOPT(45)=1,
  EDTOPT(17)=25,
  EDTOPT(20)=5,
  EDTOPT(51)=1,
  ERROPT(2)=1,
  EOSOPT(10)=1,
  HTCOPT(10)=1,
  HTCOPT(11)=2,
  HMTOPT(11)=999,
  HMTOPT(47)=1,
  HMTOPT(51)=1,
  HMTOPT(52)=2,
  HMTOPT(63)=1,
  HMTOPT(71)=1,2,1,1,
  HMTOPT(76)=1,
  HMTOPT(92)=1,
  MXFOPT(95)=1,
  HMTOPT(68)=1,
 &END
  ALGOPT(80)=100,100,100,
After 0.45s
  MXFOPT(12)=1,
  ALGOPT(80)=500,500,500,
After 0.55s
  MXFOPT(12)=1,
  ALGOPT(80)=500,500,500,

 &XMSH
  IGEOM=0,
  IB=8, JB=40, NREG=10,
  DRINP(1)= 7*1.0D-3, 10.25D-3,
  DZINP(1)= 5.0D-3, 2*1.0D-2, 5.0D-3, 3.0D-3,
       21*2.0D-3, 1.2D-3,
   2.0D-3, 2.8D-3, 5.0D-3, 1.0D-2, 1.3D-2, 1.0D-2,
   2.0D-3, 5.0D-3, 2.0D-3, 5.0D-3, 2.0D-3, 4.0D-3,
   2.0D-3,
 &END
 ### mesh size for C1 & C2 ###
   2.0D-3, 2.8D-3, 5.0D-3, 1.0D-2, 1.3D-2, 1.0D-2,
   2.0D-3, 5.0D-3, 2.0D-3, 5.0D-3, 2.0D-3, 4.0D-3,
   2.0D-3,
 ### mesh size for C3 ###
   2.0D-3, 2.8D-3, 5.0D-3, 5.0D-3, 1.0D-2, 2.0D-2,
   3.0D-2, 5.0D-2, 3.0D-2, 1.5D-2, 8.0D-3, 4.0D-3,
   2.0D-3,

 &XTME
  TSTART=0.0, TWFIN=0.45, DTSTRT=1.0D-06,
  DTMIN =1.0D-08, DTMAX=5.0D-04,
  TCPU  =1.0D+10, NDT0=10,
 &END
After 0.45s
  DTMAX=1.0D-04,

 &XRGN
  RGNAMB='COVER GAS',
  LRGN=1,ILB=1,IUB=7,JLB=28,JUB=33,
  TGINB    =6.7385D+2,
  PG4INB   =2.4000D+4,
  XENRIB(1)=6*1.0,
  ILS0IB=7,
 &END

 &XRGN
  RGNAMB='FUEL STEEL MIXTURE',
  LRGN=2,ILB=1,IUB=7,JLB=6,JUB=27,
  ALMINB(4)=6.4990D-1,
  TLMINB(4)=1.2000D+3,
  TGINB    =1.2000D+3,
  PG4INB   =2.4000D+4,
  XPINB    =1.9974D-5
  RLM0IB(4)=5.0D-6,
  RLM0IB(5)=5.0D-4,
  XENRIB(1)=6*1.0,
  ILS0IB=7,
 &END
  ALMINB(5)=2.9100D-3,
  TLMINB(5)=1.2000D+3,
  XENRIB(1)=0.0,

 ### fuel vol. frac. for C1 ###
  ALMINB(4)=6.3350D-1,
 ### fuel vol. frac. for C2 ###
  ALMINB(4)=6.4990D-1,
 ### fuel vol. frac. for C3 ###
  ALMINB(4)=6.4950D-1,
Ar)1 micro.mol/g-f =>XPINB=39.948E-6*1 =3.9948D-5
   3 micro.mol/g-f =>XPINB=39.948E-6*3 =1.1984D-4
   5 micro.mol/g-f =>XPINB=39.948E-6*5 =1.9974D-4

 &XRGN
  RGNAMB='BOTTOM OF CRUCIBLE',
  LRGN=3,ILB=1,IUB=7,JLB=5,JUB=5,
  ASMINB(6)=9.2000D-1,
  TSINB(5) =6.7385D+2,
  TSINB(6) =6.7385D+2,
  TGINB    =6.7385D+2,
  PG4INB   =2.0000D+5,
  ALCWIB   =300.0,
  XENRIB(1)=6*1.0,
  ILS0IB=7,
 &END

 &XRGN
  RGNAMB='BELOW CRUCIBLE',
  LRGN=4,ILB=1,IUB=8,JLB=1,JUB=4,
  ALMINB(3)=1.0000D-0,
  TLMINB(3)=6.7385D+2,
  TGINB    =6.7385D+2,
  PSFINB   =2.0000D+5,
  XENRIB(1)=6*1.0,
  ILS0IB=7,
 &END
  LRGN=4,ILB=4,IUB=8,JLB=1,JUB=4,

 &XRGN
  RGNAMB='COOLANT',
  LRGN=5,ILB=8,IUB=8,JLB=5,JUB=40,
  ALMINB(3)=2.23847D-1,
  ASMINB(6)=1.58351D-1,
  ASMINB(8)=6.17802D-1,
  TSINB(5) =6.7385D+2,
  TSINB(6) =6.7385D+2,
  TSINB(7) =6.7385D+2,
  TSINB(8) =6.7385D+2,
  TLMINB(3)=6.7385D+2,
  TGINB    =6.7385D+2,
  PSFINB   =2.0000D+5,
  ALCWIB   =75.635,
  ARCWIB   =96.555,
  XENRIB(1)=6*1.0,
  ILS0IB=7,
 &END

 &XRGN
  RGNAMB='LABYRINTH SHIELDING',
  LRGN=6,ILB=1,IUB=7,JLB=34,JUB=40,
  TGINB    =6.7385D+2,
  PG4INB   =2.4000D+4,
  XENRIB(1)=6*1.0,
  ILS0IB=7,
 &END

  RGNAMB='TC TUBE',
  LRGN=7,ILB=3,IUB=3,JLB=1,JUB=4,
  ALMINB(3)=3.20320D-1,
  ASMINB(6)=6.79680D-1,
  TSINB(5) =6.7385D+2,
  TSINB(6) =6.7385D+2,
  TLMINB(3)=6.7385D+2,
  TGINB    =6.7385D+2,
  PSFINB   =2.0000D+5,
  ALCWIB   =1088.0,
  XENRIB(1)=6*1.0,
  ILS0IB=7,

  RGNAMB='LEFT SIDE OF BELOW CRUCIBLE',
  LRGN=8,ILB=1,IUB=2,JLB=1,JUB=4,
  ASMINB(6)=9.20000D-1,
  TSINB(5) =6.7385D+2,
  TSINB(6) =6.7385D+2,
  TGINB    =6.7385D+2,
  PG4INB   =2.000D+5,
  ALCWIB   =300.0,
  XENRIB(1)=6*1.0,
  ILS0IB=7,

 &XEDT
  DMPC=9999999,PRTC=9999999,
  PPFC=9999999,BSFC=9999999,
  TCDMP(1) =1.0D20,
  DTDMP(1) =1.0D20,
  DTPRT(1) =1.0D20,
  LPRGN(5) =1,1,1,1,
  LPRGN(10)=1,1,0,1,1,0,
  LPRGN(16)=1,1,
  LPRGN(65)=1,1,1,1,
```

```
 LPRGN(70)=1,1,1,1,1,0,
 LPRGN(76)=1,
 LPRGN(96)=1,1,1,1,1,1,
 TCPPF(1) =1.0D20,
 DTPPF(1) =1.0D20,
 PPGRP(11)=0,0,0,1,1, 1,0,0,1,1,
 PPGRP(21)=1,0,0,1,0, 0,0,0,1,1,
 PPGRP(31)=1,0,0,0,0, 0,0,0,0,0,
 TCBSF(1) =0.40, 0.800, 1.00, 10.0,
 DTBSF(1) =0.05, 0.002, 0.02, 0.05,
 SN(1)=
  'ALPLK1','ALPLK2','ALPLK3',
  'ALPLK4','ALPLK5','ALPGK' ,
  'ALPSK2','ALPSK3','ALPSK5',
  'ALPSK6','ALPSK7','ALPSK8',
  'RBLK2' ,'RBLK3' ,'RBLK6' ,'RBLK7' ,
  'RBSK8' ,'RBSK9' ,'RBSK10','RBSK11',
  'RBGK2' ,'RBGK3' ,'RBGK5' ,
  'PGMK1' ,'PGMK2' ,'PGMK4' ,'PK'    ,
  'TLK1'  ,'TLK2'  ,'TLK4'  ,'TLK5'  ,
  'TSK2'  ,'TSK3'  ,'TSK5'  ,'TSK6'  ,
  'TSK7'  ,'TSK8'  ,'TGK'   ,'TLK3'  ,
  'VK1'   ,'VK2'   ,'VK3'   ,
  'UK1'   ,'UK2'   ,'UK3'   ,
  'SALMBK2','SALMDK2','SAGBK',
  'RLMBK2','RLMDK2','RGBK'  ,'IRGMK' ,
  'ALPGE' ,'RLMBK1','RLMDK1',
  'RBLK4' ,'TLK3'  ,'GAM2'  ,'GMFLK' ,
  'RBSK4' ,'RBSK6' ,'HTFLUX',
  'RBLK9' ,'RBLK10',
&END
  'ALPINK','ALPSK9','ALPSK4',
  'TIPINK','TSK9'  ,'TSK4'  ,
### for steady-state calculation ###
 TCBSF(1) =0.0, 100.0, 150.0,
 DTBSF(1) =0.5, 0.50,  0.50,
### for transient calculation ###
 TCBSF(1) =0.40, 0.800, 1.00, 10.0,
 DTBSF(1) =0.05, 0.002, 0.02, 0.05,

&XEOS
 ISAE(1,5)=0,
 IMRK(1,5)=0,
 TLIQUS(1,5)= 8.38000D1,
 TCRT(1,5)  = 1.50700D2,
 ELIQGD(1,5)=-8.40659D4,
 CVG(1,5)   = 3.92190D2,
 RUGM(1,5)  = 2.08133D2,
 WM(1,5)    = 3.99480D1,

 ISAE(2,2)    =  1,
 IMRK(2,2)    =  0,
 ISPN(2,2)    =  0,
 BETA(2,2)    =-1.00000D+00,
 ESOLUS(2,2)  = 5.02320D+05,
 ELIQUS(2,2)  = 8.26820D+05,
 CVG(2,2)     = 1.45600D+02,
 TCRT(2,2)    = 8.50000D+03,
 RUGM(2,2)    = 6.75976D+01,
 WM(2,2)      = 1.23000D+02,
 TSOLUS(2,2)  = 3.45000D+03,
 TLIQUS(2,2)  = 3.45000D+03,
 ELIQG(2,2)   = 5.74101D+06,
 PCRT(2,2)    = 5.16923D+08,
 ELIQGD(2,2)  = 5.74101D+06,
 VSOLUS(2,2)  = 5.99233D-05,
 VLIQUS(2,2)  = 5.99233D-05,
 ECRT(2,2)    = 1.56210D+06,
 ROCRT(2,2)   = 1.66880D+04,
 PSMIN(2,2)   = 1.81287D-08,
 DTDPS(2,2)   = 0.00000D+00,
 DVDPS(2,2)   =-5.74528D-16,
 DTDPC(2,2)   = 0.00000D+00,
 AS(1,2,2)    = 1.00000D+00, 0.00000D+00, 0.00000D+00,
 BS(1,2,2)    = 0.00000D+00, 0.00000D+00, 0.00000D+00,
 AL(1,2,2)    = 1.64600D+00, 0.00000D+00, 0.00000D+00,
                1.88929D+00, 0.00000D+00, 0.00000D+00,
 BL(1,2,2)    = 2.97105D+01, 0.00000D+00,-8.20000D+04,
                0.00000D+00,
 CL(1,2,2)    = 0.00000D+00, 0.00000D+00, 0.00000D+00,
                0.00000D+00,
 DL(1,2,2)    = 0.00000D+00, 0.00000D+00, 0.00000D+00,
                1.88929D+00, 0.00000D+00, 0.00000D+00,
 FL(1,2,2)    = 0.00000D+00, 0.00000D+00, 0.00000D+00,
                0.00000D+00, 0.00000D+00, 0.00000D+00,
 DG(1,2,2)    = 0.00000D+00, 0.00000D+00,
 FG(1,2,2)    = 0.00000D+00, 0.00000D+00, 0.00000D+00,
                0.00000D+00,
 AG(1,2,2)    = 0.00000D+00, 0.00000D+00, 1.00000D+00,
                0.00000D+00,
 BG(1,2,2)    = 8.44971D-12, 8.20000D+04, 0.00000D+00,
                0.00000D+00, 0.00000D+00, 0.00000D+00,
 CG(1,2,2)    = 1.45600D+02, 0.00000D+00, 0.00000D+00,
                1.00000D+00, 0.00000D+00, 0.00000D+00,
 ASAT(1,2,2)  = 3.62323D-04,-1.21951D-05, 0.00000D+00,
                0.00000D+00,
 BSAT(1,2,2)  = 0.00000D+00, 0.00000D+00, 0.00000D+00,
                1.00000D+00, 0.00000D+00, 0.00000D+00,
 CSAT(1,2,2)  = 1.45600D+02, 0.00000D+00, 0.00000D+00,
                1.00000D+00, 0.00000D+00, 0.00000D+00,
&END
After 0.45s
 FGRAD=1.0D-2,
 ICRBL1=1,
 ICRBL2=7,
 JCRBL1=20,
 JCRBL2=40,


&XTPP
 AKPS(1,2,1)=  2.0053+0,  3.7762D+3,-3.6784D+5,-2.9685D-3,
1.4590D-6,

 KPOPT(1,5)=0,
 MUOPT(1,5)=0,
 EPSM(1,5)  = 9.33000D1,
 SIGM(1,5)  = 3.54200D0,
 NATOM(1,5) = 1,

 KPOPT(2,2)=0,
 MUOPT(2,2)=0,
 AKPS(1,2,2)=34.0,0.0,0.0,0.0,0.0,
&END

&XERG
 REGN = 1,
 REGC(1,1)=1,1,8,40,
 MATEOS(1,1)=2,1,1,1,1,
&END
 REGN = 4,
 REGC(1,1)=1,6,4,23,
 MATEOS(1,1)=2,2,1,1,1,
 REGC(1,2)=1,1,4,5,
 MATEOS(1,2)=2,1,1,1,1,
 REGC(1,3)=1,24,4,40,
 MATEOS(1,3)=2,1,1,1,1,
 REGC(1,4)=5,1,8,40,
 MATEOS(1,4)=2,1,1,1,1,

&XSOS
 POW=2.5672D+2,
 IPOW=1,
 TIMAMP(1)=
   0.000D-0, 3.700D-1, 4.200D-1,
   4.520D-1, 4.800D-1, 5.000D-1,
   5.200D-1, 5.270D-1, 5.430D-1,
   5.580D-1, 5.700D-1, 6.000D-1,
   1.200D+0, 1.000D+2,
 AMPTAB(1)=
   1.000D+0, 1.000D+0, 2.700D+2,
   1.600D+3, 2.500D+2, 5.000D+1,
   3.500D+2, 8.000D+2, 7.600D+3,
   6.000D+2, 1.900D+2, 4.300D+1,
   0.000D+0, 0.000D+0,
 FRTP(1)  = 0.0,   1.0,  0.0,    0.0,  0.0,
 DAX(1) =
   0.000, 0.000, 0.000, 0.000, 0.000,
   1.493, 1.456, 1.418, 1.381, 1.344,
   1.306, 1.271, 1.275, 1.280, 1.285,
   1.289, 1.283, 1.273, 1.263, 1.253,
   1.264, 1.300, 1.336, 1.372, 1.408,
   1.444, 1.473, 1.470, 1.299, 1.294,
   1.282, 1.260, 1.237, 1.223, 1.215,
   1.207, 1.198, 1.187, 1.180, 1.172,
 DRAD(1)= 0.811, 0.820, 0.861, 0.891,
          0.961, 1.035, 1.166, 0.000,
&END

### initial power ###
   capsule1:POW=2.3155D+2,
   capsule2:POW=2.5672D+2,
   capsule3:POW=2.2293D+2,

### power history of steady state ###
 TIMAMP(1)=0.0, 100.0, 150.0,
 AMPTAB(1)=1.0, 1.0,   1.0,
### power history of TOP ###
 TIMAMP(1)=
   0.000D-0, 3.700D-1, 4.200D-1,
   4.520D-1, 4.800D-1, 5.000D-1,
   5.200D-1, 5.270D-1, 5.430D-1,
   5.580D-1, 5.700D-1, 6.000D-1,
   1.200D+0, 1.000D+2,
 AMPTAB(1)=
   1.000D+0, 1.000D+0, 2.700D+2,
   1.600D+3, 2.500D+2, 5.000D+1,
   3.500D+2, 8.000D+2, 7.600D+3,
   6.000D+2, 1.900D+2, 4.300D+1,
   0.000D+0, 0.000D+0,

### axial profile for C1 ###
   0.000, 0.000, 0.000, 0.000, 0.000,
```

```
   1.454, 1.421, 1.387, 1.353, 1.320,
   1.286, 1.253, 1.249, 1.256, 1.262,
   1.269, 1.275, 1.278, 1.280, 1.283,
   1.285, 1.288, 1.344, 1.413, 1.482,
   1.551, 1.606, 1.343, 1.345, 1.347,
   1.350, 1.355, 1.358, 1.359, 1.359,
   1.358, 1.358, 1.358, 1.357, 1.357,
### axial profile for C2 ###
   0.000, 0.000, 0.000, 0.000, 0.000,
   1.493, 1.456, 1.418, 1.381, 1.344,
   1.306, 1.271, 1.275, 1.280, 1.285,
   1.289, 1.283, 1.273, 1.263, 1.253,
   1.264, 1.300, 1.336, 1.372, 1.408,
   1.444, 1.473, 1.303, 1.299, 1.294,
   1.282, 1.260, 1.237, 1.223, 1.215,
   1.207, 1.198, 1.187, 1.180, 1.172,
### axial profile for C3
    with different mesh size ###
   0.000, 0.000, 0.000, 0.000, 0.000,
   1.249, 1.206, 1.163, 1.120, 1.077,
   1.034, 0.993, 0.994, 0.996, 0.998,
   0.999, 0.990, 0.976, 0.963, 0.949,
   0.956, 0.987, 1.019, 1.050, 1.081,
   1.113, 1.138, 0.955, 0.946, 0.931,
   0.910, 0.879, 0.816, 0.708, 0.549,
   0.441, 0.406, 0.392, 0.386, 0.383,

 &XMSC
  COURTN=0.4,
  IVDL(1)=1, 2, 1, 1, 1, 1, 3,
  EPST=1.0,
 &END
After 0.45s
  EPSVEL=1.00000E-06,
  EPSRO =5.00000E-04,

 &XSTR
  FL9G5 =1.0D+0,TL9G5 =1.0D+20,
  FL10G5=1.0D+0,TL10G5=1.0D+20,
  TAUST(2) = 1.0D-3,
  TAUST(4) = 1.0D-3,
 &END
After 0.45s
  FL10G5=1.0D+0,TL10G5=5.0D-03,

 &XMXF
  FCOUPL=1.0D-5,
  APJ=0.6,
  APJA1=0.6,
  APJA2=0.6,
  APJT1=1.0D9,
  APJT2=1.0D9,
  ALPMP=0.6,
  ALPSID=0.9,
  CORFZN(7,33)=1.25D+0,
  CORFZN(7,34)=4.50D+0,
  CORFZN(1,35)=1.25D+0,
  CORFZN(1,36)=4.50D+0,
  CORFZN(7,37)=9.41D+0,
  CORFZN(7,38)=4.728218D+3,
  CCD47=1.0D-1,
 &END
  CCD12=1.0D-1,
  CCD24=1.0D-0,
  CDD24=1.0D-0,
  CCD1G=1.0D-0,
  CCD17=1.0D-0,
  CCD27=1.0D-0,
  CCD57=1.0D-0,
After 0.45s
  CCD47=1.0D-5,
After 0.55s
  CCD47=1.0D-1,

 &XHTC
  HFCXS(1,3)=2.5D+3,
  HRSMUL(4)=5.5,
 &END
After 0.45s
  HRTMUL(1)=5.0D-3,
  HRTMUL(6)=5.0D-3,
  HLGMUL(1)=5.0D-3,
  HLGMUL(2)=5.0D-3,
  HGLMUL(1)=5.0D-3,
  HGLMUL(2)=5.0D-3,

 &XIFA
  MMIN   = 1.0D4,
  MMAX   = 1.0D7,
  DHPOOL = 1.0D-5,
  RLINI(4)= 5.0D-6,
  RLMIN(4)= 1.0D-6,
  RLINI(2)= 5.0D-4,
  RLMAX(2)= 5.0D-4,
  RLMIN(2)= 5.0D-4,
  RLINI(5)= 5.0D-4,
  RLMAX(5)= 5.0D-4,
  RLMIN(5)= 5.0D-4,
  ISRCDD(2)=1,1,1,
  CSSX   = 1.0D1,
 &END
  ALPBUB = 0.8,
  ALPDSP = 0.9,
  ALPNC  = 0.9,
  CLDS(2) = 0.0D+0,
  CLCS(2) = 0.0D+0,
  CPSR   = 3.5D-1,

 &XBND
  NBC=0,
  LWASET  (1,34)=1111,
  LWATME(1,1,34)=0.0,1.0D10,
  LWASET  (2,34)=1111,
  LWATME(1,2,34)=0.0,1.0D10,
  LWASET  (3,34)=1111,
  LWATME(1,3,34)=0.0,1.0D10,
  LWASET  (4,34)=1111,
  LWATME(1,4,34)=0.0,1.0D10,
  LWASET  (5,34)=1111,
  LWATME(1,5,34)=0.0,1.0D10,
  LWASET  (6,34)=1111,
  LWATME(1,6,34)=0.0,1.0D10,

  LWASET  (2,36)=1111,
  LWATME(1,2,36)=0.0,1.0D10,
  LWASET  (3,36)=1111,
  LWATME(1,3,36)=0.0,1.0D10,
  LWASET  (4,36)=1111,
  LWATME(1,4,36)=0.0,1.0D10,
  LWASET  (5,36)=1111,
  LWATME(1,5,36)=0.0,1.0D10,
  LWASET  (6,36)=1111,
  LWATME(1,6,36)=0.0,1.0D10,
  LWASET  (7,36)=1111,
  LWATME(1,7,36)=0.0,1.0D10,

  LWASET  (1,38)=1111,
  LWATME(1,1,38)=0.0,1.0D10,
  LWASET  (2,38)=1111,
  LWATME(1,2,38)=0.0,1.0D10,
  LWASET  (3,38)=1111,
  LWATME(1,3,38)=0.0,1.0D10,
  LWASET  (4,38)=1111,
  LWATME(1,4,38)=0.0,1.0D10,
  LWASET  (5,38)=1111,
  LWATME(1,5,38)=0.0,1.0D10,
  LWASET  (6,38)=1111,
  LWATME(1,6,38)=0.0,1.0D10,

  LBCSET(4)=1,1,1,1,1,1,
  LBCSET(419)=2,
 &END

 &XBND
  NBC=1,
  LBCS=3,
  LBCP=2,
  PTME(1)=0.0, 1.0D10,
  PTAB(1)=2.38D+5, 2.38D+5,
  LBCT(3)=2,
  TTME(1,3)=0.0, 1.0D10,
  TTAB(1,3)=6.7385D+2, 6.7385D+2,
 &END
  PTME(1)=0.0, 60.0, 65.0, 1.0D10,
  PTAB(1)=2.314D+5, 2.314D+5, 2.38D+5, 2.38D+5,
 If the following pressure is used,
  2312L/h = 6.422D-4m3/s = 3.67m/s.
  PTAB(1)=2.38D+5, 2.38D+5,
 In stead of this pressure, next is used
 to get larger time step size.
  PTAB(1)=2.314D+5, 2.314D+5,

 &XBND
  NBC=2,
  LBCS=3,
  LBCP=2,
  PTME(1)=0.0, 1.0D10,
  PTAB(1)=2.30D+5, 2.30D+5,
  LBCT(3)=0,
 &END

 &XCWD
  ALC(1,6,4)=   6.40836E-01,   6.40970E-01,   6.41030E-01,
6.41052E-01, 6.41022E-01,
  ALC(1,7,4)=   6.44301E-01,   6.44256E-01,   6.44141E-01,
6.43986E-01, 6.43702E-01,
  ALC(1,8,4)=   6.46880E-01,   6.46738E-01,   6.46466E-01,
6.46130E-01, 6.45551E-01,
  ALC(1,9,4)=   6.48582E-01,   6.48365E-01,   6.47954E-01,
6.47490E-01, 6.46719E-01,
  ALC(1,10,4)=   6.49655E-01,   6.49407E-01,   6.48949E-01,
6.48262E-01, 6.47337E-01,
```

```
  ALC(1,11,4)=   6.50217E-01,   6.49945E-01,   6.49441E-01,
6.48692E-01, 6.47676E-01,
  ALC(1,12,4)=   6.50450E-01,   6.50151E-01,   6.49597E-01,
6.48944E-01, 6.47866E-01,
  ALC(1,13,4)=   6.50585E-01,   6.50272E-01,   6.49691E-01,
6.49059E-01, 6.48005E-01,
  ALC(1,14,4)=   6.50706E-01,   6.50395E-01,   6.49824E-01,
6.49163E-01, 6.48056E-01,
  ALC(1,15,4)=   6.50780E-01,   6.50459E-01,   6.49860E-01,
6.49202E-01, 6.48123E-01,
  ALC(1,16,4)=   6.50873E-01,   6.50570E-01,   6.50016E-01,
6.49210E-01, 6.48106E-01,
  ALC(1,17,4)=   6.50834E-01,   6.50518E-01,   6.49933E-01,
6.49247E-01, 6.48117E-01,
  ALC(1,18,4)=   6.50776E-01,   6.50453E-01,   6.49856E-01,
6.49207E-01, 6.48126E-01,
  ALC(1,19,4)=   6.50763E-01,   6.50448E-01,   6.49870E-01,
6.49202E-01, 6.48083E-01,
  ALC(1,20,4)=   6.50764E-01,   6.50441E-01,   6.49839E-01,
6.49180E-01, 6.48098E-01,
  ALC(1,21,4)=   6.50852E-01,   6.50549E-01,   6.49995E-01,
6.49189E-01, 6.48085E-01,
  ALC(1,22,4)=   6.50857E-01,   6.50542E-01,   6.49959E-01,
6.49274E-01, 6.48145E-01,
  ALC(1,23,4)=   6.50799E-01,   6.50482E-01,   6.49892E-01,
6.49248E-01, 6.48175E-01,
  ALC(1,24,4)=   6.50636E-01,   6.50334E-01,   6.49777E-01,
6.49129E-01, 6.48042E-01,
  ALC(1,25,4)=   6.50203E-01,   6.49917E-01,   6.49369E-01,
6.48757E-01, 6.47747E-01,
  ALC(1,26,4)=   6.49377E-01,   6.49199E-01,   6.48765E-01,
6.48069E-01, 6.47094E-01,
  ALC(1,27,4)=   6.14385E-01,   6.15212E-01,   6.14486E-01,
6.21969E-01, 5.94006E-01,
  ALC(1,28,4)=   1.70000E-02,   1.70000E-02,   1.70000E-02,
1.70000E-02, 1.70000E-02,
  ALC(6,6,4)= 6.40972E-01, 6.40884E-01,
  ALC(6,7,4)= 6.43257E-01, 6.42633E-01,
  ALC(6,8,4)= 6.44760E-01, 6.43743E-01,
  ALC(6,9,4)= 6.45669E-01, 6.44389E-01,
  ALC(6,10,4)= 6.46151E-01, 6.44724E-01,
  ALC(6,11,4)= 6.46401E-01, 6.44890E-01,
  ALC(6,12,4)= 6.46534E-01, 6.44974E-01,
  ALC(6,13,4)= 6.46630E-01, 6.45037E-01,
  ALC(6,14,4)= 6.46680E-01, 6.45074E-01,
  ALC(6,15,4)= 6.46722E-01, 6.45101E-01,
  ALC(6,16,4)= 6.46723E-01, 6.45106E-01,
  ALC(6,17,4)= 6.46725E-01, 6.45105E-01,
  ALC(6,18,4)= 6.46721E-01, 6.45098E-01,
  ALC(6,19,4)= 6.46697E-01, 6.45083E-01,
  ALC(6,20,4)= 6.46697E-01, 6.45080E-01,
  ALC(6,21,4)= 6.46704E-01, 6.45091E-01,
  ALC(6,22,4)= 6.46752E-01, 6.45126E-01,
  ALC(6,23,4)= 6.46772E-01, 6.45142E-01,
  ALC(6,24,4)= 6.46681E-01, 6.45083E-01,
  ALC(6,25,4)= 6.46421E-01, 6.44872E-01,
  ALC(6,26,4)= 6.45864E-01, 6.44267E-01,
  ALC(6,27,4)= 6.18106E-01, 6.42784E-01,
  ALC(6,28,4)= 1.70000E-02, 1.70000E-02,

  ALC(4,7,5) =5.9520E-02,
  ALC(4,9,5) =5.9520E-02,
  ALC(4,13,5)=5.9520E-02,
  ALC(4,15,5)=5.9520E-02,
  ALC(4,18,5)=5.9520E-02,
  ALC(4,20,5)=5.9520E-02,
  ALC(4,23,5)=5.9520E-02,
  ALC(4,25,5)=5.9520E-02,

ALC(1,28,5)=5.0000E-02,5.0000E-02,5.0000E-02,5.0000E-02,5.
0000E-02,
  ALC(6,28,5)=5.0000E-02,5.0000E-02,

  TLC(4,7,5)= 9.17773E+02,
  TLC(4,9,5)= 1.08956E+03,
  TLC(4,13,5)= 1.16214E+03,
  TLC(4,15,5)= 1.16863E+03,
  TLC(4,18,5)= 1.16884E+03,
  TLC(4,20,5)= 1.16761E+03,
  TLC(4,23,5)= 1.17071E+03,
  TLC(4,25,5)= 1.15683E+03,
  TLC(1,28,5)=   1.21174E+03,   1.19975E+03,   1.17616E+03,
1.14610E+03, 1.09658E+03,
  TLC(6,28,5)= 1.03245E+03, 9.43804E+02,

  TLC(1,6,4)=   7.48411E+02,   7.55856E+02,   7.59163E+02,
7.60382E+02, 7.58732E+02,
  TLC(1,7,4)=   9.33834E+02,   9.31534E+02,   9.25662E+02,
9.17773E+02, 9.03223E+02,
  TLC(1,8,4)=   1.06066E+03,   1.05387E+03,   1.04080E+03,
1.02455E+03, 9.96250E+02,
  TLC(1,9,4)=   1.14032E+03,   1.13034E+03,   1.11130E+03,
1.08956E+03, 1.05294E+03,
  TLC(1,10,4)=   1.18901E+03,   1.17789E+03,   1.15711E+03,
1.12558E+03, 1.08234E+03,
  TLC(1,11,4)=   1.21412E+03,   1.20200E+03,   1.17943E+03,
1.14537E+03, 1.09831E+03,
  TLC(1,12,4)=   1.22442E+03,   1.21119E+03,   1.18642E+03,
1.15691E+03, 1.10719E+03,
  TLC(1,13,4)=   1.23036E+03,   1.21655E+03,   1.19067E+03,
1.16214E+03, 1.11365E+03,
  TLC(1,14,4)=   1.23568E+03,   1.22199E+03,   1.19659E+03,
1.16683E+03, 1.11602E+03,
  TLC(1,15,4)=   1.23895E+03,   1.22481E+03,   1.19821E+03,
1.16863E+03, 1.11915E+03,
  TLC(1,16,4)=   1.24299E+03,   1.22969E+03,   1.20518E+03,
1.16897E+03, 1.11833E+03,
  TLC(1,17,4)=   1.24131E+03,   1.22742E+03,   1.20148E+03,
1.17064E+03, 1.11885E+03,
  TLC(1,18,4)=   1.23873E+03,   1.22456E+03,   1.19804E+03,
1.16884E+03, 1.11928E+03,
  TLC(1,19,4)=   1.23820E+03,   1.22434E+03,   1.19865E+03,
1.16858E+03, 1.11729E+03,
  TLC(1,20,4)=   1.23820E+03,   1.22400E+03,   1.19729E+03,
1.16761E+03, 1.11800E+03,
  TLC(1,21,4)=   1.24209E+03,   1.22878E+03,   1.20424E+03,
1.16802E+03, 1.11737E+03,
  TLC(1,22,4)=   1.24232E+03,   1.22849E+03,   1.20264E+03,
1.17187E+03, 1.12014E+03,
  TLC(1,23,4)=   1.23976E+03,   1.22580E+03,   1.19963E+03,
1.17071E+03, 1.12155E+03,
  TLC(1,24,4)=   1.23260E+03,   1.21930E+03,   1.19451E+03,
1.16530E+03, 1.11537E+03,
  TLC(1,25,4)=   1.22305E+03,   1.21002E+03,   1.18534E+03,
1.15683E+03, 1.10850E+03,
  TLC(1,26,4)=   1.21391E+03,   1.20236E+03,   1.17925E+03,
1.14907E+03, 1.10053E+03,
  TLC(1,27,4)=   1.21174E+03,   1.19975E+03,   1.17616E+03,
1.14610E+03, 1.09658E+03,
  TLC(1,28,4)=   1.21174E+03,   1.19975E+03,   1.17616E+03,
1.14610E+03, 1.09658E+03,
  TLC(6,6,4)= 7.55981E+02, 7.52224E+02,
  TLC(6,7,4)= 8.80169E+02, 8.47403E+02,
  TLC(6,8,4)= 9.56977E+02, 9.05330E+02,
  TLC(6,9,4)= 1.00204E+03, 9.38293E+02,
  TLC(6,10,4)= 1.02559E+03, 9.55155E+02,
  TLC(6,11,4)= 1.03768E+03, 9.63471E+02,
  TLC(6,12,4)= 1.04409E+03, 9.67691E+02,
  TLC(6,13,4)= 1.04871E+03, 9.70817E+02,
  TLC(6,14,4)= 1.05110E+03, 9.72655E+02,
  TLC(6,15,4)= 1.05309E+03, 9.73979E+02,
  TLC(6,16,4)= 1.05318E+03, 9.74256E+02,
  TLC(6,17,4)= 1.05327E+03, 9.74212E+02,
  TLC(6,18,4)= 1.05306E+03, 9.73865E+02,
  TLC(6,19,4)= 1.05190E+03, 9.73107E+02,
  TLC(6,20,4)= 1.05190E+03, 9.72945E+02,
  TLC(6,21,4)= 1.05227E+03, 9.73497E+02,
  TLC(6,22,4)= 1.05452E+03, 9.75262E+02,
  TLC(6,23,4)= 1.05550E+03, 9.76063E+02,
  TLC(6,24,4)= 1.05116E+03, 9.73113E+02,
  TLC(6,25,4)= 1.04490E+03, 9.67846E+02,
  TLC(6,26,4)= 1.03797E+03, 9.59487E+02,
  TLC(6,27,4)= 1.03245E+03, 9.43804E+02,
  TLC(6,28,4)= 1.03245E+03, 9.43804E+02,

  TSC(1,5,5)=   6.75557E+02,   6.75679E+02,   6.75728E+02,
6.75728E+02, 6.75688E+02,
  TSC(6,5,5)= 6.75619E+02, 6.75595E+02, 6.73979E+02,
  TSC(8,6,5)= 6.74591E+02,
  TSC(8,7,5)= 6.75181E+02,
  TSC(8,8,5)= 6.75662E+02,
  TSC(8,9,5)= 6.75994E+02,
  TSC(8,10,5)= 6.76200E+02,
  TSC(8,11,5)= 6.76323E+02,
  TSC(8,12,5)= 6.76399E+02,
  TSC(8,13,5)= 6.76453E+02,
  TSC(8,14,5)= 6.76493E+02,
  TSC(8,15,5)= 6.76524E+02,
  TSC(8,16,5)= 6.76547E+02,
  TSC(8,17,5)= 6.76566E+02,
  TSC(8,18,5)= 6.76583E+02,
  TSC(8,19,5)= 6.76597E+02,
  TSC(8,20,5)= 6.76615E+02,
  TSC(8,21,5)= 6.76637E+02,
  TSC(8,22,5)= 6.76660E+02,
  TSC(8,23,5)= 6.76671E+02,
  TSC(8,24,5)= 6.76652E+02,
  TSC(8,25,5)= 6.76592E+02,
  TSC(8,26,5)= 6.76518E+02,
  TSC(8,27,5)= 6.76441E+02,
  TSC(8,28,5)= 6.75360E+02,
  TSC(8,29,5)= 6.74618E+02,
  TSC(8,30,5)= 6.74356E+02,
  TSC(8,31,5)= 6.74315E+02,
  TSC(8,32,5)= 6.74312E+02,
  TSC(8,33,5)= 6.74312E+02,
  TSC(8,34,5)= 6.74312E+02,
  TSC(8,35,5)= 6.74312E+02,
  TSC(8,36,5)= 6.74312E+02,
  TSC(8,37,5)= 6.74312E+02,
  TSC(8,38,5)= 6.74310E+02,
  TSC(8,39,5)= 6.74304E+02,
```

```
  TSC(8,40,5)= 6.74256E+02,

  TSC(1,5,6)=    6.75557E+02,    6.75679E+02,    6.75728E+02,
6.75728E+02, 6.75688E+02,
  TSC(6,5,6)= 6.75619E+02, 6.75595E+02, 6.73979E+02,
  TSC(8,6,6)= 6.74591E+02,
  TSC(8,7,6)= 6.75181E+02,
  TSC(8,8,6)= 6.75662E+02,
  TSC(8,9,6)= 6.75994E+02,
  TSC(8,10,6)= 6.76200E+02,
  TSC(8,11,6)= 6.76323E+02,
  TSC(8,12,6)= 6.76399E+02,
  TSC(8,13,6)= 6.76453E+02,
  TSC(8,14,6)= 6.76493E+02,
  TSC(8,15,6)= 6.76524E+02,
  TSC(8,16,6)= 6.76547E+02,
  TSC(8,17,6)= 6.76566E+02,
  TSC(8,18,6)= 6.76583E+02,
  TSC(8,19,6)= 6.76597E+02,
  TSC(8,20,6)= 6.76615E+02,
  TSC(8,21,6)= 6.76637E+02,
  TSC(8,22,6)= 6.76660E+02,
  TSC(8,23,6)= 6.76671E+02,
  TSC(8,24,6)= 6.76652E+02,
  TSC(8,25,6)= 6.76592E+02,
  TSC(8,26,6)= 6.76518E+02,
  TSC(8,27,6)= 6.76441E+02,
  TSC(8,28,6)= 6.75360E+02,
  TSC(8,29,6)= 6.74618E+02,
  TSC(8,30,6)= 6.74356E+02,
  TSC(8,31,6)= 6.74315E+02,
  TSC(8,32,6)= 6.74312E+02,
  TSC(8,33,6)= 6.74312E+02,
  TSC(8,34,6)= 6.74312E+02,
  TSC(8,35,6)= 6.74312E+02,
  TSC(8,36,6)= 6.74312E+02,
  TSC(8,37,6)= 6.74312E+02,
  TSC(8,38,6)= 6.74310E+02,
  TSC(8,39,6)= 6.74304E+02,
  TSC(8,40,6)= 6.74256E+02,

  TLC(1,1,3)=    6.73892E+02,    6.73892E+02,    6.73892E+02,
6.73892E+02, 6.73893E+02,
  TLC(1,2,3)=    6.73894E+02,    6.73893E+02,    6.73893E+02,
6.73893E+02, 6.73893E+02,
  TLC(1,3,3)=    6.73960E+02,    6.73936E+02,    6.73927E+02,
6.73922E+02, 6.73919E+02,
  TLC(1,4,3)=    6.74242E+02,    6.74188E+02,    6.74129E+02,
6.74093E+02, 6.74065E+02,
  TLC(6,1,3)= 6.73893E+02, 6.73893E+02, 6.73893E+02,
  TLC(6,2,3)= 6.73893E+02, 6.73893E+02, 6.73893E+02,
  TLC(6,3,3)= 6.73916E+02, 6.73914E+02, 6.73894E+02,
  TLC(6,4,3)= 6.74038E+02, 6.74008E+02, 6.73940E+02,
  TLC(8,5,3)= 6.73942E+02,
  TLC(8,6,3)= 6.73943E+02,
  TLC(8,7,3)= 6.73949E+02,
  TLC(8,8,3)= 6.73960E+02,
  TLC(8,9,3)= 6.73974E+02,
  TLC(8,10,3)= 6.73989E+02,
  TLC(8,11,3)= 6.74006E+02,
  TLC(8,12,3)= 6.74024E+02,
  TLC(8,13,3)= 6.74042E+02,
  TLC(8,14,3)= 6.74060E+02,
  TLC(8,15,3)= 6.74079E+02,
  TLC(8,16,3)= 6.74097E+02,
  TLC(8,17,3)= 6.74115E+02,
  TLC(8,18,3)= 6.74134E+02,
  TLC(8,19,3)= 6.74152E+02,
  TLC(8,20,3)= 6.74171E+02,
  TLC(8,21,3)= 6.74189E+02,
  TLC(8,22,3)= 6.74208E+02,
  TLC(8,23,3)= 6.74226E+02,
  TLC(8,24,3)= 6.74244E+02,
  TLC(8,25,3)= 6.74262E+02,
  TLC(8,26,3)= 6.74279E+02,
  TLC(8,27,3)= 6.74293E+02,
  TLC(8,28,3)= 6.74303E+02,
  TLC(8,29,3)= 6.74309E+02,
  TLC(8,30,3)= 6.74311E+02,
  TLC(8,31,3)= 6.74312E+02,
  TLC(8,32,3)= 6.74312E+02,
  TLC(8,33,3)= 6.74312E+02,
  TLC(8,34,3)= 6.74312E+02,
  TLC(8,35,3)= 6.74312E+02,
  TLC(8,36,3)= 6.74312E+02,
  TLC(8,37,3)= 6.74312E+02,
  TLC(8,38,3)= 6.74312E+02,
  TLC(8,39,3)= 6.74312E+02,
  TLC(8,40,3)= 6.74311E+02,

  UC(1,1,2)=    1.01086E-01,    2.00159E-01,    1.30842E-01,
1.16125E-01, 3.91206E-02,
  UC(1,2,2)=                                    3.80205E-03,
5.95853E-03,-8.08591E-03,-3.03029E-02,-5.33999E-02,

UC(1,3,2)=-2.99472E-02,-5.65321E-02,-5.84941E-02,-4.45316E
-02,-2.39185E-02,

UC(1,4,2)=-4.88007E-02,-9.90176E-02,-1.47969E-01,-1.39381E
-01,-2.89710E-02,
  UC(6,1,2)= 4.43463E-04,-1.80180E-09,
  UC(6,2,2)=-5.28344E-02,-3.96725E-02,
  UC(6,3,2)= 2.68301E-03, 2.72578E-02,
  UC(6,4,2)= 1.85708E-01, 4.70715E-01,


VC(1,1,2)=-1.01086E+00,-9.97439E-01,-8.86080E-01,-4.46875E
-01, 2.64604E-01,

VC(1,2,2)=-1.08690E+00,-1.05154E+00,-7.41381E-01,-1.69864E
-01, 5.88577E-01,

VC(1,3,2)=-4.88011E-01,-4.97472E-01,-4.91742E-01,-1.62318E
-01, 4.58509E-01,
  VC(6,1,2)= 1.30039E+00, 2.00670E+00, 1.90085E+00,
  VC(6,2,2)= 1.39131E+00, 1.94624E+00, 1.84239E+00,
  VC(6,3,2)= 1.14462E+00, 1.67748E+00, 1.88256E+00,
  VC(8,4,2)= 2.22944E+00,
  VC(8,5,2)= 3.80653E+00,
  VC(8,6,2)= 3.80653E+00,
  VC(8,7,2)= 3.80654E+00,
  VC(8,8,2)= 3.80655E+00,
  VC(8,9,2)= 3.80657E+00,
  VC(8,10,2)= 3.80659E+00,
  VC(8,11,2)= 3.80660E+00,
  VC(8,12,2)= 3.80662E+00,
  VC(8,13,2)= 3.80664E+00,
  VC(8,14,2)= 3.80666E+00,
  VC(8,15,2)= 3.80668E+00,
  VC(8,16,2)= 3.80670E+00,
  VC(8,17,2)= 3.80672E+00,
  VC(8,18,2)= 3.80674E+00,
  VC(8,19,2)= 3.80676E+00,
  VC(8,20,2)= 3.80678E+00,
  VC(8,21,2)= 3.80680E+00,
  VC(8,22,2)= 3.80682E+00,
  VC(8,23,2)= 3.80684E+00,
  VC(8,24,2)= 3.80686E+00,
  VC(8,25,2)= 3.80688E+00,
  VC(8,26,2)= 3.80690E+00,
  VC(8,27,2)= 3.80691E+00,
  VC(8,28,2)= 3.80692E+00,
  VC(8,29,2)= 3.80692E+00,
  VC(8,30,2)= 3.80692E+00,
  VC(8,31,2)= 3.80692E+00,
  VC(8,32,2)= 3.80692E+00,
  VC(8,33,2)= 3.80692E+00,
  VC(8,34,2)= 3.80692E+00,
  VC(8,35,2)= 3.80692E+00,
  VC(8,36,2)= 3.80692E+00,
  VC(8,37,2)= 3.80692E+00,
  VC(8,38,2)= 3.80692E+00,
  VC(8,39,2)= 3.80692E+00,
  VC(8,40,2)= 3.80692E+00,

  TGC(1,1)=    6.73887E+02,    6.73889E+02,    6.73890E+02,
6.73892E+02, 6.73892E+02,
  TGC(1,2)=    6.73891E+02,    6.73895E+02,    6.73897E+02,
6.73890E+02, 6.73893E+02,
  TGC(1,3)=    6.73893E+02,    6.73919E+02,    6.73932E+02,
6.73940E+02, 6.73918E+02,
  TGC(1,4)=    6.75650E+02,    6.75720E+02,    6.75719E+02,
6.75712E+02, 6.75650E+02,
  TGC(1,5)=    6.75605E+02,    6.75701E+02,    6.75729E+02,
6.75713E+02, 6.75660E+02,
  TGC(1,6)=    6.75597E+02,    6.75835E+02,    6.76025E+02,
6.76115E+02, 6.76122E+02,
  TGC(1,7)=    9.30256E+02,    9.27722E+02,    9.21971E+02,
9.12329E+02, 8.97707E+02,
  TGC(1,8)=    1.05277E+03,    1.04614E+03,    1.03393E+03,
1.01580E+03, 9.88156E+02,
  TGC(1,9)=    1.13033E+03,    1.12083E+03,    1.10358E+03,
1.07798E+03, 1.04302E+03,
  TGC(1,10)=    1.17792E+03,    1.16697E+03,    1.14644E+03,
1.11547E+03, 1.07302E+03,
  TGC(1,11)=    1.20272E+03,    1.19081E+03,    1.16854E+03,
1.13500E+03, 1.08907E+03,
  TGC(1,12)=    1.21320E+03,    1.20065E+03,    1.17802E+03,
1.14502E+03, 1.09787E+03,
  TGC(1,13)=    1.21905E+03,    1.20609E+03,    1.18298E+03,
1.14926E+03, 1.10324E+03,
  TGC(1,14)=    1.22420E+03,    1.21125E+03,    1.18812E+03,
1.15462E+03, 1.10648E+03,
  TGC(1,15)=    1.22740E+03,    1.21414E+03,    1.19035E+03,
1.15557E+03, 1.10858E+03,
  TGC(1,16)=    1.23118E+03,    1.21816E+03,    1.19409E+03,
1.15824E+03, 1.10896E+03,
  TGC(1,17)=    1.22971E+03,    1.21655E+03,    1.19288E+03,
1.15839E+03, 1.10931E+03,
  TGC(1,18)=    1.22731E+03,    1.21403E+03,    1.19035E+03,
1.15583E+03, 1.10880E+03,
  TGC(1,19)=    1.22683E+03,    1.21372E+03,    1.19033E+03,
```

```
1.15647E+03, 1.10789E+03,
  TGC(1,20)=    1.22696E+03,    1.21362E+03,    1.18974E+03,
1.15486E+03, 1.10771E+03,
  TGC(1,21)=    1.23050E+03,    1.21746E+03,    1.19338E+03,
1.15750E+03, 1.10821E+03,
  TGC(1,22)=    1.23053E+03,    1.21743E+03,    1.19385E+03,
1.15944E+03, 1.11042E+03,
  TGC(1,23)=    1.22775E+03,    1.21466E+03,    1.19129E+03,
1.15707E+03, 1.11048E+03,
  TGC(1,24)=    1.22039E+03,    1.20780E+03,    1.18523E+03,
1.15241E+03, 1.10507E+03,
  TGC(1,25)=    1.20165E+03,    1.18958E+03,    1.16753E+03,
1.13481E+03, 1.09044E+03,
  TGC(1,26)=    1.16973E+03,    1.15970E+03,    1.13927E+03,
1.10703E+03, 1.06169E+03,
  TGC(1,27)=    1.14440E+03,    1.13429E+03,    1.11350E+03,
1.07997E+03, 1.03168E+03,
  TGC(1,28)=    1.12873E+03,    1.11872E+03,    1.09779E+03,
1.06393E+03, 1.01376E+03,
  TGC(1,29)=    9.37328E+02,    9.24864E+02,    9.01629E+02,
8.67744E+02, 8.24320E+02,
  TGC(1,30)=    7.79116E+02,    7.70992E+02,    7.56811E+02,
7.38367E+02, 7.18608E+02,
  TGC(1,31)=    6.91977E+02,    6.90165E+02,    6.87240E+02,
6.83858E+02, 6.80644E+02,
  TGC(1,32)=    6.75286E+02,    6.75205E+02,    6.75069E+02,
6.74896E+02, 6.74712E+02,
  TGC(1,33)=    6.74388E+02,    6.74383E+02,    6.74376E+02,
6.74365E+02, 6.74352E+02,
  TGC(1,34)=    6.73850E+02,    6.73850E+02,    6.73850E+02,
6.73850E+02, 6.73850E+02,
  TGC(1,35)=    6.74312E+02,    6.74312E+02,    6.74312E+02,
6.74312E+02, 6.74312E+02,
  TGC(1,36)=    6.74311E+02,    6.73850E+02,    6.73850E+02,
6.73850E+02, 6.73850E+02,
  TGC(1,37)=    6.74310E+02,    6.74310E+02,    6.74310E+02,
6.74310E+02, 6.74310E+02,
  TGC(1,38)=    6.73850E+02,    6.73850E+02,    6.73850E+02,
6.73850E+02, 6.73850E+02,
  TGC(1,39)=    6.74247E+02,    6.74248E+02,    6.74249E+02,
6.74252E+02, 6.74255E+02,
  TGC(1,40)=    6.74232E+02,    6.74231E+02,    6.74228E+02,
6.74224E+02, 6.74216E+02,
  TGC(6,1)= 6.73252E+02, 6.72772E+02, 6.72829E+02,
  TGC(6,2)= 6.73891E+02, 6.73889E+02, 6.73889E+02,
  TGC(6,3)= 6.73916E+02, 6.73913E+02, 6.73894E+02,
  TGC(6,4)= 6.75557E+02, 6.75164E+02, 6.74047E+02,
  TGC(6,5)= 6.75611E+02, 6.74869E+02, 6.73982E+02,
  TGC(6,6)= 6.76094E+02, 6.79840E+02, 6.74096E+02,
  TGC(6,7)= 8.75569E+02, 8.52258E+02, 6.74456E+02,
  TGC(6,8)= 9.51217E+02, 9.15229E+02, 6.74771E+02,
  TGC(6,9)= 9.96263E+02, 9.52295E+02, 6.74981E+02,
  TGC(6,10)= 1.02026E+03, 9.71848E+02, 6.75119E+02,
  TGC(6,11)= 1.03277E+03, 9.81769E+02, 6.75207E+02,
  TGC(6,12)= 1.03951E+03, 9.86965E+02, 6.75263E+02,
  TGC(6,13)= 1.04405E+03, 9.90579E+02, 6.75303E+02,
  TGC(6,14)= 1.04654E+03, 9.92691E+02, 6.75335E+02,
  TGC(6,15)= 1.04841E+03, 9.94186E+02, 6.75361E+02,
  TGC(6,16)= 1.04861E+03, 9.94485E+02, 6.75384E+02,
  TGC(6,17)= 1.04874E+03, 9.94483E+02, 6.75403E+02,
  TGC(6,18)= 1.04848E+03, 9.94155E+02, 6.75421E+02,
  TGC(6,19)= 1.04751E+03, 9.93361E+02, 6.75438E+02,
  TGC(6,20)= 1.04747E+03, 9.93243E+02, 6.75455E+02,
  TGC(6,21)= 1.04788E+03, 9.93796E+02, 6.75474E+02,
  TGC(6,22)= 1.04985E+03, 9.95549E+02, 6.75496E+02,
  TGC(6,23)= 1.05042E+03, 9.96158E+02, 6.75513E+02,
  TGC(6,24)= 1.04585E+03, 9.92416E+02, 6.75519E+02,
  TGC(6,25)= 1.03285E+03, 9.80160E+02, 6.75502E+02,
  TGC(6,26)= 1.00398E+03, 9.47697E+02, 6.75474E+02,
  TGC(6,27)= 9.64683E+02, 8.91061E+02, 6.75451E+02,
  TGC(6,28)= 9.40996E+02, 8.30200E+02, 6.75113E+02,
  TGC(6,29)= 7.72565E+02, 7.13739E+02, 6.74568E+02,
  TGC(6,30)= 6.99939E+02, 6.83361E+02, 6.74344E+02,
  TGC(6,31)= 6.77837E+02, 6.75509E+02, 6.74314E+02,
  TGC(6,32)= 6.74538E+02, 6.74389E+02, 6.74312E+02,
  TGC(6,33)= 6.74339E+02, 6.74326E+02, 6.74312E+02,
  TGC(6,34)= 6.73850E+02, 6.74313E+02, 6.74313E+02,
  TGC(6,35)= 6.74312E+02, 6.74312E+02, 6.74312E+02,
  TGC(6,36)= 6.73850E+02, 6.74312E+02, 6.74311E+02,
  TGC(6,37)= 6.74310E+02, 6.74310E+02, 6.74312E+02,
  TGC(6,38)= 6.73850E+02, 6.74300E+02, 6.74308E+02,
  TGC(6,39)= 6.74261E+02, 6.74270E+02, 6.74294E+02,
  TGC(6,40)= 6.74204E+02, 6.74186E+02, 6.74235E+02,

  PSFC(1,1)=    2.38005E+05,    2.37990E+05,    2.37958E+05,
2.37958E+05, 2.37958E+05,
  PSFC(1,2)=    2.37875E+05,    2.37870E+05,    2.37863E+05,
2.37860E+05, 2.37859E+05,
  PSFC(1,3)=    2.38003E+05,    2.37999E+05,    2.37995E+05,
2.37992E+05, 2.37993E+05,
  PSFC(1,4)=    2.38226E+05,    2.38224E+05,    2.38216E+05,
2.38216E+05, 2.38222E+05,
  PSFC(1,5)=    2.00521E+05,    2.00549E+05,    2.00558E+05,
2.00553E+05, 2.00537E+05,
  PSFC(1,6)=    2.39763E+04,    2.39763E+04,    2.39763E+04,
2.39763E+04, 2.39763E+04,
  PSFC(1,7)=    2.39762E+04,    2.39762E+04,    2.39762E+04,
2.39763E+04, 2.39763E+04,
  PSFC(1,8)=    2.39762E+04,    2.39762E+04,    2.39762E+04,
2.39762E+04, 2.39763E+04,
  PSFC(1,9)=    2.39763E+04,    2.39763E+04,    2.39763E+04,
2.39763E+04, 2.39763E+04,
  PSFC(1,10)=    2.39763E+04,    2.39763E+04,    2.39763E+04,
2.39763E+04, 2.39763E+04,
  PSFC(1,11)=    2.39763E+04,    2.39763E+04,    2.39763E+04,
2.39763E+04, 2.39763E+04,
  PSFC(1,12)=    2.39763E+04,    2.39763E+04,    2.39763E+04,
2.39763E+04, 2.39763E+04,
  PSFC(1,13)=    2.39764E+04,    2.39764E+04,    2.39764E+04,
2.39764E+04, 2.39764E+04,
  PSFC(1,14)=    2.39764E+04,    2.39764E+04,    2.39764E+04,
2.39764E+04, 2.39764E+04,
  PSFC(1,15)=    2.39765E+04,    2.39765E+04,    2.39765E+04,
2.39765E+04, 2.39765E+04,
  PSFC(1,16)=    2.39765E+04,    2.39765E+04,    2.39765E+04,
2.39765E+04, 2.39765E+04,
  PSFC(1,17)=    2.39766E+04,    2.39766E+04,    2.39766E+04,
2.39766E+04, 2.39766E+04,
  PSFC(1,18)=    2.39767E+04,    2.39767E+04,    2.39767E+04,
2.39767E+04, 2.39767E+04,
  PSFC(1,19)=    2.39768E+04,    2.39768E+04,    2.39768E+04,
2.39768E+04, 2.39768E+04,
  PSFC(1,20)=    2.39769E+04,    2.39769E+04,    2.39769E+04,
2.39769E+04, 2.39769E+04,
  PSFC(1,21)=    2.39770E+04,    2.39770E+04,    2.39770E+04,
2.39770E+04, 2.39770E+04,
  PSFC(1,22)=    2.39771E+04,    2.39771E+04,    2.39771E+04,
2.39771E+04, 2.39771E+04,
  PSFC(1,23)=    2.39772E+04,    2.39772E+04,    2.39772E+04,
2.39772E+04, 2.39772E+04,
  PSFC(1,24)=    2.39773E+04,    2.39773E+04,    2.39773E+04,
2.39773E+04, 2.39773E+04,
  PSFC(1,25)=    2.39774E+04,    2.39774E+04,    2.39774E+04,
2.39774E+04, 2.39774E+04,
  PSFC(1,26)=    2.39775E+04,    2.39775E+04,    2.39775E+04,
2.39775E+04, 2.39775E+04,
  PSFC(1,27)=    2.39776E+04,    2.39776E+04,    2.39776E+04,
2.39776E+04, 2.39776E+04,
  PSFC(1,28)=    2.39776E+04,    2.39776E+04,    2.39776E+04,
2.39776E+04, 2.39776E+04,
  PSFC(1,29)=    2.39759E+04,    2.39759E+04,    2.39759E+04,
2.39759E+04, 2.39759E+04,
  PSFC(1,30)=    2.39758E+04,    2.39758E+04,    2.39758E+04,
2.39758E+04, 2.39758E+04,
  PSFC(1,31)=    2.39758E+04,    2.39758E+04,    2.39758E+04,
2.39758E+04, 2.39758E+04,
  PSFC(1,32)=    2.39758E+04,    2.39758E+04,    2.39758E+04,
2.39758E+04, 2.39758E+04,
  PSFC(1,33)=    2.39758E+04,    2.39758E+04,    2.39758E+04,
2.39758E+04, 2.39758E+04,
  PSFC(1,34)=    2.40000E+04,    2.40000E+04,    2.40000E+04,
2.40000E+04, 2.40000E+04,
  PSFC(1,35)=    2.39758E+04,    2.39758E+04,    2.39758E+04,
2.39758E+04, 2.39758E+04,
  PSFC(1,36)=    2.39758E+04,    2.40000E+04,    2.40000E+04,
2.40000E+04, 2.40000E+04,
  PSFC(1,37)=    2.39758E+04,    2.39758E+04,    2.39758E+04,
2.39758E+04, 2.39758E+04,
  PSFC(1,38)=    2.40000E+04,    2.40000E+04,    2.40000E+04,
2.40000E+04, 2.40000E+04,
  PSFC(1,39)=    2.39758E+04,    2.39758E+04,    2.39758E+04,
2.39758E+04, 2.39758E+04,
  PSFC(1,40)=    2.39758E+04,    2.39758E+04,    2.39758E+04,
2.39758E+04, 2.39758E+04,
  PSFC(6,1)= 2.37958E+05, 2.37958E+05, 2.37958E+05,
  PSFC(6,2)= 2.37866E+05, 2.37873E+05, 2.37896E+05,
  PSFC(6,3)= 2.37991E+05, 2.37976E+05, 2.37906E+05,
  PSFC(6,4)= 2.38221E+05, 2.38154E+05, 2.37704E+05,
  PSFC(6,5)= 2.00523E+05, 2.00302E+05, 2.35945E+05,
  PSFC(6,6)= 2.39763E+04, 2.39763E+04, 2.31802E+05,
  PSFC(6,7)= 2.39763E+04, 2.39763E+04, 2.31768E+05,
  PSFC(6,8)= 2.39763E+04, 2.39763E+04, 2.31735E+05,
  PSFC(6,9)= 2.39763E+04, 2.39763E+04, 2.31701E+05,
  PSFC(6,10)= 2.39763E+04, 2.39763E+04, 2.31668E+05,
  PSFC(6,11)= 2.39763E+04, 2.39763E+04, 2.31635E+05,
  PSFC(6,12)= 2.39763E+04, 2.39763E+04, 2.31601E+05,
  PSFC(6,13)= 2.39764E+04, 2.39764E+04, 2.31568E+05,
  PSFC(6,14)= 2.39764E+04, 2.39764E+04, 2.31535E+05,
  PSFC(6,15)= 2.39765E+04, 2.39765E+04, 2.31501E+05,
  PSFC(6,16)= 2.39766E+04, 2.39766E+04, 2.31468E+05,
  PSFC(6,17)= 2.39766E+04, 2.39766E+04, 2.31434E+05,
  PSFC(6,18)= 2.39767E+04, 2.39767E+04, 2.31401E+05,
  PSFC(6,19)= 2.39768E+04, 2.39768E+04, 2.31368E+05,
  PSFC(6,20)= 2.39769E+04, 2.39769E+04, 2.31334E+05,
  PSFC(6,21)= 2.39770E+04, 2.39770E+04, 2.31301E+05,
  PSFC(6,22)= 2.39771E+04, 2.39771E+04, 2.31267E+05,
  PSFC(6,23)= 2.39772E+04, 2.39772E+04, 2.31234E+05,
  PSFC(6,24)= 2.39773E+04, 2.39773E+04, 2.31201E+05,
  PSFC(6,25)= 2.39774E+04, 2.39774E+04, 2.31167E+05,
  PSFC(6,26)= 2.39775E+04, 2.39775E+04, 2.31134E+05,
  PSFC(6,27)= 2.39776E+04, 2.39776E+04, 2.31107E+05,
  PSFC(6,28)= 2.39776E+04, 2.39776E+04, 2.31080E+05,
```

```
 PSFC(6,29)= 2.39759E+04, 2.39759E+04, 2.31040E+05,
 PSFC(6,30)= 2.39758E+04, 2.39758E+04, 2.30975E+05,
 PSFC(6,31)= 2.39758E+04, 2.39758E+04, 2.30850E+05,
 PSFC(6,32)= 2.39758E+04, 2.39758E+04, 2.30659E+05,
 PSFC(6,33)= 2.39758E+04, 2.39758E+04, 2.30467E+05,
 PSFC(6,34)= 2.40000E+04, 2.39758E+04, 2.30367E+05,
 PSFC(6,35)= 2.39758E+04, 2.39758E+04, 2.30309E+05,
 PSFC(6,36)= 2.40000E+04, 2.40164E+04, 2.30251E+05,
 PSFC(6,37)= 2.39758E+04, 2.39758E+04, 2.30192E+05,
 PSFC(6,38)= 2.40000E+04, 2.39758E+04, 2.30134E+05,
 PSFC(6,39)= 2.39758E+04, 2.39758E+04, 2.30084E+05,
 PSFC(6,40)= 2.39758E+04, 2.39758E+04, 2.30034E+05,

 DAXDRC(7, 6)= 1.653,
 DAXDRC(7, 7)= 1.639,
 DAXDRC(7, 8)= 1.624,
 DAXDRC(7,25)= 1.613,
 DAXDRC(7,26)= 1.627,
 DAXDRC(7,27)= 1.638,
 DAXDRC(7,28)= 1.638,
&END

### power profile for C1 ###
 DAXDRC(7, 6)= 1.617,
 DAXDRC(7, 7)= 1.604,
 DAXDRC(7, 8)= 1.591,
 DAXDRC(7,25)= 1.674,
 DAXDRC(7,26)= 1.701,
 DAXDRC(7,27)= 1.722,
### power profile for C2 ###
 DAXDRC(7, 6)= 1.653,
 DAXDRC(7, 7)= 1.639,
 DAXDRC(7, 8)= 1.624,
 DAXDRC(7,25)= 1.613,
 DAXDRC(7,26)= 1.627,
 DAXDRC(7,27)= 1.638,
### power profile for C3 ###
 DAXDRC(7, 6)= 1.355,
 DAXDRC(7, 7)= 1.339,
 DAXDRC(7, 8)= 1.322,
 DAXDRC(7,25)= 1.236,
 DAXDRC(7,26)= 1.248,
 DAXDRC(7,27)= 1.258,

 TLC(4,7,5) =1.2000E+03,
 TLC(4,9,5) =1.2000E+03,
 TLC(4,13,5)=1.2000E+03,
 TLC(4,15,5)=1.2000E+03,
 TLC(4,18,5)=1.2000E+03,
 TLC(4,20,5)=1.2000E+03,
 TLC(4,23,5)=1.2000E+03,
 TLC(4,25,5)=1.2000E+03,

TLC(1,27,5)=1.2000E+03,1.2000E+03,1.2000E+03,1.2000E+03,1.
2000E+03,1.2000E+03,1.2000E+03,
```